



# Regime Analysis of the Rheology of Spherical and Non-spherical Particles

Muzahid Hossain

Student ID: 18130049

A thesis submitted in fulfilment of the requirement for the degree  
of  
**Doctor of Philosophy.**

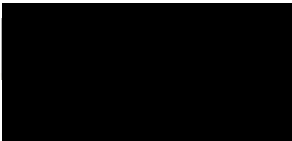
School of Computing, Engineering and Mathematics  
Western Sydney University, Australia

2018

# STATEMENT OF AUTHENTICATION

I, Muzahid Hossain, hereby declare this submission is my own work and to the best of my knowledge it contains no materials previously published or written by another person, nor materials which to a substantial extent has been accepted for the award of any other degree or diploma at UNSW or any other institute, except where due acknowledgment is made in the thesis. Any contribution made to the research by others, with whom I have worked at UNSW or elsewhere, is explicitly acknowledged in the thesis.

I also declare that the intellectual content of this thesis is the product of my own work, except to the extent that assistance from others in the project's design and conception or in style, presentation and linguistic expression is acknowledged.

(Signed) .....  .....

## **ACKNOWLEDGMENTS**

I would like to express my sincere gratitude to my supervisor, Professor Haiping Zhu, for giving me the opportunity to carry out this research project, always keeping my best interests in mind and acting as an excellent research role model. His very helpful advice and guidance are very much appreciated.

I also wish to thank Professor Aibing Yu, my co-supervisor, for his support to this research project. I wish to thank Western Sydney University (WSU) and the University of New South Wales (UNSW) for providing me with the postgraduate scholarship, which made this work possible.

Thanks also go to Dr. Kejun Dong and Dr. C.S. Campbell for their valuable suggestions and discussions.

I wish to thank my father for his continuous encouragement and support during the four years of my study in Australia.

Finally, my most special thanks go to my wife, Summa Tahira for supporting me by managing at home. Gratitude is also extended to my university friends and their company during the period of my study.

# ABSTRACT

In the early stages of granular rheology, the majority of analytical studies were based on granular assembly consisting of spherical particles. This was due to geometric simplicity and feasibility when calculating dynamic variables. Furthermore system limitation emerged as a problem when investigating more complex and realistic considerations. However, in the contemporary research field, with the steadily increasing ability to perform more complex computations and with available resources, attention has focused on non-spherical particles because of their deeper relevance to practical applications.

In this work, a 3D shear cell model is developed based on the Discrete Element Method using the commercial software platform “PFC” to study non-spherical particles’ flow characteristics. A comparison is made with those of spherical assemblies. Firstly, the simulation model of annular shear cell consisting of spherical particles is tested with PFC and this agreed well with previous results, thus justifying the use of this tool to analyse the non-spherical level.

Then the effect of platen roughness is investigated on spherical particle assembly from the microdynamic perspective, in order to establish a correlation between platen roughness and granular flow dynamics. This is undertaken in terms of particle size that is used to construct the platens. It is found that linearity and non-linearity of gradient profile across several important parameters are distinguishing features affected by variations in platen texture.

The externally applied load is the most important aspect that bridges studies where gravity is considered and yet often overlooked. This point is established through in-depth investigation of granular flow in presence and absence of gravity where comparison of an number of flow characteristics is presented.

Following this, the effects of particle shape are microdynamically investigated with reference to aspect ratio of non-spherical (ellipsoidal) particles and compared with spherical particles. The following key properties - particle linear velocity, angular velocity, contact normal force, contact shear force, total contact force, total contact moment and porosity - are

analysed to explain the effect of variation of the above-mentioned geometric properties on each of these parameters.

Then, macrodynamic analysis is performed in a comparative study between spherical particles and ellipsoidal particles of varying aspect ratios with focus on the variables that are important in general constitutive model such as velocity, density and stress tensors. Physics underlying the observation is discussed to highlight effect of particle aspect ratio.

Finally and most importantly, regime transition of ellipsoidal particle assembly is contrasted with the findings for spherical particles. In this study, the techniques that are generally used to identify regime transition for granular rheology of spherical particles are tested on flow of non-spherical (ellipsoidal) particles of varying shapes (aspect ratios). This includes correlation between elastically scaled force, kinetically scaled force, coordination number, apparent coefficient of friction and porosity. Some observations are found to be similar and useful for non-spherical particles while others found not suitable for non-spherical particles.

# TABLE OF CONTENTS

---

	<b>Statement of Authentication</b>	2
	<b>Acknowledgement</b>	3
	<b>Abstract</b>	4
	<b>Table of contents</b>	6
	<b>List of tables</b>	11
	<b>List of figures</b>	11
	<b>List of symbols and abbreviations</b>	18
	<b>List of publications</b>	20
<b>1</b>	<b>Introduction</b>	21
<b>2</b>	<b>Literature review</b>	25
2.1	Introduction to granular rheology	25
2.2	Modelling granular rheology	29
2.2.1	Discrete element method	30
2.2.2	Averaging method	39
2.3	Regime transition of flow of granular materials	42
2.3.1	Flow regimes	42

---

2.3.2	Regime transition	46
2.4	Background and associated challenges in the study of non-spherical particles	48
2.5	Shear flow of granular materials	53
2.5.1	Popular shear testers	54
2.5.2	Relevant studies using shear cell	61
2.5.2.1	Numerical studies	62
2.5.2.2	Experimental studies	68
2.6	Remarks	72
<b>3</b>	<b>Linearity and non-linearity of velocity profile of solid flow in a shear cell: Effect of platen roughness</b>	<b>73</b>
3.1	Introduction	74
3.2	Simulation method and conditions	75
3.2.1	DEM overview	75
3.2.2	Preparation of model	78
3.2.3	DEM simulation and conditions	81
3.3	Results and discussion	82
3.3.1	Velocity field	82
3.3.1.1	Translational velocity	82
3.3.1.2	Angular velocity	87

3.3.2	Force field	91
3.3.2.1	Contact force	91
3.3.2.2	Contact moment	96
3.3.3	Packing structure	99
3.4	Conclusion	102
<b>4</b>	<b>Role of gravity in the flow of particles in a shear cell</b>	<b>104</b>
4.1	Introduction	105
4.2	Simulation conditions	106
4.3	Results and discussion	108
4.3.1	Velocity field	108
4.3.2	Coordination number and porosity	111
4.3.3	Contact force	114
4.3.4	Stress tensors	118
4.4	Conclusion	124
<b>5</b>	<b>Microdynamic analysis of ellipsoidal particle flow in a shear cell</b>	<b>126</b>
5.1	Introduction	127
5.2	Simulation method and conditions	129
5.3	Results and discussion	131
5.3.1	Particle alignment	131



5.3.2	Velocity field	135
5.3.3	Porosity	143
5.3.4	Contact force	146
5.3.5	Energy analysis	154
5.3.6	Role of particle alignment on volume fraction	158
5.4	Conclusion	162
<b>6</b>	<b>Macrodynamic analysis of granular rheology for Ellipsoidal and Spherical Particle Assemblies in a Model Annular Shear Cell</b>	<b>165</b>
6.1	Introduction	166
6.2	Simulation method and conditions	167
6.3	Results and discussion	169
6.3.1	Density and velocity	169
6.3.2	Stresses	174
6.3.3	Forces	180
6.3.4	Relationship between shear and normal forces and stresses	183
6.3.5	Inertial number	185
6.3.6	Effect of particle friction coefficient	189
6.4	Conclusion	195
<b>7</b>	<b>Regime transition of non-spherical particle flow in shear cell</b>	<b>198</b>

---

7.1	Introduction	199
7.2	Simulation	200
7.3	Results and discussion	202
7.3.1	Determination of regime transitions	202
7.3.2	Structural analysis	215
7.3.3	Force statistics	218
7.3.4	Shear to normal stress ratio	222
7.3.5	Coordination number	225
7.3.6	Effect of aspect ratio on regime transition	227
7.4	Conclusion	228
<hr/>		
<b>8</b>	<b>Summary and future work</b>	<b>230</b>
8.1	Summary	230
8.2	Future work	235
<hr/>		
<b>9</b>	<b>Reference</b>	<b>237</b>

---

## LIST OF TABLES

---

2.1	Two popular numerical models	39
3.1	Parameters used in the simulations	80
4.1	Parameters used in the simulations	108
5.1	Parameters used in the simulations	131
6.1	Parameters used in the simulations	168
7.1	Data point between quasistatic and intermediate regime	209
7.2	Data point between inertial and intermediate regime	210

---

## LIST OF FIGURES

---

2.1	Particle contact model	33
2.2	Particle interaction in steps	33
2.3	Particle contact dynamics	35
2.4	Fundamental flow diagram of a basic DEM process	36
2.5	A two-dimensional schematic illustration of the concepts of probe point, and interior and exterior cells	41
2.6	Granular flows at different regimes and their corresponding constitutive behavior	43

---

2.7	Regime map in different literature	48-49
2.8	Configuration of Jenike's shear Cell	55
2.9	Configuration of triaxial cell	57
2.10	Configuration of biaxial test	59
2.11	Uniaxial test step by step	61
2.12	Configuration of annular shear cell	55
2.13	Variation of overall mean particle velocity $V_x$ at different conditions	64
3.1	Simulated model shear cell (a: platen particle dia. 0.9d, b: platen particle dia. 1.5d)	79
3.2	a) Scaled velocity gradient profile of particle assembly for cases with different platens constituting monodispersed particles with sizes of 0.9d, 1.1d, 1.3d, 1.5d and 1.7d, respectively; b) gradient profile of scaled standard deviation of particle scale velocities ( $V_x$ ) for previously mentioned cases. c) Overall averaged values particle linear velocity (in x-direction) adjacent to platen for platen constituting particles of different sizes, $\sqrt{(gd)}$ .	85-86
3.3	a) Scaled particle angular velocity at different levels along the z-direction for varying platen roughness b) probability distribution of scaled angular velocity for the platens' varying texture c) Overall time-averaged values particle angular velocity adjacent to platen for different platen-constituting particle sizes (rad/s) d) time-averaged overall angular velocity for different cases (rad/s)	88-89
3.4	Figure 3.4: a) Scaled total particle force from normal contacts at varying heights of shear cell with 5 different platen roughness b) probability distribution of scaled contact normal force for different cases c) average	93-94

	particle force for all cases ( $\pi\rho d^3g/6$ )	
3.5	Contact force network of assembly particles for a slice yz plane for a) 0.9d and b) 1.7d	95
3.6	a) Scaled total contact moment at varying heights of shear cell with 5 different levels of platen roughness b) probability distribution of scaled contact for these different cases	96-97
3.7	Graph depicting the relationship between overall volume fraction and platen roughness with remaining considerations being kept the same	100
3.8	Time-averaged spatial distribution of porosity in generated yz-plane the cell for different platen roughness: a) 0.9d b)1.1d c)1.3d d)1.5d e)1.7d, here, W is the width of the cell in y direction	101
4.1	Simulated model shear cell	107
4.2	Scaled velocity gradient profiles in various conditions: a) with gravity, and b) without gravity (units of load are given by 'L' ( $= \pi\rho dg/6 \times 10^5$ ) and units of shear rate 's')	110
4.3	Distributions of: a) coordination number, and b) porosity in various conditions	112
4.4	Relationship between coordination number and porosity at the conditions of: a) high load, and b) low load	113-14
4.5	Distributions of the total contact force in various conditions	115
4.6	Contact force network in the yz plane for: a) low load with gravity, b) high load with gravity, c) low load without gravity, and d) high load without gravity	116-17
4.7	Distributions at high load condition for: a) stress-xx, and b) stress-zz, and at low load condition for: c) stress-xx, and d) stress-zz	119-21

4.8	Distributions of stress-xz at: a) high load, and b) low load conditions	122
4.9	Correlation of stress-zz with stress-xz at: a) low load, and b) high load	123
5.1	Simulated model shear cells with: a) spherical particles, and b) ellipsoidal particles with aspect ratio 2.5:1)	130
5.2	Flow patterns of assemblies of particles with aspect ratios: a) 1.0, b) 2.5, and c) 5.0.	132
5.3	PDF of orientation of particles: a) y-euler (pitch angle of the particle about y-axis) b) z-euler (roll angle of the particle about z-axis)	133
5.4	Distributions of the orientation angle of the particles with respect to the streamlines for (a)-(c) least, medium and highest aspect ratios, respectively. In each case rice, glass cylinders and our simulation data are compared	134-35
5.5	Velocity fields for assemblies of particles	136-37
5.6	a) Scaled velocity gradient for different particle assemblies in identical properties and base conditions. $V_x$ and $V$ are the average velocity of particles at a layer and shear velocity of the platens, respectively, and $h$ and $H$ are the layer height and segment height, respectively. b) Normal distribution of scaled velocities of spherical and ellipsoidal particles	138-39
5.7	a) Time-space averaged particle velocity fluctuation at different laminar layers of flow for particle assemblies with constituents of different aspect ratios b) average standard deviation of particle velocity with respect to aspect ratio	140
5.8	a) Variation of angular velocities along height of cell for different particulate assemblies b) average particle angular velocity of the assembly for particle constituents with different aspect ratios	142

5.9	Variation of statistical distribution of particle angular velocities with aspect ratio	143
5.10	Spatial distribution of porosity of ellipsoidal particle assemblies with different aspect ratios: a) 1.0 (spherical), b) 1.75, c) 2.5, d) 3.75, and e) 5.0	144
5.11	Effect of aspect ratio on overall porosity	145
5.12	Contact force network for a) spherical particle assembly and b) ellipsoidal particle assembly	147
5.13	a) Average particle total contact force of the assemblies with constituents of varying aspect ratios, b) particle total contact force gradient profile (	148-49
5.14	Correlation of aspect ratio with a) total normal force of assembly, b) average normal force per contact, c) total shear force of assembly and d) average shear force per contact	150-51
5.15	Probability distribution of a) normal force and b) shear force	153
5.16	Gradient profile for average scaled a) dashpot energy per contact, b) slip energy per contact and c) strain energy per contact, d) relationship between average scaled contact energies and particle aspect ratio	155-56
5.17	Overall fluctuation of energy within individual particles (standard deviation) for a) damping energy and b) slip energy	157
5.18	Probability distribution of particle orientation angle about y-axis for particle assembly subjected to different loads at shear rates a) $1.07\sqrt{(gd)}$ , b) $4.02\sqrt{(gd)}$ and c) $12.8\sqrt{(gd)}$	159-60
5.19	Relationship between particle orientation angle and volume fraction for different combinations of externally applied load and induced shear velocity	161

6.1	Example of spherical regions to obtain data for stress, density and velocity	168
6.2	Contour plot of particle density for a) spherical particle assembly, b) ellipsoidal particle assembly	170
6.3	a) variation of macrodynamic value of density across the flow in y axis; b) relationship with density of assembly and particle aspect ratio	171-72
6.4	Scaled velocity distribution of a) spherical particle assembly, b) ellipsoidal particle assembly	173
6.5	Variation of the magnitude of stress tensor components along the y-axis: (a) $T_{xx}$ , (b) $T_{yy}$ , (c) $T_{zz}$ , and (d) $T_{xz}$ for particles of four different aspect ratios (spherical, 2.5:1, 3.75:1 and 5:1). Note that different scales are used for stress components.	175-76
6.6	Effect of particle aspect ratio on a) $T_{xx}$ , b) $T_{yy}$ , c) $T_{zz}$ and $T_{xz}$	177-79
6.7	Effect of particle aspect ratio on $T_{xz}/T_{zz}$	180
6.8	Spatial distribution of normal and shear forces for spherical particles in a) and b), respectively, and for ellipsoidal particles (2.5:1 aspect ratio) in c) and d), respectively	181-82
6.9	Relationship between shear and normal contact force for a) spherical and b) ellipsoidal particles	184
6.10	Relationship between externally shear and normal stress	185
6.11	Spatial distribution of inertia number for left: spherical and right: ellipsoidal particles	186-87
6.12	Relationship between friction coefficient and inertia number (left spherical, right: ellipsoidal)	188
6.13	Effect of aspect ratio on overall inertia number	189



6.14	Probability distribution of density of particle assembly (volume fraction) for different particle friction coefficients a) spherical b) ellipsoidal	190-91
6.15	Probability distribution of different stress components for spherical particles and ellipsoidal particles (base case: friction coefficient 0.5)	192-95
7.1	Variation in elastically scaled applied stress ( $\sigma^*$ ) with packing fraction ( $\nu$ ) for different values of scaled stiffness in a), c), e), g) and i). Also, variation in kinetically scaled applied stress ( $\sigma'$ ) with packing fraction ( $\nu$ ) for different values of scaled stiffness in b), d), f), h) and j) for spherical particles, ellipsoidal particles of 1.75:1, 2.5:1, 375:1 and 5:1 aspect ratios, respectively	204-08
7.2	Regime map in the parametric space of: ( $\sigma^*, k^*$ ) in a), c), e), g) and i) and ( $\sigma', k^*$ ) in b), d), f), h) and j) for spherical particles, ellipsoidal particles of 1.75:1, 2.5:1, 375:1 and 5:1 aspect ratios, respectively	211-15
7.3	Networks of scaled forces ( $f = F_n / \langle F_n \rangle$ ), $\sigma^*$ and $\nu$ when $k^* = 2920$ different loads for ellipsoidal particles of 2.5:1 aspect ratio	216-17
7.4	Probability density distributions of the scaled normal forces ( $f = F_n / \langle F_n \rangle$ ) for different $\sigma^*$ 's at low shear and high shear for spherical and ellipsoidal particles (2.5:1 aspect ratio), respectively	219-20
7.5	Variation in the power index $n$ with volume fraction for high and low shear rate for a) spherical and b) ellipsoidal particles	221-22
7.6	Relationship between shear to normal stress ratio and volume fraction for high and low shear rate for a) spherical and b) ellipsoidal particles (2.5:1 aspect ratio)	224
7.7	Correlation between coordination number and volume fraction at different scaled stiffness for a) spherical particles and b) ellipsoidal particles of 2.5:1 aspect ratio	226

## LIST OF SYMBOLS AND ABBREVIATIONS

Symbol	Description	Unit
$m_i$	mass of particle 'i'	Kg
$V_i$	velocity of particle 'i'	m / s
t	elapsed time	s
$F_{ij}^c$	Contact force applied by particle 'i' on particle 'j'	N
$F_i^g$	gravitational force on particle 'i'	N
$I_i$	inertia of particle 'i'	Kg / m <sup>2</sup>
$\omega_i$	angular velocity of particle 'i'	rad / s
$M_{ij}$	angular moment of particle 'i' with respect to particle 'j'	N-m
$F_d$	damping or dashpot force	N
$F_l$	linear force	N
$F_c$	contact force	N
$M_c$	contact moment	N
$F_n^d$	damping force in normal direction	N
$F_s^d$	damping force in shear direction	N
$F_n^l$	linear force in normal direction	N
$F_s^l$	linear force in shear direction	N
$g_s$	gravitational spring constant	N-m / s <sup>2</sup>
$k_n$	spring constant (stiffness coefficient) in normal direction	N-m / s <sup>2</sup>
$k_s$	spring constant (stiffness coefficient) in shear direction	N-m / s <sup>2</sup>
$\mu$	friction coefficient	( - )
$\beta_s$	damping constant in shear direction	N-s / m
$\Delta_{ij}$	deformation (strain) rate between particles 'i' and 'j'	m / s
T	granular temperature	<sup>0</sup> K
u	velocity fluctuation	( - )
$\sigma^*$	dimensionless elastically scaled stress	m / s
$\sigma'$	dimensionless kinetically scaled stress	( - )
B	dimensionless shear rate	( - )
$k^*$	dimensionless scaled stiffness	( - )
$B_0^*$	scaled cohesiveness	( - )
$F_{vdW}^{max}$	the cohesive force exerted by a particle on a contacting particle	N
$\sigma_1$	major principal stress on platen with boundaries around particles	N / m <sup>2</sup>

$\sigma_c$	critical principal stress on platen without boundaries around particles at which cracks appear in the assembly	$N / m^2$
$g$	gravity	$m / s^2$
$H$	height of particle assembly / distance between upper and lower platen	$m$
$R_i$	inner radius of annular shear cell	$m$
$R_s$	split radius of annular shear cell	$m$
$R_o$	outer radius of annular shear cell	$m$
$\Omega$	angular velocity	$rad / s$
$\hat{n}_c$	vector normal to the contact surface	( - )
$F_h$	Hertz contact force	$N$
$\alpha$	non-linearity exponent for Hertz contact force	( - )
$G$	shear modulus of particles	$GPa$
$\bar{R}$	effective radius of a pair of particles	$m$
$m_{eqv}$	equivalent mass of a pair of particles	$Kg$
$\theta$	poisson's ratio	( - )
$\sqrt{gd}$	unit of scaled particle linear velocity	( - )
$\sqrt{g/d}$	unit of scaled particle angular velocity	( - )
$\pi\rho dg/6$	unit of scaled particle contact pressure, stress	( - )
$\pi\rho d^3 g/6$	unit of scaled particle contact force	( - )
$\pi\rho d^4 g/6$	unit of scaled particle contact energy, moment	( - )
$T_{xx}, T_{yy}$ and $T_{zz}$	Principal stress tensors parallel to x, y and z directions respectively	$N / m^2$
$T_{xz}$	Shear stress tensor	$N / m^2$
$V$	volume	$m^3$
$F_{xx}$	force in x-direction	$N$
$N_c$	number of contacts	( - )
$L_{xx}$	branch vector along which force acts	( - )
$I$	inertia number	( - )
$P$	pressure on particle	$N / m^2$
$W$	width of shear cell (extent in y-direction)	$m$
$v$	volume fraction	( - )

Kg: Kilogram, m: meter, s: second, Pa: pascal, G: Giga, rad: Radian, N: Newton, K: Kelvin

## ABBREVIATIONS

PDF: probability distribution function

DEM: Discrete element method

Eg. : For example

PFC3D: Particle flow code three-dimensional

CFD: Computational fluid dynamics

FEA: Finite element analysis

## LIST OF PUBLICATIONS

1. Hossain, M., Zhu, H., A. Yu (2017) "*Comparison of Regime Transition between Ellipsoidal and Spherical Particle Assemblies in a Model Shear Cell.*" International Journal of Mechanical, Aerospace, Industrial, Mechatronic and Manufacturing Engineering 11(2): 267-272.
2. Hossain, M., Zhu, H., A. Yu (2015). "*Microdynamic analysis of ellipsoidal particle flow in a shear cell.*" IV International Conference on Particle-based Methods – Fundamentals and Applications, PARTICLES 2015: 833-841.
3. Hossain, M., Zhu, H., A. Yu (2016). "*Microdynamic analysis of effect of gravity on granular rheology in a shear cell.*" The 12th International Conference on Bulk Materials Storage, Handling and Transportation (ICBMH 2016), Engineers Australia: 341-348
4. Hossain, M., Zhu, H., A. Yu (2017). "*Role of gravity in the flow of particles in a shear cell.*" International Journal of Trends in Chemical Engineering:, vol 16, 15-29
5. Hossain, M., Zhu, H., A. Yu (2017). "*Particle Alignment and Volume Fraction for Ellipsoidal Particles.*" 1st International Conference on Water and Environmental Engineering (iCWEE2017), 20-22 Nov 2017, Sydney, Australia: 69-75.
6. Hossain, M., Zhu, H., A. Yu (2018). "*Numerical investigation on effect of particle aspect ratio on the dynamical behaviour of ellipsoidal particle flow.*" (Under Review)

# Chapter 1: Introduction

The study of granular rheology is a popular topic emerging from the recent industrial research field because of its relevance to the mechanics that take place in a variety of activities in the industry. The complex nature of granular flow behavior makes it essential to study it both at the macromechanical level by using computational fluid dynamics as well as at the micromechanical level through Newton's laws of motion. Macromechanical studies of granular flow are easier to perform through experimental work. It is difficult, if not impossible, to ascertain the microdynamic behavior through practical experiments. This is because extracting data from the practical experiments at a micro-level is expensive. Moreover, indirect linking of data from sample particles to the aggregate flow is likely to be unrepresentative of realistic phenomena because of the inherent uncertainty. Yet, they contribute greatly to obtaining a better understanding of the subject.

To compensate for the drawbacks of experimental work, numerical models were developed. The numerical study of granular rheology at the microdynamic level goes back as far as 1881 when Hertz proposed a theory to describe the elastic contact between two spheres in a normal direction [1]. The study of granular flow mechanics was revolutionized with the development of the Discrete Element Method (hereafter referred to as DEM) by Cundall and Strack which uses simple tools for Newton's laws of motion [2-4] to explain the collective behavior of granular assembly during motion. This is done by combining each constituent particle's individual resultant characteristics in a dynamic process. It could not be utilized to a significant extent during that period due to system constraint, i.e. limitations with computational capacity. With the rapid advances in technology, the computational capacity greatly improved and provided the opportunity to use DEM in a more effective level. Realistic phenomena can be simulated to study the behavior in a much more efficient method which, otherwise, was not experimentally practicable. Thus, the good link between experimental work and numerical analysis in granular rheology was strongly emphasized by researchers who wanted to obtain reliable data of ambiguous phenomena.

In striving to obtain better knowledge of the mechanism, the greatest challenge in the research area of granular rheology has been to develop a universal model to describe the flow nature of particles in order to predict and consequently control it. Currently, however, researchers are far from achieving the model that can explain the granular dynamics throughout its entire regime. Nevertheless, promising developments have occurred following important findings for regime transitions [5-8] which narrowed the researchers' focus to identify the key elements describing this remarkable phenomenon. Here the goal was to create a constitutive model [6, 8, 9]. In the direction of that goal, flow regimes helped researchers to divide particle flow dynamics into parts. so that each part could be uniquely identified and explained. With good agreements between experimental findings and numerical simulations, there is now a better knowledge of phases and corresponding phase transitions of particle flow. However, the majority of studies were based on granular assembly consisting of spherical particles. This was because of its simplicity and feasibility in calculation as well as logistical limitations in computational ability.

In the contemporary research field, attention has focused on the non-spherical particles because of their steadily increasing ability to perform more complex computations with available resources. It is becoming more feasible to study the non-spherical particles extensively in numerous directions to obtain findings with deeper relevance to practical applications (eg. [10]). There is a chronology to understanding how this research field developed alongside technological advances [11, 12]. To the best of the author's knowledge, shear flow of non-spherical particles has not been explored much compared to spherical particles and this makes the topic worthwhile. Therefore, extending the work done by Wang et al. [13, 14], a 3D model in PFC software is developed where non-spherical particle flow characteristics will be studied and compared with the spherical model. The simulation model for the annular shear cell comprising spherical particles were tested with PFC and agreed well with previous results. This justifies employing the tool to further study the non-spherical level.

The study seeks to better understand granular rheology of non-spherical particles at the microdynamic level. The ellipsoidal particle is chosen due to the fact that it is presumably the closest to the geometric features of spherical assembly and will provide more analogous results for understanding non-spherical particles. Consequently, this will progress the field one step closer to the general constitutive model for describing granular dynamics.

Specific topics covered in this thesis are as follows:

1. Investigating the effect of platen roughness on granular rheology in shear cell at the microdynamic scale.
2. Studying the effect of gravity on granular flow in shear cell.
3. Analysing granular flow behavior of ellipsoidal particles in an annular shear cell at a *microdynamic* level and comparing it to spherical particle assembly and evaluating the effects of aspect ratio on different flow characteristics.
4. Analysing granular flow behavior of ellipsoidal particles in an annular shear cell at a *macro-dynamic* level and comparing it to spherical particle assembly and assessing the effects of aspect ratio on different flow characteristics.
5. Conducting comparative research on the regime transition of ellipsoidal particle flow in a shear cell at particle scale, in order to correlate to spherical particle assembly, and discovering the effects of particle shape on regime transition.

Chapter 2 is the literature review where it discusses the background knowledge on this topic. It provides a solid foundation of knowledge for better understanding the context. This chapter covers introduction to granular rheology, different approaches to modelling granular rheology, different regimes and regime transition in granular flow, development in research field on non-spherical particles, key differences between spherical and non-spherical particles and different methods of construction of non-spherical particles.

Chapter 3 focuses on granular rheology of spherical particle assembly and how it is affected by boundary condition. In studying boundary condition, the boundary roughness of the platens in shear cell varies by changing the size of the particles used to construct it in order to detect a relationship between particle flow characteristics and boundary roughness in terms of particle size. This study offers a simpler alternative novel method of studying the important features of boundary roughness influence on granular rheology.

Chapter 4 highlights the effect of gravity on granular flow study in otherwise similar conditions, in shear cell. This is important because many studies consider gravity while other analyses do not. This study identifies a researcher's need to focus on ensuring the investigation is not affected by gravity. This work is important for understanding the part played by gravity in the core project described in this thesis.

Chapter 5 firstly validates PFC3D 5.0 for studying granular rheology of spherical and non-spherical particles. Here the results from previous publications [9, 13, 14] based on the annular shear model constituting the granular assembly of spherical particles are followed to regenerate qualitatively similar results in the PFC platform and compare them with existing ones. Secondly, the objective here is primarily concerned with microdynamic analysis of ellipsoidal particle flow in a shear cell and a comparison with spherical particles. Among the key properties – particle velocity, porosity, velocity, contact force and energy - will be thoroughly investigated for ellipsoidal particles and compare them with spherical particles [13]. This will lead to a better understanding of the characteristics of rheological behavior of ellipsoidal particles.

Chapter 6 focuses on macrodynamic properties of granular rheology of spherical and ellipsoidal particles, particularly those which are popularly considered in developing constitutional model of granular rheology, such as average values stress tensors, velocity, inertia number, particle friction coefficient and assembly friction coefficient. Particles of spherical and ellipsoidal shapes of 4 types of elongation are studied through annular shear cell to identify the outcome in terms of particle aspect ratio. I-rheology is tested between spherical and ellipsoidal particulate flow. The effect of particle elongation is observed when employing this approach.

Chapter 7 discusses the regime transition of non-spherical (ellipsoidal) particles in an annular shear cell. The primary concern is the relationship between volume fraction, shear velocity and applied external load. Also investigated here is the structure of the force chain network and regime map. The effectiveness of the novel power index method from [9] and coordination number that help identify the regime transition points of flow for ellipsoidal particle assembly is further investigated. Finally, the influence of particle elongation is observed here.

Chapter 8 summarises the important findings and conclusions from the work done under this thesis. Further it discusses on the future scopes of work as extension to this study.



# Chapter 2: Literature Review

## 2.1. INTRODUCTION TO GRANULAR RHEOLOGY

Granular materials comprise microscopic to mesoscopic particles that are part of our daily lives; yet they demonstrate the most complex nature in the world of dynamics. From cooking rice at home to burning pulverized coal in a power station, from using a grinder mixer in the construction of cities to the manifestation of landslides in the mountains, countless phenomena represent granular materials with regards to rheology. Although commonplace, it has the most unique characteristics of rheology and is affected by numerous parameters and conditions in the case of pure fluid or pure solid materials.

The study of granular rheology is related to small particles which are not small enough (to the level of molecular size) so that their properties of rigid bodies can be overlooked. Yet again they are not large enough which allows them to collectively produce somewhat fluid-like phenomena (for example, taking the shape of a container) while in a static condition but more pronouncedly in motion (for example, viscous fluidity). A well-illustrated comparison is made by Jaeger [15] between granular matter and fluid matter in terms of flow characteristics. Such unique characteristics can be seen in natural occurrences: firstly, avalanches, landslides; and secondly, industrial processes such as coal industry, food industry, pharmaceutical industry. Both the fluid-like and Newtonian solid-like characteristics are investigated for a reasonable extent of time both individually [2, 16] as well as in combination [17]. An interesting analogy of granular assembly with glass is made by Corwin et al. [18] as follows: “Glasses are rigid, but flow when the temperature is increased. Similarly, granular materials are rigid, but become unjammed and flow if sufficient shear stress is applied. The rigid and flowing phases are strikingly different, yet measurements reveal that the structures of glass and liquid are virtually indistinguishable.” Some unique characteristics of granular assembly that distinguish granular properties from fluid properties are as follows:

1. *Shape of assembly*: Liquid cannot take any stand-alone shape while a heap of granular material can have various shapes. For example, if water falls from a hopper to the ground it will spread. On the other hand, sugar falling from a hopper to the ground will take the shape of a cone. However, both can take the shape of a container vessel so that sugar will take the shape of its container jar just as water would in a bottle.

2. *Hysteresis*: The flow behavior of granular rheology is significantly affected by its initial form or position as well as how it formed into that shape / position, i.e. a memory of initial condition. That means, two identical instantaneous dynamic phenomena can lead to very different results based on their history.

3. *Angle of repose and angle of stability*: for liquid, there is no angle of repose or stability and it will fall due to gravity until it reaches an equilibrium state on the basis of cohesion. In the case of granular material, the assembly is stationary below the angle of repose and spontaneously flowing above the angle of stability. Between the two angles, the assembly can either be at rest or in motion, a state that is referred to as 'bi-stability'. This metastable state is affected by hysteresis.

4. *Couette flow (flow at boundary layer)*: Granular particles flow in laminar layers even if the assembly consists of identical isotropic spherical particles. In the case of liquid, the gradient of the flow is much wider than that of granular material.

5. *Ineffectiveness of height* (after a certain level) on the weight at the bottom of container: the higher a column of liquid in a container, the more weight the base of the container has to carry. However, for granular assembly, after a certain height, the load on the base remains constant due to the wall friction carrying excess loads from the height.

6. *Arching*: In study of granular matter, arching often occurs from compaction heterogeneity with height where less dense assembly is observed below high dense assembly; however, this sort of heterogeneity is not observed in the case of fluid. This occurs due to the fact that nano-particles in the fluid create isotropic pressure in the surrounding environment and the internal energy is perfectly distributed. Conversely, force distribution in granular flow is heterogenous which creates pockets inside the assembly. Here there might be little or no pressure since these pockets are protected by the arches surrounding them.

7. *Absence of thermal velocity*: In granular rheology, particles only have drift velocity, whereas the fluid has both random thermal velocity and drift velocity. A new term called 'granular temperature' has emerged to describe the unique thermal behavior of particles. This *athermal* nature of granular material plays a crucial role in influencing the rheological behavior.

8. *Dilatancy*: This is a noteworthy property of granular assembly where the conglomerate needs to expand in order to flow which is not a property of pure fluids. It causes the particles to become rigid under pressure but become fluid when the pressure is removed from the assembly. This phenomenon leads to *sustainability of voids* within the granular assembly which is not observed in the case of liquids.

9. *Bridge formation*: In granular rheology, the formation of force chains by multiple particles through their contact points is a common observation, whereas in liquids it is not possible due to the perfect distribution of internal pressure among the particles.

10. *Quasistatic state*: This is the most profound phenomenon that differentiates granular matter from liquid. In this state of flow, granular assembly behaves very differently from fluids in many respects, such as deformability, stress-strain relationship, granular temperature.

11. *Miscibility*: Miscibility of liquid is a contrast feature of fluid matters compared to solid ones where two or more liquid substances can fully dissolve in each other to produce a homogeneous solution whereas solid matters retain their individuality. In light of this property too, granular matter holds a unique position in mechanics. Through the statistical mechanical framework of Edwards [19], it is theorized that granular conglomeration can be completely miscible at large compactivity but may be separated at low compactivity; based on this the Hamiltonian function is constructed.

12. *Heterogeneity*: Granular rheology demonstrates non-homogeneous distribution in flow unlike fluid displacement. The primary cause is the heterogenous interaction force distribution. This is unlike fluid particles which invariably produce isotropic pressure in static or uniformly directed pressure in dynamic conditions.

13. *Granular segregation*: is a phenomenon that is vaguely comparable to a mixture of two immiscible liquids that separate due to their physical properties. It is governed by quite different physical laws to those concerning liquids. We know that liquid segregation occurs primarily due to density where, in the case of two immiscible liquids being mixed, the liquid with higher density fall down and the liquid with lower density stays on top of it. For multiple types of liquids, it follows a gradient of layer based on density. For granular conglomerate consisting of different types of particles, the phenomenon is more extensive as many variables affect it, for instance size, shape, percolation mechanism, and applied load.

14. *Brownian flow*: It is an interesting property of granular rheology which is very different from our conventional understanding of gravitational effect. In granular flow, when

particles organize themselves in the assembly, larger particles move upwards against gravity while smaller particles move downwards.

Based on the above, a discussion on correlating between fluid, solid and granular mechanics is provided in the next section.

In dynamics, granular flow exhibits complex behavior. As a result, flow dynamics of granular matter is a hybrid comprising primarily two different expressions: one aspect is fluid-like while the other is solid-like which causes two different descriptions of granular flow. The former one is that of fluid dynamics where the flow of particles is compared with fluids throughout various stages ranging from kinetic theory of gases [20] to dense flow theory [21]. From this outlook, the particles are treated as molecules of fluid and their individual contribution to the aggregate flow is overlooked and the phenomenon is observed as a global behavior. This perspective considers granular rheology at the macro-mechanical level and compares phenomenological behavior with fluid flow characteristics. Key boundary conditions considered here are turbulence, compressibility, viscosity, steadiness, single/multiphase, etc. Furthermore the key properties assessed here are volume fraction, shear rate, thermal conductivity. While the global flow behavior significantly influences the assembly, it is most relevant to very small particle conglomerates. When the flow with larger size particles is considered, it further needs to be considered at particle scale. Later in this chapter, a detailed comparison will be presented among different methods.

The latter relates to the theory of rigid bodies where each particle is individually considered to be a rigid body and their dynamics are explained micromechanically following Newton's laws of motion [2]. According to this viewpoint, particles are said to be rigid bodies with physical and material properties of dimension, weight, density, surface friction, deformability, yield strength, etc. They collide with each other in motion and behave according to the mechanical laws and consequently exhibit properties such as restitution, damping, breaking, etc. The propagation of energy primarily occurs at the contact points and the forces considered are normal and shear. In doing so, the model is assumed to be basically a spring and dashpot model [2] where the spring represents stiffness of the particles and dashpot represents damping after collision. Details will be discussed below. However, there are many offshoots from this basic model such as flat joint [22], parallel bond [4, 23], etc. The main limitation of this approach is the demand for computational capacity. Therefore,

this problem was resolved through the averaging method by combining the two approaches to maximise their benefits while minimizing the drawbacks [24].

In an effort to capture the ubiquitous nature of granular rheology, different approaches have been considered. An overview is presented in the next sub-section.

## **2.2. MODELLING GRANULAR RHEOLOGY**

Granular rheology has been explained in various ways as mentioned earlier. It is essentially studied through phenomenological models to analyse practical problems in simulated platforms. The most important approaches comprise three methods, these being computational fluid dynamics, finite element method and discrete element method. They are described in more detail below.

**Computational Fluid Dynamics (CFD):** In this approach, granular rheology is studied as if it were fluid. This conventional method regards granular assembly as a continuum which is determined by averaging the physical characteristics of a large collection of particles. The flow behavior is studied from a macro-view using two approaches: Lagrangian method and Eulerian method. In Lagrangian method a particle is closely followed along its pathway during its flow. The purpose is to describe its motion that would represent the flow of a very large number of particles from the same assembly. By tracking the particle, the properties that can be studied are: velocity, granular temperature, mass density in the flow field. In Eulerian method, the attention does not lie on a particle motion. Rather, a sample space is identified as a function of time. That space in the flow field is followed to investigate changes in properties of flow such as granular temperature, velocity, mass density or mass flow rate. The main differences between these two approaches are as follows:

- Lagrangian method applies moving frame of reference for the tracked particle whereas Eulerian method has stationary frame of reference through which arbitrary particles flow.
- In Lagrangian method, elements of investigation are matter whereas for Eulerian method they are spatial.
- The results obtained in Lagrangian method are in pathlines of particle, but for Eulerian method, the results are in streamlines.

Each approach has its own significance, merits and drawbacks. Lagrangian method is advantageous when investigating particle dynamics in discrete manner. However, it is computationally demanding to obtain reliable results of granular flow as a whole because more number of particle needs to be tracked to get satisfactorily accurate results, otherwise averaging of data becomes nonrepresentative of flow. On the other hand, Eulerian method is more applicable when studying flow field macrodynamically. Again, it has the limitation of not being able to study individual particles. Moreover, to obtain reliable and accurate results, there is a limitation on timestep because of the grid of space. A sound combination of these two approaches can complement each other's limitation in studying granular rheology. Detailed discussions on this method is discussed on [25, 26]. The kinetic theory of gases and rapid flow of granular particles which is related to our research is well connected to CFD [27].

Finite Element Analysis (FEA): This approach lies between the CFD and DEM (discrete element method) as it divides the dynamic particle into small sections within which it applies the macro-mechanical perspective.. The advantages of FEM is that it is relatively simple and compact method to obtain macrodynamic results of granular flow. It is more efficient modelling tool than DEM in terms of computational requirement. Boundary conditions are easier to apply in the system. Particles with complex shapes and particles with different properties can be easily incorporated within one element. However, this method too has limitations. Results may vary more because of macrodynamic approach. As a result, large volume of data needs to be collected to determine acceptable results. It cannot obtain microdynamic information from granular flow directly. Some notable outcomes from this viewpoint are published elsewhere [28, 29].

The third and last approach is DEM which is used in our study, and discussed in more detail below.

### **2.2.1. Discrete Element Method (DEM)**

Discrete element method is a simple but ingenious numerical model describing the granular dynamics at a micro-level. Micro-level means that this approach can capture inter-particle dynamic information like contact forces, individual linear velocities and corresponding displacements, angular velocities and related moments, deformation and many more mechanisms at particle level. It is very difficult if not impossible to obtain data from

experimental procedures. It begins with an interaction between two particles among the aggregate granular assembly and following simple Newton's law of motion ( $F=ma$ ) where  $F$ ,  $m$  and  $a$  represent force, mass and acceleration (as generally understood), respectively. So, two particles at a certain velocity  $v$  each of mass  $m$  collide together and may or may not experience a certain amount of deformation based on the momentum and particles' relevant mechanical properties, for example stiffness, elasticity, and have a final velocity vector after the interaction. There are two types of DEM: rigid particle simulation and soft particle simulation.

The rigid particle approach in DEM uses the event-driven method. It assumes that particles interact with each other through instantaneous binary collision. Binary collision also means that only one collision can happen at a time. In between two collisions, particles travel in straight lines at a constant speed as if they are in free motion. The entire flow mechanism is governed by the calculation of dynamic state of pairs of particles based on the collision event. This approach is popular in the study of granular rheology in rapid flow conditions when the kinetic theory of gases is applied [27]. Here binary collision of particles is compared with the random continuous collision of gaseous particles in space. The primary difference between them is that in rigid particle simulation, deformation is ignored. So, on the other hand, soft particle simulation goes through a basic 4-step process following the law of conservation of energy and taking into account the micro-level deformation of particles at the point of collision: 1) particles are in contact, 2) deformation is calculated, 3) velocity and force change is calculated, and 4) particles break contact and have new force and velocity both in magnitude and tensor following Newton's law of motion. Note that the second step in this 4-step process is omitted in the case of rigid particle simulation, making it a 3-step process.

The soft particle approach is a time-driven method which can accommodate multiple particle collisions and is, therefore, closer to practical scenarios. This method, developed by Cundall and Strack [2], correlates dynamic interactions between particles to a spring-dashpot model. The spring component represents particle deformation at the micro-level at the point of interaction which is, of course, determined by particle weight and velocity in a dry environment not affected by external conditions (such as interstitial medium or magnetic field). The dashpot component is incorporated to introduce the dynamic relaxation method in the particle interaction process. This is a very important component because it allows the

granular flow to arrive at a steady state flow or equilibrium static condition at the global scale. This is essential to represent slow and medium flow in moderate to dense granular assembly as observed in real life. Consequently, while the rigid particle method makes a valuable contribution so that studies can be conducted more efficiently using a less complicated model, soft particle simulation is more popular because the physical phenomenon is better understood. For this reason, this thesis implements the soft particle method and is described in more detail below.

### Simple Soft particle model

The governing equations for the translational and rotational motion of a particle in a particulate system are:

$$\mathbf{m}_i \frac{d\mathbf{v}_i}{dt} = \sum_j \mathbf{F}_{ij}^c + \mathbf{F}_i^g \quad (2.1)$$

$$\mathbf{I}_i \frac{d\boldsymbol{\omega}_i}{dt} = \sum_j \mathbf{M}_{ij} \quad (2.2)$$

Here,  $m_i$  and  $I_i$  are mass and inertia of each particle 'i', respectively.  $\mathbf{v}_i$  and  $\boldsymbol{\omega}_i$  are linear velocity and rotational velocity of the same particle, respectively.  $\mathbf{F}_{ij}^c$ ,  $\mathbf{F}_i^g$  and  $\mathbf{M}_{ij}$  are the contact force, gravitational and moment of inertia between particle i and j, respectively.  $\mathbf{F}_i^g$  is not considered in some considerations [6]. The most important part of DEM is the development of the models for  $\mathbf{F}_{ij}^c$  and  $\mathbf{M}_{ij}$ . There have been some models developed in the past. The simplest one is the linear model developed by Cundall and Strack[2]. In this model,  $\mathbf{F}_{ij}^c$  and  $\mathbf{M}_{ij}$  comprise the combined effect of spring and dashpot in the simplest spring-dashpot model, as illustrated in Figure 2.1.



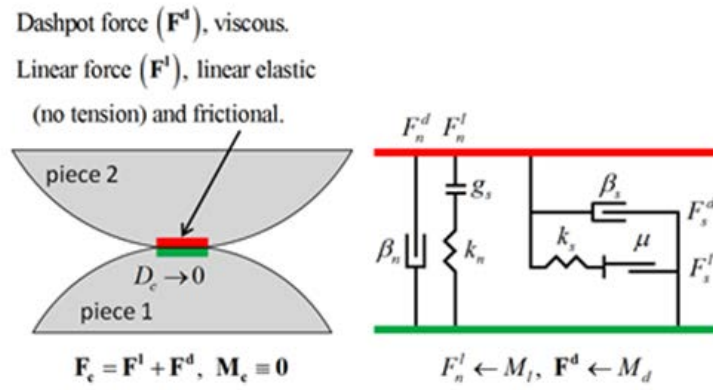


Fig. 2.1: Particle contact model [30]

The particles interact linearly as force columns along the contact surface to gain normal force and corresponding deformation and velocity components and as sliders tangential to contact point for shear force and corresponding deformation and tangential velocity components (for moments).

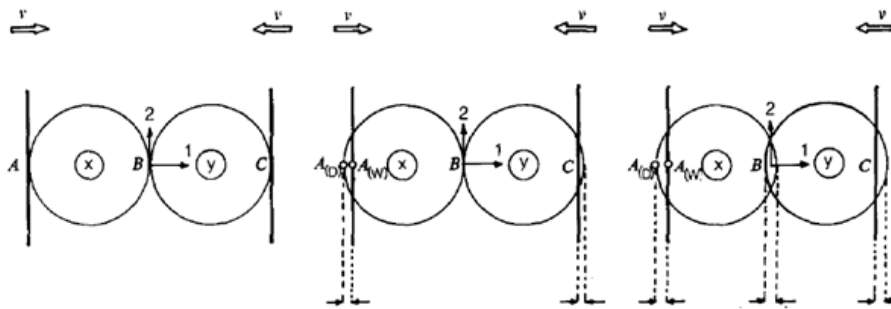


Fig. 2.2: Particle interaction in steps [2]

Figure 2.2 illustrates how two spherical particles proceed through the steps at a micro-level during percolation of particles in a particle assembly. This contact phenomenon is preceded by establishing the contact. In this time-driven process, at first, the contacts are checked by calculating the distances between particles at each time-step (this is discussed later). If the gap is found to be zero, a contact is considered to be established as shown in

Figure 2.2. Then, the calculation process begins as shown in Figure 2.3. Each particle has its own velocities  $v_i$  and  $v_j$  and their corresponding momentum. During the contact period, each goes through a minute deformation based on the following basic equation:

$$\mathbf{F}_{ij}' = -\mathbf{k}\Delta_{ij} \quad (2.3)$$

where, stiffness of the particle 'k' determines the elasticity in the deformation and  $\Delta$  ( $= d_i + d_j - D$  in figure 1.3) is the overlap from the deformation. The process is also damped by:

$$\mathbf{F}_{ij}'' = -\mathbf{d}\dot{\Delta}_{ij} \quad (2.4)$$

where, restitution coefficient of the particle determines the viscous effect of the interaction through damping coefficient 'd'. Thus

$$\mathbf{F}_{ij}^c = \mathbf{F}_{ij}' + \mathbf{F}_{ij}'' \quad (2.5)$$

The same method applies to angular velocities  $\omega_i$  and  $\omega_j$  and their corresponding moments of inertia. Then the calculation determines the post-collision force and velocity tensors applicable until the next time-step. This calculation is performed in iteration for all particles of the granular assembly. To make this rigorous calculation more efficient, the global scale is used.

In Figure 2.3, x-y axis is the global axis in the 2D model. Here, normal contact force acts in coaxial of the unit vector  $e_i$  which is along the line connecting the particles' centers. Additionally, the tangential force is parallel to unit vector  $t_i$  that is perpendicular to  $e_i$ . These forces are active at point C in the center of the deformed region between the two particles. So in order to obtain equivalent global values, the variables (forces and velocities) need to be resolved in x and y direction.

To obtain shear force following relationship is applied:

$$\mathbf{F}_s = \begin{cases} \mathbf{F}_s^* & \text{where, } \mathbf{F}_s^* \leq \mathbf{F}_s^\mu \\ \mathbf{F}_s^\mu \frac{\mathbf{F}_s^*}{\langle \mathbf{F}_s^* \rangle}, & \text{else} \end{cases} \quad (2.6)$$

Here,  $F_s^* = F_s^* + k\Delta_{ij}$  in incremental method and  $F_s^\mu = \mu F_n$  where  $F_n$  refers to contact normal force.

The newly obtained dynamic information (forces and velocities) are then used as initial values for the next time-step. This event is then continued to be iterated through employing an appropriate incremental time-step for all contact phenomena between individual particles of the entire assembly. Using this large amount of computation, a holistic outcome of the flow is achieved at a real-time simulation. The time-step is kept very low to ensure there is no run-time error from particle-overlapping which may occur when calculating the displacement. Figure 2.4 illustrates clearly how the process continues throughout the simulation.

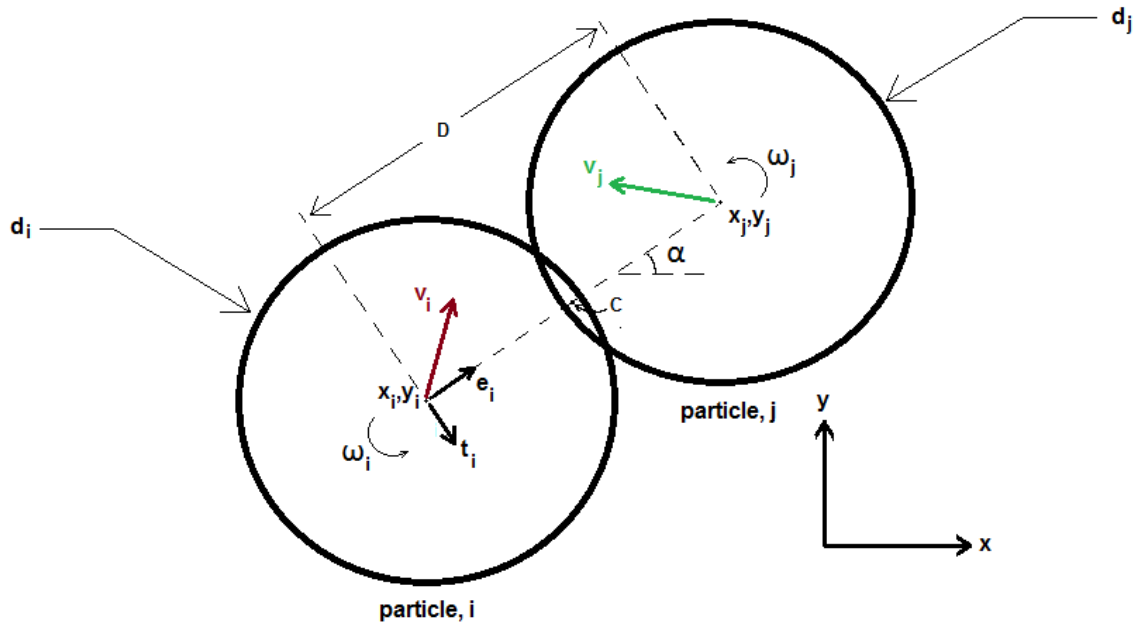


Fig. 2.3: Particle contact dynamics [2]

The algorithm shows that the first pair of particles is chosen and the distance between their center points are calculated. Then it is checked if the difference between the center of the particles is larger than the sum of diameters. If yes, the contact is not established and the sequence moves to the next pair of particles. If no, then the contact is said to be established

and the particle velocities, forces and other dynamic parameters are updated by applying a numerical model from Discrete Element Method such as “Cundall&Strack” or “Hertz-Mindlin&Deresiewicz”; consequently, new particle position, velocity and forces are obtained. Change or no change, these parametric values are retained for the next time-step. By permutation (using iteration), all the particle pairs are considered. When there are multiple contacts, the calculation becomes more complicated. The resultant velocities forces are obtained by considering all the contacts established for the particle to update to a new position. Once all the particles are calculated, and new positions of the particles are updated, the algorithm is completed for that time-step and moves on to the next time-step.

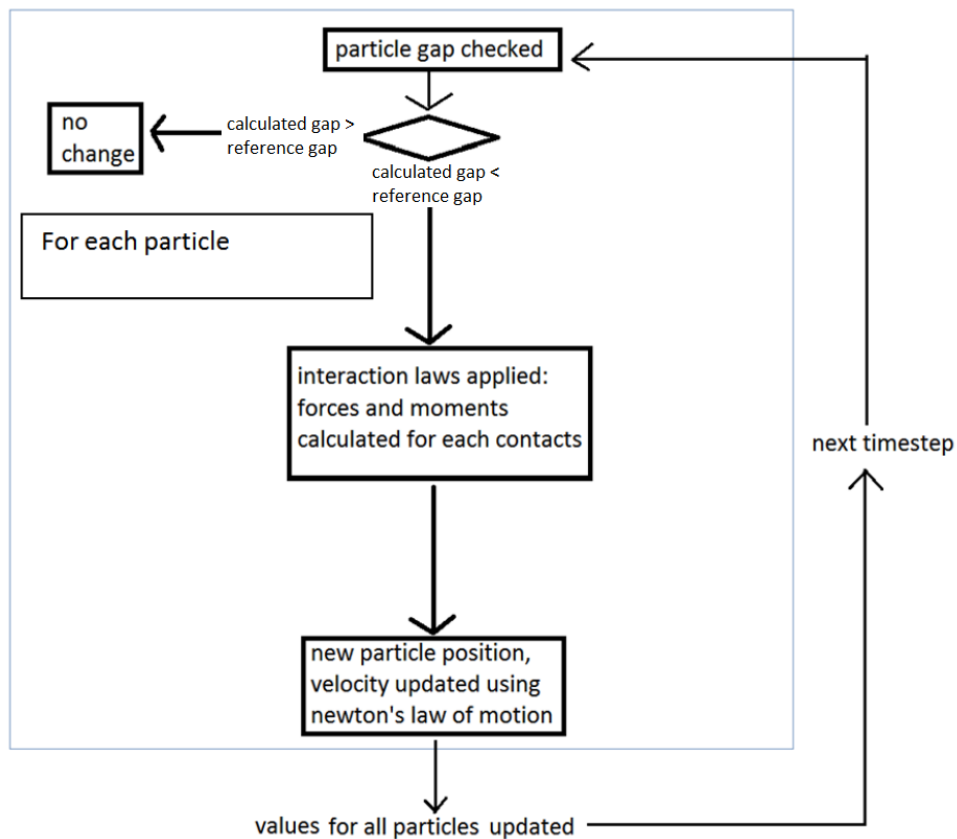


Fig. 2.4: Fundamental flow diagram of a basic DEM process

This iterative method can proceed endlessly to mimic infinite flow. Multiple contacts are predominantly found in dense granular flows. This is why it is very important to consider low

time-step because it ensures that a particle can displace only a miniscule amount and thereby avoid overlapping with another neighboring particle which results in an erroneous and untrue simulation. As a whole, the higher the number of particles, the more difficult the calculating process will be. The long process of calculation explains why it was not possible in earlier computational technology and it is astonishing that such complex processes can be seamlessly executed with modern computers. A comparison of experimental method Particle Emission Positron Tracking (PEPT) and simulation method Discrete Element Method (DEM) is given below:

<b>Technique</b>	<b>PEPT</b>	<b>DEM</b>
Feature	<ul style="list-style-type: none"> <li>• An experimental technique for tracing the motion of a radioactively labeled particle within a particle system</li> </ul>	<ul style="list-style-type: none"> <li>• A numerical technique for simulating the dynamics of a particle system</li> </ul>
Information generated	<ul style="list-style-type: none"> <li>• Trajectory of a labeled particle from which flow field can be derived</li> </ul>	<ul style="list-style-type: none"> <li>• Trajectories and velocities of all particles</li> <li>• Particle/particle and particle/device interactions</li> </ul>
Advantages	<ul style="list-style-type: none"> <li>• Real physical measurement</li> <li>• Tracing for a long time</li> </ul>	<ul style="list-style-type: none"> <li>• Low cost</li> <li>• Full dynamic information</li> </ul>
Disadvantages	<ul style="list-style-type: none"> <li>• Expensive</li> <li>• No force information and hence incomplete dynamic information</li> <li>• Indirect link between behaviours of a single particle and particles in a system</li> </ul>	<ul style="list-style-type: none"> <li>• Limited by computing capability (relatively small number of particles and short time simulation)</li> <li>• Only applied to situations where equations for calculating inter-particle forces are well established</li> </ul>

## **The Hertz-Mindlin-Deresiewicz model and its simplified models**

A more complex and theoretically sound model was developed by Hertz [1] and Mindlin and Deresiewicz [31, 32]. Hertz developed the model that takes into account normal forces by using elastic contact between spheres. These forces act over a line in the 2D model or in a circular plane in a 3D model rather than a single point. Complementing that, Mindlin and Deresiewicz developed the tangential interaction of the phenomenon using the same assumption. In general, however, this model is found to be inefficient because its complicated nature makes the simulation time too long for an analysis of a reasonably large number of particles. As a consequence, it is necessary to strike a balance between an unrealistic over-simplified model such as the hard-sphere method and a sophisticated but inefficient simulation model like the Hertz-Mindlin and Deresiewicz model. Therefore, a number of derivative models have been invented to simplify the Hertz-Mindlin and Deresiewicz model to improve its efficiency. However, the iterative process remains the same for all time-driven methods

One of the models derived from the Hertz-Mindlin and Deresiewicz model was developed by Walton and Brown [33] and Walton [34]. It simplifies the Hertz-Mindlin and Deresiewicz model by assuming tangential force is constant and direct derivative from friction coefficient. They further distinguish between loading and unloading phenomenon when studying effect of force on granular assembly. Both normal and tangential force is taken into account the reversing loading conditions. Langston et al.[35, 36] designed a model using the reverse approach and in particular the direct force-displacement relationship in order to calculate tangential force, while calculating the normal force based on Hertz's theory. They incorporate the effect of direction of force through consideration of vector for individual particles. Table 2.1 shows summary of the two models.

In general, the simple form of models incorporate mainly inter-particle contact force. However, often other conditions generating non-contact forces also influence granular flow in a practical application. Some of the best known forces are Van der Waals force, cohesive force, capillary force, electrostatic force, etc. These forces become significant in different circumstances. For example, Aaron and Sundaresan [7] incorporated the cohesive force in their model to study how relatively dense interstitial medium causes cohesive force to affect the flow. Electrostatic force is adopted in the study of granular rheology by Lu et al. [37]. The

impact of external magnetic field on magnetic forces when the particles are conductors is studied with a more modified model by Yoshino et al. [38].

In addition to the basic process of simulation described earlier with reference to the simple soft particle model, this special model incorporates the finite element method to increase the calculation's efficiency. The entire space is subdivided into small chunks of cubic segments. Each segment is calculated individually by considering only the particles within the segment. These segments are designed to overlap, in order to maintain uninterrupted outputs. Then all the results are summed to obtain the total resultant values of the assembly for that time-step in which the calculation is performed.

Table 2.1: Two popular numerical models[39]

Force models	Normal force	Tangential force
Walton and Braun's model	$f_n = \begin{cases} -k_1 \delta_n n_c, \dot{\delta}_n \geq 0 \\ \text{(loading)} \\ -k_2 (\delta_n - \delta_n) n_c, \dot{\delta}_n \geq 0 \\ \text{(unloading)} \end{cases}$	$f_t = \begin{cases} f_t' + k_t^0 \left(1 - \frac{f_t - f_t^*}{\mu f_n - f_t^*}\right)^{1/3} \Delta v_c^t \\ \text{where, } v_c^t \text{ in initial direction} \\ f_t' + k_t^0 \left(1 - \frac{f_t^* - f_t}{\mu f_n - f_t^*}\right)^{1/3} \Delta v_c^t \\ \text{where, } v_c^t \text{ in opposite direction} \end{cases}$ <p>Here, <math>f_t =  f_t </math>, <math>f_n =  f_n </math></p>
Simplified Hertz-Mindlin And Deresiewicz model by Langston and Tüzün	$\mathbf{f}_{ij}^{ne} = -\frac{4}{3} E_i^* \sqrt{R_{ij}^*} (\delta_{ij}^n)^{3/2} \mathbf{n}_{ij}$ $\mathbf{f}_{ij}^{nd} = -c_n \left(8m_{ij} E_i^* \sqrt{R_{ij}^*} \delta_{ij}^n\right)^{1/2} (\mathbf{v}_{ij} \cdot \mathbf{n}_{ij}) \mathbf{n}_{ij}$ $f_{ij}^n = f_{ij}^{ne} + f_{ij}^{nd}$	$\mathbf{f}_{ij}^{te} = -\mu  \mathbf{f}_{ij}^{ne}  \left(1 - \left(1 - \min( \mathbf{v}_{ij}^t , \delta_{ij}^{\max}) / \delta_{ij}^{\max}\right)^{3/2}\right) \hat{\mathbf{v}}_{ij}^t$ $\mathbf{f}_{ij}^{td} = 2c_t \left(1.5 \mu m_{ij}  \mathbf{f}_{ij}^{ne}  \sqrt{1 -  \mathbf{v}_{ij}^t  / \delta_{ij}^{\max}} / \delta_{ij}^{\max}\right) (\mathbf{v}_{ij} \times \mathbf{n}_{ij}) \times \mathbf{n}_{ij}$ $f_{ij}^t = f_{ij}^{te} + f_{ij}^{td}$

### 2.2.2. Averaging method: From micro- to macro-dynamics

While the present work is with particle characteristics at the micro-level, the main objective here is to obtain the outcome at a particle scale that connects to the experimental

results for validation. The averaging method is the right tool for this because it can approximate the practicalities of an averaged system, which is numerically easier to analyse. Yet it has the ability to deduce properties of the granular rheology's dynamics with reasonable tolerance. This can be achieved by observing the averaged system which is a bridging method between continuum approach of study and microdynamic studies of granular rheology. Several methods have been applied to obtain the averaged values of key variables in the research field. The most important averaging methods are: time averaging, volume averaging, time-volume averaging and weighted time-volume averaging methods. These are explained in more detail below.

**Time averaging:** It is the simple form of averaging and involves only time dependency of variables. For example, a particle or a number of particles is/are tracked in granular flow over a period of time. The data obtained from the observation is expected to represent the overall characteristics of the system (eg. [40]). The problem with this method is that it is a relatively gross estimation and there is a high possibility of deviating from the practical application.

**Volume averaging:** This type of averaging, also recognized as Eulerian averaging, involves fixing an aspect of volume around a reference point which is the Control Volume. It does not consider time but rather presents an overview of the system. It is particularly useful when studying a multi-phased system. For example, the volume fraction of a shear cell segment is the result of volume averaging of entire shear cell (or from a larger perspective, seamless infinite flow) where particle volume is averaged by the total space of that segment (eg. [41]). It is suitable for stationary particle assembly or a quasistatic regime in studies of packing of particles. It was first tried by Drescher and de Josselin de Jong [41] to study stress tensor in terms of external forces on boundaries of assembly. Other examples of application of volume averaging method are [42-44].

**Time-volume averaging:** To overcome the limitations of volume averaging, an extended version of the Eulerian method of averaging was introduced. Here the control volume is not studied for an instant moment but instead over a period time. The multiple data is obtained with volume averaging method and then further averaged with time. While it is relatively more time-consuming, it is definitely more reliable than volume averaging given that granular rheology is rapid. This method was first applied by Walton and Braun [33] when



they investigated rapid granular flow. Another example of application of time volume averaging method can be found in [14, 44]).

Weighted time-volume averaging: This method was developed by Babic [45] and then extended to more complex systems by Zhu and Yu [25] to obtain a more reliable solution that can cover multiple states or regimes of flow. In this method, exterior cells near boundaries and interior cells or regions are considered that are far from boundaries (Fig 2.5).

The local average of physical property  $\bar{X}$  obtained from interior cell is given by

$$\bar{X}(\mathbf{r}, t) = \int_{T_t} \sum_i h_i X_i(\mathbf{s}) d\mathbf{s} \quad (2.7)$$

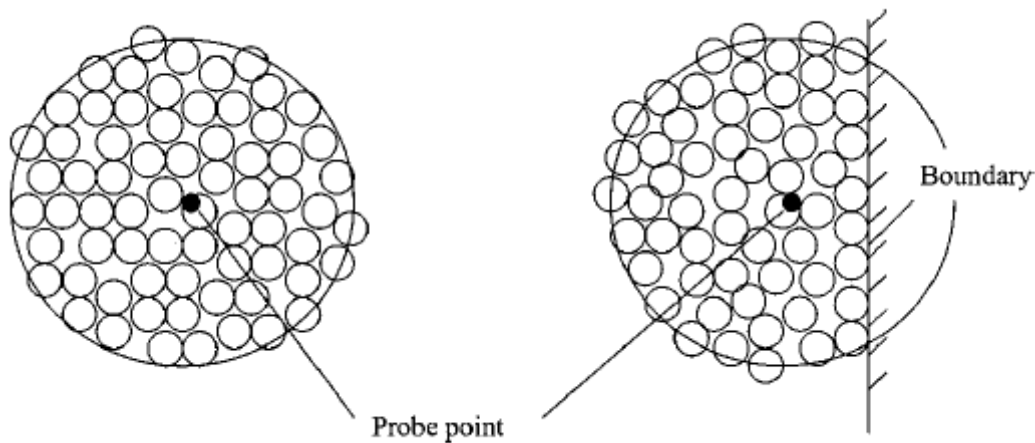


Fig. 2.5: A two-dimensional schematic illustration of the concepts of probe point, and interior and exterior cells. [24]

Where,  $h$  is function of  $r\{x, y, z\}$ [46] and  $t$ . And  $T_t = [T_0+t, T_1+t]$ . 'i' denotes particles involved in the probe point. (Therefore, this method can be applied to all particles in the assembly.) And for exterior cell it is given by

$$\bar{\mathbf{X}}(\mathbf{r}, \mathbf{t}) = \int_{T_t} \sum_i \mathbf{g}_i \mathbf{X}_i(\mathbf{s}) d\mathbf{s} \quad (2.8)$$

This method can give the local averages of mass, linear momentum, angular momentum, and energy, which are commonly used in the continuum description of granular flow. Further with this method, the parameters obtained are mass density, velocity, stress, strain rate, couple stress, etc. This is generally done by creating several arbitrary volumes within the test assembly which are then averaged to obtain the desired value. The advantage with this method is that it can be used for both solid-like and fluid-like state of granular materials. However, it is difficult apply this method to practical applications like a hopper or other vessels used in different industries. A discussion regarding different averaging methods can be found in [24].

However, in the case of non-spherical particles, this task becomes quite daunting because complexity in the dynamic nature makes it very sensitive to the slightest parametric discrepancy. It is therefore a challenge to address this limitation while investigating the virtual platform through numerical analysis. Here, the initial approach is a comparison with spherical particles where there is a lack of knowledge specifically on the particle specimens concerned.

## **2.3. REGIME TRANSITION OF FLOW OF GRANULAR MATERIALS**

### **2.3.1. Flow regimes**

A significant aspect of non-constitutive behavior of granular flow is the regime variation (Fig. 2.6). Regimes are complex attributes of granular flow which depend on multiple variables such as: firstly, constituting particle properties (like hardness and friction coefficient); secondly, assembly properties (like overall volume fraction, shear); and thirdly, external conditions, for instance externally applied load. There are two primarily distinguishable regimes in granular rheology: Inertial regime and quasistatic regime. There is a transitional/intermediate regime that lies in between them.

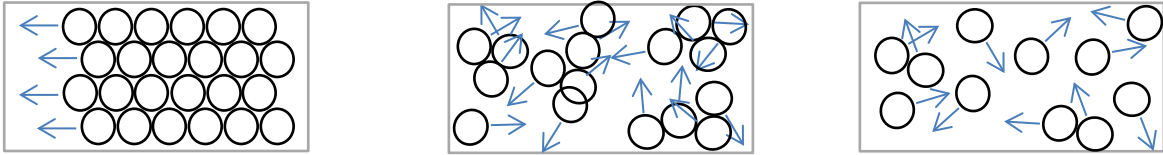


Fig. 2.6: Granular flows at different regimes and their corresponding constitutive behavior (left: quasistatic regime, middle: intermediate regime, right: inertial regime)

*Inertial regime:* It is observed that when the shear rate is high, the volume fraction is low and the imposed stress is also low. The particle dynamics are assumed to resemble that of gas molecules and were compared to kinetic theory of gases devised by Savage et al. [20]. To elaborate the phenomenon, particles collide with each other and are in contact for a short period. conducted energy such as heat and momentum are transferred through impact and the collisions are said to be inelastic with a restitution coefficient of approximately 1. The contribution of stress due to deformation of colliding particles is negligible. No force chain or cluster is seen at all in the particle assembly. Therefore, both the hard particle and soft particle simulation models can be equally useful. This analogy of behavior with gases introduces a new concept in granular flow, i.e. granular temperature where external shear represents heat input. The higher the induced shear rate is, then particles are more agitated and velocity fluctuation increases. Consequently, granular temperature rises which is given by,

$$T = \frac{1}{3} \langle u^2 \rangle \quad (2.10)$$

Where, T and u are symbols of granular temperature and velocity fluctuation, respectively. However, the limitation of Savage's hypothesis is that it did not consider angular momentum. Furthermore, unlike gases, even purely inertial flow experiences dissipation of energy through collision even in an insulated environment. As a result, continuous energy input (eg. Shear) is required to hold a particular granular temperature in an isolated condition. Earlier, Babic et al. [47] looked at regimes from the point of view of coordination number. If the coordination number is equal to or less than 1, granular rheology is said to be in an inertial flow regime. The limitation of this approach is that it is difficult to relate to a physical phenomenon or phenomena, which motivate the adoption of alternate methods developed by Campbell in identifying flow regimes.

Contact time investigation is an important part of identifying the inertial regime. The flow is said to be at a pure inertial state when the time required to complete a binary collision of two particles  $t_c$  does not exceed the time interval between two consecutive collisions  $T_{bc}$ .  $t_c = T_{bc}$  is the critical point which is classified by Campbell as inertial-collisional. Beyond this point, the pure inertial regime ceases to exist and granular flow enters the regime which is sub-classified by Campbell [6, 48] as inertial non-collisional. It falls within the intermediate regime that is nearer to absolute inertial regime. Although macroscopically they hold certain volume and average stress, stable force chains do not form. However, at the micro-level it is heterogeneous and may form localized clusters. As a result, sparsely distributed strong force chains are observed in the flow [9]. Therefore, at this stage, it can be said that the granular assembly has not yet fully attained the kinetic properties of gases. Babic refers to this state as a ‘Type A’ transition.

The biggest issue with inertial regime and rapid flow theory as addressed by Campbell [49] is that it is impossible to obtain a pure inertial regime in an experiment. As well, there are no examples of a practical application of such an event. Moreover, rapid flow theory does not take into account the effect of gravity. Most of the rapid granular flow found in nature or realistic applications are at best, inertial non-collisional, i.e. intermediate regime.

*Quasistatic:* It is the other extreme regime of granular flow dynamics. As the name suggests, the granular aggregate seems apparently motionless. This flow condition is observed when particle concentration is very high and shear is very small. Also known as the ‘jamming state’, this regime is dominated particle properties like friction coefficient and dynamic characteristics like particle deformation resulting from stress rather than shear of assembly. In this scenario, the hard particle simulation model loses its reliability in depicting quasistatic flow behavior and the soft particle model is applied to investigate this regime.

The study of quasistatic regime is based on Mohr-Coulomb theory (from Coulomb’s law of friction [50, 51]) which decides the shear stress at which particles in the assembly start to flow. This observation resembles the characteristics of the assembly to solid bodies [52]. A dense and tightly knit stable and persistent force chain network spans the entire assembly that holds any external perturbation with distributed effort. Particle collision time is much higher than the free path of particles so that the effect of shear rate ceases to exist. Coordination number in the ideal quasistatic regime is maximum value (which is about that of hexagonal

distribution for spherical particles). Consequently, dilatancy of particle assembly is an essential prerequisite for the flow of assembly. Granular temperature is no longer applicable and is referred to as a 'zero' temperature state [53, 54]. This phase is sub-classified by Campbell as elastic-quasistatic. Here, the granular assembly has fully entered the quasistatic state. This means that the effect of inertia is negligible and particles interact primarily through deformation. The elastic properties of the granular material strongly affect this regime which is in fact independent of shear rate.

In contrast to the pure inertial regime, this state is widely found in all aspects of practical application from natural events like landslides to human activities like storage in a silo. For this reason, it has garnered more attention from researchers compared to rapid flow. The study of granular flow behavior starts with the quasistatic flow theory which dates back to 1983 [55]. Practical [18, 56] as well as numerical [57, 58] research work has been carried out on quasistatic flow regime under different conditions.

*Intermediate regime:* When, granular flow at quasistatic regime is subjected to steady increase of shear, a point called critical volume fraction comes where inertial effect starts to show. This is the start of intermediate regime. Similarly, when shear rate is reduced from granular flow at inertial regime, there comes a point of volume fraction where the quadratic relationship ceases to exist. The range in between corresponds to intermediate regime. According to Campbell, this regime has two sub-classifications: elastic inertial and inertial-noncollisional. In the sub-section of intermediate regime known as elastic-inertial: there is the stage where granular assembly is about to enter the inertial regime but has not quite exited the elastic phase. Characteristics of both regimes are partially observed here. It means that the particles of the assembly still demonstrate elastic behavior through deformation but also achieve inertial properties. Force chains are not as persistent and densely spread throughout the assembly as is in the elastic-quasistatic regime. This regime is observed when the shear rate is increased substantially to mobilize particles at, otherwise, a pure quasistatic condition. In this stage, the stress is not only affected by particle deformation but also increases linearly with shear rate [6]. Granular flow is governed by the life cycle of force chains: the force chain is created, it rotates, and then it is compressed and becomes unstable and fractures. Lifetime of force chain is inversely proportional to shear which is also a determinant of regime identification. Babic referred to this state as 'Type B'; state of force chain formations. It should be noted that force chain study is a mainly qualitative indicator and no quantitative

study has been done on the force chain network either in terms of length or number in the analysis of regimes.

When the shear rate is further increased, the granular assembly becomes more dilute and constituent particles are found in clusters. This is the inertial-noncollisional subsection. This is the stage where granular flow is about to enter pure inertial regime and kinetic theory of gases is on the way to become prevalent. Babic referred to this state of flow as ‘Type A’ regime. More on this in the next section.

### **2.3.2. Regime transition**

Regime transition is the phenomenon where granular flow exits from one regime and enters the next. It is primarily dependent on two external conditions: shear rate and applied load. Volume fraction is the main indicator that is used to identify the point at which regime transition occurs. Further, regime transition is also influenced by particle material properties such as particle friction coefficient, particle rigidity and particle shape. Regime transition (also known as phase transition [52]) is used to differentiate these characteristic stages over varying external and internal conditions. As a part of this research program, it can be incorporated along with the study of non-spherical particles to further identify the similarities and differences from these two considerations.

*Two approaches to studying regime transition:* The regimes in the shear flow of granular particles are primarily studied in two boundary conditions: volume controlled [5, 7] and stress controlled [6, 8]. An interesting analogy of the two boundary controlled conditions is found from comparison between drained soil test and undrained soil test. In case of undrained soil test, water carries much of the load even after soil breaks. This test is compared to volume controlled boundary condition because here tendency of volume change is suppressed with change of applied pressure. On the other hand, in drained soil test, volume can change with change of pressure because water can escape easily. But here, the pore water pressure does not change due to external loading. The model based on volume controlled boundary condition is, though less realistic, more feasible and efficient in simulation-based studies. Conversely, the model based on stress-controlled condition, though more practical, consumes more system resources and consequently requires more time to get the same number of

results. Several studies have been conducted for comparing these two methods and opinions differed. Throughout our work, the stress controlled boundary condition is applied from the point of view that in a practical scenario, it is more likely to happen due to the overlying weight of particulate materials, whereas boundary tends to change primarily due to dilatancy effect and variation of contact network at the boundary condition.

Many studies have been done to understand the regime transition of particle flow. As early as 1990, we find an investigation of regime transition where mono disperse 2d study was performed using disks in [59]. There, a relationship between dimensionless (scaled) stress  $\sigma^*$  and dimensionless shear rate B was identified where  $\sigma^*$  is the function of particle density, diameter of the disks, shear rate and stress tensor and B is the function of shear rate, particle mass and particle stiffness. In that study,  $\sigma^* = a_{ij}B^{b_{ij}}$  function was obtained as such that function parameters depend on particle density and shear rate. Here,  $\sigma^*$  is given by  $\frac{\sigma_{ij}}{\rho_s D^2 \dot{\gamma}^2}$ , where,  $\sigma_{ij}$ ,  $\rho_s$ , D,  $\dot{\gamma}$  are particle contact stress applied by particle 'i' on 'j', particle material density, particle diameter and shear rate respectively. Parameter B is given by  $\frac{\dot{\gamma}}{(K_n/m)^2}$ , where, ' $K_n$ ' is normal contact stiffness and 'm' is particle mass,  $a_{ij}$  and  $b_{ij}$  are functions of particle concentration (volume fraction) and are obtained from regression analysis based on the correlation among  $\sigma^*$ , B and C.

Using this function, regimes were identified as either Type A or Type B where Type A corresponds to regime where multiple collisions were existent, while Type B corresponds to the regime where forces are existent. Further study showed that function parameter  $b_{ij}$  approached (-2) with increase of concentration at the highest level. This meant that shear rate can no longer affect scaled stress (quasistatic regime).

Campbell studied regime transition in volume controlled environment using 1000 spheres [48]. He investigated regime transition in forward and reverse direction and found that in the volume controlled model they do not follow same path: a transition can only be obtained through reduction of concentration. He provided details of the contact model and observed a relationship between scaled stress and scaled stiffness (function of shear rate) by varying the coefficient of restitution to obtain points of regime transition. He also observed the relationship between scaled stiffness and ratio of contact time and binary collision time, in an

effort to find points of regime transition. The generated regime map was relatively ambiguous.

Campbell further studied regime transition in a stress-controlled environment in [6]. Here, he observed the force network structure and regime transition's effect on it. The relationship between scaled stress, scaled stiffness and volume fraction produced a much clearer point of regime transition. However, the ratio of contact time proved to be less effective in identifying the regime transition point. However, the map drawn for the purposes of regime transition was more different in nature than what was obtained for the volume controlled method.

Aaron considered introducing cohesiveness in the study of regime transition in the volume controlled method[7]. His finding was that cohesive force could influence stress when volume fraction was less. He developed a new scaling method in the form of  $B_0^*k^*$  that incorporates cohesion between particles. Here,  $k^*$  stands for scaled stiffness and  $B_0^*$  stands for scaled cohesiveness and is given by  $B_0^* = \frac{F_{vdW}^{max}}{kd}$  where  $F_{vdW}^{max}$  is the cohesive force exerted by a particle on a contacting particle. Aaron also extended his investigation into the stress-controlled model like Campbell in [8] where he drew similar regime transition results using the correlation between scaled stress, scaled stiffness and volume fraction incorporating cohesion between particles. In a recent study, he noted the relationship between size distribution and regime transition in [60]. In this work, he used a different scaling method similar to inertia number to denote regime transition. An example of a regime map for the volume and stress controlled conditions, respectively, is shown in Fig. 2.7.

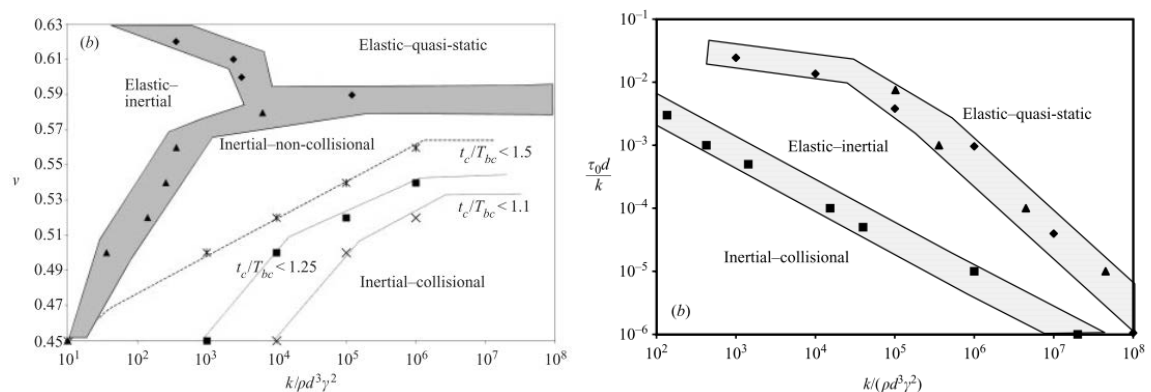


Fig. 2.7: Regime map in different literature (left: volume controlled [48], right: stress controlled [6])



## 2.4. BACKGROUND AND ASSOCIATED CHALLENGES IN STUDY OF NON-SPHERICAL PARTICLES

*Construction of non-spherical particles:* The primary distinction between the spherical and non-spherical of particles is, of course, the shape. This brings forth a very complex challenge: how the particle can be geometrically defined. Numerical definition is approached from many perspectives where different people tried to generate particles in various ways. Some of the approaches are introduced here. Butchholtz et al. [61] obtained square particles, Dziugys et al. [62], Langston et al. [63] and Campbell [64] created ellipsoids. Wouterse et al. [65] had spherocylinders and Guo et al. [66] generated disks and elongated rods with straight forward geometric definition of those shapes. This approach requires a complex calculation due to variation in the contact method but can be numerically efficient because the number of components for interaction is less. However, this approach is limited to ideal conditions and far from practical events where particle features are often of irregular shapes. The remaining methods are less efficient in terms of computability. Matuttis et al. [67] and Pena et al. [68] created irregular shaped particles using multiple sided polygons in their study of granular physics. Hosseininia et al. [69] as an extension to the previous method applied Fourier transformation on irregular multifaceted polygons to obtain smooth non-spherical particles. Multiple facets were used in [70-72] that are meshed into a closed form to generate ellipsoidal particles.

Particle dynamics are obtained from the combined effect of the interaction through the different facets of the particle (or sides for polygons). Jia et al. [73] used the digitization technique which is similar to discretization of smooth signals. In this technique many square blocks are placed in a mesh to obtain a non-spherical particle. Lastly, the popular method of constructing non-spherical particles is the overlapping of particles. This method is applied in many numerical investigations [74-78]. It is particularly attractive because it can be directly compared with the well-established concept of granular rheology based on simple spherical particles. With rapid advances being made in the computational capacity of the latest computers, this method is now feasible. In this work the bubble-pack algorithm [79] is used which is an extension of the overlapping particles technique. At first, a template of non-spherical particles is created by using a closed volume formed out of facets. Then, the best fit

method is applied using overlapped spherical particles. This method can be determined by controlling precision.

The anisotropic shape of non-spherical particles inherently introduces complexity in particles' interaction. As a consequence, while spherical particles have only one form of interaction (as discussed by Hertz [1] or Cundall and Strack [2]), non-spherical particles require additional attention regarding how particles are interacting with neighbors. For example, when geometrically defined particles are considered [66, 69], each of the sides has a unique method of interaction with other particles. Or in the case of discretization [73], particle dynamics result from the sides of the squares at the outer boundary of the particle. Another important feature of non-spherical particles is that, because of its shape, the contact force vector does not necessarily go through the centre of mass of the particle; therefore torque exists even when there no tangential force is present. However, the complexity is minimized when non-spherical particles are composed of overlapping spherical particles. The non-spherical particles interact through component overlapped spherical particles which have the same dynamic principles established in studies of spherical particles. Nevertheless, it does not relieve the non-spherical particles as a whole from the unique multiple types of interactions well illustrated by Azema and Radjai [80]. Moreover, non-spherical particles are more susceptible to particle properties in the context of interaction than spherical particles [81]. This attribute of complex interaction contributes to the complicated numerical mechanics model in terms of analysis of force tensors. Referring to spherical particles, consideration of stress tensor is sufficient for force calculation. In contrast, for non-spherical particles, inertia tensor is required due to the spin and the orientation of the individual particles.

This brings forward another difference: orientation. Sphere has isotropic geometry and therefore no effect in terms of orientation. For non-spherical particles this is not the case. A non-spherical particle, whether regularly shaped (eg. ellipsoidal, cylindrical) or irregularly shaped (eg. rocks, meteors) are likely to have major and minor axes. This phenomenon further complicates the research field and evolves into a new field of study in granular rheology; it has been considered in various papers concerned with non-spherical particles (eg. [82, 83]) in creating numerical models. This hurdle makes the study of non-spherical particles even more complex and slows down numerical simulations. Dong et al. [84] made an effort reduce the inefficiency of computation of non-spherical particles by discretizing orientation.

However, this study is based on the simple case of contact force and has not yet been applied to other non-contact forces.

As a consequence of orientation, the history of initial packing, analogous to hysteresis of angle of repose, has a much more profound impact on the behavior of flow compared to that of spherical particles. It has been observed in our work where we found that it takes much more time to obtain a steady state condition for ellipsoidal particle assembly flowing through the shear cell than what is observed for spherical particle assembly in a similar configuration. Moreover, the more elongated the particles are, the longer it takes to attain a steady state flow condition. Nevertheless, significant developments have occurred in non-spherical granular rheology. A very detailed discussion on this subject can be found in [85].

Some important developments in study of non-spherical granular rheology are classified into three segments based on important topics pertinent to non-spherical particles.

### **On generating shapes and rheological models of non-spherical particles in DEM**

Lin et al. [86] developed a computer model for ellipsoidal particles in three-dimensional space, presenting findings on the effect of shape on shear stress and deformation behavior. Abou-Chakra et al. [83] developed computer models to generate non-spherical particles in a 3D platform and tested them with experiments. Zhao et al. [72] designed an algorithm to obtain a 3D simulation model for non-spherical granular materials using DEM, highlighting the details of new algorithms for contact resolution and various dynamic calculations. Jia et al. [73] introduced a different algorithm for creating non-spherical particles: digital packing. In their method, non-spherical particles of any shapes can be generated by placing square blocks in a mesh to closely match the original shape. Fineness of these blocks determined the precision of the shape. Shamsi et al. [75] described rather complex shaped non-spherical particles using overlapping spherical particles and present some comparative analyses on correlations among applied pressure, friction angle and axial strain with reference to the angularity of the particle constituents. Torquato et al. [87] compared non-spherical particles based on the number of lattices the particles had. Kriebitzsch et al. [88] established a different approach of modelling the simulation of non-spherical particle rheology: immersed boundary computational fluid dynamics code. While simulation results are consistent with theoretical predictions, the model has limitations in its usability. Dong et al. [84] invented a novel method of DEM for non-spherical particles based on orientation discretization in order to

improve the efficiency of simulation runtime. They used this method on multiple types of non-spherical particles such as cylinders, ellipsoids, spheres, discs and spheroids.

### **On non-spherical particles under dynamic conditions**

Butchholtz et al. [61], in the earlier stages of simulation of non-spherical granular study, developed, at a two-dimensional setup, a numerical model for square particles that flows inside a rotating drum. Vu-Quoc et al. [70] developed a code to study dry granular flows of ellipsoidal particles flowing down chutes using DEM where they created ellipsoids with clusters of spheres and used the simplified model of Mindlin and Deresiewicz [31]. Further, they verified their code utilizing physical experiments with soy beans. Dziugys et al. [62] studied ellipsoidal particle flow in a combustion chamber where they developed a numerical model to simulate a packed or fluidized bed of fuel particles. Cleary et al. [82] used DEM to analyse circular and super-quadric particles flowing through hopper in a 2D virtual environment. Their paper concentrated on the relationship with flow of particles through a hopper with blockiness and aspect ratios of the particles. The paper also presents a series of other cases like mills and vibrating beds. Langston et al. [63] studied the packing and discharge of spherical particles and ellipsoidal particles with a silo using DEM. Li and Holt [89] used DEM to simulate angular grains and super particles. Superparticles are constructed with cluster of simple or regular-shaped constituents to obtain irregular complicated shapes such as rocks. They employed clustering of circular particles and did a comparison study with regards to sandstone failure.

Mortensen et al. [90] worked with ellipsoidal particles subjected to turbulent channel flow where they primarily presented the effect of particle elongation (aspect ratio) and response time of particle dynamics. Tao et al. [77] studied non-spherical particles percolating through a hopper using DEM. They used corn-shaped particles that are designed using four spheres and compared spherical particles to the new non-spherical particles in terms of velocity, discharge rate, and volume fraction. Zhou et al. [91] applied DEM and CFD (computational fluid dynamics) to the assembly of ellipsoidal particles going through gas fluidization with attention paid to the correlation among properties, namely: fluid drag force, pressure drop, particle velocity, coordination number, orientation and force chain network. Wang and Pu [74] introduced a DEM to observe plugging of granular materials in a fracture and identified

an optimum volume fraction of particle assembly to achieve the maximum effect of granular lost circulation material.

### **On packings of non-spherical particles**

Matuttis et al. [67] investigated the mechanical characteristics of static piles of spherical and polygonal particles using DEM and compared them in terms of the relationship between hysteresis and angle of repose and stress distribution. Donev et al. [92] used a hard model to study packing of ellipsoidal particles with numerical simulation under various conditions. Grof et al. [78] conducted numerical research on needle-shaped particles subjected to uniaxial compression where the non-spherical particles are generated using a string of spherical particles. This work primarily involves size distribution of particles. Wouterse et al. [65] studied the packing of elongated particles with spherical ends and particularly how key granular flow parameters such as contact number, volume fraction are affected by the aspect ratio of particles constituting the assembly. Fraige et al. [93] investigated granular packing and flow for cubical particles similar to what was discussed in [61] but they used a 3D analysis using DEM for the cubical particles flowing through a hopper, aiming to verify their work with physical experiments. Nouguier-Lehon et al. [94] also studied using DEM in a 2D platform the assembly of non-spherical particles subjected to biaxial compression. Here the effects of particle elongation on axial strains and rotations of particles were noted and hexagonal particles were the subject of their study.

Azema and Radjai [76] evaluated the elongated particles with spherical ends further in biaxial shear where they focused on probability distribution of forces and their spatial distribution. Azema and Radjai [80] also studied the packing of elongated particles with spherical ends under biaxial compression where they established the relationship between elongation of particles and shear strength. Hosseininia et al. [69] examined the relationship between stress tensors and anisotropic characteristics of non-spherical particle assembly using the DEM method, which was in agreement with experimental outcomes. Stroeven and He [95] studied the packing of eight different shapes of polyhedral grains using DEM and investigated the effect of elongation in terms of sphericity and facet number volume fraction and coordination number.

## **2.5. SHEAR FLOW OF GRANULAR MATERIALS**

Shear properties are important parameters in granular rheology as they directly affect the strength or flow-ability of particle conglomerates. It is an important subject that corresponds to natural events like landslides or solid handling issues such as designing silos, obtaining solutions for flow problems like segregation, irregular flows and so on. In order to investigate these things, shear testers were invented that can analyse granular flow in a laboratory setup which can be correlated to realistic applications. Although other apparatus have been developed in recent years (eg. Evolution Powder Tester [96]), shear testers are still widely used in granular rheology because of their simplicity and well-established analytical models. Some major types of shear testers are discussed below with a description of their configurations and uses.

### **2.5.1. Popular shear testers**

#### **Direct shear tester**

An example of direct shear tester is Jenike's shear cell. It was first introduced by Jenike in [97]. It has 4 main components: lid, upper ring, lower ring and the base as shown in Fig. 2.8. At first, a consolidated specimen granular assembly is placed on the base inside the upper and lower ring. Then, the lid is placed on top of the assembly. Desired normal load is applied on the particle assembly vertically downwards using the lid to provide a uniform compression over the assembly. Finally, another horizontal force is applied through the upper ring using a bracket. This horizontal force offsets the upper half ring from its place and the shear of specimen particle assembly occurs around the dashed centreline shown in the Figure (2.8). A different combination for normal load and shear load is used to obtain yield locus of particle assembly which is utilized to obtain important characteristics such as yield strength, effective angle of internal friction, etc. This testing method comprises two parts: consolidation of particle assembly in the cell; and obtaining steady state displacement at the shearing zone. Numerous studies have been done using this apparatus.

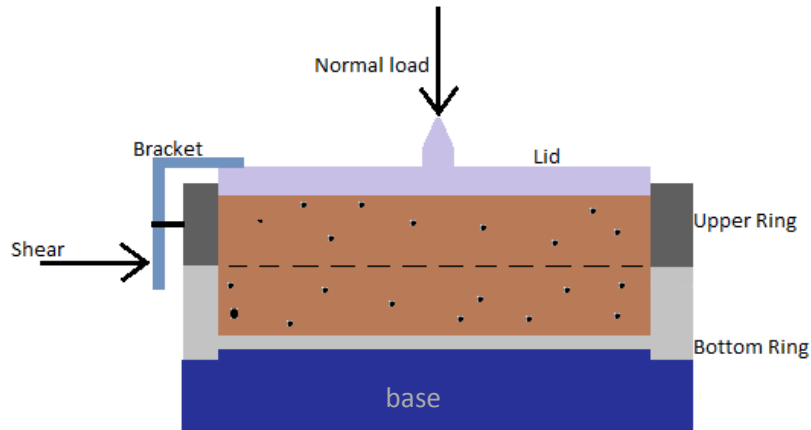


Fig. 2.8: Configuration of Jenike's shear Cell

Some more recent work are introduced here to overview the utility of the testing method. Sun [98] utilized the knowledge of Jenike's shear to identify the minimum required pressure to obtain sufficient powder flow in high-speed manufacturing of tablets. Opalinski et al. [99] investigated different crop seeds and food powders in Jenike's shear cell and found that moisture content significantly affects the strength of assembly. They also observed that a lubricating effect may develop to produce unexpected bed behavior in a silo. Chen et al. [100] measured fuel powders using Jenike's method of shear testing to identify that their flow functions are located in different regions, which can help obtain critical hopper dimensions for different fuels. Chatteraj et al. [101] used Jenike's method to demonstrate that surface coating of powders with nano-silica through comilling significantly improves flowability of the granular assembly. On the other hand, in their numerical analysis, Harti et al. [102] used DEM to study bulk friction of non-spherical particles in Jenike's direct shear test and compared it with physical experiments with glass beads. They found that particle interlocking affects the bulk friction more than volume fraction does for different shaped particles. Aigner et al. [103] used DEM in simulating Jenike's shear test to determine coefficient of friction of granular assembly which agreed well with physical experiments. The shear tester has advantages and limitations as follows:

**Advantages:** It is less expensive and easier to understand. It is easier to adapt to the varying need of practical applications. It can be developed to meet extreme conditions like

very high pressure or very high temperature. It is easy to study friction between conglomerate of two different materials by filling top and bottom compartments with different materials.

Limitations: Firstly, it cannot produce an infinite flow condition which makes it difficult to obtain a steady-state condition. Following this method for bin flow, critical yield surface in terms of flow and no-flow criteria can be obtained. It is a time-consuming procedure to create a consolidated specimen and is affected by the operator's skills. It is usable only at higher loads (greater than 3kPa). It is not suitable to study near inertial regimes. Also, it is discovered that complex stress is evident in particle assembly through experimental and numerical studies; these proved that inhomogeneity exists in shear testing [104].

### **Triaxial shear tester**

This tester is used particularly in geotechnical engineering and soil mechanics but can be used for other granular materials and powders. In this technique load is controlled by three dimensions (x-, y- and z- axis) on the specimen particle assembly inside the cell. In order to do so, sample particles are put between two platens which establish a vertical load on them. Surrounding the sample assembly is the flexible latex membrane that puts varying pressures in terms of x- and y- axis (see Fig. 2.9). Through the variation of the pressures in different directions, shear stress develops within the specimen assembly. Applied load is increased until a critical point is reached when the cylindrical particle assembly fails. Then sliding region evolves; it is known as shear band. During the test, when the applied vertical pressure is higher compared to lateral pressure by membranes, particles tend to bulge out pushing the membrane out and the cylindrical column becomes shorter. Again, by increasing lateral pressure by membrane relative to vertical pressure, the column can be made tall again. Stress-strain data is collected from cycling of this process. The key parameters that can be investigated through this process are: yield strength, angle of shearing resistance, dilatancy angle and apparent cohesion. These studies help understand the strength of soil which is vital in engineering applications.



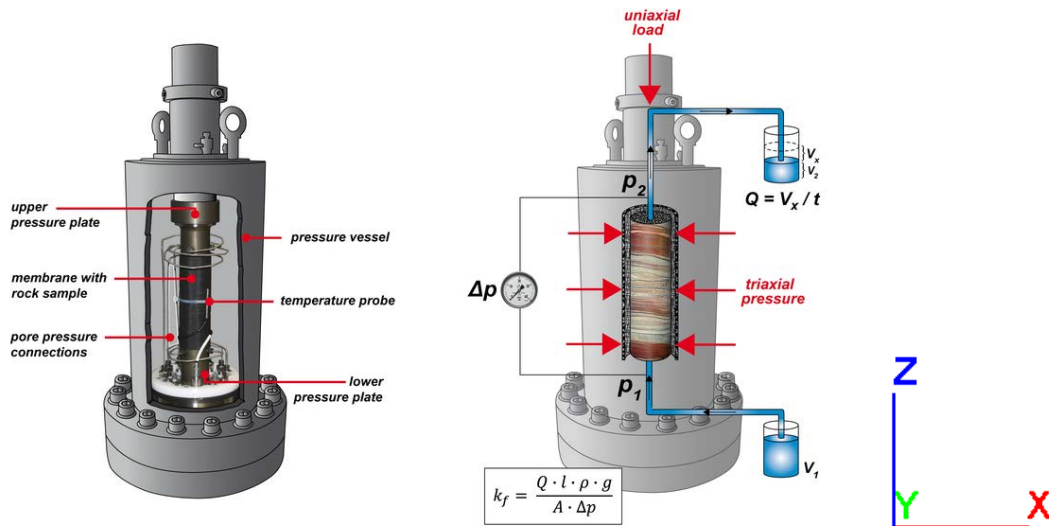


Fig. 2.9: Configuration of triaxial cell [105]

The first triaxial tester was developed by von Karman in 1910 [106] and this was also mentioned in [107]. Then it went through a long development progress but is still popular. An important aspect of this test is that it can produce different boundary conditions for testing particle assembly through drained and undrained analysis. A few recent analyses highlight the effectiveness of the method. Cerni et al. [108] physically experimented on the resilient behavior of unbound granular materials for pavement unbound layers using the triaxial test with a focus on conditioning stress and stress paths. Wu et al. [109] performed both experimental and numerical analyses through the triaxial test on glass beads under quasistatic loading condition to observe saturation condition on shear behavior. Chen et al. [110] utilized DEM to produce a triaxial test that investigated the mechanical properties of sand and indicated a good agreement with physical experiments. Zhou et al. [111] used DEM to study fracture of particles in their triaxial test. A limitation of the triaxial test is that non-uniform strains develop due to [112] friction between specimens and end plates which causes stress concentration. It may result in erroneous stress-strain, volume change or pore pressure response. The advantages and disadvantages of triaxial shear tester are summarised below:

#### Advantages of Triaxial Test

- There is uniform distribution of stress found on the failure plane.

- The failure of the column occurs on the weakest plane
- The drainage can be controlled totally as required during the test.
- Direct measure of changes in pore pressure and the changes in volume possible.
- The stress state can be identified at all intermediate stages upto failure at any shear stage by drawing the Mohr circle.
- This test setup is configurable to meet special requirements suitable for accurate research work.

#### Disadvantages of Triaxial Test

- Expensive setup.
- Requires own space in laboratory.
- Long time is required (compared to direct shear test).
- In case of larger strains, the column's cross-sectional area is not uniform because column does not stay cylindrical uniformly.
- Dead zones can be formed at the ends of the column because of frictional restraint produced by the loading cap and the disc. As a result, the strain conditions in the column become heterogeneous.
- The consolidation of the column of granular particles in the test is isotropic. But in practical application, the consolidation of any granular matter is generally anisotropic.

#### **Biaxial shear tester**

This is a more simplified version of the triaxial shear test in the sense that it is a 2D model (Fig. 2.10). It was first created by Harder and Schwedes [113] to investigate yield strength. Unlike the triaxial tester, it has restricted upper and lower plates. A load can be applied laterally by side plates on the specimen particle assembly that is placed inside the cell. This test can be used to obtain Mohr stress circles for different stress combinations. Some recent developments which used the biaxial shear test are mentioned here to highlight the benefits.

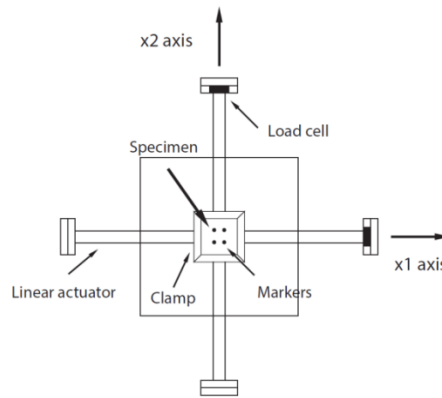


Fig. 2.10: Configuration of biaxial test [114]

Le Bouil et al. [115] designed a biaxial apparatus in order to investigate the yield of granular materials using latex membrane and glass plate where pressure is applied by vacuum. It can be used to obtain heterogeneous and intermittent strains through glass using spectroscopy. Bi et al. [116] used DEM to study granular material properties, namely stress-strain process, volume strain, coordination number, under biaxial loading. The shear zone centralizes gradually when the strain increases. Jiang et al. [117] looked at loose cemented particle assembly under the biaxial test using DEM to demonstrate the influence of bond strength and confinement level on the assembly's mechanical properties and characteristics of shear bands. This method too has its limitations. For example, Zhu et al. [118] found that the assembly is heterogeneous at the meso-scale unlike the general assumption of the test in macro-scale conditions. There is also a large problem of wall friction. For this reason, this test has not replaced the Jenike method.

### Uniaxial shear test

This is the simplest form of shear test (Fig. 2.11) but very useful in research and industrial applications. The testing method is explained to illustrate how it is used. Firstly, the specimen particle assembly is placed in a confined space (eg. cylinder). Then, vertical force is applied to consolidate the assembly, followed by the confined space (i.e. cylinder) being removed. Again the vertical load is applied to the consolidated assembly until it fractures which is revealed as unconfined yield strength. A good overview of this method can be found in work of Freeman [119]. Here,  $\sigma_1$  refers to major principal stress for vertical preconsolidation while surrounding wall of cylinder is still in place. And  $\sigma_c$  refers to the stress

for unconfined column fractures when the cylinder is removed and there is no minor principal stress from the wall.

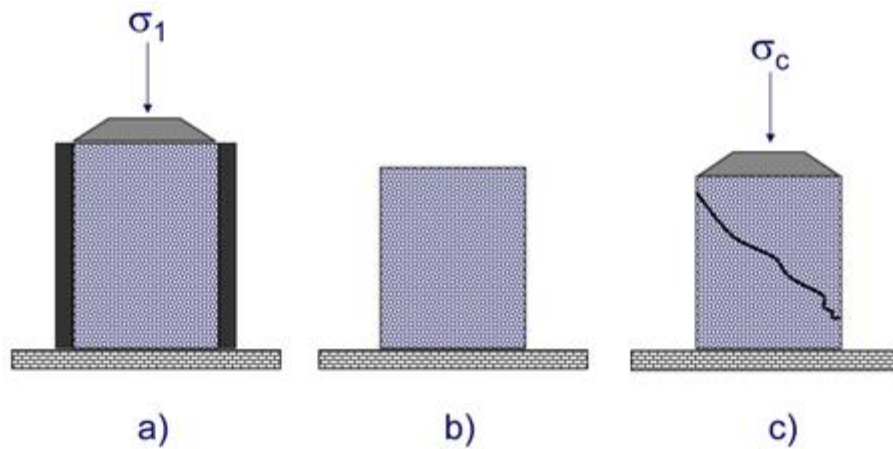


Fig. 2.11: Uniaxial test step by step [120]

Similar to the previous discussions, this test is also applicable in current research. Qin et al. [121] designed a new uniaxial system to investigate elastic modulus of granular materials. They discovered that elastic modulus has a positive relationship to particle size and a negative relationship to cell size. Neugebauer et al. [122] experimented on silica aerogels using the uniaxial method in order to determine the optimum level of compaction where thermal conductivity is minimized. Beyond this point conductivity increases when particle interaction contact area also increases. In their numerical analysis, Imole et al. [123] studied the frictional property of particles in dense assemblies under uniaxial load using DEM to show a correlation between microstructural features and nontrivial macroscopic behavior of granular rheology. Thakur et al. [124] performed a uniaxial test with DEM using the adhesive elasto-plastic contact model to investigate non-spherical particles. It predicts different aspects of experimental flow function correctly with more microdynamic insights on flow-ability of cohesive granular materials. The main limitation of this testing method is that although it provides essential information regarding yield strength of materials, it has very limited use due to the limitations on varying the configuration.

### **Annular shear tester**

Annular shear tester is the another common setup for assessing the principles of granular rheology. The history of this tester goes back to 1936 when it was invented by Hvorslev

[125]. Then it was redesigned by Carr et al. in 1968 [126] to analyse wall friction angles, internal friction angles and yield strength characteristics of granular assembly under slow and continuous flow conditions. Since then, it has gone through many modifications and developments although the principle remains the same. Basically, it involves an annular setup with upper platen, lower platen, inner wall and outer wall as illustrated in Fig. 2.12. Because of the design, the tester is also known as the ‘ring shear tester’. The specimen granular assembly is placed within the confined spaced formed by these boundaries. The shearing method is equivalent to what is found for Jenike’s shear cell. However, this setup has been used in various ways: the upper platen is rotated while the lower platen is kept stationary [127]; both platens are rotated in opposite directions [6, 14]; volume is kept constant while rotational velocity varied [7, 48]; constant load is applied by the upper platen while both platens are rotated [8, 13]. The inner wall is rotated while the outer wall is loaded (inwards) [128] and so on. Based on the shearing technique, the design of the tester varies. The annular cell in the figure has rough walls at inner radius  $R_i$  and outer radius  $R_o$ . The top of the cell is open and the bottom is split at some radius  $R_s$ . It contains granular substance upto a height  $H$ , The outer portion (gray in the figure) is then rotated at a angular velocity  $\Omega$ , while the center portion (blue in the figure) is held stationary. The shear tester has advantages and limitations as given below:

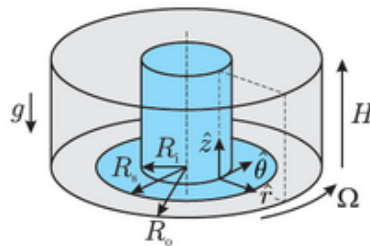


Fig. 2.12: Configuration of annular shear cell [129]

**Advantages:** The annular shear cell is very popular given that it has certain advantages. Unlike Jenike’s shear cell, it can produce a steady-state flow condition. Moreover, it does not require consolidation of granular materials. It is not influenced by the operator’s skills and is precise in conducting experiments. There is more scope for controlling the granular flow while it is at its dynamic state, making it possible to observe changes in real time which

makes it less time-consuming relative to experiments conducted with Jenike's shear tester. It is better at obtaining variations in boundary conditions. As a result, more variables can be investigated with this testing method. Also, by use of different visual techniques (such as Positron Emission Particle Tracking, i.e. PEPT), it is possible to observe the real path of particle trajectories over an extended period. Averaging method is easier to perform with experiments conducted through this tester. An aspect of comparison between Jenike's shear cell and annular shear cell can be found in [130].

Limitations: Despite its advantages, it too has limitations. It is expensive compared to direct shear tester. It is not easy to customise to meet varying requirements. It is not suitable for investigation in extreme industrial conditions such as very high temperature or very high pressure. It is harder to analyse multiphase granular flows. This is why, Jenike's testing method still exists and is popular alongside annular shear cell testing method.

## **2.5.2. Relevant studies using shear cell**

In the following section, application of shear cell will be introduced in studies relevant to present work. For convenience of comparison, numerical and experimental studies will be separately discussed.

### **2.5.2.1 Numerical studies**

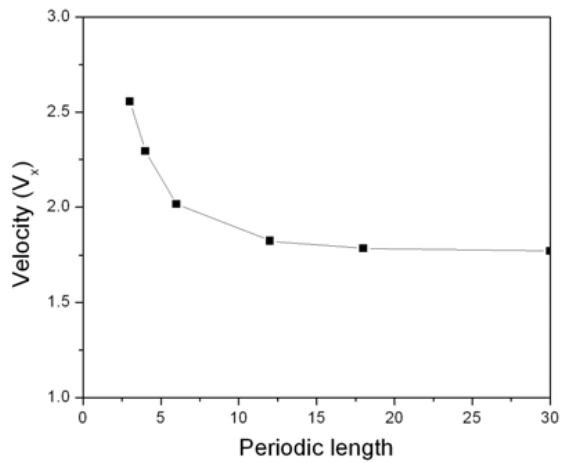
Our work is done through numerical analysis, therefore a sound background is beneficial before presentation of our work. This section separately highlights work on flow properties, regime transition and non-spherical particles which are the main focuses of this thesis.

#### **On flow properties through shear cell**

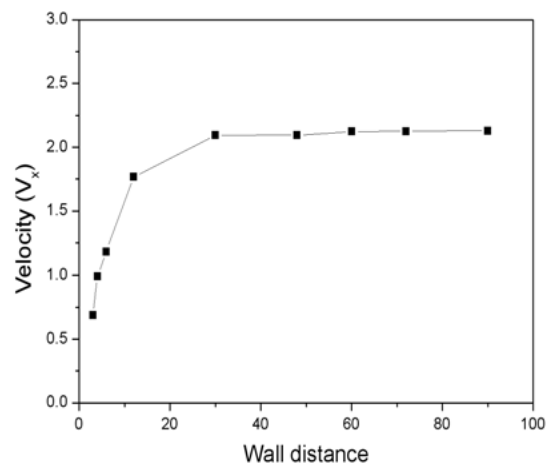
This approach to investigation of granular rheology through shear cell includes observation on key properties of flow behaviour under varying external condition through numerical analysis. In this group of work, flow properties granular assembly such as profiles and distribution of velocity, contact force, angular velocity, particle density etc. are observed under varying externally applied pressure and/or induced shear by platens or side walls. It involves generally spherical particles under monotype steady-state flow condition where

objective is to find out how external factors like boundary roughness, gravitational force etc. or internal factors like particle material friction coefficient affect granular rheology.

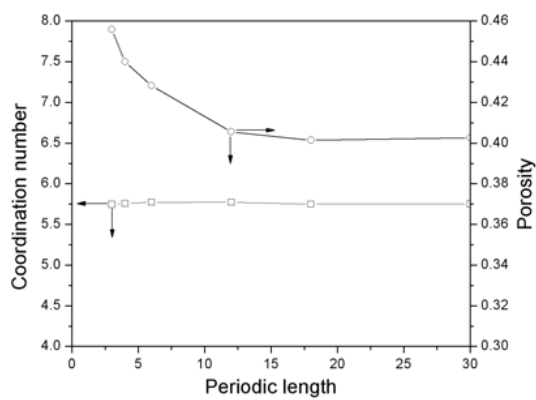
In study of flow properties of spherical particles through shear cell, Wang et. Al. presented a comparison of different sized shear cells They have focused on the effect of 1) periodic length parallel to direction of flow  $L_p$  and 2) distance between side walls  $L_t$  on distribution of microdynamic variables: velocity, porosity, coordination number and contact force as well as macroscopic variables: stress components. The aim of the work was to identify optimum length the shear cell segment that can produce satisfactory reliable results. Weighted time-volume averaging method was applied to collected data for the variables. Simulation is run for each case study until steady state flow was reached before data collection commenced. Some of important results of scale effect from that study are shown below:



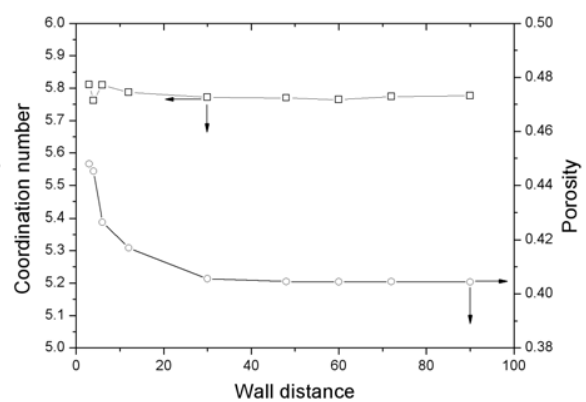
(a)



(b)



(c)



(d)

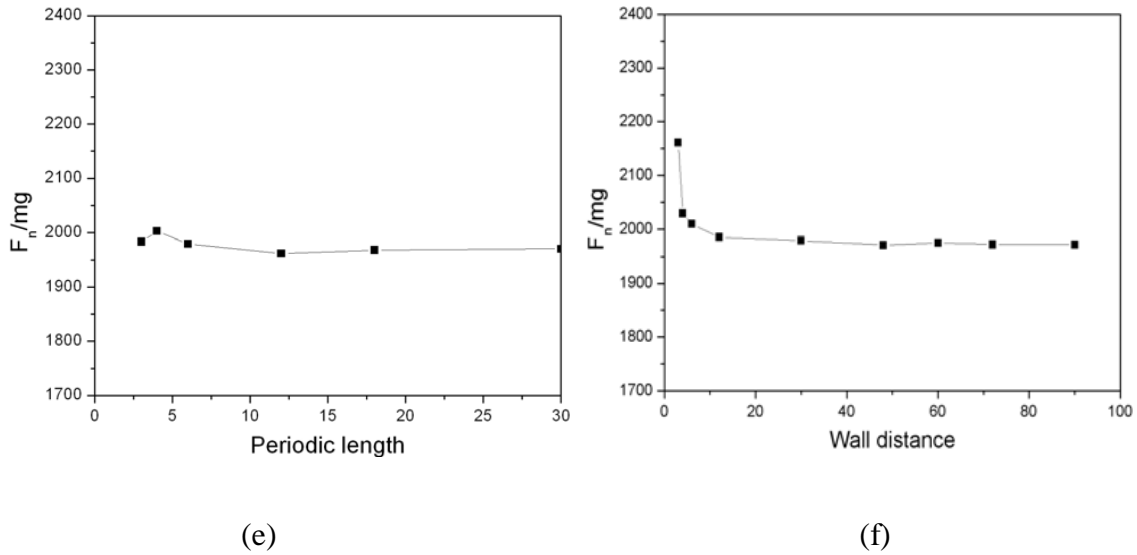


Fig. 2.13. Variation of overall mean particle velocity  $V_x$  with a) periodic length  $L_p$  and b) wall distance,  $L_t$  (the unit for velocity is  $\sqrt{(gd)}$ ; variation of overall mean porosity and coordination number with c)  $L_p$  and d)  $L_t$ ; variation of the overall mean normal contact force with e)  $L_p$  and f)  $L_t$  (unit for distance is  $d$ ).

From the above-discussed study, by comparing results with different sized shear cells, an acceptable size of the shear cell segment has been confirmed to be  $12d$  for  $L_p$  and  $30d$  for  $L_t$ . Their study is of particular significance for our thesis, because same standard of shear cell model, scaling method of variables and construction of platens using spheres are followed for our numerical investigation.

Campbell investigated the granular rheology of dry spherical particles through shear cell using numerical analysis [131-135]. During the analysis he focused on a number of key important variables: gradient profiles of linear velocity, angular rotation, volume fraction, granular temperature, stresses and couple stresses. Couple stress is analogous to Cauchy stress tensor which reflects transport of angular momentum. Therefore, it is a function of particle moment of inertia. Mathematical description can be found in [133]. He used a double-shear pressure-controlled cell where applied pressure is perpendicular to the shear direction. He found there is a symmetric or near-symmetric pattern in the gradient profiles of these variables and explained the phenomenon in light of boundary interaction from where the shear and normal force is transmitted externally. Savage et al. [136] further investigated on effects of boundary characteristics at similar configurations. They observed granular temperatures, volume fraction of assembly, particle mean velocities and wall slip velocities.



Also, they identified the phenomenon of layering of particles in the assembly during the flow and determined there was an inverse relationship between velocity slip occurring at the boundary and coefficient of restitution of the particles. Da Cruz et al. [137] analysed spherical particles through a shear cell in similar configurations to those of Campbell using DEM. However, they extended this study further to the influence of variation of shear velocity and applied pressure (that externally applied on the assembly) on apparent coefficient of friction (which he called macroscopic friction coefficient) and inertia number.

Ning et al. [138] used DEM to study granular flow through shear cell but noted another phenomenon: particles get damaged. In their work the variables like shear strain, velocities and force chains are observed. Shojaaee et al. [139] identified a critical microscopic friction coefficient at the walls beyond which the granular assembly can be mobilized by the wall friction. Wang et al. [13, 14] studied granular rheology through annular shear cell developed in a virtual platform using DEM. Similar to previous analyses [6-8, 48], Wang et al. use a rectangular segment of the shear cell as a representative cross-section. In that work, Lee-Edwards boundary conditions is applied in the direction of flow. Rough platens are constructed to shear slightly polydispersed spherical particles. These investigations involve an analysis of velocity, coordination number, porosity, force chain network, and particle friction coefficient by obtaining various correlations, spatial profiles and probability distribution functions. The main objective of these two papers is to determine the effect of variation of external influences, namely, applied shear velocity by the two opposite moving platens at the top and the bottom of the shear. The normal load that is applied by the upper platen to the particle assembly is also considered here.

Baran et al. added another variable - 'oscillation' - in their numerical study of granular rheology through Couette shear cell at zero gravity subjected to single shearing boundary presented in [140]. They analyse similar parameters: boundary properties, velocity slip, volume fraction profile and velocity profile for different external conditions both in controlled volume and controlled pressure conditions. Although oscillation is not in the scope of this thesis, it is interesting to note the similarities of our work given the absence of oscillation which will be compared later. However, Baran et al. [46] then studied the effect of gravity on their earlier study and identified non-dimensional acceleration which is a function of oscillation and gravity. It should be noted that they used the hard-sphere model to create the particles. It is one that does not consider deformation of particles and is event-driven and

hence not relevant to a practical application compared to the soft-sphere model used in this work.

### **On regime transition of particle flow through shear cell**

This group of numerical analysis of granular rheology through shear cell specifically focuses on a particular phenomenon called ‘regime transition’. Details of it can be found in section 2.3.2. It is separately highlighted because it is significantly important as it derives distinct complexity in study of granular rheology that is not observed in other rheological studies in fluid or solid mechanics. The main objective in this study is to identify the method to identify points of regime transition and how each regimes can be distinguished from others. Further, it also includes study of internal factors (like particle friction-coefficient) and external factors of flow (like pressure-controlled or volume-controlled environment) and how they play important roles the event of regime transition.

Campbell [48] contributed significantly to the field of granular rheology by identifying different regimes of particle flow. He used a numerical model to obtain monodisperse spherical particle assembly flowing through shear cell in a fixed-volume environment. Here, the soft model is used to develop the particles. Different combinations of applied load and shear rate are utilized for investigation. He concentrated on the relationship between volume fraction of the assembly and applied shear stress and normal stress at the macrodynamic level. Four regimes or states of granular flow were identified: elastic-quasistatic, elastic-inertial, inertial-non-collisional and inertial-collisional (these keywords are discussed in detail later). However, this study has limitations in trying to clearly identify transition points; there is a discrepancy between loading and unloading path. Campbell studied regime transition of granular flow in shear cell in his paper [6] using a similar setup reported in [48]. But this time, he used stress-controlled boundary condition and overcame the hurdles he faced in volume controlled condition. He provides a comparative study and concludes that stress-controlled model provides a different outcome relative to volume-controlled model and is able to capture a clearer transition between different flow states. In this study, he also incorporated contact force chain network as an element of microdynamic analysis.

Da Cruz et al. in [141] attempted to identify different regimes of granular flow through inertia number. Aarons et al. [7] performed numerical analysis similar to that of Campbell’s study [48] in volume-controlled shear cell but they added the cohesive property in the particle

assembly along with the other variables such as shear rate, particle stiffness, volume fraction and coefficient of friction. They observed stresses and coordination numbers and obtained the effect of cohesiveness on different regimes of granular flow with respect to volume fraction and stresses. In contrast to Campbell's findings [6], Aaron et al. found in their study with similar setup in [8] but nevertheless in a stress-controlled condition, that volume-controlled and stress-controlled conditions do not affect outcome. However, Campbell argues in [6] that stress-controlled condition suits better to practical application than volume-controlled condition.

Ji et al. [142] performed their analysis in volume-controlled condition using DEM on three-dimensional shear cell with soft polydispersed spherical particles. Here, they studied coordination number along with stresses, volume fraction and shear velocities and obtained a phase diagram. While the usual results agree with earlier work (eg. [6]), the coordination number-based outcomes add value to the study. In Wang et al.'s paper on regime transition [9], attention is mainly on the relationship between applied load, shear and volume fraction in order to identify flow regimes and regime transition points. An extended analysis is done on the flow characteristics at the microdynamic level by obtaining the transformation of force chain network along with the variations in condition/conditions. Lastly, an index has been generated from probability distribution of contact force; it is proposed to serve as an identifier for regime transition between quasistatic and intermediate state.

### **On non-spherical granular flow through shear cell**

Since this thesis is focused on the study of non-spherical particle flowing through a ring shear cell, it is important to understand the background of non-spherical particle assembly through shear cell as well. There are less numerical studies on non-spherical granular rheology in earlier literature because of its complexity and computer limitations. It additionally includes effect of shape on granular mechanics along with the regular investigations generally conducted on spherical particles. It also involves different methods of obtaining non-spherical shapes.

Pena et al. [143] examined irregular non-spherical particles flowing through a double-loaded double-shear Couette cell for specific properties, namely fabric orientation, fabric tensors and inertia tensors. They concluded that shear band width depends on particle shape because of its tendency for preferential orientation. Bharadwaj et al. [29] with the help of

DEM, studied granular flow of non-spherical particles that are subject to direct shear similar to Jenike's cell. They presented a comparison between the experiment, finite element analysis and DEM and showed how they can produce different results.

Campbell [64] analysed ellipsoidal particles flowing through a shear cell in terms of elastic and inertial regimes. Here, Campbell discusses his usual correlations among stress, shear rate and volume fraction, and the probability distribution of particle orientation with a new parameter added to the characteristics of non-spherical elongated particles. Guo et al. [144] created a DEM contact model for cylindrical particles and made them flow through the shear cell in a 3D virtual environment. They also discuss different types of contact scenarios. Guo et al. [66] published a detailed paper on cylindrical particles in a similar scenario to that of [144] where they related the particles' elongation to correlations among shear stress, volume fraction and stress tensors. This was similar to Campbell's study of spherical particles [6]. They also gave a statistical account of different types of contacts. This type of contact is not considered in this thesis as spherical particle components are used to build the non-spherical particles. Guo et al. [81] investigates flexible fibres using DEM to study the flow of the assembly through shear cell under double-shear and stress-controlled conditions. In this work, an additional consideration is the interaction resulting from flexibility of the fibres, where the effective coefficients of restitution are less than rigid fibres. This is despite both showing similar tendencies of aligning themselves parallel to the direction of the shear. Tong et al. [145] used DEM in their 2D study non-spherical granular flow from a more complex perspective of non-coaxial flow. Variations in particle shape, friction coefficient, initial packing and stress ratio, were compared with experimental values, and presented. This is done to show the usability of numerical analysis to produce relevant results from the experimental findings.

### **2.5.2.2 Experimental studies**

To complement the discussion on numerical analysis, the following section presents experimental work done using similar categories: flow properties, regime transition and non-spherical shape in granular rheology. Understanding of experimental background is important because it is the foundation on which numerical analysis is based.

#### **On flow properties through a shear cell**

This approach of studying granular rheology through shear cell is essential and complementary components of numerical analysis because findings in virtual platform need to be verified through physical experiments. In this method, similar key properties like particle velocity and force profiles and distributions are investigated generally with data from sample particles observed through glass or through indirect means such as pressure imprint on carbon paper.

Howell et al. [146] conducted a physical experiment using annular shear cell. They found a gradient pattern of angular velocity of particles scaled by the shearing velocity of the wheel whereby increase in scaled angular velocity is found as the particles are positioned further away from the platens. Lower scaled angular velocity results in sharper drop in particle flow away from the platens. This is equivalent to the setup concerning the numerical analyses found in [46, 134]. They further discovered a trend in probability distribution function of contact forces, roughly showing in semi-log scale that tails develop at the higher end of values of forces as a function of volume fraction. Similar force trends is also shown in numerical analysis is [13]. Hsiau et al. [147] examined the effect of boundary properties by physically experimenting on granular flow created in shear cell. They employed a stress-controlled condition on spherical particle assembly that is sheared by one boundary only. Elements of observation in this work are velocity, its fluctuation and stress components. The work shows that self-diffusion coefficient has a positive relationship with velocity fluctuation, shear rate and stresses which are influenced directly by boundary condition. Similar kind of configurations have been incorporated in [46, 140] in simulated environment which showed similar results to the experiment conducted by Hsiau. Their other experiment based papers using shear cell [148] also presents good quality results on gradient profiles and probability distribution and findings for the diffusion coefficient.

Chambon et al. [149] experimentally observed shear band in the shear cell using a glass window in the setup. They captured digital pictures of granular flow to obtain superimposed vectors of particles to show displacement field. They confirmed the dynamics of the band extends outside in terms of velocity. Corwin et al. in their short letter, [18] experimented using shear cell on spherical particles using an optical device and observed probability distribution of force chains. They used glass beads in a shear cell where the upper platen both applied pressure as well as rotated to produce shear in specimen particle assembly. They found similar trend to the experimental study found in [146]. They demonstrated a

distinguishing feature in jamming transition from the investigation of probability distribution of particle force. Cheng et al. [150] performed a comparative study (with numerical analysis and experiment) to show the velocity gradient profile in shear cell that is similar to earlier findings. However, they did not use externally applied pressure but rather extended height of particle assembly so that the shear band begins lower than the surface. Nevertheless, the trend remains the same as far as shear band is concerned.

Latzel et al. commendably summarized their experiment and numerical study in shear cell in their paper [151]. Jasti et al. [152] conducted a physical experiment using a two-dimensional shear cell study on spherical particle assembly by varying wall roughness. They analysed the usual parameters, i.e. velocity, volume fraction, and granular temperature. In addition, they obtained various relationships with roughness factor, which is defined by the fraction of granules that fit exactly between the cylindrical wall disks (a definition derived by Jenkins and Richman [153]). Although this study was similar to their previous work, nonetheless it contributes significantly because physical experiments are essential to ensure the reliability of numerical analyses. Wildman et al. [154] used the experimental method to study granular material flowing through shear cell. However, unlike the previous cases we discussed, they emphasized rapid granular shear flow and observed kinetic-theory of gases for parameters, specifically granular temperature, particle velocity, and volume fraction. They used Positron Emission Particle Tracking (PEPT) technique to obtain location of particles and study packing fraction and velocity fields.

Boyer et al. [127] introduced dimensionless viscous number when they observed the viscoelastic behavior of dense particle assembly flowing through shear cell in their laboratory set up. They investigated relationship between friction coefficient, volume fraction and the dimensionless viscous number to study viscoplastic behaviour of the dense suspensions. Orlando et al. [155-157] conducted a laboratory experiment, their objective being to obtain the effect of boundary condition on particle flowing through annular shear cell. They also observed correlation between effect of particle size and boundary conditions. They found that dilute flows do not show notable effect of boundary when the particles are small. On the other hand, when particles are larger and particle assembly is in dense condition, the effect of boundary is more evident. Murdoch et al. [158] investigated the effects of gravity on formation of shear bands in their experiment. He used Taylor-Couette shear cell to generate

granular flow under less external pressure. The gravitational environment was simulated inside an experimental rack specially designed to achieve parabolic flight environment.

### **On regime transition through shear cell**

Not many experimental studies have been conducted on regime transition through shear cell because it is quite difficult if not impossible to obtain details of varying flow structures physically. Lu et al. [159] did an experimental investigation using shear cell in both volume-controlled and stress-controlled conditions to observe flow regimes. They used single shear upper platen loaded cylindrical shear cell as experimental setup and beach sand as specimen particle assembly. They have demonstrated a comparable result between experiment and numerical model and argued that particle sphericity has a strong influence on the results. Koval et al. [160] also looked at particle flow through shear cell using DEM where they concentrate on flow regimes and their transition utilizing a microdynamic perspective. They highlighted the contrast between dynamics particles that are near the shearing walls and away from the ones that are away from shearing walls and showed that particles near boundaries have traits comparable to inertial regime while the furthest particles show creep that are found in quasistatic regime.

### **On non-spherical granular flow through shear cell**

Similar experimental studies are found for non-spherical particles as with spherical particles. Salmon et al. [161] conducted an experiment on the flow of elongated particles (referred to as wormlike micelles) in the region where shear-banding develops. They focused on velocity profiles at different regions of the flow. This work similarly considered what is observed in the case of spherical particles flowing through shear cell, which makes it very relevant to our work. Borzsonyi et al. [17] performed both numerical and experimental analyses on elongated particles under shear through a Couette cell. Their observation was primarily based on orientation of the particles and they also expanded on the analysis of angular velocities and torque of particles in [162]. Ghadiri et al. [163] studied attrition of non-spherical particles through shear cell to verify Neil and Bridgwater model. They further identified that beyond a certain stress level, there is a point when body fragments affect significantly in particle breaking with surface damage to lesser extent.

## 2.6. REMARKS

So far, many studies have been introduced to show extensive work done on granular rheology, particularly, through shear cells. Different aspects have been highlighted through them which affect flow behaviour. However, a few things can be identified which were not addressed by them. These scopes of study are summarised below.

In existing studies, we have found literature on platen roughness. However, extension to microdynamic consideration is not available which is an interesting topic to explore into. We also have found studies about effect of gravity. But none of them highlighted on the point on how we can resolve the issue of connecting the study based on gravity and where gravity is overlooked. If we reflect on the existing research on granular rheology, we find that exhaustive work has been done on spherical particle flow but equally work has not been done on non-spherical particles, even though they have greater significance for practical applications. Further we find that although much work has been done on non-spherical particles from different shapes, sizes and conditions, not enough attention has been given to bridging the knowledge gap concerning spherical and non-spherical particles. Finally, we have not found any research that has directly addressed the important topic of regime transition for non-spherical particles. In this thesis, we cover all these interesting shortcomings and add more to the existing knowledge, thereby highlighting their significant contribution to the research field.



# **Chapter 3: Linearity and non-linearity of velocity profile of solid flow in a shear cell: Effect of platen roughness**

## **OVERVIEW**

Granular rheology is numerically investigated in an annular shear cell setup with an emphasis on effect of the roughness of cell platen on the flow behavior of particles inside the cell. The platen of the cell constitutes spherical particles, and its roughness is controlled by the diameter size of these particles to study how the flow behavior is affected by platen roughness. It is done through analysis of some key dynamic variables, i.e. particle linear velocity, angular velocity, contact force, contact moment and porosity. It is found that platen roughness is directly responsible for the transition of the velocity gradient profile of particle flow from non-linear to linear. This transition is reflected in the profile and distribution of angular velocity, contact force and contact moment as such that these parameters indicate a non-linear trend with higher value near the boundary and lower value near the core region when the platen is smoother. On the other hand, the trends for corresponding variables maintain a uniform and linear distribution throughout the core region with a rough boundary-platen surface. Finally, according to the microdynamic analysis at the boundary based on simulation, the method by which boundary platen transfers energy to adjacent particles affects the whole flow characteristics of the assembly.

### 3.1. INTRODUCTION

Granular rheology is a complex analysis of mechanics of such materials that demonstrate a discrete nature relative to fluids, yet are not large enough to be considered as solid especially when compared to their conglomerate size. Despite its complexity, it is essential to comprehend granular flow dynamics because it is very important to industrial operations. Some examples of industrial applications are coal transportation, drug mixing and limestone storage. Many studies have been conducted to understand the flow behavior of granular assembly under various conditions, for example, in hopper [164, 165], rotating drum [166], vibrating bed [167], and inclined bed [168]. Granular rheology is mainly categorized into three principally identified regimes: quasi-static, intermediate and kinetic [48]. Quasistatic flow refers to very slow displacement of particles in a very dense condition. Kinetic regime is the other extreme with particles being agitated as gaseous molecules in a very diluted state. In between exists the intermediate regime. Much work has been performed on the quasistatic regime of flow mechanics while relatively less has been done on the inertial regime.

In the study of granular rheology, two approaches have been applied to DEM: fundamental and applied. While the applied approach concentrates on practical usage of the granular system such as rotating drum, conveyor among others, it is unable to address directly the underlying principles of this field. To overcome this deficiency the fundamental approach uses simple systems in laboratory setup. Among such setups, shear cell or tester is a classical tool for investigating the flow characteristics of particulate assembly [9]. It can be of several types. The two most common used ones are Jenike's shear cell [97] and annular shear cell [126]. Annular shear cell, which is used in our study, comprises two concentric cylinders with two caps located at the top and bottom known as 'platens' (Fig. 3.1 inset). The advantage of the shear cell is that it can mimic the infinite flow of granular materials within a confined space. Therefore, such setups have been mainly used for validating continuum theories and continuum models [169-171]. Further, effect of particle properties like particle shape [143], yield strength [150, 172] and cohesiveness [7] on flow characteristics are extensively investigated. Studies are conducted in various conditions obtained from manipulating external parameters like applied normal and/or shear load. These manipulations are conducted in various ways: a) upper platen is rotated while the lower platen is kept

stationary [127]; b) both platens are rotated in the opposite direction [13]; c) volume is kept constant [7]; d) constant load is applied while volume varies [13]; and e) the inner wall is rotated while outer wall is loaded (inwards) [128].

Velocity gradient profile analysis is the first objective of this work. It is an old and well-recognized observation in the field of granular rheology and has been done on numerous occasions [eg. [6, 9, 48, 140]]. Some observations found it linear [6] while others found it to be non-linear [140]. However, it has not been extensively investigated what makes the profile linear or non-linear. Da Cruz [137] found linear and non-linear velocity profiles from variation of inertia number but did not address this point as it was not the core focus of that study. Hsiao et al. [173] argued that the non-linearity of velocity profile is attributed to the gravitational effect. Campbell [133] worked on a continuum model with a hypothesis concerning boundary conditions where both linear and non-linear velocity profiles were examined through variations in dynamic behavior at the boundary condition. However, there is no clear understanding of what happens in a realistic context which produces differences in findings.

In this study, the effect of platen roughness on granular rheology in a shear cell in a stress-controlled condition is studied using the discrete element method (DEM). A detailed discussion addresses this subject at a microdynamic level where a wide range of different variables are considered, namely, profiles and statistical distribution of angular velocity, velocity fluctuation, contact force, contact moment and porosity. These are also referred to at the macrodynamic level. The study is on boundary characteristics and their influence on granular rheology with a focus on effect of linearity and non-linearity of velocity profile.

## **3.2. SIMULATION METHOD AND CONDITIONS**

This section describes the setup and method of analysis for granular flow through shear cell. At first, discrete element method (DEM) is introduced. Then we describe how the model is prepared and then simulated to obtain desired data.

### **3.2.1. DEM overview**

This study is conducted using commercial software platform, PFC3D. The software was created by Itasca Consulting Group Inc., which was founded by the pioneers of Discrete

Element Method of Granular Mechanics, namely, Dr. Cundall et al. It was first released in 1994 along with FLAC and has been used worldwide. It also heavily relies on findings documented by Potyondy et al. [22, 23] and has successfully simulated realistic particle propagation such as conveyor event, avalanche, hopper flow among many others. What made it more popular is its versatility, virtual representation and user-friendliness. It provides a specialized platform for particle mechanics to investigate a wide range of practical possibilities and observe in a real-time vivid graphical output. Also, it is easy for researchers to use through its comprehensive tutorials and examples of easily readable code language. Many examples of its applications can be found in the web [174, 175]. At the end of 2014, PFC has gone through major redesigning with much improved efficiency and versatility.

The principal final forces acting on each particle resembles a simple spring-dashpot configuration. The equation is as follows:

$$\mathbf{F}^c = \mathbf{F}^h + \mathbf{F}^d \quad (3.1)$$

Where,  $\mathbf{F}^h$  and  $\mathbf{F}^d$  are spring force (Hertz model) and damping force, respectively. The extended form of the equation is given below:

$$\mathbf{F}^c = -\mathbf{F}_n^h \hat{\mathbf{n}}_c + \mathbf{F}_s^h - \mathbf{F}_n^d \hat{\mathbf{n}}_c + \mathbf{F}_s^d \quad (3.2)$$

The numerical model used in our work implements a progressive calculation of velocities and forces in each time-step. It is derived from an approximation of the Hertz-Mindlin and Deresiewicz model and includes non-linear formulation of normal contact force as follows:

$$\mathbf{F}'_{nij} = -\mathbf{k}_{nij} |\Delta_{nij}|^\alpha \quad (3.3)$$

Where,  $\alpha$  is the non-linearity exponent to obtain the Hertz contact force and 'n' stands for the normal force-related component.  $\alpha$  is found to be in the range between 1.0 to 1.5 in the experimental study by Crossley et al. [176]. The spring component  $k_n$  is derived from particle shear modulus,  $G$  and Poisson's ratio  $\nu$  using the following equation:

$$\mathbf{F}'_{nij} = -\mathbf{k}_{nij} |\Delta_{nij}|^\alpha \quad (3.4)$$

$$\mathbf{k}_{nij} = \frac{2|\mathbf{G}|\sqrt{2\bar{\mathbf{R}}}}{3(1 - |\mathfrak{g}|)} \quad (3.5)$$

where,  $\bar{\mathbf{R}}$  is the effective radius ( $=d_i d_j / (d_i + d_j)$ ) in Fig. 2.3). The viscous component of normal force is obtained by:

$$\mathbf{F}'_{nij} = 2\beta_n \sqrt{\mathbf{m}_{eqv} \mathbf{k} v_n} \quad (3.6)$$

where,  $v_n$  is relative velocity between the two particles in the normal direction (in direction of  $\mathbf{e}_i$  in Fig. 2.3),  $\beta_n$  is normal critical damping ratio of the particles and  $\mathbf{m}_{eqv}$  is equivalent mass given by:

$$\mathbf{m}_{eqv} = \frac{\mathbf{m}_i \mathbf{m}_j}{\mathbf{m}_i + \mathbf{m}_j} \quad (3.7)$$

where  $m$  represents mass of the particles and is obtained from density  $\rho$  by using the basic volume equation  $m = \rho V = \rho \times \frac{4}{3}\pi(d/2)^3$ . ( $\mathbf{m}_{eqv} = m$  in case of wall and particle interaction).

The tangential (or shear) force is obtained via the incremental method:

$$\mathbf{F}'_{sij} = \mathbf{k}_s |\Delta_{sij}|^\alpha + \mathbf{F}'_{sij0} \quad (3.8)$$

which is directly related to the normal contact force by the following equation:

$$\mathbf{k}_s = \frac{2(1 - \mathfrak{g})}{2 - \mathfrak{g}} \alpha \mathbf{k}_n (\mathbf{F}'_n)^{(1-\alpha)/\alpha} \quad (3.9)$$

$$(\mathbf{F}'_s)_0 = \begin{cases} \frac{\mathbf{k}_s}{(\mathbf{k}_s)_0} (\mathbf{F}'_s)_0 & \text{where, } \mathbf{F}'_n < (\mathbf{F}'_n)_0 \\ (\mathbf{F}'_s)_0, & \text{else} \end{cases} \quad (3.10)$$

where,  $(\mathbf{F}_n^h)_0$ ,  $(\mathbf{F}_s^h)_0$  and  $(\mathbf{k}_s)_0$  are the normal force, the shear force and the tangent shear stiffness computed at the beginning of the time-step, respectively. Again,  $\mathbf{F}'_{sij} = \mu \mathbf{F}'_n$  following simplified model discussed earlier. Then the shear force is updated accordingly.

However, the dashpot component remains similar (please refer to Fig. 2.1):

$$\mathbf{F}''_{sij} = \left( 2\beta_s \sqrt{\mathbf{m}_{eqv} \mathbf{k}} \right) \mathbf{v}_s \quad (3.11)$$

where,  $v_s$  is relative velocity between the two particles in shear direction (in direction of  $t_i$  in Fig. 2.3),  $\beta_s$  is shear damping ratio of the particles. All the particles in the assembly are taken into account individually using the above-discussed equations to obtain dynamics of overall granular flow.

Annular shear tester setup is simulated to generate particle flow in double-shear stress-controlled condition. Large spherical particles are considered so that effect of interstitial fluid, Van der Waals force, electrostatic force and other non-contact forces can be ignored. Here, particle mechanics are governed primarily by: a) coefficient of friction,  $\mu$  b) shear modulus of elasticity,  $G$  c) Poisson's ratio,  $\nu$  and d) damping ratio  $\beta_n$  and  $\beta_s$  for normal and tangential (shear) interaction, respectively. Gravitational force is nullified so that it does not influence the impact of platen roughness. The assumption is reasonable based on the fact that the force applied by the upper platen is significantly high and its effect combined with induced high shear rate makes the influence of gravity practically negligible.

### 3.2.2. Preparation of model

A rectangular segment of the used annular shear cell [126, 131] is considered to have the dimensions of approximately  $12d \times 30d \times H$ , where  $d$  is the mean diameter of spherical particle used for the study and  $H$  is the height of the platen. A similar configuration is found in [9]. The segment is small enough that the radius of curvature can be overlooked. This is well illustrated by the comparison in Fig. 3.1 (inset). Periodic boundary condition is applied at the walls across the direction of flow to generate seamless continuity in shear. This is analogous to annular shear cell such that a particle exiting from one wall will enter at the same position (in terms of  $y$  and  $z$  components) with the same dynamic values such as force, velocity and so on. Upper and lower platens are created within the segment with reasonable

space between them to generate particle assembly for the purpose of investigation. The upper and lower platens each constitute varying spherical particles of different scaled diameters so that the entire area of the domain x-y plane is filled, which creates walls with varying degrees of surface roughness. For platen-constituting spherical particles,  $0.9d$ ,  $1.1d$ ,  $1.3d$ ,  $1.5d$  and  $1.7d$  are considered. Spherical particles have been used previously to construct the rough platens of annular shear cells. It helps control the surface roughness more easily. It can also be related to adjacent particles because of similar properties between constituent platen particles and specimen particles. Examples of this treatment can be found in [13, 134, 138, 160]. Two smooth (frictionless) walls are generated through the centers of platen particles with the same rigidity to ensure that no particles escape through the gap of the platen particles when any pressure is applied. However, there is no dynamic effect between the platen particles and these two walls mimic the single solid rough platen boundary. When platen-constituting spheres are small, the platen is considered to be relatively smooth and less frictional. When the platen-constituting spheres are large, the platen is considered to be relatively rough and more frictional. The variation of diameter of these spheres causes variation of platen roughness.

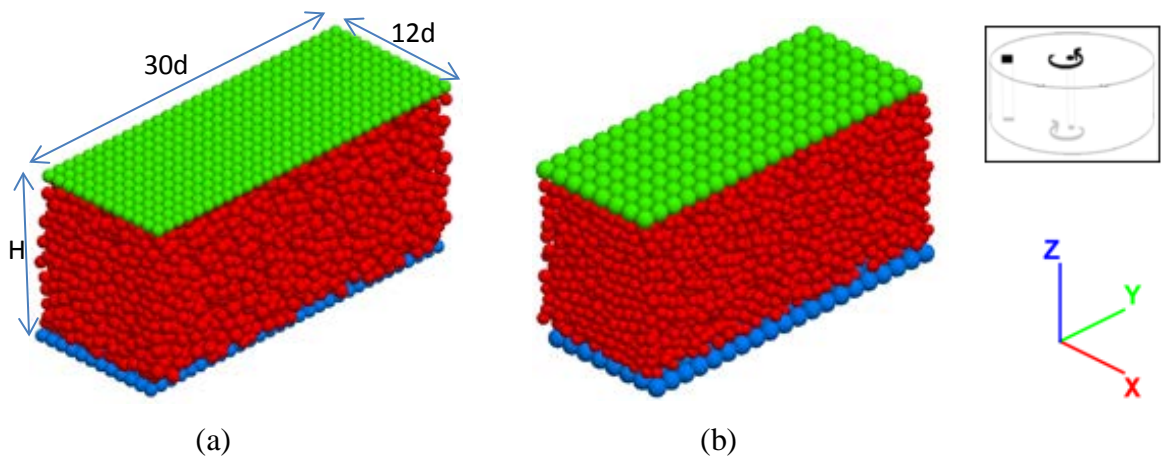


Fig. 3.1: Simulated model shear cell (a: platen particle dia.  $0.9d$ , b: platen particle dia.  $1.5d$ )

Two such shear cell models are shown in Fig. 3.1. The platen particles possess the same microdynamic properties (material density, damping co-efficient, friction coefficient and

material stiffness) of the constituents of particle assembly. The effect of platen roughness can be highlighted through variations in the platens' particle size. Particles of the same platen are stationary relative to each other and therefore exert no force or torque between them. Stationary side walls are also provided parallel to the direction of flow at the terminal points of y-axis. Their friction coefficient is set as zero to minimize the effect on the flow. However, there are still some minor outcomes from the rigidity of the walls that are reflected in the results. Approximately 5000 slightly poly-disperse large particles are generated randomly between the upper and lower platens with an initial dimensionless volume fraction of about 0.65. Similar number of particles are used in [13]. Key particle properties and simulation parameters applied in the model are the same for both as given Table 3.1. Particle internal properties are matching with that of glass beads.

Table 3.1: Parameters used in the simulations

Property	Value	Unit
Friction coefficient, $\mu$ (particle-particle and particle-wall)	0.3	(-)
Damping ratio, D (normal and shear)	0.3	(-)
Young's modulus	$2.5 \times 10^6$	$\pi \rho d g / 6$
Poisson's ratio	0.3	(-)
Time-step	0.00001	$\sqrt{d/g}$
Normal pressure	710	$\pi \rho d g / 6$
Shear velocity of each platen	6.5	$\sqrt{g d}$

In order to obtain probability distribution, the following numerical treatment is applied.

$$P(f_i) = \frac{n_i}{N \times df} \quad (3.12)$$

where, N is the total number of particles considered;  $n_i$  is the number of particles in  $[f_i, f_{i+1}]$ ;  $df = f_{i+1} - f_i$  and subscript 'i' identifies one particle and 'i+1' will be the next particle. This same method is applied to obtain the probability distribution in this chapter.



### 3.2.3. DEM simulation and conditions

At first the tightly packed particle assembly is allowed to naturally relax within the finite space between the platens and sidewalls. After some time, the particles occupy the entire space. Then the upper platen is loaded heuristically to a lesser load so that it does not create any strong initial local concentrated regions when shearing is induced because it would affect the final result. The loading by the upper platen on the particle assembly is achieved by gradually lowering the platen at each time-step and calculating the development of load as a reaction force on the platen from adjacent particles. Once the pre-set load is achieved, the upper platen adjusts its height at every time-step to maintain constant stress. This adjustment is based on the reactionary force on the platens from the adjacent contacting particles. Then the upper and lower platens slowly move horizontally in opposite directions and their velocity gradually increases in the stress-controlled condition. There two common types of system-scale constraint considered in such kind of study: 1) strain- or volume-controlled condition and 2) stress-controlled condition. Examples of volume-controlled condition are found in [7, 47, 48, 142] and for stress-controlled condition in [6, 8, 13]. Wang et al. [9] argued that whilst both volume and stress controlled condition was useful in analysis of granular flow, stress-controlled condition was more relevant in practical application because of the presence of free space within granular matter which allows the flow to expand or compress as the applied stress is varied. Further, we found from comparison between Campbell's two studies [6, 48] that stress-controlled condition gave better analytical results than strain-controlled condition. When the desired shear velocity is nearly reached, the loading by the upper platen is slowly increased to the desired value. The simulation is run for a reasonably long time to obtain a steady state condition with the best possible spatial distribution. The time-step is kept as low as  $\approx 0.00001\sqrt{(d/g)}$  at all times to ensure that contact detection occurs appropriately and overlapping is avoided for effective application of DEM.

Then various microdynamic and macrodynamic data are collected to investigate the phenomena. It should be mentioned that near-quasistatic intermediate regime is the main consideration of this chapter. Near-quasistatic intermediate regime refers to the state of flow where particles are predominantly in clusters (see Fig. 2.6 of this thesis) and the flow is not-yet independent of induced shear rate. The time averaging method is quite straight forward. Once the steady state at the desired condition is reached, data for each parameter are collected

for each time-step over a long period of time. Microdynamic variables that are analysed are: particle velocity, inter-particle contact force and contact moment and particle angular velocity. The localized property that is inspected is porosity. For microdynamic properties, individual particles are considered and for localized properties measurement regions are applied. However, the measurement spheres are kept relatively small (1.5d) so that the results for microdynamic characteristics can also be accounted for. All microdynamic values are obtained directly from simulations whereas macrodynamic values are obtained through manual calculations. Obtained data are resolved in the gradient profile across flow and/or probability distribution functions. Finally, to understand how the platen texture impacts on the flow dynamics of granular particles, the results are correlated with the change in size of platen particles and linearity and non-linearity of velocity profiles.

### **3.3. RESULTS AND DISCUSSION**

This section is organized into three successive stages for examining the effect of platen particle size on velocity profile. (1) the primary and most important result of the velocity profile, which is the foundation of the work, is discussed. (2) angular velocity is shown with respect to variation of linear velocity as indicated in case studies. (3) contact force and contact moment are described in terms of how their influence is reflected on the velocity profile. (4) a deeper microdynamic analysis of internal structure is done, based on the obtained data of porosity at finite element scale, to understand the restructuring that takes place phenomenologically.

Accounted for here is the variation in platen particle size which is responsible for linearity and non-linearity of velocity gradient of particle flow through shear cell.

#### **3.3.1. Velocity field**

Two types of velocities are looked at here (i) translational or linear velocity; and (ii) angular or rotational velocity.

##### **3.3.1.1. Translational velocity**

The velocity profile is obtained for the cases using different levels of platen roughness. Individual particle velocities are scaled to the platen velocity as  $v_i/V$  where  $v_i$  is particle

velocity and  $V$  is platen velocity. Here, only the velocity along the direction of shear, i.e. x-axis is considered since velocities along the y-axis and z-axis are negligible in the steady state condition which is discussed in [13]. This is confirmed in earlier experiments [148]. It can be seen from the study of particle arrangements that layers of particles with similar velocities (in terms of magnitude as well as direction) are developed through the process of attaining steady-state flow condition. This was well established in earlier research [136]. There is symmetry in the velocity gradient for all generated results which is found in numerous previous observations [6, 14, 140]. The observation is confirmed through time-space averaged velocity profile obtained from the simulation normalized by platen velocity across the particle assembly, i.e. perpendicular to the flow in scaled heights such as  $h_i/H$  where  $h_i$  is particle z-position and  $H$  is upper platen z-position with respect to lower platen (as shown in Fig. 3.2a). It should also be noted that the distance between the two platens is not the same for all case studies. It is influenced by platen roughness and will be shown later in the macrodynamic analysis of the porosity of assemblies in section 3.3.3. So, for clear comparison of different cases, the height of each segment is also scaled. It is evident that velocity is at inflexion point with zero or near-zero values near the central region of the particle assembly. In contrast the layer of particles near the shearing platens obtains the highest velocity. This is due to the fact that the shear effect at the central part of shear cell is being balanced between forces generated from the two opposite moving platens at the same velocity. On the other hand, the particle velocity is the highest towards the platens in the direction of platen displacement which gradually dissipates layer by layer. This is because frictional interaction becomes weaker gradually further away from the platens. Also, there is a noticeable fall in velocity near the platens which is reasonably affected by platen roughness. These findings regarding decrease are qualitatively in sound agreement with previous studies [46]. As expected, as the platen surface becomes smoother, the velocity slip is higher.

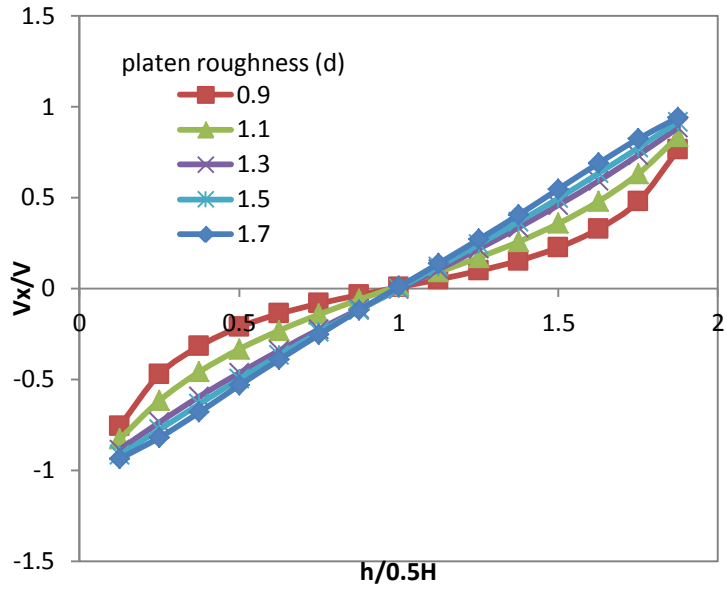
The most significant finding that has been recognized in this profile is that it shows how the profile gradually changes from non-linear to linear and this finding informs the present work. There have been numerous papers on velocity profiles, some highlighting a non-linear relationship while others show a linear relationship between particle velocities and height. These differences were not addressed extensively except in one hypothetical study [133].

These phenomena can be explained using simulations based on the fact that when the shear-inducing platens are relatively smoother, the normal load dominates the shear

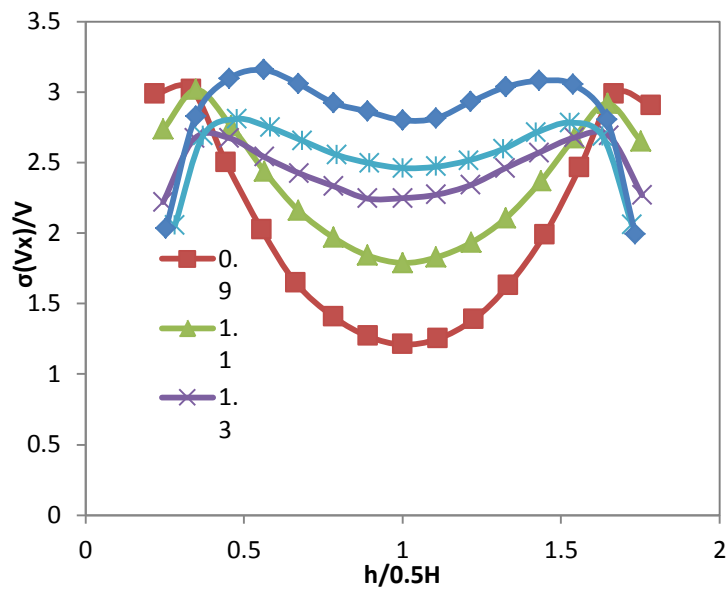
interaction force. It causes the platens to transfer the momentum to the surface rather than at the centre of the adjacent particles. On the other hand, as the surface of the shearing platen becomes rougher, shear interaction becomes increasingly significant and at one point balances out the normal loading effect while the platens' interaction with the adjacent particles is dominated by forces that seem to pass through the centre of those particles. More needs to be known about what happens at the boundary which causes this variation. It is analysed in detail in each of the following sections where boundary values of each set of parameters are specifically investigated.

The next important consideration that strongly influences the rheology is the fluctuation in velocity which is directly related to granular temperature. In order to illustrate this point, time-space averaged standard deviation of individual particle velocity from its fluctuations is obtained at the microdynamic level, scaled by platen velocity and presented in a similar gradient format. It is clear from Fig. 3.2b that velocity dispersion is at its highest near the platens when platen particle size is smaller. It also reduces as the platen texture becomes rough. In the central region, inverse effect is found to what is observed near the platens: low velocity fluctuation for smooth platens and fluctuation increases as platen particle size increases.

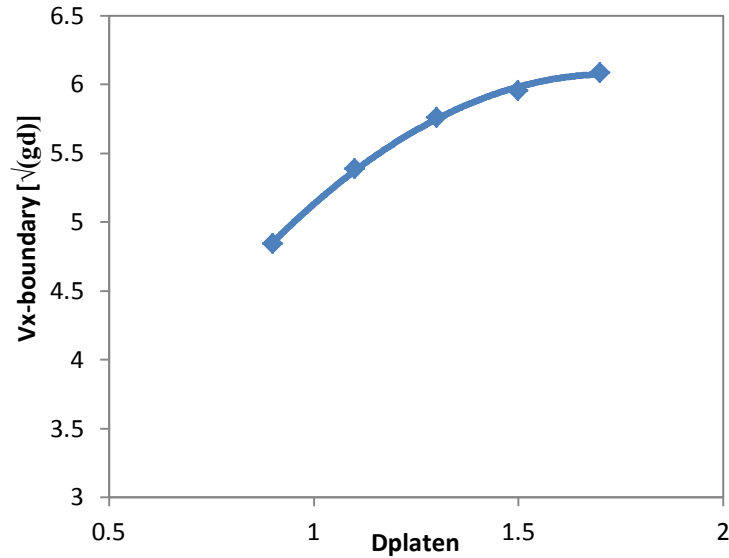
This is because when the platens are smoother, they are less able to organize in an orderly way the adjacent particles through shear effect. However, due to the high fluctuation, the dissipation of energy also increases across the layers causing minimum to reach the core and hence the fluctuation is least at the central part of shear cell. On the other hand, with cases of rougher platens, the fluctuation of velocity gradually increases to a certain level further from the platens until the fluctuation of velocity becomes constant across the layers. This is due to the higher shear impact of rougher platens having stronger command to the flow and direction of the adjacent particles which reduces further away from the platens to a certain extent until there is uniformity of the fluctuation of velocity. Velocity fluctuation represents granular temperature.



(a)



(b)



(c)

Fig. 3.2: a) Scaled velocity gradient profile of particle assembly for cases with different platens constituting monodispersed particles with sizes of 0.9d, 1.1d, 1.3d, 1.5d and 1.7d, respectively; b) gradient profile of scaled standard deviation of particle scale velocities ( $V_x$ ) for previously mentioned cases. c) Overall averaged values particle linear velocity (in x-direction) adjacent to platen for platen-constituting particles of different sizes,  $\sqrt{(gd)}$ . (All data are obtained for the rheology at base values from Table 3.1).

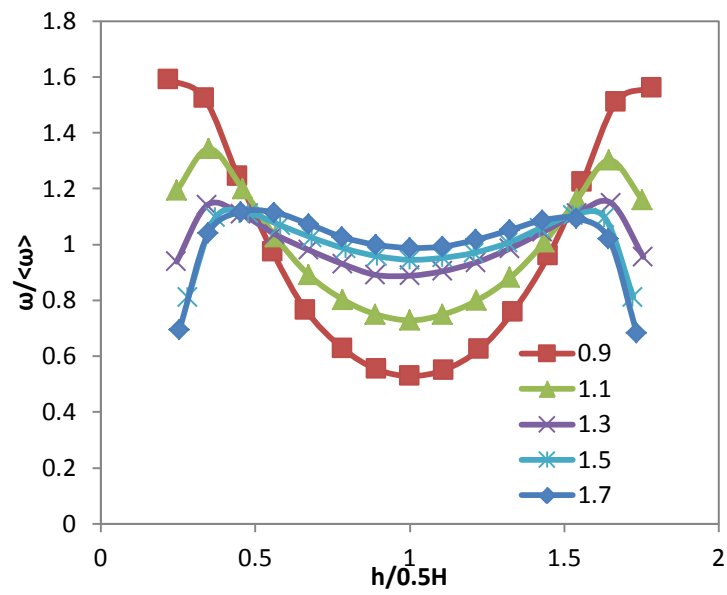
As the platen friction increases, it causes overall higher granular temperature. This causes the force to propagate through the cell's central region. This is reflected by near-constant high fluctuation of velocity across the flow around the core section. It works as a medium of velocity gradient propagation which, consequently, becomes uniformly distributed which is not possible when the platen is less frictional. As such, velocity profile becomes from non-linear to linear when platen particle increases. Better understanding will be obtained through force analysis in this work. It is also important to note that there is a jag near the platens in rougher cases which diminishes with decrease of platen particle size. This suggests that, even in smoother cases, there is a certain degree of control from the rigidity of the platens that causes the adjacent particle's velocity fluctuation to reduce.

In order to closely monitor the dynamics adjacent to the upper platen (the loading platen), a control volume is considered next to the platen wall so that the height can contain only one layer of particles. In the illustration of the upper boundary platen, Fig. 3.2c shows time-averaged velocity of particles adjacent to the platens. Averaged velocity is observed to be increasing as the platen roughness also increases. It suggests that velocity slip gradually decreases until it becomes near constant at the boundary; here the case study moves from smooth to rough and the adjacent particles try to catch up to the platen velocity. However, there will always be some amount of velocity slip as previously suggested [9]. Higher velocity slip at the boundary is identified as an important factor in that the distribution of velocity across layers of cannot be linearly uniform when the platen surface is smooth. As the platen friction increases, velocity distribution catches up to the entire height of the flow. Thus, velocity slip is mostly an outward reflection of velocity gradient profile transforming from linear to non-linear.

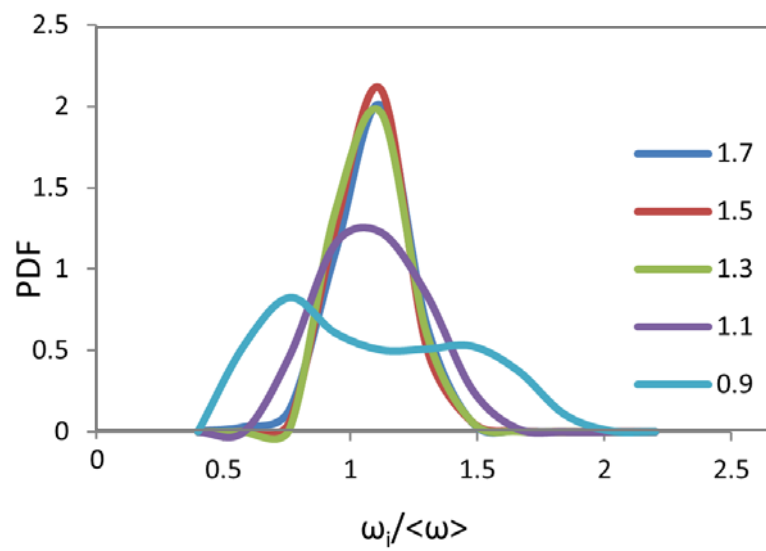
### **3.3.1.2. Angular velocity**

The second most obvious variable that has a direct significance next to velocity profile characteristics is angular velocity. Fig. 3.3a shows variation of angular velocity scaled to the overall mean value for the assembly across the flow (in a vertical direction) based on simulation outcome. This qualitatively agrees with [133], meaning that when the platen is smoother, the angular velocity is transferred to the contact point which causes highest angular velocity near the platens. However, it reduces through dissipation towards vertical centre and reaches its lowest point at the central region as it goes further from the shear-inducing platens. However, as the platen roughness increases, this trend becomes gradually more linear, leading to two subsequent events: a) there is less angular velocity at the boundary; and b) it is uniformly distributed across the profile. It should be noted that jags have been formed in all cases to varying degrees. Jag means that there is a sudden drop in angular velocity in specimen particles right next the the platens. The expression of jag can also be found in [134]. It can be found that the platens show characteristics of a sink for the adjacent layers even though they really are the source of angular velocity through shear induction as a whole. The idea of sink means that particles absorbs angular velocity of those adjacent particles. The expression of sink can also be found in [134]. The sink happens because the particles constructing the platen are non-rotationary which consequently obstructs the rotational ability

of adjacent particles, especially when the platen particle sizes are larger. In this scenario they tend to lock the adjacent particles within the roughness of the boundary.

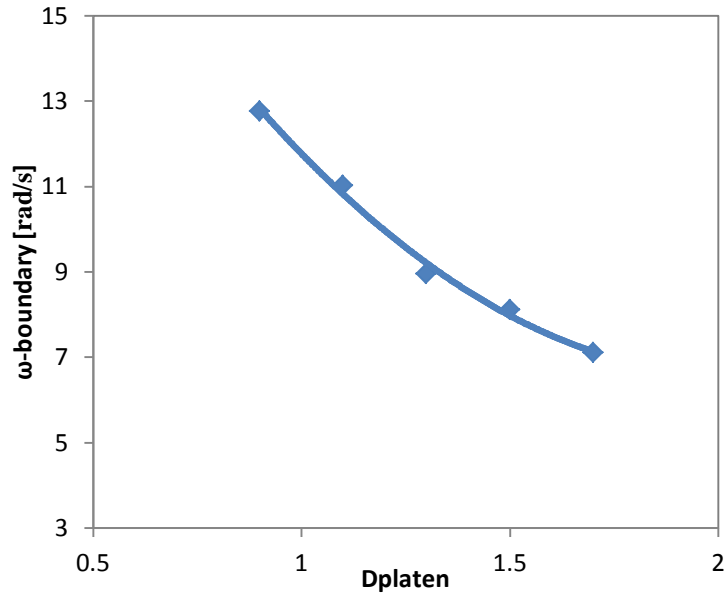


(a)

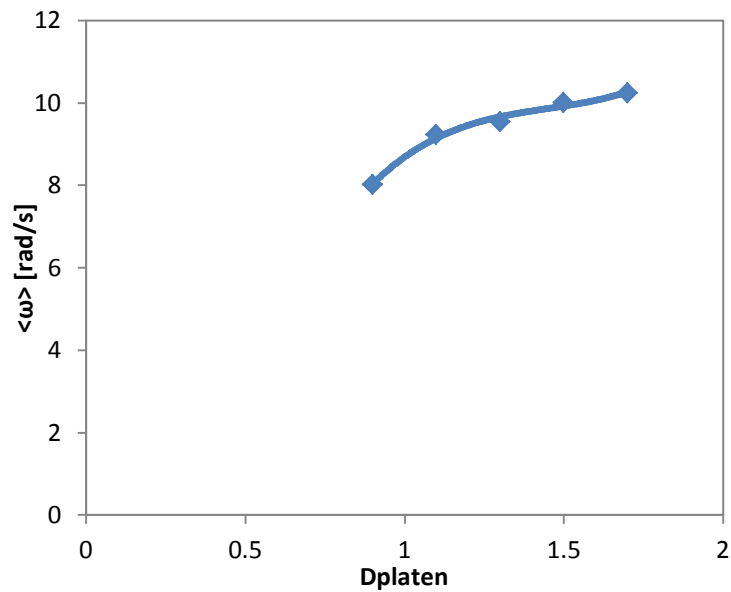


(b)





(c)



(d)

Fig. 3.3: a) Scaled particle angular velocity at different levels along the z-direction for varying platen roughness b) probability distribution of scaled angular velocity for the platens' varying texture c) Overall time-averaged values particle angular velocity adjacent to platen for different platen-constituting particle sizes (rad/s) and d) time-averaged overall angular velocity for different cases (rad/s).

The 0.9d case is the least affected because the platen roughness is too little to lock the adjacent layer of particles between itself and the second layer. Thus the sink's nature is less manifested. This phenomenon is related to linearity of the velocity profile in a way that, because of the lack of granular temperature, the angular velocity quickly dissipates and is not transferred to the central region as shown in Fig. 3.2a with reference to the 0.9d platen particle size. Furthermore, the dispersion of scaled magnitude of angular velocities at particulate level is evident in its probability distribution.

Fig. 3.3b shows the probability distribution (PDF) of time-averaged individual particle angular velocities  $\omega_i$  normalized by mean angular velocity  $\langle\omega\rangle$  of the assembly in order to further understand what Fig. 3.2a shows. It can be seen that for the cases 0.9d and 1.1d platen roughness (which predominantly shows non-linear velocity profile), the probability distribution deviates more from the mean and there is no distinct single peak at the mean value. As the platen particle size increases, the peak at the mean value becomes stronger while the deviation from the mean decreases. As such, it confirms the uniformity of particle angular velocities across the flow with high peak at the mean while for cases with platens with smaller particles, particles with mean value of angular velocity are progressively much fewer in number. The phenomenological implication of this is that when platens are less frictional, they are less able to dominate particle angular velocity throughout the assembly. Consequently there is diminishing effect at further distance from platens. This observation is also found in velocity fluctuation in Fig. 3.2b. However, when the platens are more frictional, they obtain control through the core. Additionally, this uniformity of angular velocity is equally reflected in the velocity profile while the largest angular velocity is reflected in the highest linear velocity slip. It should be noted that for 1.5d the peak is slightly higher and requires further investigation. However, it does not affect the present discussion.

Then, flow dynamics are investigated adjacent to the upper boundary similar to what is done for linear velocity. Through the study on the angular velocity of particles at the boundary, it is found in Fig. 3.3c that angular velocity decreases at the same time. This phenomenon goes hand-in-hand with the increase of linear velocity. The normal force and shear velocity of platens being constant, the platen roughness actually causes the angular velocity of particles to transform into linear velocities in the direction of platen displacement. As a consequence, angular velocity is less evident when the platen is constructed with larger particles and is rough. Contrarily, when the platen is less frictional, it is less capable of so-

called transformation and subsequently, higher velocity-slip and higher angular velocity. Thus, rotational distribution of particles is derived from linearity (and non-linearity) of the velocity profile. Fig. 3.3d shows that the overall angular velocity understandably increases with platen roughness despite the fact that angular velocity drops adjacent to the platens. This occurs because in a macrodynamic consideration of the particle assembly, the rough platens are better able to rotate the assembly with their shear effect. This characteristic has a strong impact on the granular temperature which is evident in Fig. 3.2b as overall velocity fluctuation is higher when platens are more frictional. In the following section on force analysis, it is shown how these velocity characteristics are driven by force factors.

### **3.3.2. Force field**

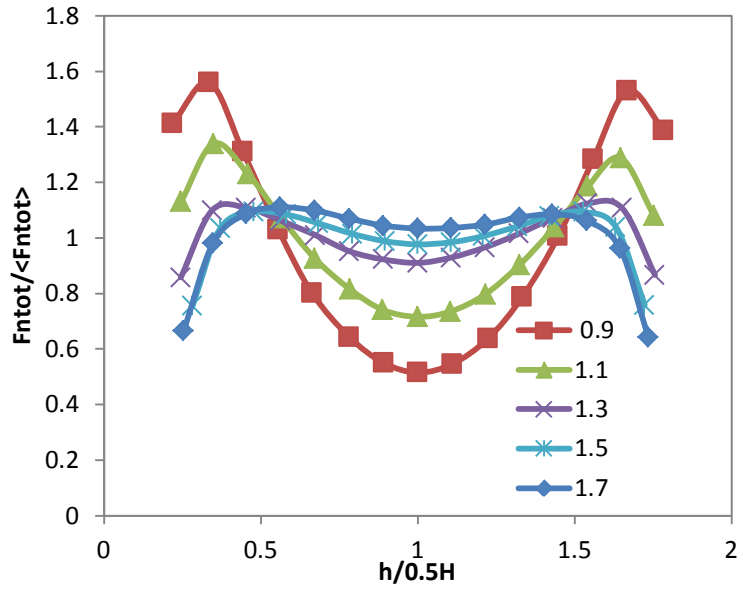
Contact forces and moments are the primary internal drivers in granular rheology. Therefore, the study of such forces at a microdynamic level is crucial to understanding the mechanics behind the events discussed so far. There are two types of primary forces involved in DEM: normal contact force and torque, also known as contact moment (from couple force transmitted ultimately by the opposite moving platens). In the following section, the internal forces and moments are discussed at particulate level and how their arrangement and distribution are responsible for the velocity profile transformation.

#### **3.3.2.1. Contact force**

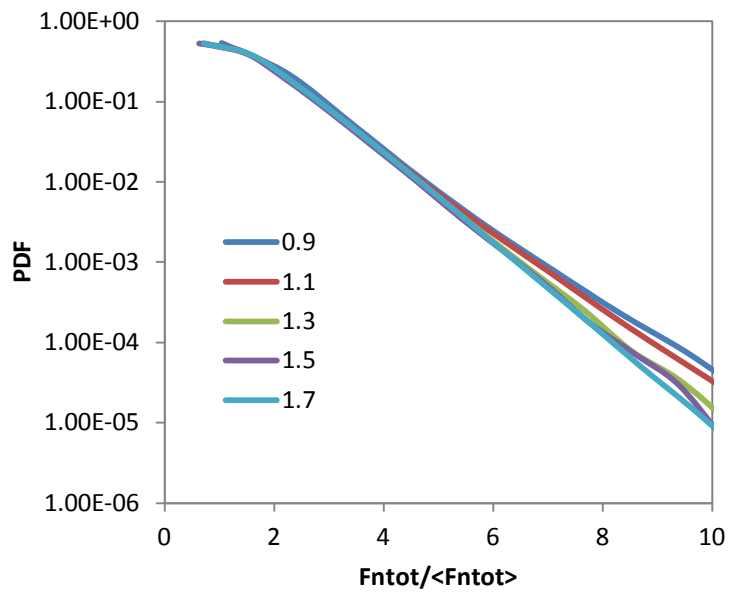
Fig. 3.4a shows variation in total forces of particles developed from normal contact across flow (in the z-direction) through shear cell directly from simulation. Qualitatively, the force distribution is uniform across the region when the platen surface is rough. When the platen surface is smoother, the contact force decreases near the central region compared to that near the platens which is, in other studies [173], considered to be a fluid-like region. On the other hand, contact forces are highest nearer the platens, which are attributed to forces being applied by the platens to the adjacent particles. These are dissipated gradually layer by layer and the effect is lowest at the center. As the platen roughness increases, the dip reduces and gradually it becomes uniform because the dissipation of force is not enough and the impact of platens reaching the core, dissolving the fluid-like region. This has been discussed elsewhere [13].

Force gradient profile is observed to have a similar distribution trend as is the case for angular velocity as well as velocity fluctuation distribution. This finding is reasonable because when the platens have less frictional capacity and the slip is higher, impact of shear is unable to reach the core of the assembly. It then becomes almost analogous to arching. For the same reason, the shear component of force makes less contribution to the average total contact force. As a result, average total particle contact force,  $F_{n_{tot}}$  is less as can be seen in Fig. 3.4c. The inability of the platens to transfer shear force to the central region is the root cause of linearity and non-linearity of velocity profile. Again, because of this shear force transfer, the granular temperature and angular velocity spread right through the core area with rough platens; the final output of velocity gradient is found to be linear. It is also important to note that, right next to the platens, there is a reduction of contact force as was found for the angular velocity profile in Fig. 3.3a. Platens act as sink of force at the boundaries. This sink of force varies with platen roughness which agrees with [133]. The sink of force is consistent with the observation that as particles become locked from the boundary roughness and tend to move in streamline along with the boundary displacement, the contact force reduces as far as the force along the x-axis is concerned.

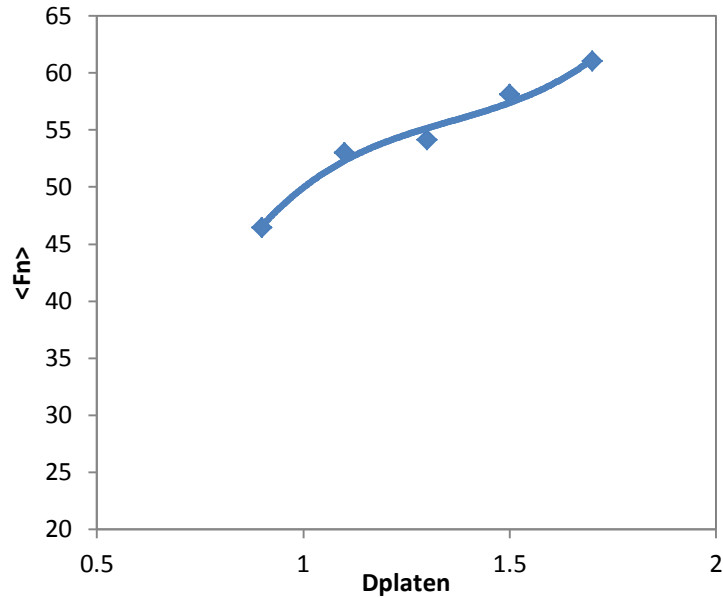
Probability distribution of scaled contact normal force is shown in log scale in Fig. 3.4b for different platen roughness conditions. It is observed that, while the majority of forces exist around the mean value ( $F_n/\langle F_n \rangle = 1$ ), there is a variation in decay at higher loads for different cases. It means that deviation from mean normal contact force declines as the platen roughness increases. The trend shows that, for the contact normal forces that are about 6 times larger than the average contact normal force, the decay of PDF increases as the platen roughness increases. This indicates that after a certain point of platen roughness, any variation in the trend decreases significantly. At this stage, it can be said that the distribution of force is saturated throughout the particle assembly in rheology.



(a)



(b)



(c)

Fig. 3.4: a) Scaled total particle force from normal contacts at varying heights of shear cell with 5 different platen roughness b) probability distribution of scaled contact normal force for different cases c) average particle force for all cases ( $\pi\rho d^3 g/6$ )

Fig. 3.5 show the contact force network of the particles for two extreme cases of 0.9d and 1.7d for comparison in order to show what happens in a microdynamic level. Entire segment of the shear cell is considered to obtain the figure. These figures show that there are random strong force chains existing in 0.9d network while weaker force chains are dilutely knit which means that force has not been uniformly strongly distributed throughout the flow. On the other hand, force network of 1.7d consists of weak and medium force chains that are densely spread throughout entire segment which suggests that forces are uniformly distributed among the particles in flow. This finding is in sound agreement to what is suggested from Figs. 3.4a and 3.4b. Another thing to notice here is particle contact forces are much lesser in Fig. 3.4c than individual contact forces. It is because multiple contacts on a particle with forces in different direction causes the resultant magnitude to become less from balancing mechanism.

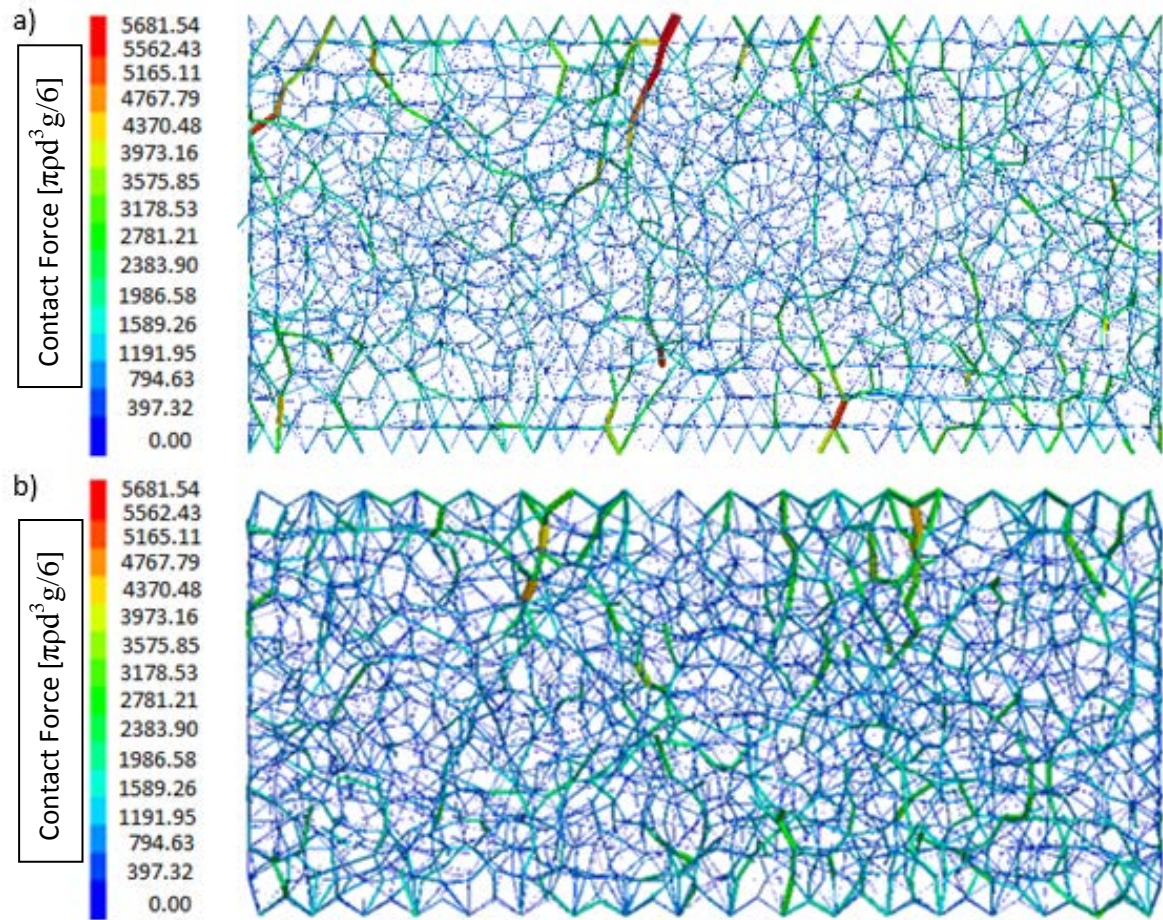
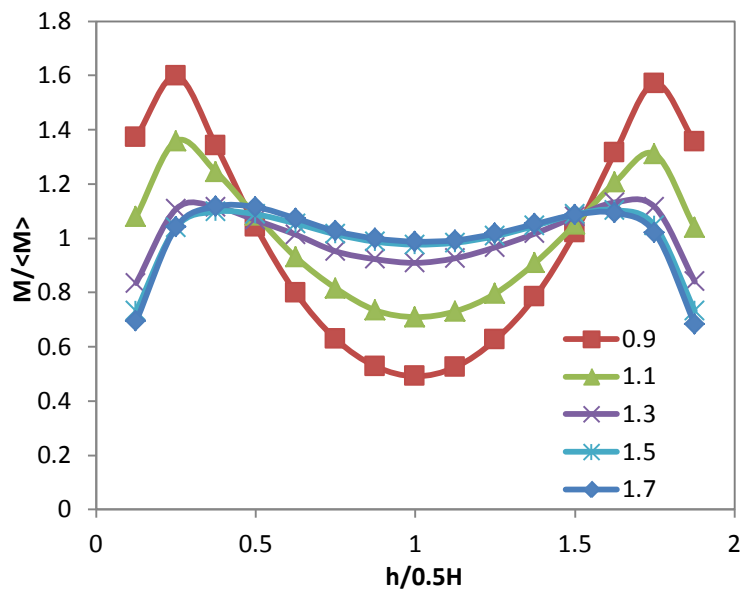


Fig. 3.5: Contact force network of assembly particles for a slice yz plane for a) 0.9d and b) 1.7d ( $\pi\rho d^3 g/6$ )

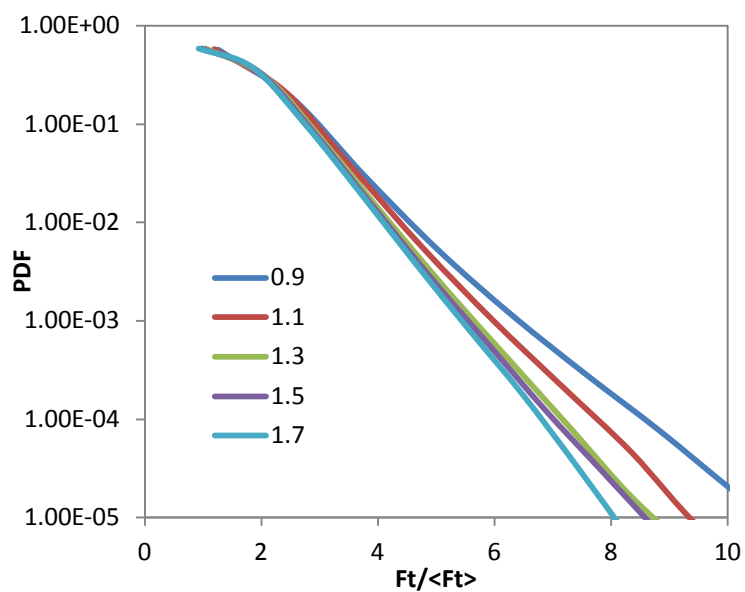
Another crucial point to note from the network is that when platen is smooth, forces are stronger near the boundaries with several of them with high magnitude. But near the core region, the force strength becomes much less as can be seen from the thickness of force chains based on the simulation. As for rough platen case study, although there are some medium strength force chains, they are more distributed and forces are much higher at the center in the closely knit network as obtained from the simulation. This is reflected in Fig. 3.4a which shows higher force near boundary for 0.9d case study and in Fig. 3.4c which shows overall higher force for 1.7d case study as deduced from the simulation's microdynamic evidence of Fig. 3.5a and b.

### 3.3.2.2. Contact moment

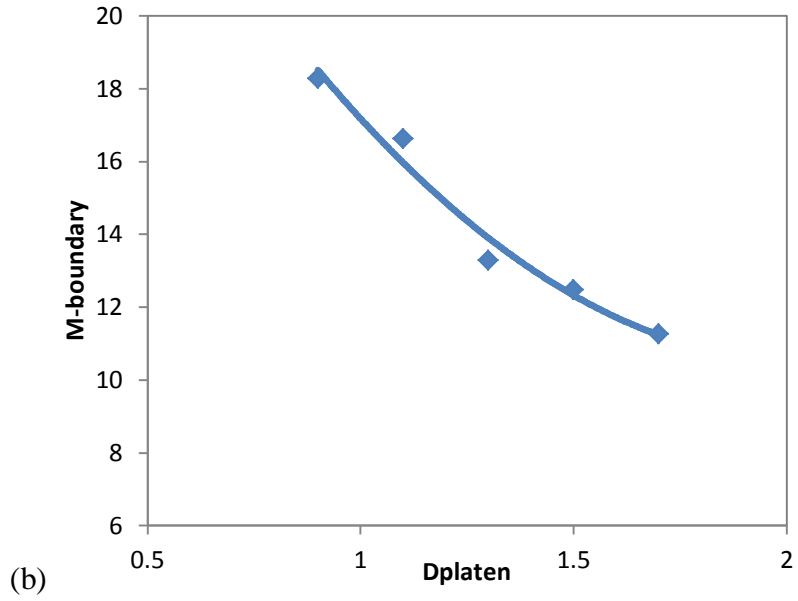
Torque of particles is more directly influenced by the variation of platen surface texture than contact force. Thus, particle moments are studied for the assembly at micro-level as a continuation of force field analysis. Fig. 3.6a shows how the total moment generated from contact forces in the simulated environment is distributed across the shear cell perpendicular to the flow.



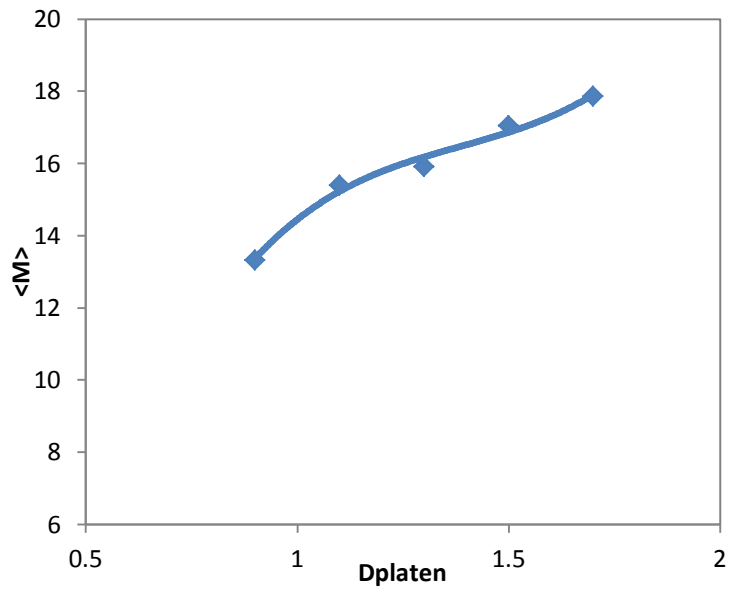
(a)







(c)



(d)

Fig. 3.6: a) Scaled total contact moment at varying heights of shear cell with 5 different levels of platen roughness b) probability distribution of scaled contact for these different

cases ( $\pi\rho d^4g/6$ ) c) Overall averaged values particle contact moment adjacent to platen for platen-constituting particles of different sizes ( $\pi\rho d^4g/6$ )

It shows that the graduation of the profile is fairly similar to that of force with non-linear symmetric profile for case of low friction platen and near-linear profile for highest friction platen. However, compared to normal contact force, the jag near the platens is slightly higher. This occurs because the variation of boundary condition more strongly influences rotation-driving element compared to the translation-driving element, i.e. contact force. In the end, with the combined effect of contact moment, contact force and granular temperature the phenomenological characteristic of angular velocity distribution is developed, which consequentially, contributes to the formation of linearity or non-linearity of velocity gradient profile.

Fig. 3.6b shows probability distribution of scaled tangential contact force which is responsible for generating particle moment. It reveals a stronger variation in decay of distribution than normal forces. It is understandable because platen roughness, from the mechanical point of view, has a more direct impact on the tangential component of force than the normal one. Also, the decay variation starts much earlier (it is twice as big as mean contact tangential force). It suggests that contact moment plays a more important role than contact normal force in transforming velocity profile from non-linear to linear by distributing the applied force faster throughout the particle assembly. Again, the decay variation declines at higher platen roughness where linearity of velocity profile has already been achieved.

In Fig. 3.6c it can be seen that although normal stress is controlled, the contact moment decreases at the boundary with the roughening of the platen surface through an increase in the platen-constituting particles' diameter. It is interesting to note that while the platen roughness influences torque generation through friction, the shear effect actually converts most of the load to linear velocity in the flow direction. As a consequence, angular velocity is found to be reduced at the boundary (see Fig. 3.3c). In other words, when an increase in platen roughness occurs, more torque is converted to normal force near boundary in shear direction, resulting in angular velocity being converted to linear velocity. However, from a macrodynamic point of view, overall average contact moment increases with the platen's frictional capacity as shown in Fig. 3.6d. This is consistent with overall angular velocity in Fig. 3.3d since the

platen's ability to rotate the particle assembly increases. Thus, contact moment is another precedent of velocity profile transformation from non-linearity to linearity.

Based on the analysis of linear and angular velocity, contact force and moment, it is found that the transition point is about 1.1d to 1.3d of platen roughness for the given setup. Linear profile is distinguished from the angular velocity profile scenario since it positions itself at the edge of linearity and non-linearity. In the third stage, the focus is on a macro and micro-analysis of this phenomenon, so that what takes place during this transition with respect to the internal structure of particle assembly can be visualized.

### **3.3.3. Packing structure**

Micro analysis of packing structure is conducted through segmentation of a sample 3D space within the shear cell segment. An imaginary measurement volume is generated using 675 spheres with a 1.5d diameter at the central section across the flow. Here the objective is to obtain localized variable data namely, porosity. The spheres are arranged in a 3D matrix of 3x15x15 (corresponding to x-direction, y-direction and z-direction, respectively). This consideration also reduces side-wall effect further since terminal points in the y-direction are reasonably away from the side-walls. The terminal points along z-direction are very close to the platens. All spheres record local variable data.

Relevant to the macrodynamic analysis, overall porosity of each case is observed. Fig. 3.7 shows the relationship between the total porosity of particle assembly and the platen particle size. Here, it can be found that as the platen roughness increases, the porosity of the assembly increases. This happens because when the friction is lower at the platens, the shear effect does not reach the core and consequently particles are less mobilized there. It is inferred in the velocity profile in Fig. 3.2a. Therefore, the particles can be more compact and not necessarily in uniform layers. However, as the friction of the platens increases, the shear effect reaches the central part of the cell. As a result, more distinct layers are produced perpendicularly to the flow between the upper and lower platens. Through this dilatancy effect the volume fraction then decreases and it is more closely observed in the microdynamic analysis through the slice of region created.

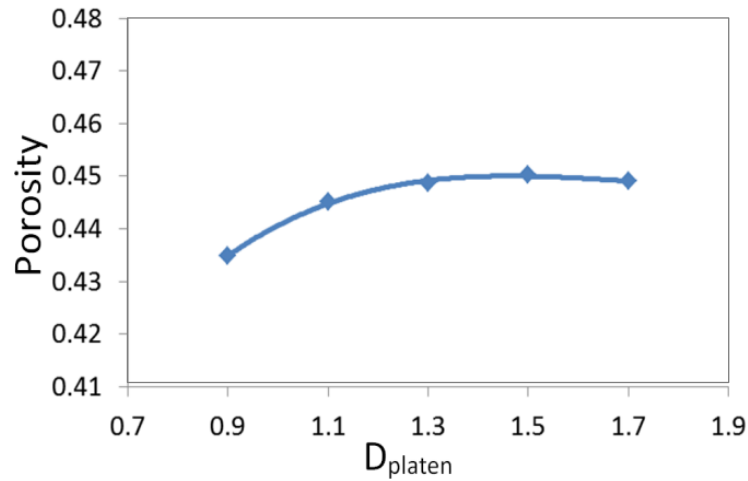


Fig. 3.7: Graph depicting the relationship between overall volume fraction and platen roughness with remaining considerations being kept the same.

Figs. 3.8a-e illustrate the time-averaged spatial distribution of porosity on the  $yz$  plane which is perpendicular to the flow direction. When the platen surface friction is less, there is a clear gradient of low porosity at the central region. This becomes higher away from this area where the particles are more agitated. Similar outcomes have been documented in other studies [13, 177]. However, when the friction of the platen surface has a higher value, the porosity tends to spread throughout the region. The progression can be seen in Figs. 3.8 b, c, d and e which correspond to 1.1d, 1.3d, 1.5d and 1.7d particle size constituting the platens. These observations are consistent with the fact that when the platen friction level is higher, contact force distribution becomes uniform after it reaches the segment's core. The dilatancy effect occurs as a reaction to the propagation of contact force in this stress controlled model resulting in porosity becoming uniformly distributed as well. As the platen particle size reduces and platens smoothen, however, porosity at the central region decreases due to the absence of dilatancy, which occurred due to the formation of layers when more platen roughness was evident. It is a very significant factor for enhancing the linearity of the velocity profile because this effect of uniform layer creation facilitates the development of uniform velocity along with force propagation. Hence, the volume fraction is the 3rd element for the transformation of velocity profile from non-linearity to linearity. It is also important to note that less uniformity in porosity is due to natural anisotropy in the compaction to a certain

level. This localization is reasonable in a given practical consideration and has been observed in previous studies [177].

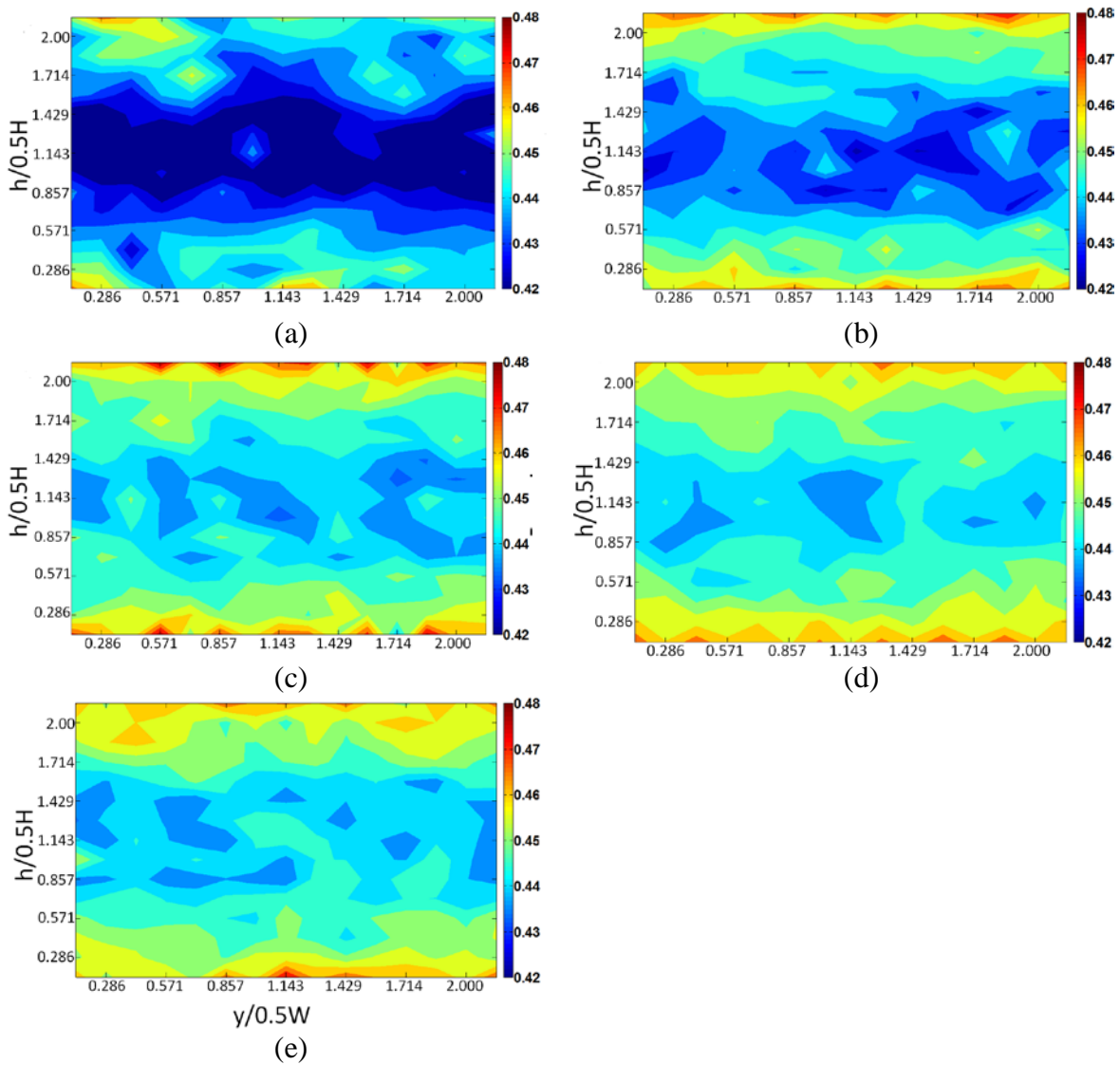


Fig. 3.8: Time-averaged spatial distribution of porosity in generated yz-plane the cell for different platen roughness: a) 0.9d b)1.1d c)1.3d d)1.5d e)1.7d. Here, W is the width of the cell in y direction.

It is important to point out that, with reference to porosity analysis, there are discrepancies between Campbell and our work on the hypothetical study of platen interaction. While it

agrees with the point that slip of velocity along with the large velocity gradient decreases when the surface roughness of the boundary platen increases, the argument for a correlation between granular temperature and particle density is debatable. The previous work suggests that in the stress controlled model there is no vertical acceleration, but this overlooks the fact that there is continuous adjustment through vertical displacement which actuates the platen to move upwards to relax additional force when the platen roughness increases. Consequently this causes the particle arrangement to become increasingly laminar. The dilatancy effect causes the platen to rise and so overall porosity as well as boundary porosity increases until particle assembly becomes fully laminar in structure. Contrary to what the hypothesis claims, it is found that collision is proportional to the dissipation of impact velocity rather than impact velocity itself. This is supported by the finding on velocity fluctuation in Fig. 3.2b and Fig. 3.4b, which show lower contact force and velocity fluctuation concerning the rough surface at the shearing boundary.

### **3.4. CONCLUSION**

This study highlighted the unique phenomenon of transformation of the velocity gradient profile perpendicular to the flow direction from non-linearity to linearity. It is based on the outcome of variation in shearing surface texture. The investigation is performed in annular shear cell setup with moderate load and shear velocity. Particle assembly is kept near random close packing ( $RCP \approx 0.55$ ). All internal and external considerations are kept the same except for upper and lower platen roughness. When the platen roughness is less, i.e. constituted platen-particles' size is smaller, the velocity gradient profile is non-linear. As the size of the platen particles expands, the velocity gradient profile becomes gradually linear. It is identified that the transformation mainly takes place between 1.1d and 1.3d. This transformation incorporates the following microdynamic events that have been described in this study.

- Velocity slip is the first and the most superficial indicator of velocity profile transformation. Velocity slip being higher at the platen adjacent areas with smoother platens causes less transfer of shear effect which in turn means the effect does not reach the core region.

- Velocity dispersion is the next issue that reflects the velocity profile transformation. When the platens are sufficiently rough, the dispersion across the flow remains reasonably uniform. But when the platens are less frictional, there is non-linearity with more variations near the platens. This finding concurs with earlier research on granular temperature [133].
- Angular velocity is another property that demonstrates the velocity profile configuration. When platens are less frictional, angular velocity varies more strongly across the flow with the highest being near the platens and least at the core. As platens become more frictional, the angular velocity is converted to linear velocity and angular velocity becomes uniformly distributed.
- Force distribution wields a phenomenologically deeper influence on profile transformation. When the surface of platens is smoother, force profile is non-linear with the lowest values being at the core region. As the surface becomes rougher, the force will be more uniformly distributed and consequently so does the velocity across the flow.
- Moment distribution shows a similar pattern to contact force. Yet this variable has another indicator near the driving boundaries, i.e. platens. Although this is a stress controlled model and contact force at the boundary adjacent region is constant, contact moment increases as an effect of roughness. This occurrence is considered to be the significant contributor along with angular velocity, granular temperature and velocity slip which cannot satisfy the event's full description alone.

Packing structure is also an important indicator of velocity profile transformation. Porosity is increasingly homogeneous across the region as the platens become more frictional.

# Chapter 4: Role of gravity in the flow of particles in a shear cell

## OVERVIEW

This work numerically investigates the effect of gravity on the dynamic behavior of particle flow in an annular shear cell under stress-controlled conditions. Some key properties such as particle velocity, inter-particle force and stress tensors are examined by using a virtual platform developed based on the discrete element method (DEM). The results indicate that gravity has a strong influence on these properties when low pressure is applied on the particles flowing through the shear cell. This influence gradually diminishes as the applied load increases. In particular, velocity and contact force are asymmetrically distributed along the height of the shear cell for low pressure when gravity is considered. They have a symmetric distribution if low pressure is imposed and gravity is included or if high pressure is imposed. These features are explained through the analysis of contact force network.



## 4.1. INTRODUCTION

A popular method of investigating granular rheology is employing the shear cell. Pioneered by Jenike [97] and Carr *et al.* [126], shear cell is a laboratory setup basically used for analysing the correlation among particle properties, applied load and induced shear by cell walls or platens on specimen particle aggregate. There are two main types of shear cells: Jenike's shear cell (eg. [178]) and annular shear cell (eg. [14]). Annular shear cell, which is used in this study, comprises an annular space enclosed by two concentric cylindrical walls, i.e. upper platen and lower platen. This setup can be used in a variety of ways: the upper platen is rotated while the lower platen is kept stationary [127]; both platens are rotated in opposite directions [14, 134]; volume is kept constant while rotational velocity varies [151]; constant load is applied by the upper platen while both platens are rotated [8]; the inner wall is rotated while the outer wall is loaded (inwards) [128], and so on. The advantage of annular shear cell is that it can produce continuous flow of granular particles within a confined setup compared to Jenike's shear cell. The disadvantage of annular shear cell is that it can only work with limited number of particles under research.

Due to the particle system's unique position between solid and fluid systems, it is difficult to develop a simple constitutive model. In the discrete element modelling, aggregate outcome of the assembly is obtained from averaging the cumulative outcomes of particles existing in the specimen assembly. It is a cumbersome process which limits the number of particles that can be considered for analysis. Further, models have been simplified in various aspects to increase the model's efficiency.

One of the simplifications considered is absence of gravity. Although advances have been made in computational capacity in recent years, significantly higher and more complex considerations can be introduced. However, the effect of gravity is often scaled in numerical model or avoided altogether [8]. In reality, except for special cases like cosmic rocks and condition simulated lab environments, most events involving granular mechanics are subject to gravity. Nevertheless, while the outcomes from the simplified studies make a valuable contribution to better understanding this complex phenomenon, it also provides an avenue to studying the effect of gravity so that existing popular works are linked to practical

applications. Murdoch *et al.* [158] conducted physical experiments for assessing the effect of gravity on the granular flow in an annular shear cell. Their study, however, was limited to velocity distribution. Baran and Kondic [46] addressed the issue of gravity in single-shear and vibrated granular system in different gravity conditions in a shear cell. Although he evaluated the volume-controlled environment using a hard-sphere model to show how gravity affects some properties, his work did not provide a microdynamic explanation of the underlying phenomenon.

To understand the effect of gravity on the behavior of particle flow under various conditions, an annular shear cell model under a stress-controlled condition was generated in this work based on the DEM. In the model, spherical particle assembly is mobilized with different prescribed combinations of induced shear and load applied by the upper and lower platens of the shear cell. Key parameters such as particle velocity, particle force, stress tensors, coordination number and porosity are investigated in similar flow conditions with and without gravity. This is achieved through observation of distributions of time-space averaged properties and correlations of different variables.

## 4.2. SIMULATION CONDITIONS

In this study, a soft particle non-linear model is used in the discrete element method (DEM) based on the Hertz-Mindlin and Deresiewicz theory [31]. The test is done in stress-controlled boundary conditions. During the simulation, the interparticle forces are calculated based on numerical models founded upon spring and dashpot mechanics [3] and then, the velocities and corresponding displacements are derived from these calculated forces. This method continues throughout a predefined period. The time-step is kept reasonably small to: firstly, approximate continuity in dynamics; and secondly, avoid possible overlapping particles during displacement calculation.

A rectangular segment of an annular shear cell is generated using a commercial software particle flow code (PFC). The rectangular segment has the dimensions  $12d \times 30d \times H$  and is perpendicular to the flow, where  $d$  is the average diameter of the assembly's particles and  $H$  is the shortest distance between the upper platen to the lower platen ( $H = 14.5d$  in this work). The segment size compared to the full annular shear cell is small enough to ignore the radial curvature of the side walls (see Fig. 4.1 inset). To obtain a stress-controlled condition, the

height of the cell's upper platen can be adjusted to maintain regulated pressure on specimen particle assembly. A similar simulation method has been applied in [8].

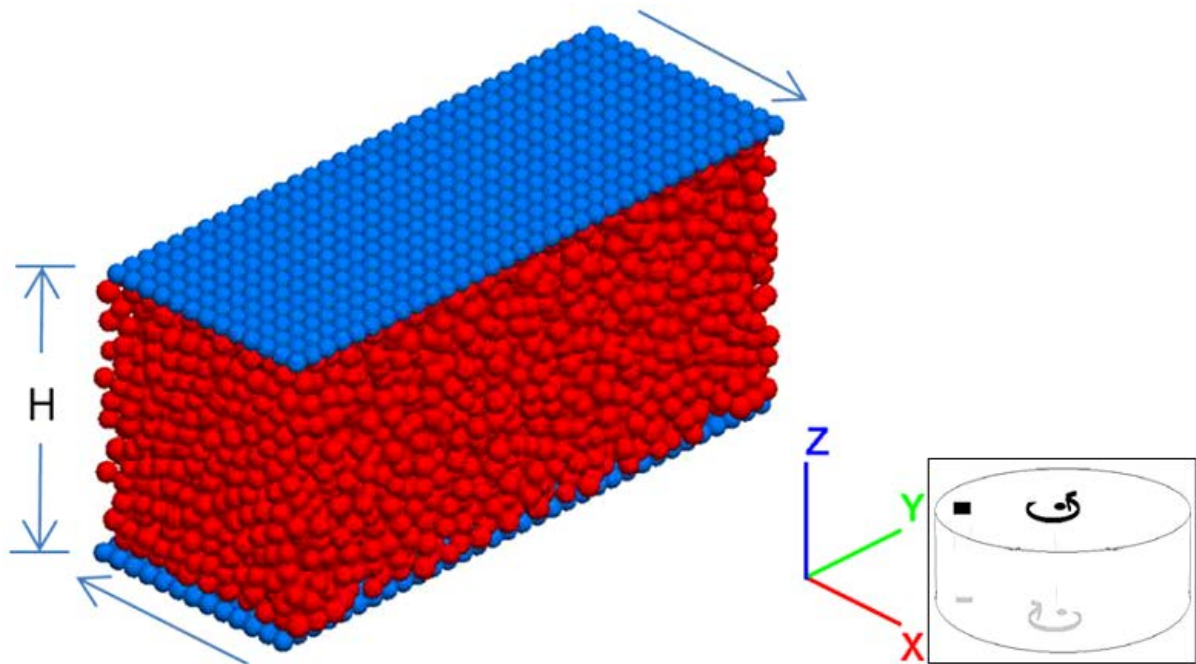


Fig. 4.1: Simulated model shear cell.

In each simulation, at first, the upper and lower platens are created at the top and bottom planes of the shear cell using 429 particles with diameter of  $0.9d$  arranged in an orderly fashion. They mimic the rough boundary which is designed to induce shear. Side walls are generated in a regular fashion with reduced friction to minimize wall effect on granular flow. The two boundaries perpendicular to the direction of flow ( $x$ -direction in this study) are created to be periodic such that a particle leaving one of the walls will immediately enter the other with the same  $y$ - and  $z$ -components of position and same dynamic values. These include, for example, magnitude and direction of velocity, rotation, force and moments. In this way, this setup represents infinite continuous flow of particles. Then, 5000 slightly polydispersed ( $0.9d - 1.1d$ ) spherical particles are created at random positions in the space confined by the two platens, two periodic walls and two side walls, with a high volume fraction of  $0.63$ . After that, the simulation is run so that the particles can relax from the tight packing and naturally occupy the entire enclosure. This state of particles distribution within the shear cell segment can be seen in Fig. 4.1.

Once the particles are reasonably in a natural equilibrium state, velocity is applied to the upper and lower platens in the opposite direction along the x-axis so that the platens shear the assembly. This shear velocity is gradually increased until the defined value is reached and the defined value is kept for a reasonably long time so that the flow achieves a steady state condition. At the same time, the load on the particle assembly applied by the upper platen is increased up to the pre-set value gradually. In order to increase the load, the upper platen moves slowly downwards. After reaching the desired load, the upper platen continuously adjusts its position to maintain a constant pressure. When the fluctuation of the upper platen reaches the minimum level, this means the granular flow is in a steady-state condition. The data for variables at a particle scale such as particle velocity and contact force as well as variables at a macro-scale such as stress, coordination number and porosity are collected over a period of time to obtain these variables' time-averaged values. Particle properties and applied conditions on the particle assembly are given in Table 4.1.

Table 4.1: Parameters used in the simulations.

Definition	Value	Unit
Friction coefficient (particle-particle and particle-wall)	0.3	(-)
Damping ratio (normal and shear)	0.3	(-)
Young's modulus	2.5	$\pi\rho dg/6 \times 10^6$
Poisson's ratio	0.3	(-)
Applied pressure	0.14 – 2.56	$\pi\rho dg/6 \times 10^5$
Shear rate	3, 6.5	$\sqrt{gd}$
Time-step	0.00001	$\sqrt{d/g}$

## 4.3. RESULTS AND DISCUSSION

This section includes analysis of effect of gravity on particle velocity, coordination number, porosity, contact force and stress-tensors in granular rheology. Here, profiles of different variables are shown to highlight how gravitational force influences particle flow.

### 4.3.1. Velocity field

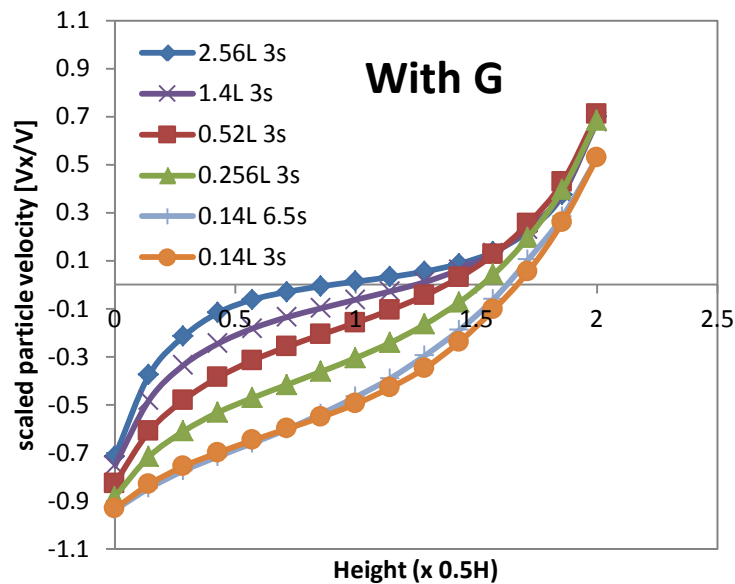
The investigation starts by examining the velocity gradient profile which has been considered in previous studies (e.g. [9, 48]). Only the velocity component in the direction of

flow, i.e. the x-direction, is shown here (for brevity) as other components of velocity are observed to be relatively less significant. Fig. 4.2 shows the velocity gradient profiles along the z-direction under different platen load and shear rate conditions. It can be seen that the effect of the shear rate on the velocity gradient profile is limited. In contrast, the platen load has a significant influence on the profile.

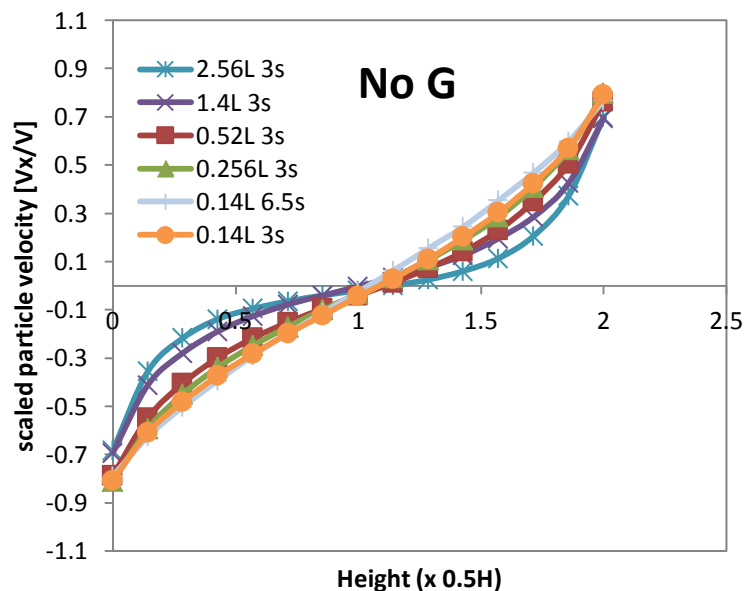
From Fig. 4.2a, we find that, with the introduction of gravitational force, the flow has an asymmetric velocity gradient profile for the low load ( $0.14 \times 10^5 \pi \rho d g/6$ ) regardless of the shear rate of 3 or  $6.5\sqrt{gd}$  induced from the platens. When the load is increased ( $0.256-1.4 \times 10^5 \pi \rho d g/6$ ), the profile becomes more symmetric. At the high load ( $2.56 \times 10^5 \pi \rho d g/6$ ), the velocity profile becomes symmetric on the central axis. When closely examined, it is evident that at the low load, the profile has a tendency to incline towards the lower platen. As a consequence, there is less velocity slip in the region near the lower platen when compared to the upper platen. This finding is unlike the case regarding the high load, where similar velocity slip is found adjacent to both the upper and lower platens. However, when the effect of gravity is removed, the velocity profile becomes symmetric for both the high and low applied load conditions as shown in Fig. 4.2b. This appearance of symmetry is consistent with previous work [140]. From the balancing point of view, in the absence of gravity, the overall average velocity of particle assembly in the x direction is well-balanced from the shear effect of opposite moving platens, which is independent of applied load and demonstrated by data points being near zero. In the presence of gravity, however, the average velocity of particles in the shear direction is negative which is actually the direction of displacement of the lower platen. It goes as high as -3.5 and this means the effects of the upper and lower platens are not balanced. In fact the lower platen dominates the upper platen in influencing particle behavior. With the increase of load, the velocity becomes well balanced until it coincides with this finding in the absence of gravity.

The difference of velocity gradient profiles in the presence and absence of gravity is due to the physical phenomenon that, when gravitational force is included, the lower platen is subjected to higher overall normal forces than the upper platen in the vertical direction. As a result, there are larger frictions between shearing particles near the lower platen compared to the dynamic interaction happening adjacent to the upper platen. Appropriately, greater friction causes higher resistance for the particles to slip relative to the lower platen. Yet when the load is increased, gravitational effect on the interaction between the platens and

neighboring particles diminishes gradually and velocity profile becomes symmetric gradually (as seen from observing medium load and high load conditions in Fig. 4.2a). When the load is high it dominates the shearing of particles, which leads to similar velocity gradient profiles for both conditions with the presence and absence of gravity. A more detailed discussion on the contact forces between particles is presented in section 4.3.3.



(a)



(b)

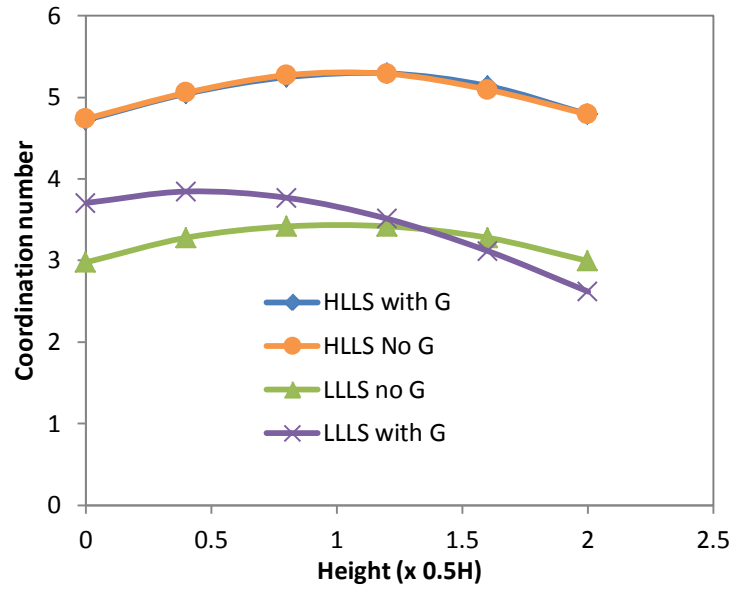
Fig. 4.2: Scaled velocity gradient profiles in various conditions: a) with gravity, and b) without gravity (units of load are given by ‘L’ ( $= \pi \rho d g / 6 \times 10^5$ ) and units of shear rate ‘s’ ( $= \sqrt{gd}$ )).

### 4.3.2. Coordination number and porosity

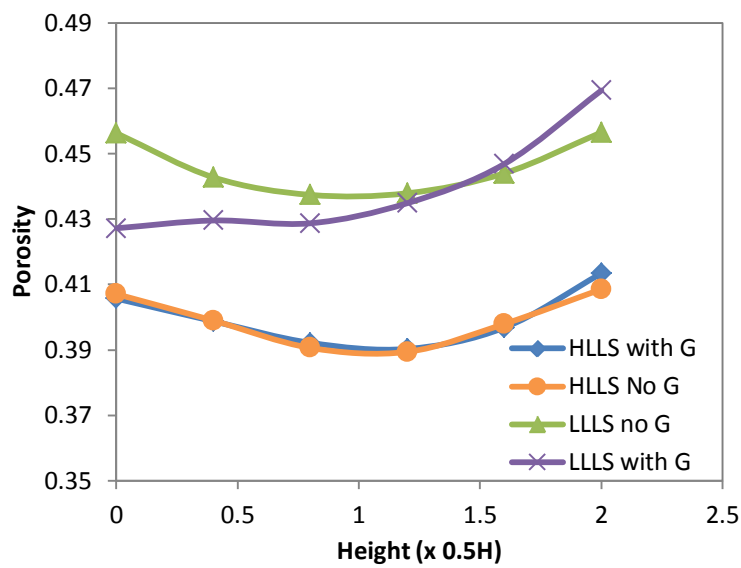
Coordination number and porosity are two important properties that help us to understand the structural changes taking place when the condition varies. In order to obtain the distributions of the two properties, the rectangular segment of the shear cell is divided into 512 overlapping spherical regions that have a size of  $2d$ . The overlap is considered in order to maintain the continuity of the spatial distribution of the variables throughout the field. For each spherical region the coordination number is obtained for an instantaneous step by detecting the number of contacts and dividing it by half of the number of particles [179]. Contacts are detected by measuring the distance between the two centers of adjacent particles. If the distance is less than or equal to the sum of the radius of the two particles being assessed, the contact is considered to be established. Porosity is obtained by calculating the empty space within the region and dividing it by the volume occupied by the particles residing within the region for that instantaneous step. In this case, the particles cutting the periphery of the spherical region are considered for partial volume calculation to improve the accuracy of the result.

Fig. 4.3 shows the distributions of the coordination number and porosity along the vertical direction. Here, only high load ( $0.14 \times 10^5 \pi \rho d g/6$ ) and low load ( $2.56 \times 10^5 \pi \rho d g/6$ ) condition and both of them for low shear rate ( $3\sqrt{gd}$ ) are considered for contrasting the two extreme scenarios. For brevity, LLLS and HLLS refer to low load and high load, respectively. This abbreviation is applicable for all figures for the rest of this work. It can be seen that at the high load, the distribution of coordination number and porosity when gravity is included are similar to those when gravity is not included. At the low load, however, the distributions are different. Furthermore, as shown in Fig. 4.3a, when the load applied by the upper platen is less, the coordination number is higher near the lower platen which remains constant in about one third of the cell and starts decreasing further upwards. This agrees with the proposal made earlier that particles near the lower platen tend to settle like a pile due to the gravitational effect, while moving in the same direction as the lower platen. This is because the shear effect from the upper platen cannot penetrate through the entire depth of the flow region. However, at higher load, along with the increase in the overall coordination number, the pressure applied by the upper platen on the granular assembly reaches the region adjacent to the lower platen through more dense and tightly knit contact force network (discussed in the following section). Consequently, a symmetric distribution is found which is

similar to [13]. On the other hand, in the absence of gravity, the distribution of coordination number is symmetric even at the low load because particles do not tend to settle and sort of float in the space.



(a)



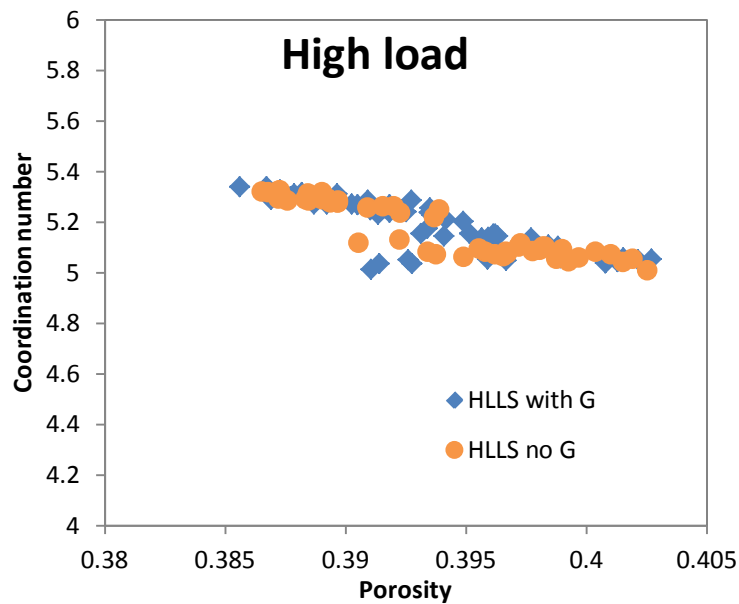
(b)

Fig. 4.3. Distributions of: a) coordination number, and b) porosity in various conditions.

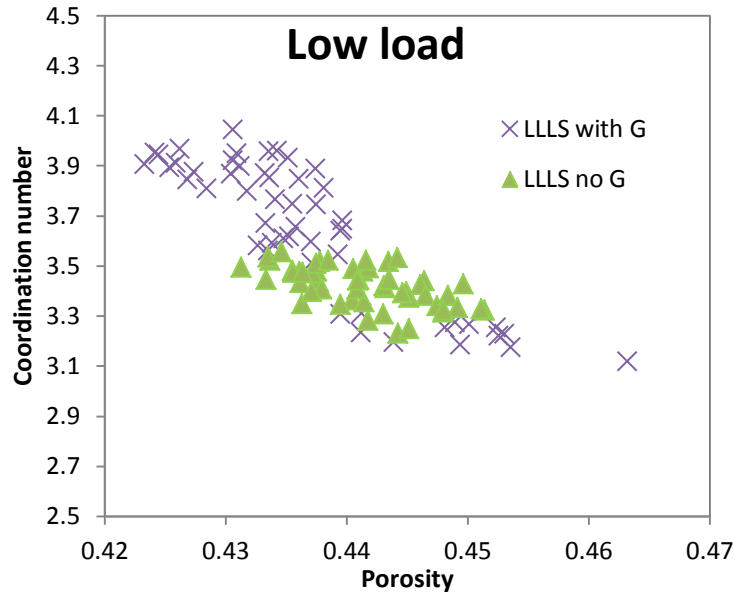


In that event, the upper and lower platens both equally contribute to the introduction of shear effect to the particle assembly. As the load increases, only the coordination number increases as expected but without variation in the gradient's trend. The reverse trend for porosity is observed in Fig. 4.3b. At the low load the porosity is obviously higher but with gravitational effect, the porosity is asymmetric with lower values near the lower platen. It increases after  $\frac{1}{3}H$  distance away from the lower platen for the same reason discussed above regarding the coordination number. At the high load, the porosity decreases and becomes symmetric, similar to what found in earlier studies [180].

Figs. 4.4a and 4.4b show the correlations between coordination number and porosity for the cases with and without gravity. One layer of particles from the walls has been excluded to avoid the wall effect on the results. Normally, the coordination number increases with an increase in porosity for particle packing or flow [13]. This tendency has been confirmed in all four cases considered in the present work,. In the high load scenario as seen in Fig. 4.4a, the correlations are similar for the presence and absence of gravity's effect. At the low load shown in Fig. 4.4b, the difference in correlations is significant: there is a larger range at which coordination number and porosity is dispersed when gravity is present.



(a)



(b)

Fig. 4.4: Relationship between coordination number and porosity at the conditions of: a) high load, and b) low load.

### 4.3.3. Contact force

In this section the total contact forces of particles are first considered. Fig. 4.5 shows the distributions of the components of the averaged total contact forces in the x-direction along the bed height for four conditions considered in Fig. 4.2: low load and high load in the presence and absence of gravity. Similar to the velocity gradient profile, the particle contact force exhibits different characteristics in the presence and absence of gravity when the applied pressure from the upper platen is small; it is similar when the pressure is high. Echoing the finding for velocity, as the load is increased, the force profile changes from asymmetric at the low load to symmetric at the high load. At this stage, the effect of gravity is overpowered by the load maintained by the upper platen on the particle assembly. In contrast, without gravity, the force profile is symmetric even at the low load. At the high load the trend is the same as that concerning gravity. In other words, force profile is independent of applied load in the absence of gravity. The observation of symmetry agrees with earlier studies based on an earlier hypothesis [133]. Furthermore, there is a dip in the distribution of force near the

platens when there is no gravity. With gravity, the dip of the force is only visible at the upper platen at the low load and both platens at the high load. It occurs because of particles being locked adjacent to the platen as the platen particles do not have rotational movements. A detailed analysis of this phenomenon was carried out with respect to granular temperature in [134].

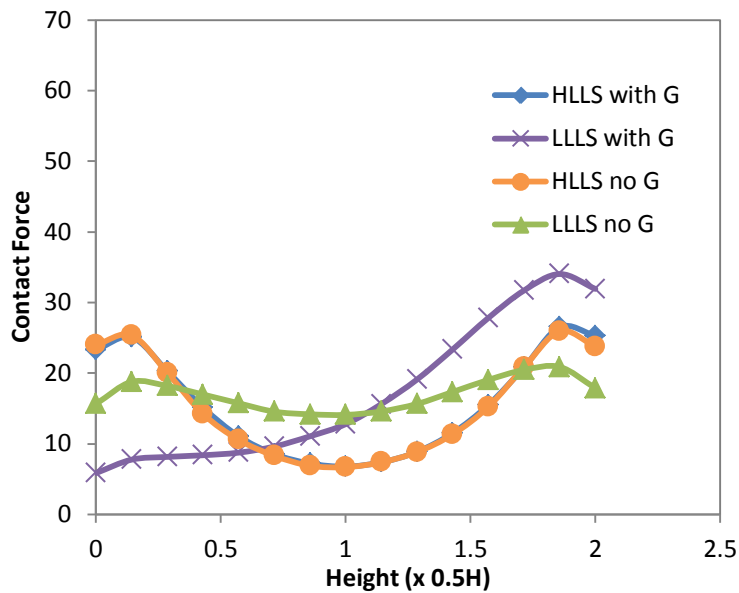
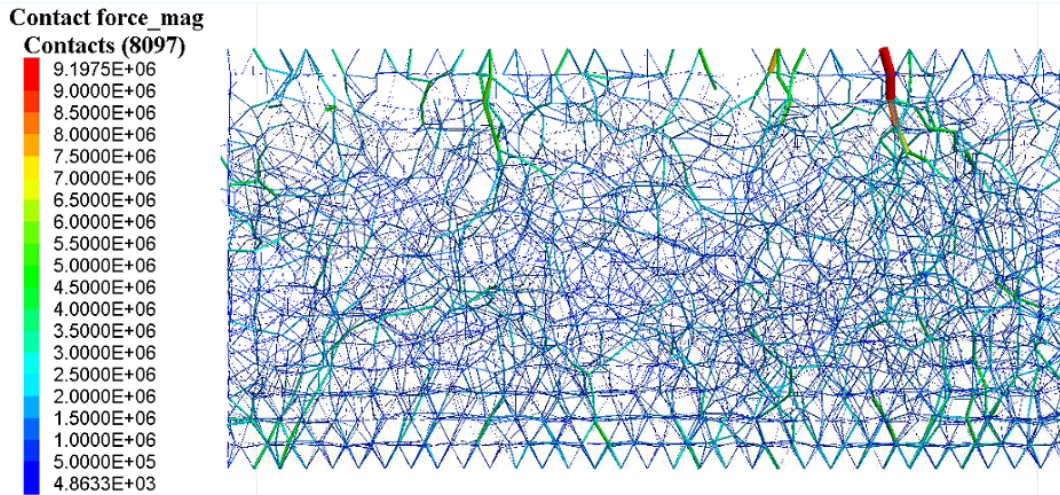
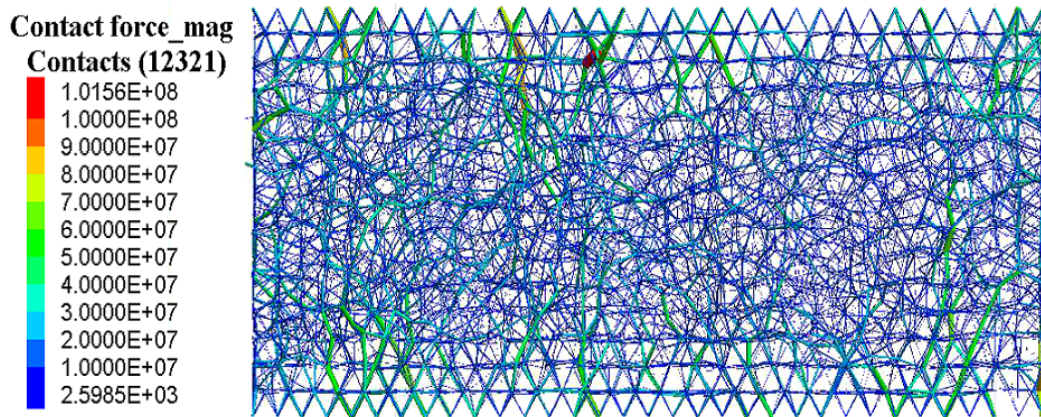


Fig. 4.5: Distributions of the total contact force in various conditions.

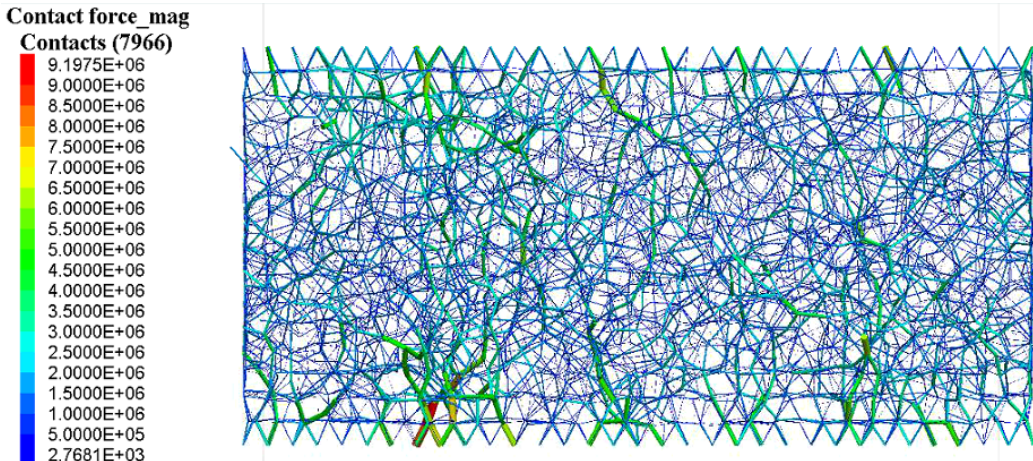
To further understand the phenomena observed from the distributions of the properties considered above, contact force network is examined. Fig. 4.6 is a snapshot of the contact force network of the two distinct cases in the presence and absence of gravity: high load and low load. The network is generated by connecting the centers of the particles with a joining line whenever contact is established (i.e. the distance between the concerned particles are less than or equal to their combined radius). Both thicknesses of the connecting line represent the magnitude of the contact force which is predominantly the normal contact force. Here, contacts among the platen particles and between the walls and platen particles are eliminated as they are manually controlled to mimic a rigid wall. Also the contacts between assembly particles and the side walls are ignored since the friction coefficient of the walls is kept negligible, which reduces the effect of the walls on the flow.



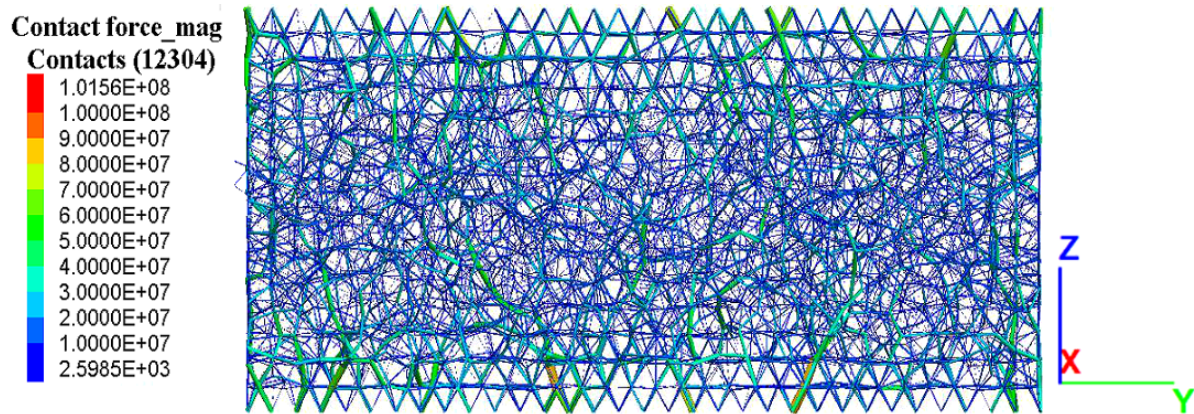
(a)



(b)



(c)



(d)

Fig. 4.6: Contact force network in the yz plane for: a) low load with gravity, b) high load with gravity, c) low load without gravity, and d) high load without gravity.

For the low load with gravity, as shown in Fig. 4.6a, the contact network near the upper platen is very diluted. There are a few short strong force chains while the rest of the force chains are weak. As they move toward the lower platen, the strong force chains cease to exist and the weak force chain network becomes denser. At the bottom one-third region of the shear cell, an organized uniform force chain network is found. The organized structure of the contact network at the lower region proves that the articles settle down on the lower platen while the upper platen is unable to match with the shear effect from the lower platen. It should also be noted that unlike the upper platen, the lower platen does not have strong force chains but instead a larger number of organized weak chains uniformly spanned over the entire surface. This is the main reason why the region near the lower platen exhibits low contact forces. The structured network has opposing forces balancing each other while the upper region has a larger number of unbalanced forces from the dispersed contact network producing more resultant contact forces. At the high load with gravity, as shown in Fig. 4.6b, the contact network is closely knit at the central region with an organized structure mirroring both the upper and lower platens. It means that the upper platen's shear effect matches that of the lower platen. This is the major cause for the force having a dip right adjacent to the platens. The significant shear effect takes place about a layer away from the platens.

The dense network also represents that the high applied load is carried by a large number of weak force chains spanning the entire network similar to what was found in [9]. On the

other hand, in the absence of gravity, the contact network at the low load shown in Fig. 4.6c is similar to that shown in Figs. 4.6b and 4.6d in terms of pattern. Obviously, the force chains are weak in this case, but they span the entire region with a mirroring structure near the platens. Fig. 4.6c also shows a few long force chains reaching from one platen to another, meaning that both platens are contributing to the shear effect on the particle assembly equally. There is a portion of the region near the platens which is organized like the high load, which causes the shear to have a strong effect at a layer away from the platens. At the high load the microdynamic structure of the force network in the absence of gravity shown in Fig. 4.6d is nearly identical to that in the presence of gravity indicated in Fig. 4.6b. This suggests the two cases have similar outcome as found above in Figs. 4.2, 4.3 and 4.4.

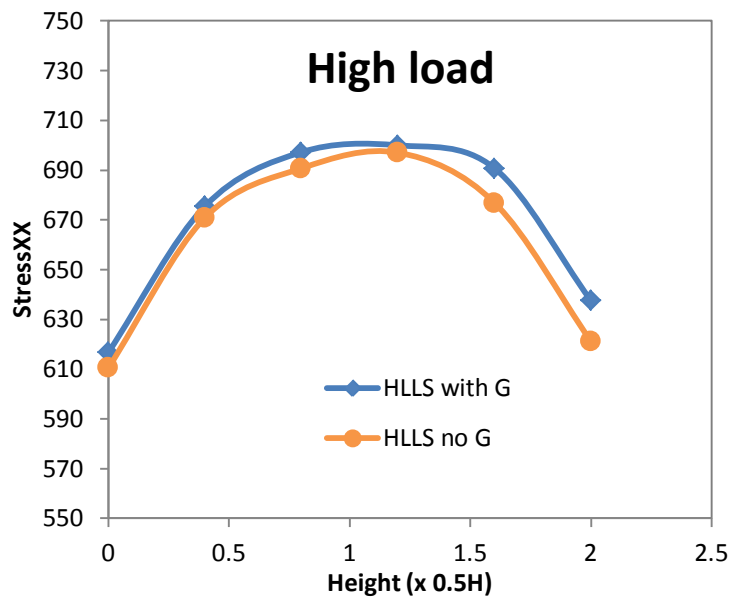
#### **4.3.4. Stress tensors**

Three key stress components are studied to understand the effects of gravity: normal stress in the direction of shear (x-direction), normal stress in the direction of applied load (z-direction) and shear stress in the direction of shear. They are denoted as stress-xx, stress-zz and stress-xz, respectively.

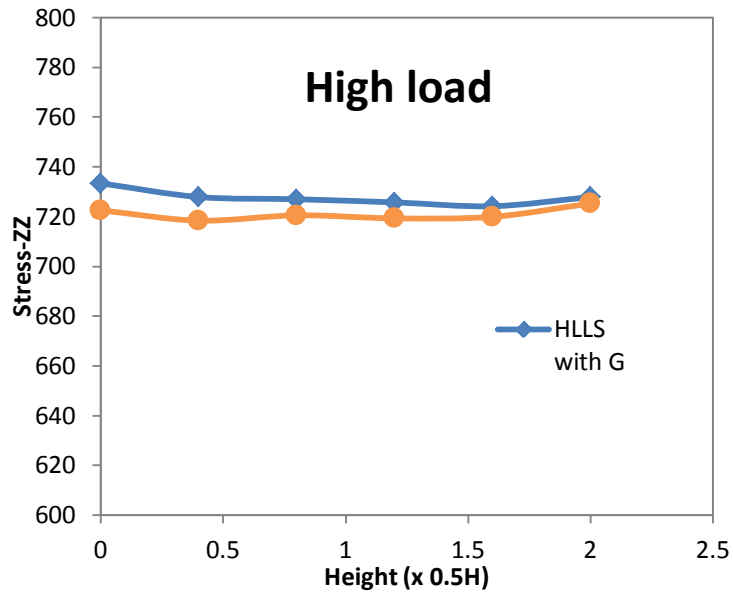
Fig. 4.7 illustrates the profiles of stress-xx and stress-zz in the high load and low load conditions in the presence and absence of gravity. From Fig. 4.7a, we find that the normal stress in the x-direction has a symmetric distribution across the shear flow. It is logical because the main driving factor for this component of normal stress is the shear effect from the upper and lower platens moving in the opposite direction.

As a result, the highest magnitude of stress-xx is observed at the central region where particles are nearly stagnant and are subject to equal and opposite shearing forces, and the stress gradually reduces as it moves towards the platens. The magnitude of the stress at the central region is about 14% higher than that near the platens. The symmetry also implies that both platens have equal contribution to the shear effect imposed on the particle assembly. Fig. 4.7b demonstrates the fact that the normal force has a uniform distribution across the flow, meaning the effect of applied load from the upper platen has reached the bottom of the shear cell. With the low load condition, the distributions of the normal stresses are found to vary in the presence and absence of gravitational force. Consistent with earlier findings, Fig. 4.7c and

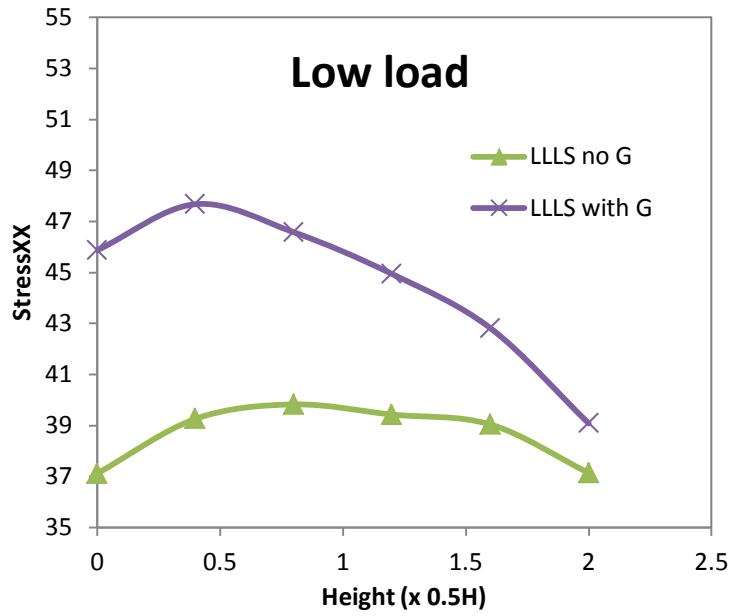
4.7d show that when there is no gravity, normal stresses  $-xx$  and  $-zz$  at the low load have a similar trend to high load except that their values are less: stress- $xx$  shows a symmetric profile with a peak at the central region while stress- $zz$  reveals a uniform distribution profile. Stress- $xx$  at the central region is about only 5% higher than that near the platens. On the other hand, the trends are different when gravity is present. There is a large difference between stress- $xx$  near the upper platen and lower platen by a magnitude of 17% higher adjacent to the lower platen. Stress- $xx$  shows a slight increase in its value adjacent to the lower platen and then decreases steadily towards the upper platen. The slight increase is in agreement with the earlier analysis that the shear effect is the highest at a layer away from the platen. However, the clear distinction is in the observation of stress- $zz$  distribution with a linear decrease from the bottom region to the upper region, which confirms the phenomenon discussed in the force network distribution. There is a big difference in stress- $zz$  at the upper and lower platens in that it is about 25% higher at the lower platen. In both studies of stress- $xx$  and stress- $zz$  profiles, even adjacent to the upper platen, stress slightly increases by about 4.5%, resulting from the contribution of gravitational load.



(a)

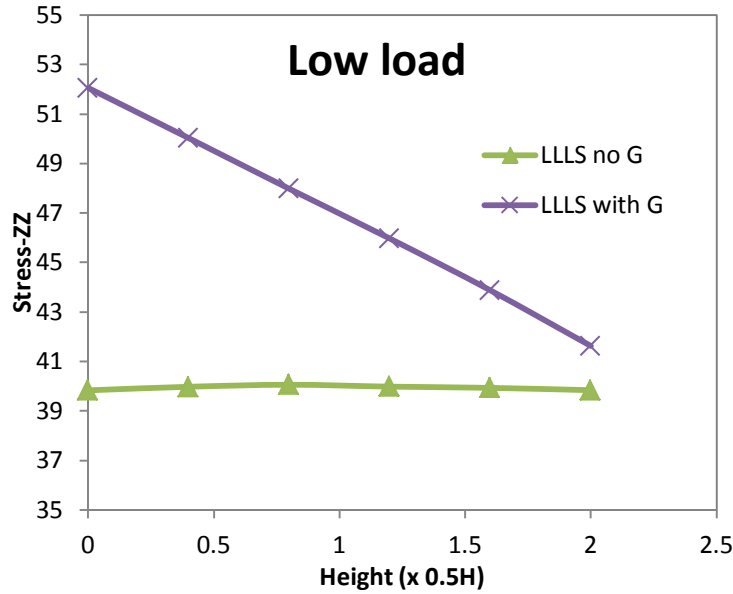


(b)



(c)

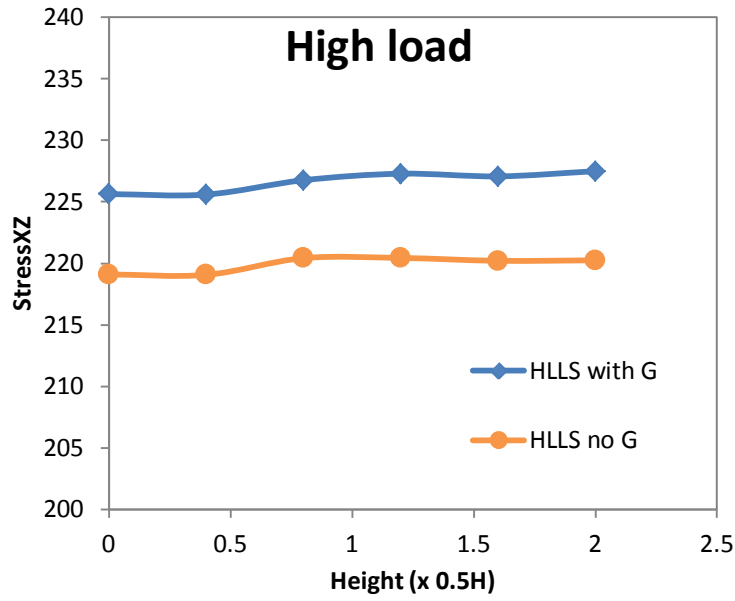




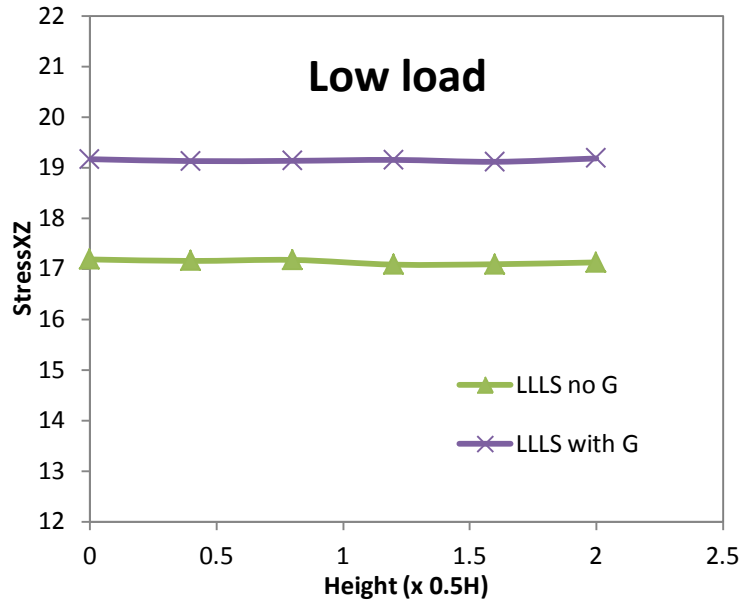
(d)

Fig. 4.7: Distributions at high load condition for: a) stress-xx, and b) stress-zz, and at low load condition for: c) stress-xx, and d) stress-zz (units of stresses are  $\pi\rho dg/6$ ).

Conversely, in Fig. 4.8, shear stress does not show any variation in terms of profile pattern either in the low load or high load when comparing the case with gravity to that without gravity. However, the variation is observed in the values where stressXZ is  $225\pi\rho dg/6$  with gravity and  $220\pi\rho dg/6$  without gravity in high-load-low-shear condition and  $19\pi\rho dg/6$  with gravity and  $17\pi\rho dg/6$  without gravity in low-load-low-shear condition. The shear stress, stress-xz, increases by about 2% at the high load and by about 12% at the low load when gravitational force is introduced. High variation at the low load agrees with the earlier findings that show a larger deviation for the same cases. The reduced influence of gravity is understandable because gravitational force acts downwards and perpendicular to the shear direction, inferring that it would have more impact on forces acting downwards. At the end, it is alluded that gravity has the highest influence on stress-zz, then stress-xx and the least on stress-xz.



(a)

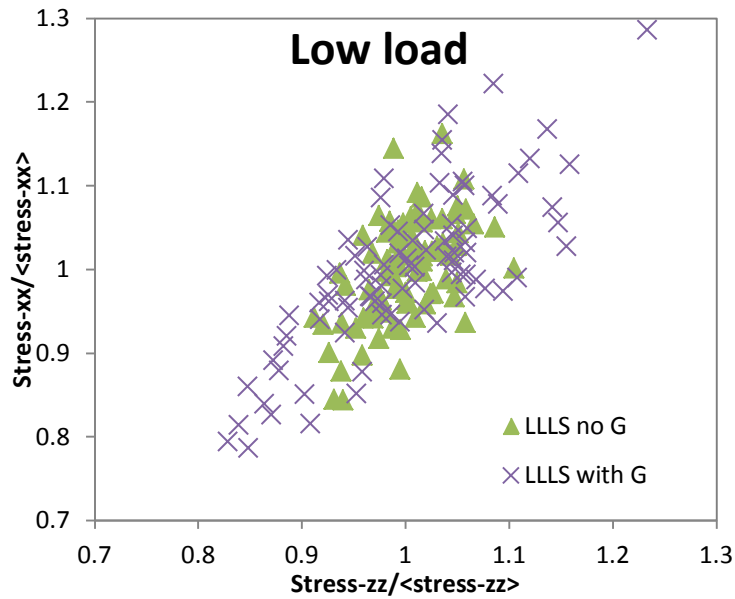


(b)

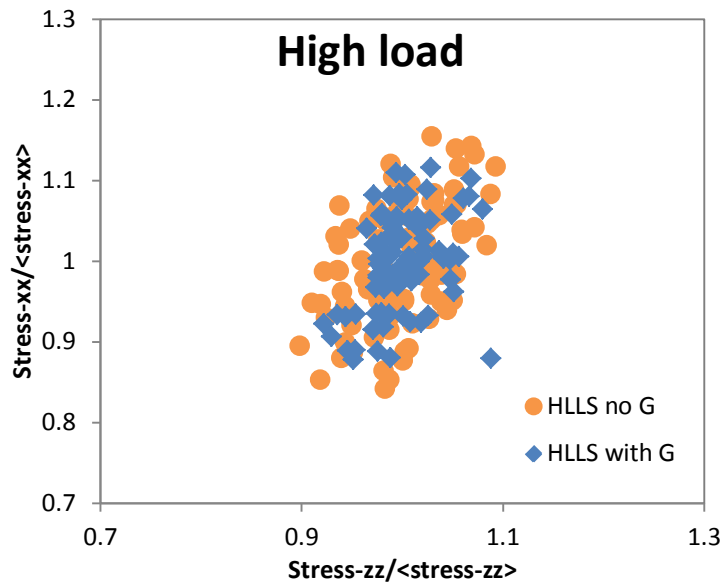
Fig. 4.8: Distributions of stress-xz at: a) high load, and b) low load conditions (units of the stress is  $\pi\rho dg/6$ ).

In Fig. 4.9, we analyse the correlation between the scaled shear stress ( $\text{stress-xz}/\langle\text{stress-xz}\rangle$ ) and scaled normal stress ( $\text{stress-zz}/\langle\text{stress-zz}\rangle$ ) in the presence and absence of gravity. At the low load condition, as depicted in Fig. 4.9a, in the presence of gravity, the data is

scattered across a large range although an approximately positive relationship between the shear stress and normal stress can be observed. For the case without gravity, however, the data becomes consolidated, which is similar to what was observed for the high load condition for both with and without gravity (see Fig. 4.9b). The results further demonstrate that gravity affects the dynamic behavior of the particle flow in the shear cell when the pressure acting on the assembly is low, but the effect is limited for high pressure.



(a)



(b)

Fig. 4.9: Correlation of stress-zz with stress-xz at: a) low load, and b) high load.

## 4.4. CONCLUSION

The effect of gravity on the particle assembly flowing through an annular shear cell in a stress-controlled double-shear condition is investigated at particle scale using the DEM. The key findings are summarized below:

- Different features are observed from the profile of velocity: the pattern is asymmetric particularly at low load when gravity is in effect and gradually becomes symmetric as the load is increased. In the absence of gravity, the symmetry of the gradient profiles exists in all the cases considered. At the highest magnitude of the applied loads considered in this study, profiles with and without gravity overlap, implying that the result is independent of gravity. At this point, applied load at the cell's upper platen is matched by that at the lower platen. Average velocity is strongly affected by gravity at low load. In the presence of gravity, particle velocity in the double-shear condition is unbalanced, with more particles tending to flow towards the direction at which the lower platen is moving.
- Porosity and coordination number have distribution trends similar to velocity. Their distributions are symmetric for all cases, except for those with low load when gravity is present. Porosity increases as height also increases, while the coordination number decreases at low load when gravity is present. Overall coordination number decreases with the increase of overall porosity. The correlation between the coordination number and porosity is not affected by gravity for high load, but is affected by gravity significantly for low load.
- Based on the analysis of network distribution, at low load with gravity, it is suggested that the organized structure of particle assembly at the lower region causes the load to be uniformly distributed. This in turn causes individual particles to carry less load compared to the upper region of the cell where the less sparsely dispersed contact network carries the applied load from the upper platen. The result is asymmetry in force distribution with lower average particle force near the lower platen. This explains why the particle contact force at the lower region is less even though the total contact force at this region is higher due to gravity. This is also the cause of asymmetry in the

distributions of particle velocity, coordination number and porosity at low load when gravity is considered.

- With low load condition, the distributions of the normal stresses are found to vary in the presence and absence of gravitational force. When there is no gravity, normal stresses reveal a similar trend to the high load case, except that their values are less. On the other hand, the trends are different in the presence of gravity. Nonetheless interestingly enough, there is no difference in the shear stress distribution across the flow except that gravity causes the value of shear stress to increase. These results indicate that gravity has a strong influence on behaviors of particle flow in some conditions. This should be considered when developing models to describe the dynamics of particle flow in the future.

# **Chapter 5: Microdynamic analysis of ellipsoidal particle flow in a shear cell**

## **OVERVIEW**

Flow of ellipsoidal particles in a modal shear cell was analysed at the microdynamic level based on discrete element method simulations. In a stress-controlled double-shear condition, the flow was studied by varying the aspect ratio of ellipsoidal particles and compared with the flow of spherical particle assembly in terms of some key properties, including particle alignment, linear velocity, angular velocity, porosity, contact force and contact energy. It was found that particle alignment towards shear flow direction has strong influence on overall flow pattern as such that the two types of velocities, force network and distribution, energy distribution are affected at both macro and micro level. Particle elongation primarily impacts its restriction of rotational displacement through preferential alignment which causes percolation of force across the flow become more uniform. Further, it resonates through energy and angular velocities as such that fluctuations damping and slip energies as well as angular velocities reduce.

## 5.1. INTRODUCTION

The dynamics of particle flow are very complicated because it has a dual nature. Its characteristics include expressions ranging from solid mechanics to fluid dynamics which not only vary with particle properties but also with manipulation of surrounding conditions and external influences. Because of the wide range of conditions affecting particle dynamics, it is very difficult to develop suitable constitutive models which can accurately interpret the dynamic behaviour of particles. In application, the majority of such particles are non-spherical, which is a crucial feature that affects the nature of flow. Accordingly, the research on non-spherical particle flows is immensely significant.

DEM has an important purpose of translating real systems in virtual platform especially to investigate shear, microdynamical responses. In real systems, when we observe granular rheology, we find how the flow is impacted by externally applied conditions: increase in shear means increase of flow, increase in pressure on particle assembly results in more compact assembly and so on. But we cannot find out what mechanism takes place inside the granular assembly. These phenomena are governed by particle properties such as particle mass, density, shape, surface texture/friction, electrical conductivity, adhesiveness, as well flow conditions like applied pressure, shear, interstitial medium, gravitational force, magnetic field and so on. To incorporate the microdynamical responses among particles in granular rheology, it is necessary to utilise law of mechanics and establish numerical model so that the correlations among these internal and external parameters can be obtained to have deeper knowledge in granular rheology. DEM significantly contributes to understanding such shear, microdynamical responses by incorporating relevant variables to produce outcome that can then be compared to real systems in order to verify and understand mechanical phenomena in real systems and benefit for further advancement in research of granular rheology.

Similar set-up is used in this chapter as was used in chapter 3 and 4. The study has been now extended from spherical particles to non-spherical particles of complex shapes to simulate more practical phenomena [75]. To simulate the flow of non-spherical particles using the DEM, the initial challenge is to construct the shape of a non-spherical particle along with how it would interact with other constituents. Various methods have been proposed.

Some of the popular methods are the voxelization method [62], geometric method [82] and spherical particle clumping method [79].

The numerical study of non-spherical particles has been conducted at various static and quasistatic conditions [181], as well as complex scenario of flow [82]. Various particulate shapes such as spherocylinders [88], discs/cylinders [66] and cubes [93] have been considered. Stroeven and He [95] and Dong et al. [84] investigated the static packing of particles of different aspect ratios and found that the volume fraction of assembly reduces with an increase in aspect ratio. Campbell [64] examined the flow of ellipsoidal particles through a shear cell in a volume controlled environment. He found the correlations among volume fraction, stress and shear rate, and identified that force chains were formed more quickly in more elongated particles. Azema and Radjai [76] studied elongated particles with spherocylindrical shape at a double-shear condition and investigated force distributions, contact angles and contact networks. Guo et al. [66] explored the flow of flat disc and elongated rods in a stress-controlled double-shear cell, and found that particle elongation strongly influenced granular flow behaviour. Guo et al. [81] studied dry, thin, long and flexible fibres in a volume controlled shear cell environment and discovered that contact force and coordination number increase with aspect ratio of the fibres. However, to the authors' knowledge, systematic studies are lacking on the dynamics of flow of non-spherical particles in shear cells at the microdynamic level, especially the correlation of aspect ratio with different key parameters of dynamics of granular rheology. Such studies are very important in order to have a comprehensive understanding of particle flow.

In this work, a rectangular segment of an annular shear cell was simulated through the well-established DEM for investigating particle flow dynamics. The flow of ellipsoidal particles in the intermediate regime was studied in a stress-controlled double-shear condition to obtain micro-scale dynamic information for the investigation of the effect of particle shape on the particle flow. The ellipsoidal particles were constructed by spherical particles of varying sizes through overlapping method so that well-established knowledge on spherical particles can be applied to the ellipsoidal particles. The effect of aspect ratio on various parameters such as particle orientation, velocity, porosity, force and energy was examined in different external conditions.



## 5.2. SIMULATION METHOD AND CONDITIONS

DEM is used in this investigation to simulate granular flow through annular shear cell. Details of DEM is discussed in Chapter 2. A rectangular segment of an annular shear cell was generated in a three-dimensional virtual space for both spherical and ellipsoidal particles (Fig. 5.1). The segment has the dimension of  $12d \times 30d \times H$ , where  $d$  is the mean effective diameter of particles and  $H$  is the height of the upper platen (i.e., the distance from the upper platen to the lower platen). In this stress-controlled model, 'H' changes under different applied load and shear rate combinations to maintain steady state. A similar configuration has been utilised in the previous studies, for example, in [182]. Larger shear cells have also been considered and demonstrate similar results to those from the current size, confirming the reliability of the current size for the present study of ellipsoidal particles (not shown here for the reasons of brevity). Periodic boundary conditions were applied to the two boundaries perpendicular to the direction of flow to generate seamless continuity in shear analogous to annular shear cell, similar to previous studies [182]. The upper and lower platens were created within the segment with reasonable space to generate particle assembly to be investigated. Each of the two platens constitutes 160 spherical particles of  $1.5d$  diameter so that the entire area of the platen is filled. The larger particles were used to form the platens so that a stronger shearing influence on their adjacent particles is created. The platen particles possess the same properties (density, damping coefficient, friction coefficient and stiffness) of the constituents of particle assembly that are subject to analysis. The particles of the same platen are stationary relative to each other to mimic a rough wall producing the shear effect. Stationary side walls of the segment were generated parallel to the direction of flow.

About 5000 mono-disperse particles (spherical and ellipsoidal in individual cases, respectively) were generated randomly between the upper and lower platens with an initial volume fraction of 0.67. Then the particles were allowed to naturally relax and distribute within the space between the platens and side walls. The ellipsoidal particles with aspect ratio of 1.75:1, 2.5:1, 3.75:1 and 5:1 were considered. Other key particle properties and simulation parameters applied in the model remained the same for all cases considered, and given in Table 1. Gravitational effect is nullified similar to the previous treatments [7, 8, 140].

Once the particles were in a natural equilibrium state reasonably, a very low velocity was applied to the upper and lower platens in the opposite directions along the x-axis so that the

platens sheared the assembly. The simulation was run for a considerably long time to allow the particle assembly to obtain a state with a relatively uniform spatial distribution. Then, the shear velocity was slowly increased step-by-step until the defined value was reached. Concurrently, when the shear velocity was applied to the platens, a load was also applied to the upper platen, and was increased to the pre-set value gradually. In order to increase the load, the upper platen was lowered slowly. After reaching the desired load, the upper platen continuously adjusted its position to maintain a constant pressure. When the fluctuation of the upper platen reached the minimum level, it was considered that the granular flow was at a steady-state condition. Low time-step of  $0.00001\sqrt{(d/g)}$  has been used in the simulations to ensure that contact detection occurs appropriately and overlapping is avoided. The data for variables at a particle scale such as particle velocity and contact force as well as variables at a macro-scale such as porosity were collected for an extended period to obtain the time-averaged values of these variables. The simulation procedures are similar for both spherical and non-spherical particles. However, the simulations for ellipsoidal particles took much longer due to the more extensive calculations for non-spherical particles.

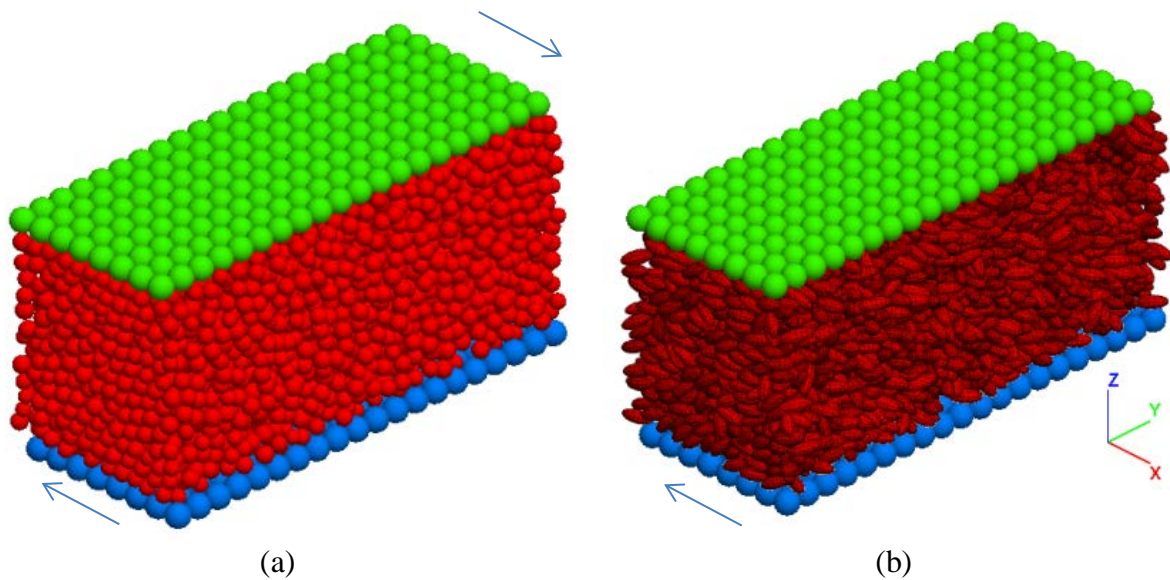


Fig. 5.1: Simulated model shear cells with: a) spherical particles, and b) ellipsoidal particles with aspect ratio 2.5:1.

The so-called bubble-pack algorithm [79] was used to construct the ellipsoidal particles in this work. In the algorithm, the closed surface of the non-spherical particle is first constructed with triangular meshes of various sizes. Then spherical particles of various sizes are used to fill the space within the surface to obtain a specific volume. These particles are then glued and made immobile relative to each other, and thus the particle of desired shape is constructed. One of the main advantages of this method is that well-established knowledge on spherical particles can be used to examine non-spherical particles. In dynamic analysis, in contrast to the geometric method where multiple interaction conditions need to be considered [66], this method allows the simulation to consider the monotype spherical interaction. Each spherical component of an ellipsoidal particle returns a value to form the resultant forces which determine the velocity and position of the ellipsoidal particle.

Table 5.1: Parameters used in the simulations

Property	Value	Unit
Friction coefficient, $\mu$ (particle-particle and particle-wall)	0.3	(-)
Critical damping ratio, $D$ (normal and shear)	0.3	(-)
Young's modulus, $E_y$	$2.5 \times 10^6$	$\pi \rho d g / 6$
Poisson's ratio, $\vartheta$	0.3	(-)
Time-step	0.00001	$\sqrt{(d/g)}$
Normal load in (-)ve z direction	1434.75	$\pi \rho d g / 6$
Shear rate	6.5	$\sqrt{(gd)}$

## 5.3. RESULTS AND DISCUSSION

### 5.3.1. Particle alignment

Particle orientation (alignment) is of special interest in the study of non-spherical particles because of its strong influence on the dynamic properties of granular particle assembly. In this study, we observed that the ellipsoidal particles were approximately aligned with the direction of the shear velocity, which means that the major axes of the particles are mainly parallel to the flow (i.e., the x-axis), as shown in Fig. 5.2. This is a characteristic of non-spherical particles distinct from spherical particles as the spherical particles are isotropic in terms of their orientations. When the aspect ratio increases, particles become more aligned to the direction of flow. A similar feature has been observed in previous experimental and

numerical studies, for example, the experimental study by Borzsonyi et al. [162] and Wegner et al. [183] on rice and wooden pegs flowing through a shear cell; the 2D numerical study by Reddy et al. [184] on inelastic dumbbells in a shear cell; and the 3D numerical study by Guo et al. [66] regarding flat disks and elongated cylindrical sticks in a Couette cell. To have a clearer picture of the orientation of particles, a statistical study of particle orientation was conducted. Fig. 5.3 shows the particle orientations about the y-axis (pitch Euler angle) and the z-axis (roll Euler angle).

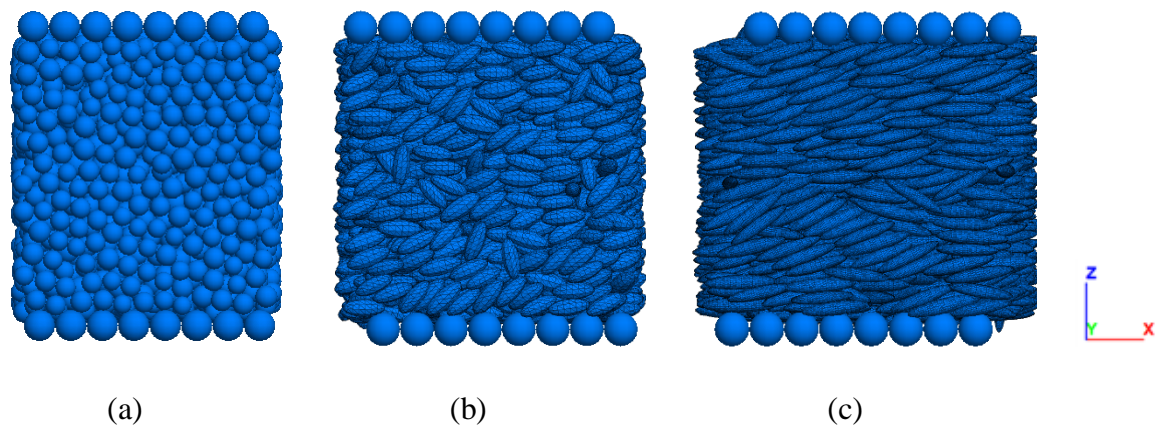


Fig. 5.2: Flow patterns of assemblies of particles with aspect ratios: a) 1.0, b) 2.5, and c) 5.0.

It can be observed that for the case of more elongated particles, more particles in the assembly are aligned towards the shear flow, as inferred from Fig. 5.2. In all cases, the distribution comes down to zero at  $\pm 90^\circ$  because the particles cannot stand perpendicularly against shear flow. When the aspect ratio is small (1.75:1 or 2.5:1), the particle alignment distribution is relatively uniform and does not vary much with particle shape variation. However, at higher aspect ratios (3.75:1 and 5:1), particles increasingly tend towards the shear direction as depicted from the extension of the graph towards 0 degree angle. Similar probability distributions of orientation of particles have been observed in the numerical analysis on the flows of flat disks, cylinders and elongated rods [66]. The result of ellipsoidal particles with the high aspect ratio 5:1 in this study is similar to that of the elongated rods, while the case of the low aspect ratio 1.75:1 aspect ratio is similar to that of the cylinders with aspect ratio 1:1 in [66].

The distributions are nearly symmetrical about a line slightly tilting to the radial line at  $0_0$ , indicating that the particles are not exactly parallel to the x-axis but there is a little rise at their front ends. This is caused by the boundary conditions we used. In the present study, the upper platen's height is continuously adjusted to maintain constant pressure on the particle assembly while the lower platen has a constant height. This causes the particles to be raised slightly towards the upper platen statistically. A similar phenomenon has been observed in [66, 81].

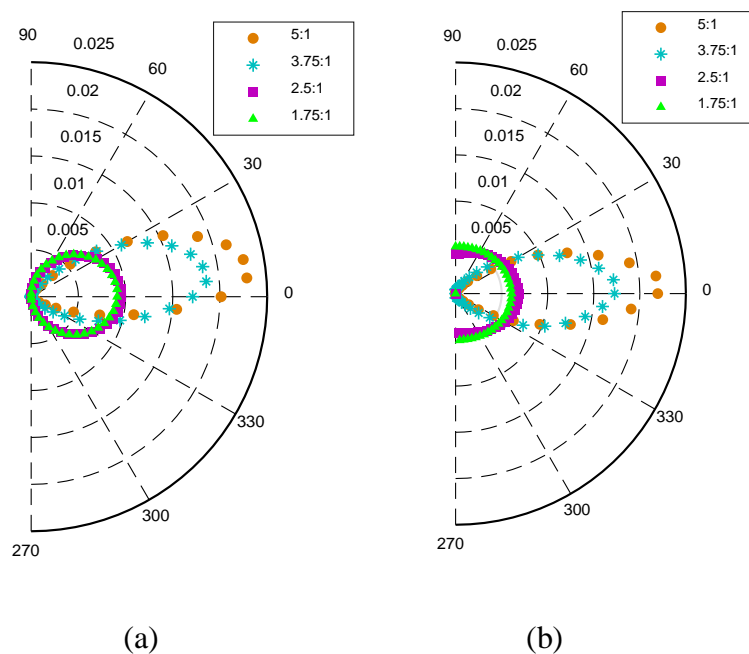
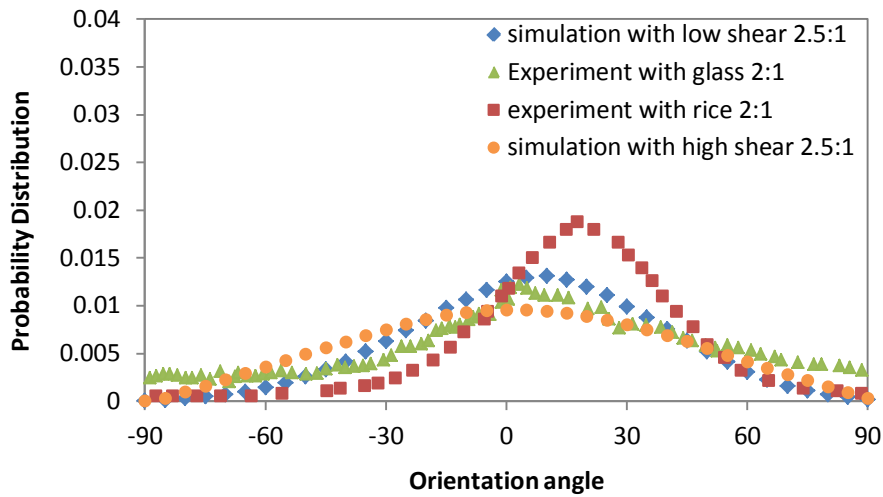


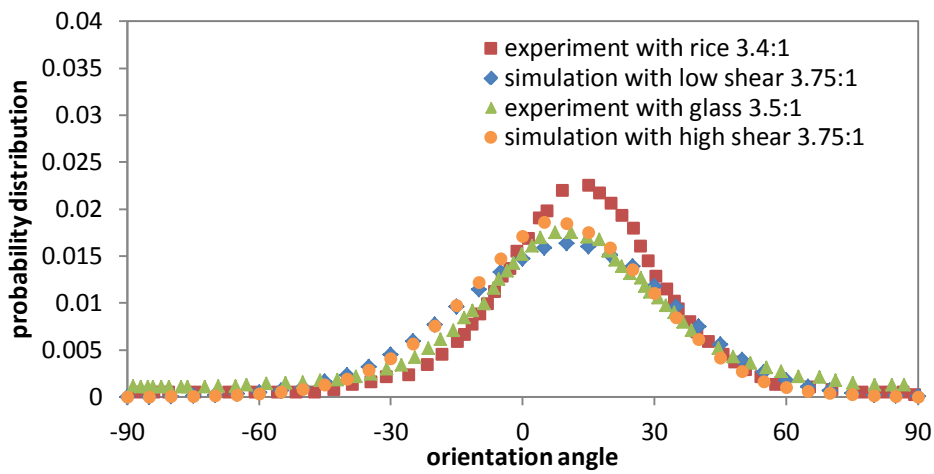
Fig. 5.3: PDF of orientation of particles: a) y-euler (pitch angle of the particle about y-axis), and b) z-euler (roll angle of the particle about z-axis).

In the lack of physical experimental results for ellipsoidal particles for the system considered in the present work in the literature, the probability distributions of particle orientation obtained in this study are used to compare with those obtained in the experimental study of Botzsonyi et al. [162] for rice and glass cylinders, as shown in Fig. 5.4. To be more convincing, another case with 1.0d platen particle size and lower shear rate ( $1.07\sqrt{(\text{gd})}$ ) has been considered. A qualitatively similar trend of distributions for particle orientation can be observed in the simulation and experiment in spite of different particle shapes considered: they are symmetric Gaussian probability distributions, with a peak increasing with elongation

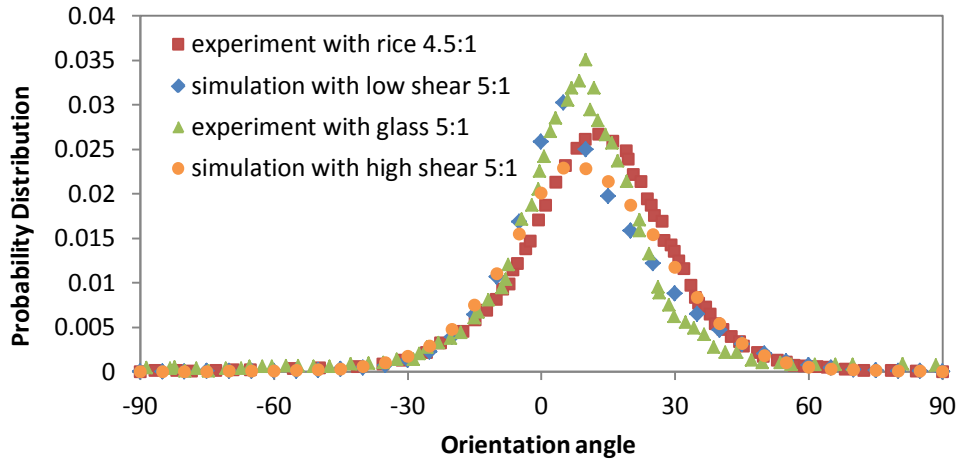
of particles. The peaks are not exactly at the angle of  $0^{\circ}$  but a positive value slightly larger than zero, which is consistent to what observed in Fig. 5.3. The distributions for different shaped particles can be close by adjusting the values of some particle properties, which indicates that non-spherical particles with different shapes may possess common features controlling their orientation.



(a)



(b)



(c)

Fig. 5.4: Distributions of the orientation angle of the particles with respect to the streamlines for (a)-(c) least, medium and highest aspect ratios, respectively. In each case rice, glass cylinders and our simulation data are compared [162].

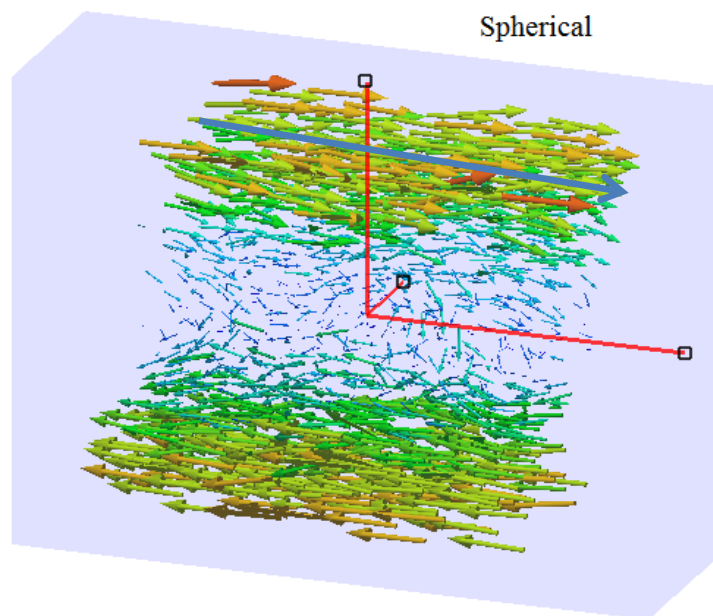
### 5.3.2. Velocity field

The velocity profile was examined along the three major axes, and it was found that the components of velocity in the y and z directions are minimal and can be ignored for both spherical and ellipsoidal particle assemblies (not shown for the reason of brevity), which is discussed in previous studies [13]. Therefore, only the component of velocity at the x direction is considered here.

Fig. 5.5 shows the profiles of velocity at the x direction in the middle slice of the rectangular segment on the xz-plane. For both spherical and ellipsoidal particles, the velocity profile shows that there is a symmetric velocity field with particles having nearly zero velocity at the central region. Meanwhile the velocity gradually increases towards both the moving platens with the maximum shear velocity in the regions near the platens. The driving force in this event is the interaction forces between the platens and their adjacent particles in contact. This gradient develops due to the dissipative interaction force between the particles in the adjacent laminar layers. The large velocities of the particles near the platens are mainly driven by the interaction forces between the particles and platens. The particles in the central region move in the two flow directions and counterbalance each other there, resulting in

negligible velocities. The velocity gradient is similar to that observed in our previous study on spherical particles [13].

The time-averaged velocities of particles at different layers along the z-axis are analysed in Fig. 5.6a, where the averaged velocity at a layer,  $V_x$ , is scaled by the magnitude of the shear velocity applied to the platens,  $V$ , and the layer height,  $h$ , is scaled by half of the upper platen height,  $H$ . All particle assemblies exhibit similar linear velocity gradient with near-zero value at the central plane. Further, all the velocity gradients show that slips occur near the platens. With the increase of elongation of constituent particles, there is a marginal increase in the velocity slip. A similar feature has been observed both numerically [13, 137, 139] and experimentally [129] for spherical particles.



(a)



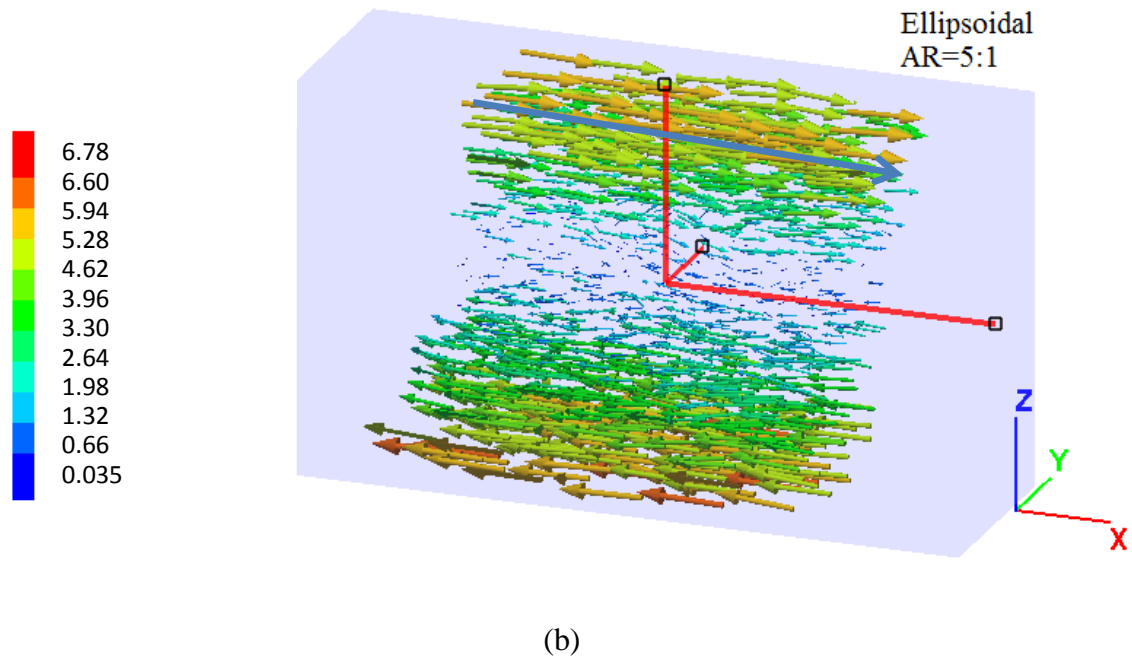
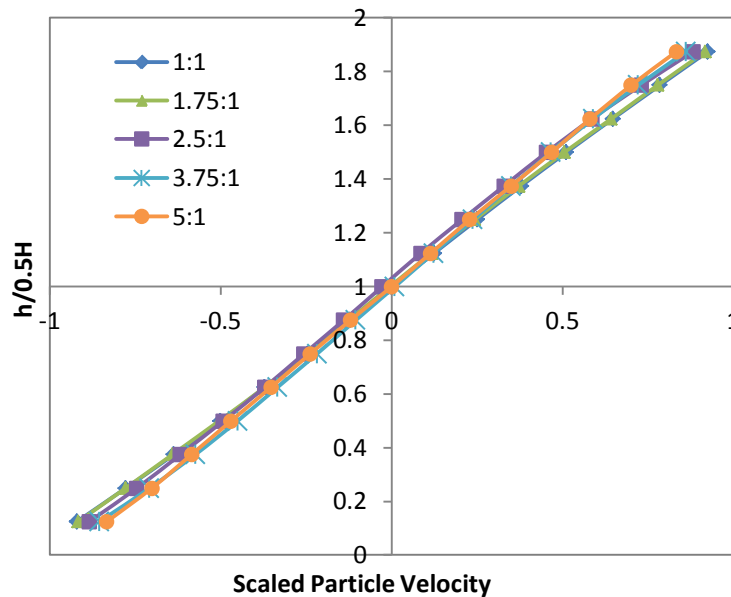


Fig. 5.5: Velocity fields for assemblies of particles: (a) spherical, and (b) ellipsoidal with aspect ratio of 5:1.

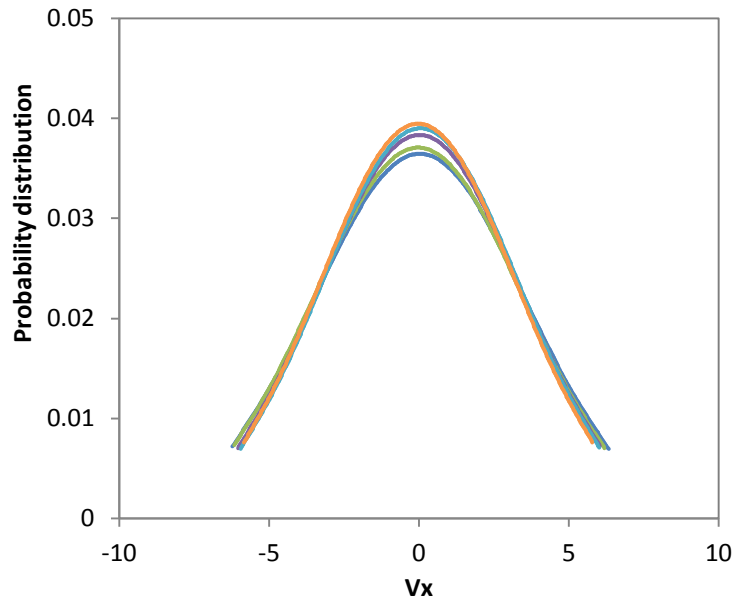
Fig. 5.6b shows the statistical distributions of the velocity in the x direction for different aspect ratios. It can be seen that the velocity exhibits symmetric Gaussian distribution with the peak at the zero velocity for all particle assemblies, suggesting that many particles have very low velocities. Comparing the velocity profile shown in Fig. 5.6a with the distribution curve of Fig. 5.6b indicates that the peak velocity around zero value corresponds to the central region of the cell. In our previous study with spherical particles [13], it has been found that a peak exists at zero magnitude for different particle properties such as variation of friction coefficient and different flow conditions such as variation of shear velocity and applied load. It should be this case for ellipsoidal particles although more simulations may need to confirm this. Furthermore, Fig. 5.6b shows that, for ellipsoidal particles, there is an increase in the peak of the distribution curve when the aspect ratio increases. It means that variation of velocity slightly reduces with increasing elongation of particles. Moreover, the peak at the zero value also implies that the number of stationary particles marginally increases with particle elongation. This phenomenon can be explained by particle alignment. As the particles become aligned with the direction of flow, the more elongated the particles,

the higher the frictional surface between two laminar layers of the flow. This causes more energy dissipated and hence more particles having low velocities.

The fluctuation of particle velocity was investigated. Fig. 5.7 shows the standard deviation of particle velocities and the gradient of the standard deviation of particle velocities across the flow. From Fig. 5.7a, we can find that the velocity fluctuation of particles drops as the aspect ratio of particles increases, although the change of velocity fluctuation is not significant when the aspect ratio changes from 3.75:1 to 5:1. This feature can be further confirmed in the distributions of standard deviation along the height, as shown in Fig. 5.7b. It can be seen that the velocity fluctuation decreases when the particle aspect ratio increases from 1:1 (spherical) to 3.75:1.



(a)

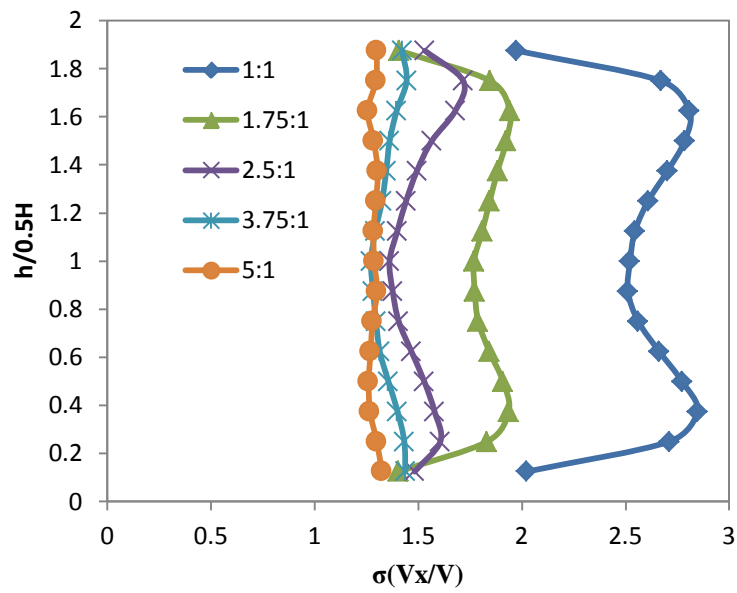


(b)

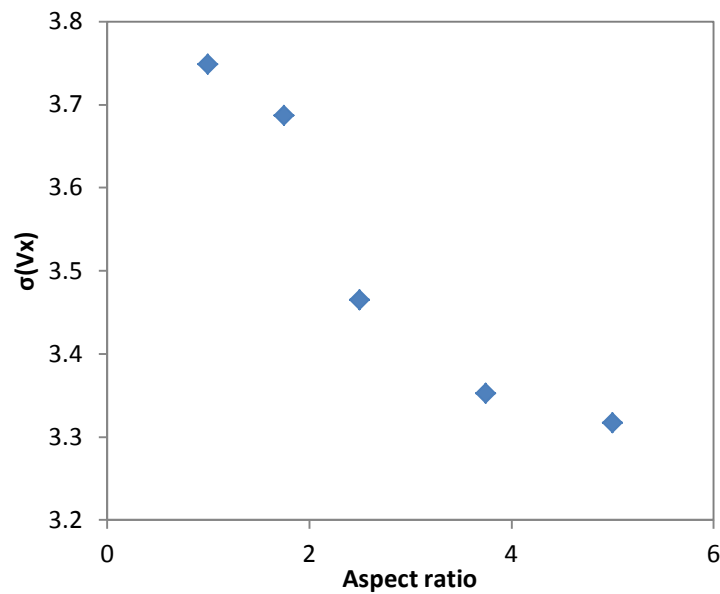
Fig. 5.6: a) Scaled velocity gradient for different particle assemblies in identical properties and base conditions.  $V_x$  and  $V$  are the average velocity of particles at a layer and shear velocity of the platens, respectively, and  $h$  and  $H$  are the layer height and segment height, respectively. b) Normal distribution of scaled velocities of spherical and ellipsoidal particles (unit:  $\sqrt{gd}$ ).

For the cases with aspect ratios of 3.75:1 and 5:1, the distributions are very close. The distribution trends of the standard deviation are different for cases with ratios of 3.75 – 5.0 and 1 – 3.75. For the former ones, the standard deviations are almost constant across the flow. For the latter, there is a reduction in the velocity fluctuation near the platens. This jag indicates that the platens act as a sink for granular temperature because immediate neighbouring particles become locked between the grooves of the rough platens. Furthermore, the temperature propagation occurs at a layer away from the platens. One should also note that the particle velocity fluctuation reveals a dip at the central region for the systems with lower aspect ratio, suggesting that temperature dissipates on its way towards the core of the segment. It is similar to what was found for spherical particles in [180]. This dissipation disappears for the elongated particles with aspect ratios of 3.75:1 and 5:1. This is

an important aspect, and it is one related to the contact force distribution, which will be discussed in Section 3.4.



(a)

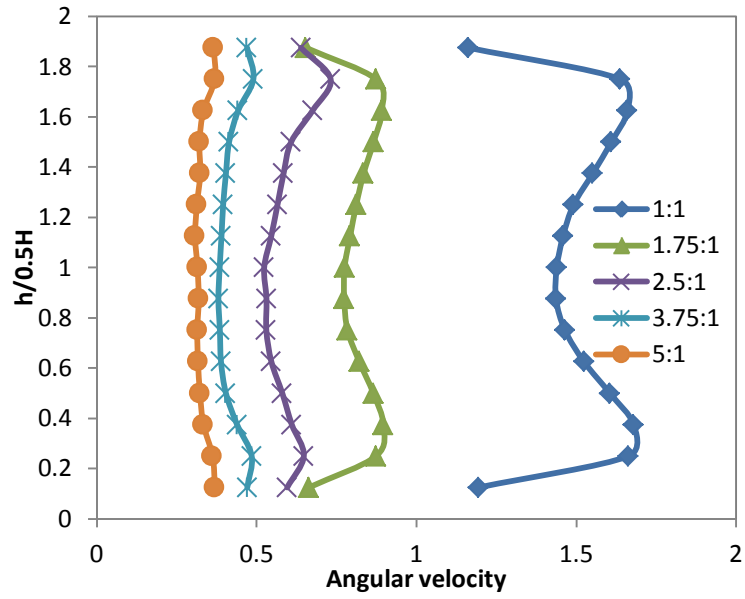


(b)

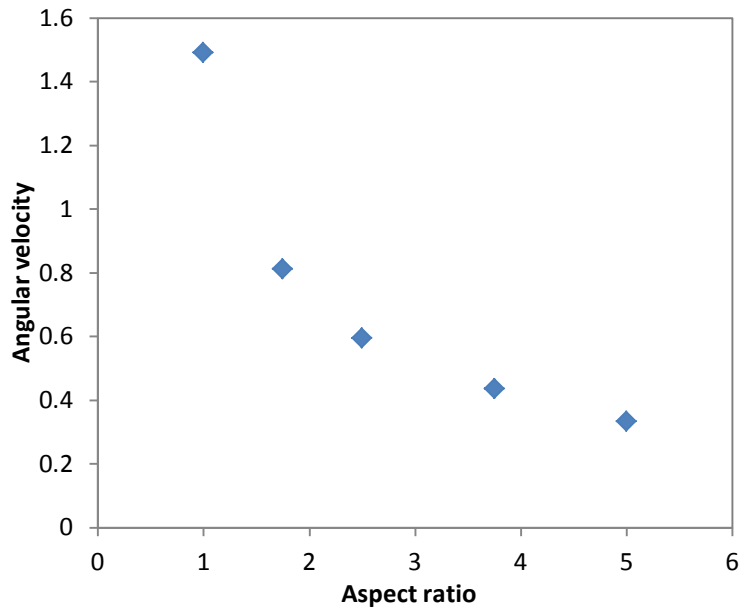
Fig. 5.7: a) Time-space averaged particle velocity fluctuation at different laminar layers of flow for particle assemblies with constituents of different aspect ratios b) average standard deviation of particle velocity with respect to aspect ratio (unit:  $\sqrt{gd}$ ).

Particle angular velocity is also an important parameter, especially, for non-spherical elongated particles. Fig. 5.8 depicts the effect of particle shape on particle angular velocity. The distribution of angular velocity at different heights is considered in Fig. 5.8a. It can be seen that angular velocity and velocity fluctuation have similar distribution trends. For particle assembly with a lower aspect ratio (1:1, 1.75:1 or 2.5:1), the angular velocity is higher near the platens, and gradually reduces when moving away from the platens. In the immediate neighbourhood of the platens, there is a sudden drop in angular velocity due to particles getting locked between the solid platens and the particles in the next layer. This finding is similar to what was observed for velocity fluctuation. A similar pattern has been observed earlier [133] for spherical particle assembly.

In comparison, the effect of the platens is not obvious in the region adjacent to them for ellipsoidal particles with higher aspect ratio (3.75:1 and 5:1). As the particle gets more elongated, angular velocity profile steadily flattens. Particles are less likely to get locked in the texture of platens. Also, angular velocities for elongated particles are much less for all elongated particles than that for spherical particles. The higher the elongation, the lower the angular velocity, as shown in Fig. 5.8b. This is because of the physical event where elongated particles are oriented into nematic order at a steady state. The more elongated a particle, the more restricted its rotation becomes due to extended local axis along the direction of flow causing increased interference to angular displacement. On the other hand, as the elongation reduces, the particle is easier to rotate within its local space as interference abates from the surrounding particles.



(a)



(b)

Fig. 5.8: a) Variation of angular velocities along height of cell for different particulate assemblies b) average particle angular velocity of the assembly for particle constituents with different aspect ratios (unit:  $2\sqrt{\frac{g}{d}}$ ).

Probability distribution of angular velocity of spherical and elongated particles exhibits distinguishing features in Fig. 5.9. In the semi-log graph, the angular velocities of spherical particles have a higher tail. It suggests that particle angular velocity is more dispersed from its mean value for spherical particles. As the particle aspect ratio increases, the tail of probability distributions becomes lower. It means that the angular velocity has a narrower distribution for a higher particle elongation. This outcome is consistent with the finding for the angular velocity gradient (Fig. 5.8a).

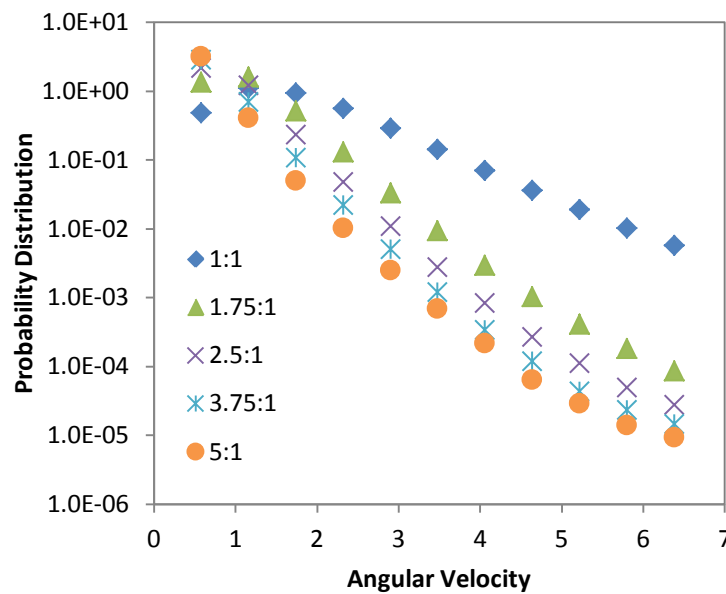


Fig. 5.9: Variation of statistical distribution of particle angular velocities with aspect ratio (unit:  $2\sqrt{\frac{g}{d}}$ ).

### 5.3.3. Porosity

In granular rheology, porosity is a key parameter that is often utilised to understand the flow structure of particle assemblies [12]. To obtain the spatial distribution of porosity across the cell segment, a vertical mid-section of the cell segment in the  $yz$  plane is considered. The porosity at a point in the section is that of a spherical region of  $2d$  diameter centred at the

point. It should be noted that slight distance from the walls is maintained to minimise the wall effect on respective parameters.

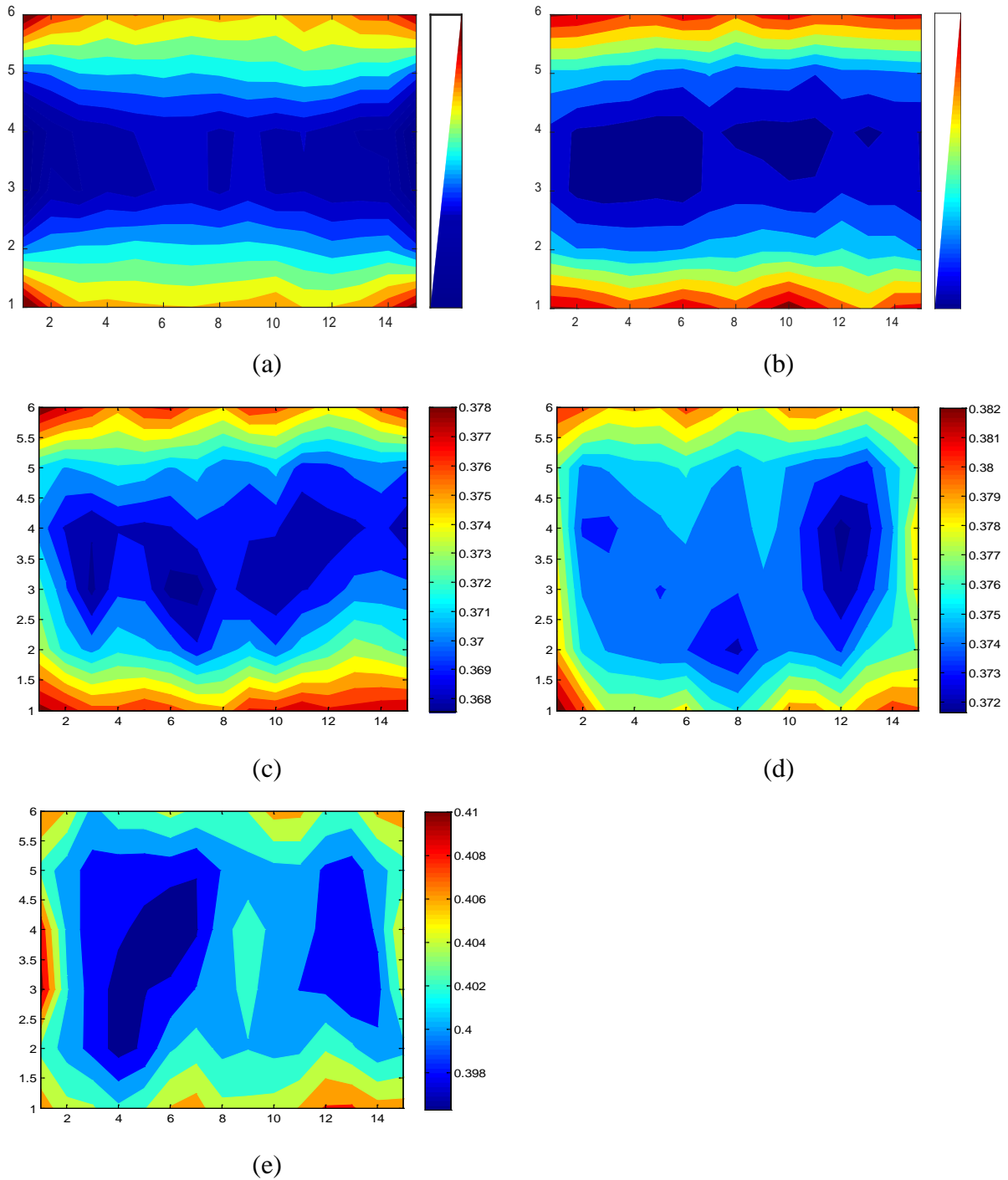


Fig. 5.10: Spatial distribution of porosity of ellipsoidal particle assemblies with different aspect ratios: a) 1.0 (spherical), b) 1.75, c) 2.5, d) 3.75, and e) 5.0.



Fig. 5.10 shows the spatial distributions of porosity across the flow of spherical and ellipsoidal particles. To minimise the possibility of errors derived from large fluctuations in local porosities, the data for a large period of time is obtained to get time-averaged values. It should be noted that different scales have been used for different aspect ratios since the overall porosity varies with particle elongation. It is clear that all the cases considered have a gradient trend: higher porosity near the platens, and gradually lower with the lowest value in the central region. Compared with the more elongated particles, less elongated particles have clearer distributions near the platens. The porosity spatial distribution for spherical particles in the present study is similar to that observed in [14, 46].

Fig. 5.11 shows the time-averaged overall porosity for different cases. It can be observed that there is a small dip for the cases with low aspect ratios. After that, there is a slow but steady increase in porosity as the particle elongation increases. This happens because less elongated particles are able to squeeze in the central region under high pressure since they are less compelled to be in distinguishable layers.

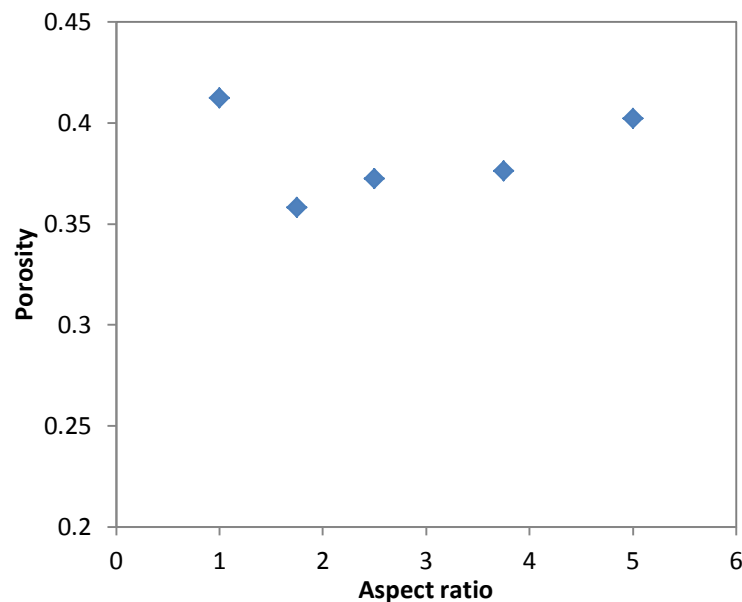


Fig. 5.11: Effect of aspect ratio on overall porosity.

On the other hand, elongated ellipsoidal particles are bound to be in distinguishable layers even at the highest pressure region because of the particles' orientation. Similar findings were shown for static elongated particles in [184]. In the fixed-load boundary condition, the contact force acting between layers significantly influences the rheological structure. As the particles become elongated, there is more surface area between layers to sustain friction (or shear force). While the shear velocity remains constant, the shear force between layers increases as expected. To maintain a constant pressure on the assembly, the upper platen is raised. As a result, the overall porosity increases.

### 5.3.4. Contact Force

Fig. 5.12 depicts the contact force chain network of ellipsoidal particle assembly with particles with an aspect ratio of 5:1 compared to that of spherical particle assembly in a slice of the cell on the  $yz$  plane. It can be seen that, for spherical assembly, many larger force chains are sparsely spread throughout the flow. Conversely, the elongated particles show a much more densely knit span of force chain network across the region. The larger force chains observed in the spherical assembly are absent across the flow of the elongated particles. This relatively uniform structure of force network is a direct result of ellipsoidal particles homogeneously being distributed as a consequence of preferential orientation (as illustrated in Fig. 5.2). The particles across the flow with higher aspect ratio are more explicitly found to interact between layers rather than between individual particles. The relatively uniform structure of force network leads to that the velocity fluctuation and angular velocity are uniformly transferred across the region as seen in Fig. 5.7b and Fig. 5.8a. On the other hand, the relative heterogeneous distribution of spherical particles is manifested in forces being heterogeneous across the span of chain network. This implies that layer formation is less distinct and particle interactions are more individual than layer-based ones in collective form, which causes more velocity fluctuation (as seen in Fig. 5.7a) and less restricted particle rotation (i.e., higher angular velocity) (as shown in Fig. 5.8b) compared with ellipsoidal particles.

Fig. 5.13 illustrates the effect of particle aspect ratio on particle contact force. In Fig. 5.13a, we can find that, with the increase of particle aspect ratio, the average particle contact

force initially sharply decreases and then the rate of decrease eases off until it becomes almost constant. This happens because as the particles are elongated, there are more contacts established between particles, which consequently results in more force chains bearing the same overall load. The number of weak force chains is larger for more elongated particles. As a result, the average particle force in the assembly decreases until the streamlining (preferential orientation) of particles is fully achieved.

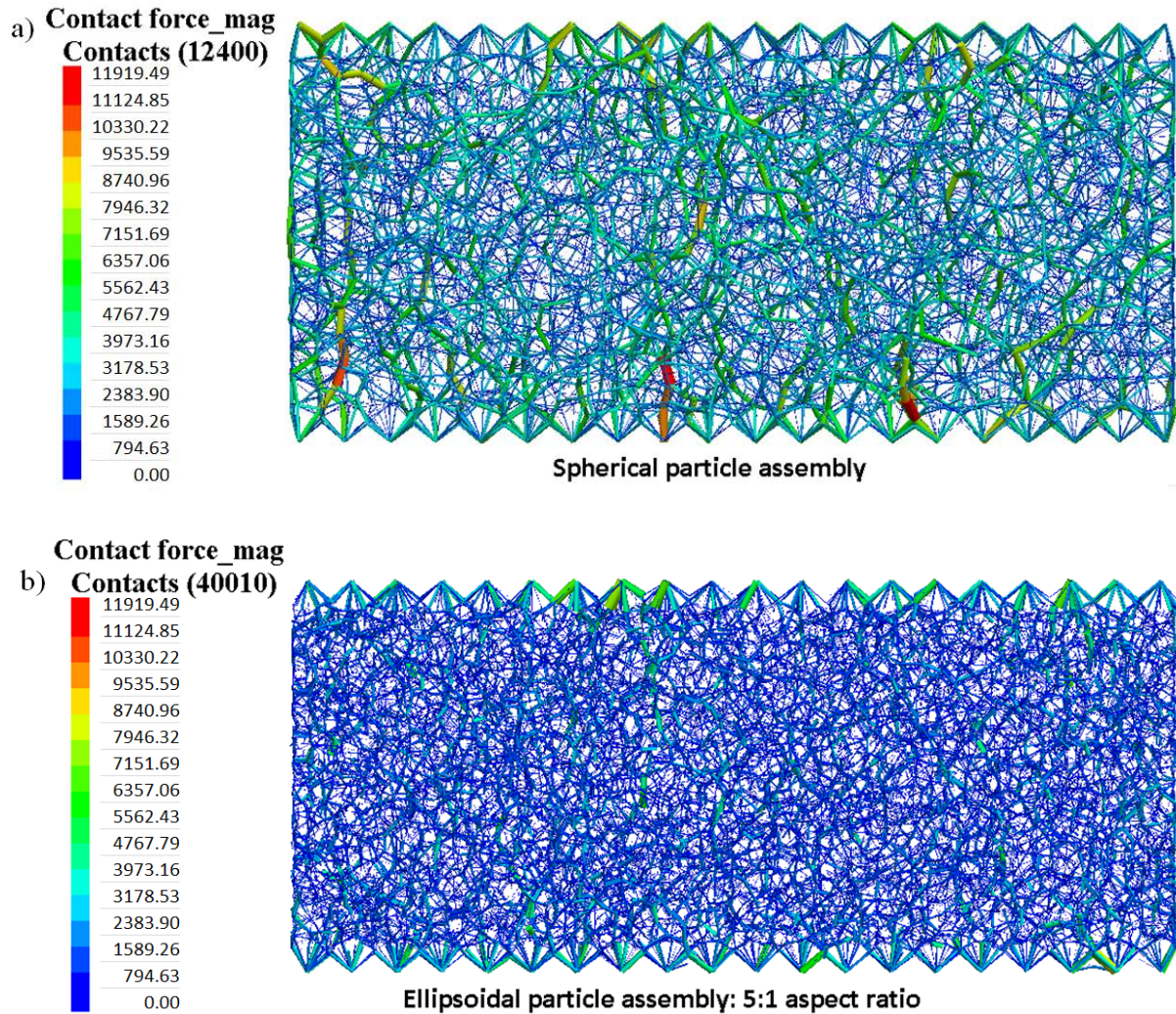
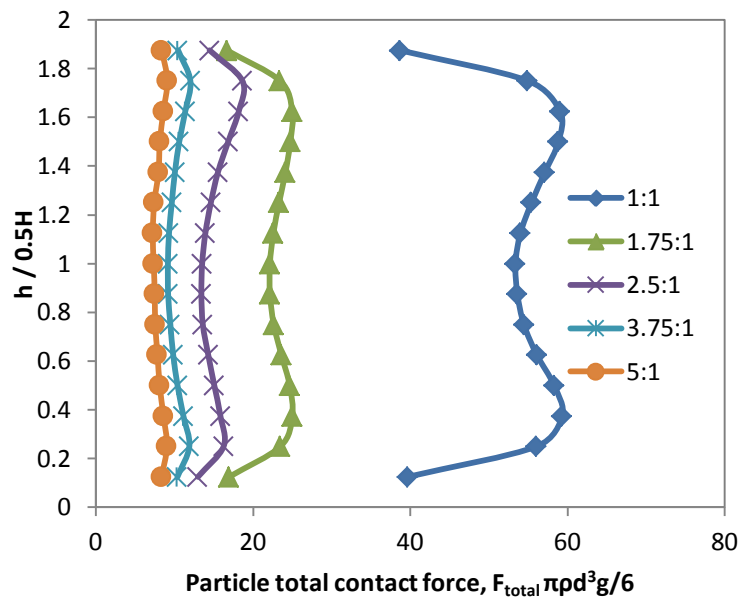


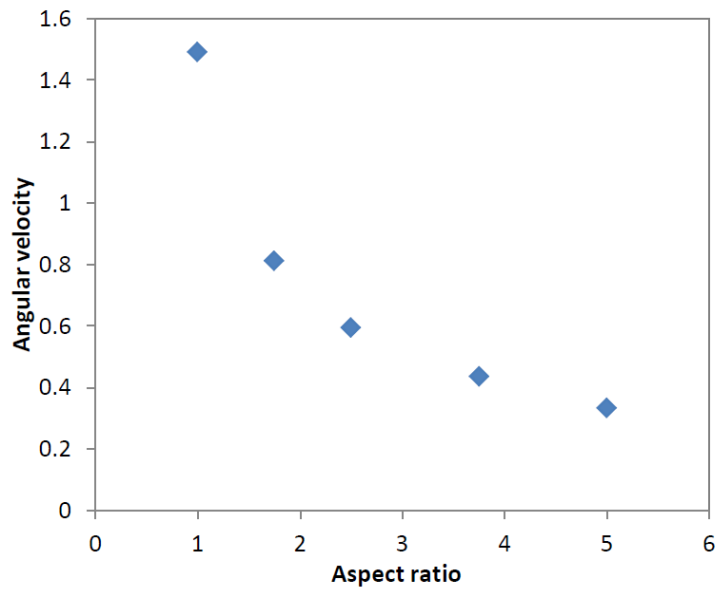
Fig. 5.12: Contact force network for a) spherical particle assembly, and b) ellipsoidal particle assembly (unit:  $\pi\rho d^3 g/6$ ).

This constant contact force is an early indicator of the fact that the structuring of the particles within the flow reaches a stable layered state and become independent of the elongation of particles. Fig. 5.13b shows the variation of total particle contact force along the

height for different aspect ratios. It can be observed that there is larger variation in the contact force in the case of spherical particles. This variation gradually diminishes as the particles become more elongated. The uniform force distribution for ellipsoidal particles with higher aspect ratios agrees with the characteristics of uniformity of the force network in Fig. 5.12. Another phenomenon to note here is that the boundaries have a stronger influence on spherical particles with larger gradient of force near the platens. For spherical particles, there is a dip in the distribution of the contact force near each platen. This is a consequence of spherical particles getting locked adjacent to the platens.



(a)



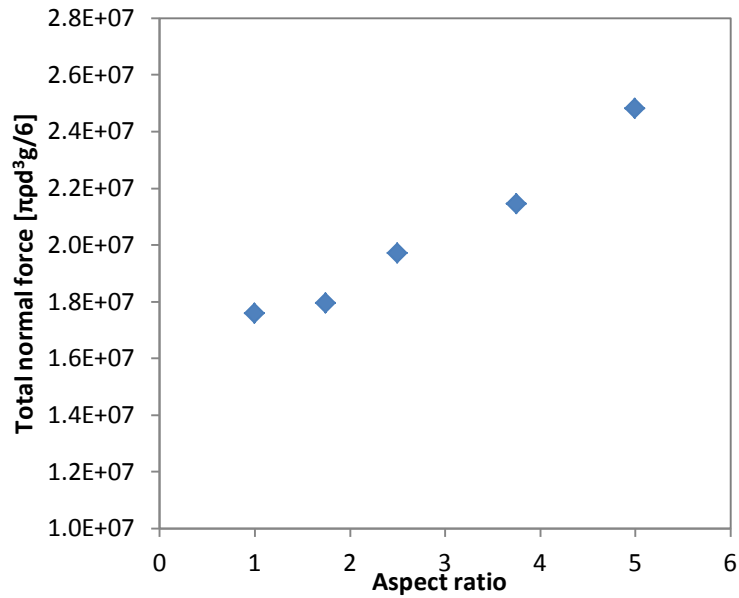
(b)

Fig. 5.13: a) particle total contact force gradient profile , b) Average particle total contact force of the assemblies with constituents of varying aspect ratios (unit:  $\pi\rho d^3 g/6$ ).

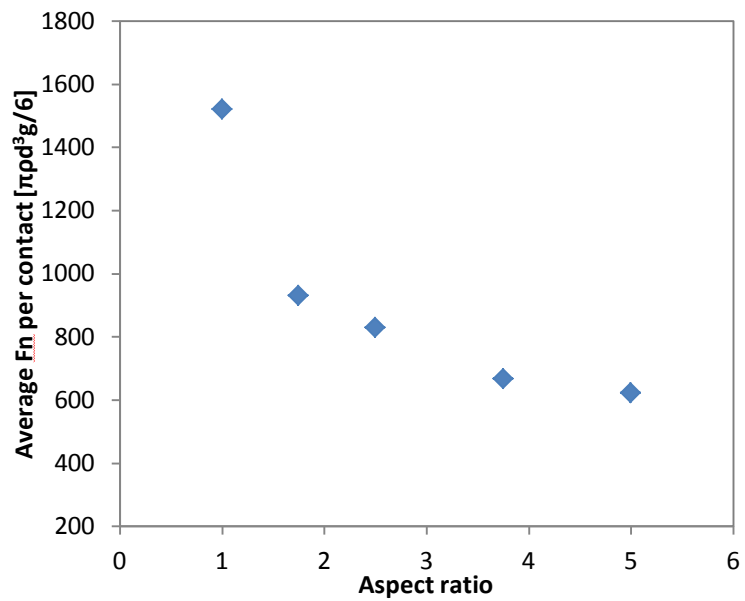
In a more in-depth analysis, the effect of aspect ratio on the components of individual contact forces between particles is considered, as shown Fig. 5.14. It can be observed from Figs. 5.14a and c that the total normal force and total shear force (i.e., tangential force) increase with particle aspect ratio. In contrast, negative correlation is observed for normal and shear forces per contact in Figs. 5.14b and d. This is mainly because there are more contacts acting on a particle for higher particle aspect ratio. The feature indicates that overall, each contact needs to carry higher load (both normal and shear) for spherical particles than ellipsoidal particles, which is consistent with the force chain network in Fig. 5.12. Further, it is noticed that the reduction rate of the force per contact reduces and becomes very small when the aspect ratio varies from 3.75:1 to 5:1.

Fig. 5.15 shows the probability distribution of magnitudes of normal contact force and shear contact force for the assemblies with particles of different shapes. Similar studies have been conducted on spherical shaped granular flow through shear cell in different contexts [9, 18, 185, 186]. In all the referred cases, one common characteristic has been observed: all the

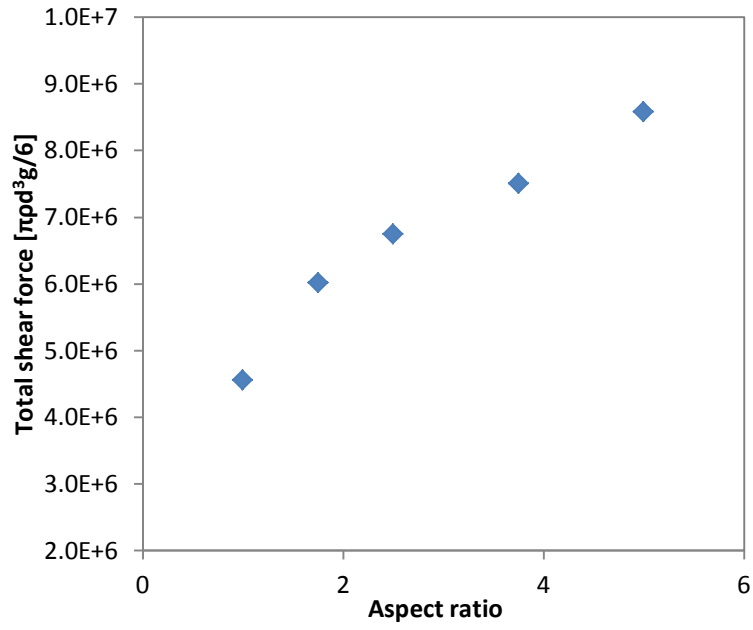
distributions show variation in low probability tail at the higher range of forces. This highlights that the effect of different characteristics of particles and/or flow conditions are indicated at the farthest end of probability function.



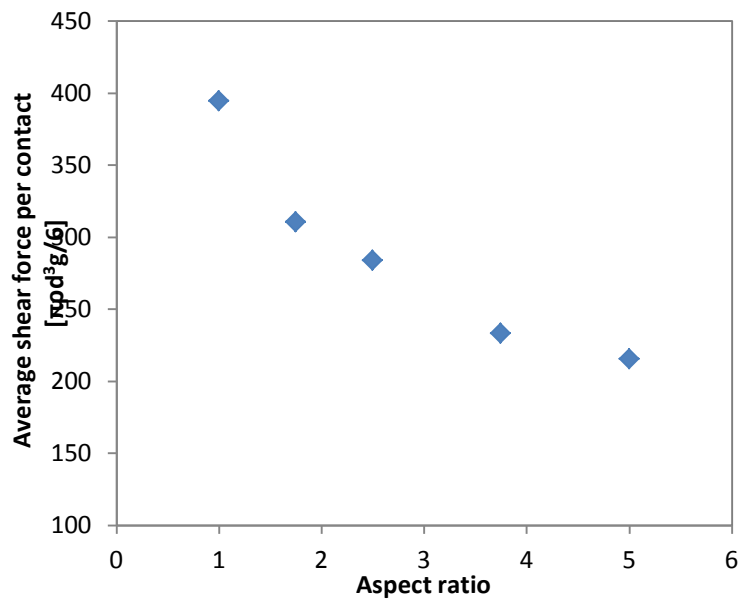
(a)



(b)



(c)



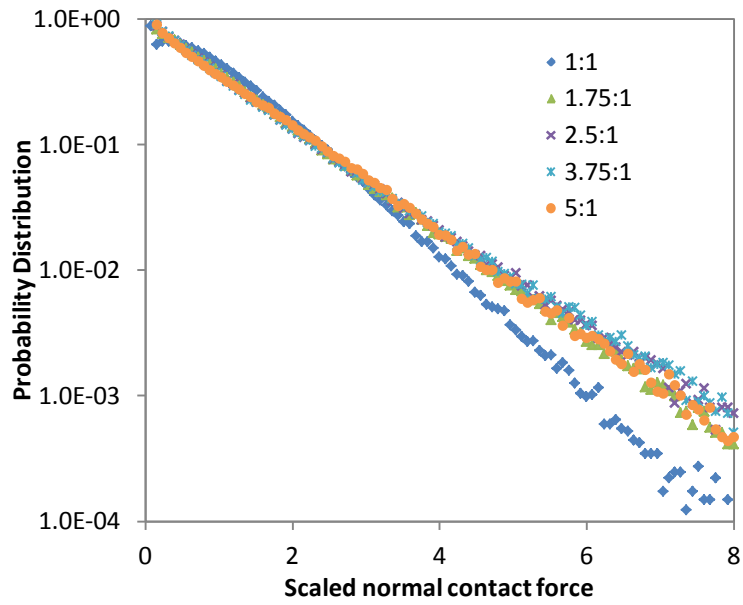
(d)

Fig. 5.14: Correlation of aspect ratio with a) total normal force of assembly, b) average normal force per contact, c) total shear force of assembly and d) average shear force per contact (unit:  $\pi\rho d^3 g/6$ ).

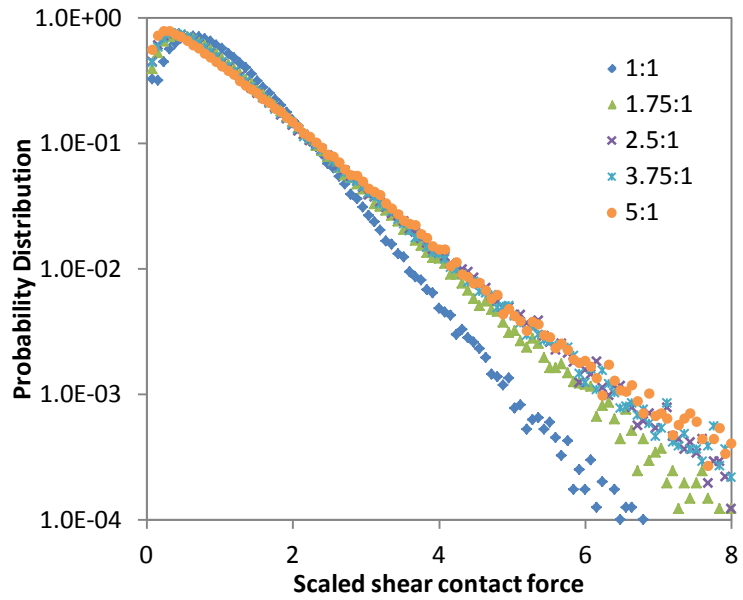
Similar trends were found in the present study of the flow of ellipsoidal particles. It can be seen from Fig. 5.15 that the forces decay exponentially. The dependence of particle forces on particle aspect ratio near the mean value is not significant. However, away from the mean value of force magnitude, the effect of particle shape emerges as the distributions start to spread and at a much higher range of magnitude, the decay of the distribution function clearly increases when the particle aspect ratio increases. Compared to elongated particles, the distribution of particle forces at a higher magnitude range is more heterogeneous for spherical particles. The higher variation of magnitude also is consistent with the force variation observed in the spatial distribution at the microdynamic level in Fig. 5.12.

It is interesting to note a distinguishing feature, specifically that the magnitude variation of probability is much higher for spherical particles than ellipsoidal particles. As for normal force in Fig. 5.15a, there is clear difference among the ellipsoidal particles with different aspect ratios with a clear trend of reduction of fluctuation with increased elongation. For shear force in Fig. 5.15b, however, the trend is less clear. Nevertheless, it follows similar relationship with aspect ratio as such that there is a loose relationship with aspect ratio. It is exhibited through lowering of the tail with increase of aspect ratio. Again, it is consistent with force variation at the microdynamic level as seen in the spatial distribution in Fig. 5.12. A qualitatively similar observation was found in the numerical study of capsule-shaped particles in [76] for probability distribution of both normal and tangential forces. In their work, Azema and Radjai [76] demonstrated how the shape function affects the probability distribution tail of elongated capsule-shaped particles. They came to the conclusion that the more elongated a particle, the higher the exponential tail of the probability distribution of force rises which shows inverse effect.





(a)



(b)

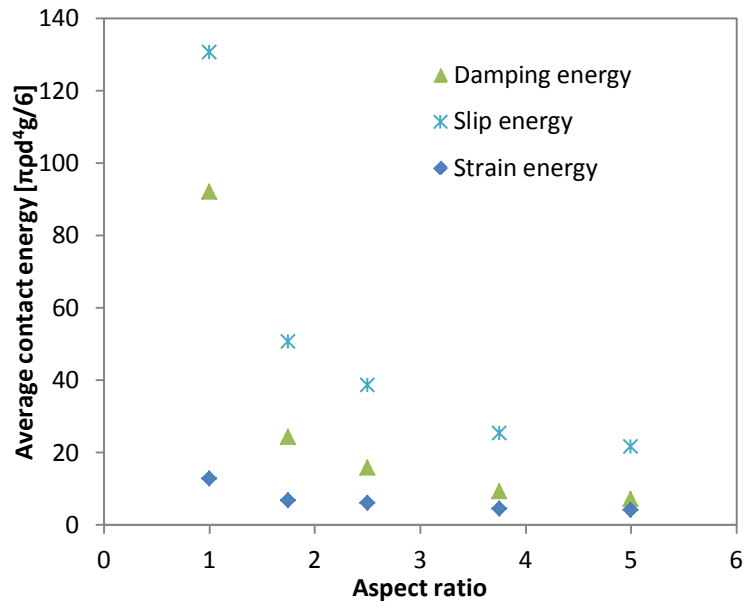
Fig. 5.15: Probability distribution of a) normal force and b) shear force (unit:  $\pi\rho d^3g/6$ ).

Even though, it is lower than slipping shear force (when,  $F_s = \mu F_n$ ), it still has a reasonable impact on the PDF as we find from comparing the figure.

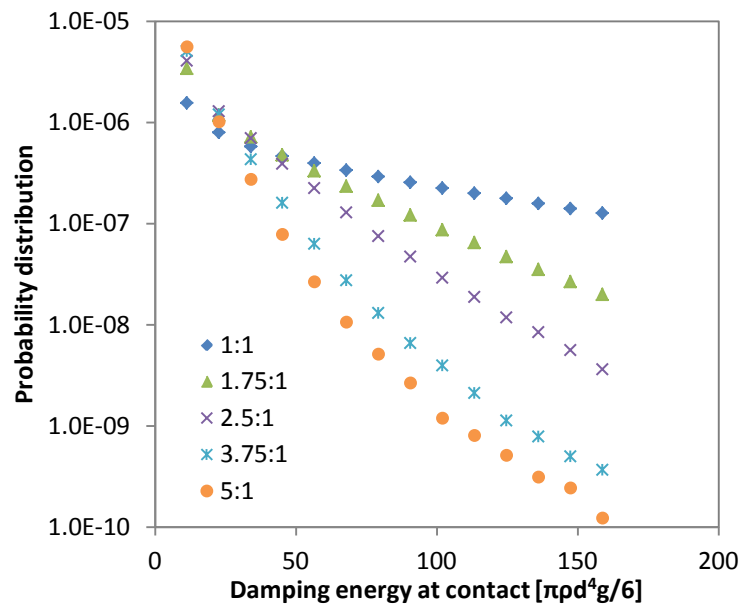
### 5.3.5. Energy Analysis

For each contact in granular rheology, three types of energy, i.e., strain, slip and damping energies, are dissipated or stored in dynamic activities. In the spring-dashpot model, strain, slip and damping energies are defined as the total energies stored in springs, dissipated by frictional sliding and dissipated by dashpots, respectively [2]. Fig. 5.16a shows the time-averaged overall energies for different cases and implies that particle shape has a strong influence on slip and damping energies. There are high energies dissipated for spherical particle assembly. A sharp reduction in slip and damping energies is observed with the increase of particle aspect ratio, and then the reduction becomes small gradually. The strain energy is small compared with the other two energies. Similar to slip and damping energies, it decreases with particle aspect ratio, eventually becoming independent of particle elongation.

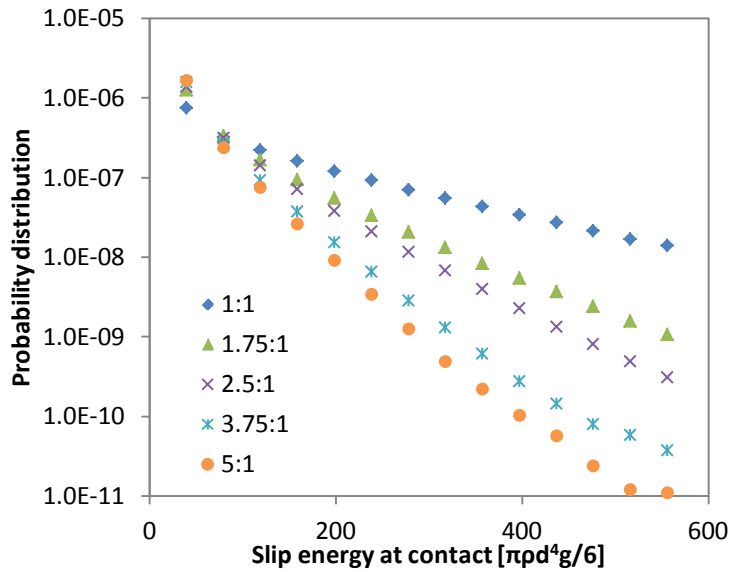
The probability distributions of damping and slip energies were examined, as shown in Fig. 5.16b and c. It can be found that in the probability distributions of the energies, there is clear evidence of the impact of particle elongation. Near the energies' lower range, the deviations of damping and slip energies are higher when the particles are elongated while at the higher range of energy, there are more contacts with higher energies for spherical particles than elongated particles. The elevation of the 'tail' of the probability distribution graph shows an explicit relationship between the statistical distribution of the energies and particle aspect ratio, whereby as the particles become more elongated, the probability distribution tail becomes lower. It means that there is a decrease in the overall deviation of energy from the mean value when the aspect ratio increases.



(a)



(b)

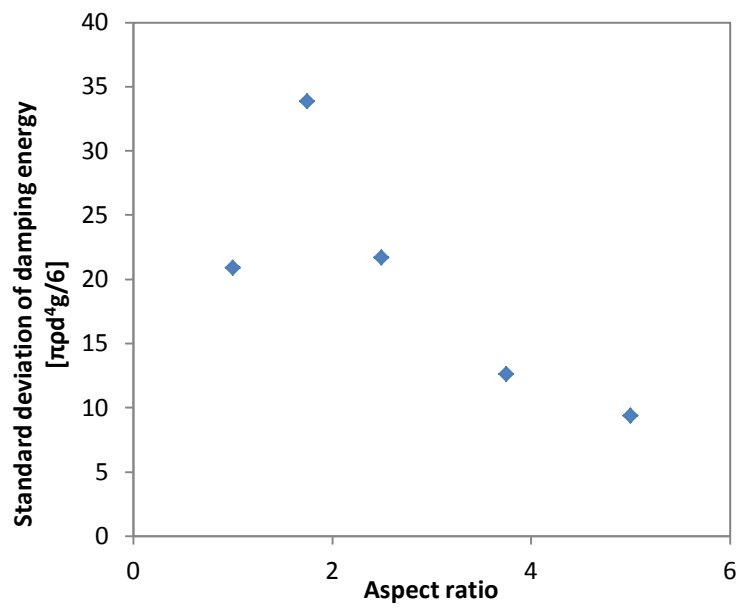


(c)

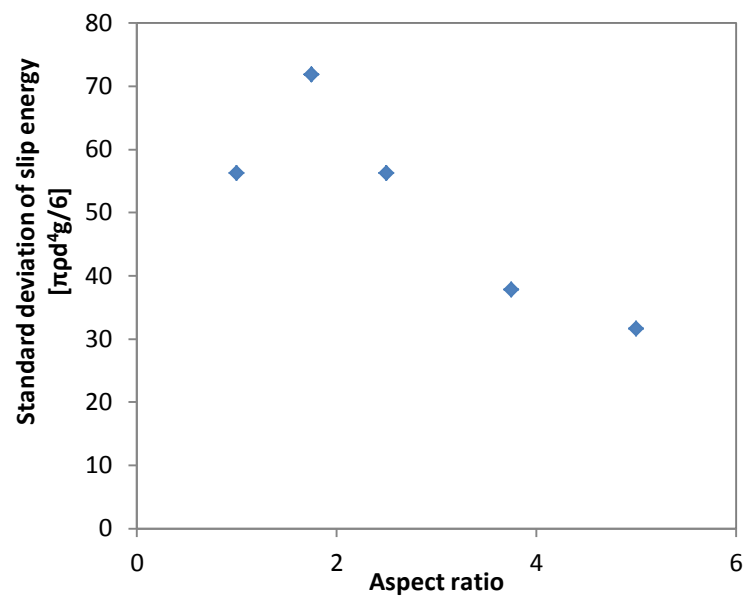
Fig. 5.16: Gradient profile for average scaled a) dashpot energy per contact, b) slip energy per contact and c) strain energy per contact, d) relationship between average scaled contact energies and particle aspect ratio (unit:  $\pi\rho d^4 g/6$ ).

Furthermore, the fluctuation of the energies was investigated. Slip and damping energies were focused on as they are much larger than strain energy. Fig. 5.17 illustrates the standard deviation of the slip and damping energies for different particle aspect ratios. Comparison in the values of the standard deviation for the two energies indicates that the slip energy has higher fluctuation than damping energy. For both energies, standard deviation increases and then reduces when an increase in particle aspect ratio occurs. The trend is opposite to that for porosity where the porosity decreases and then increases when aspect ratio increases as shown in Fig. 5.11, suggesting that the energy fluctuation and porosity are related. Our study implies that particle preferential alignment may be responsible for the trends of energy fluctuation and porosity. If we compare particle orientation for assemblies with ellipsoidal particles of AR 2.5:1 and 5:1 from fig. 5.2, we can see that particles are much less aligned with AR 2.5:1. We further observe that the less elongated particle assembly (AR2.5:1) has

the ability to accommodate squeezed in constituent particles between the gap which is not possible for particles of AR5:1.



(a)



(b)

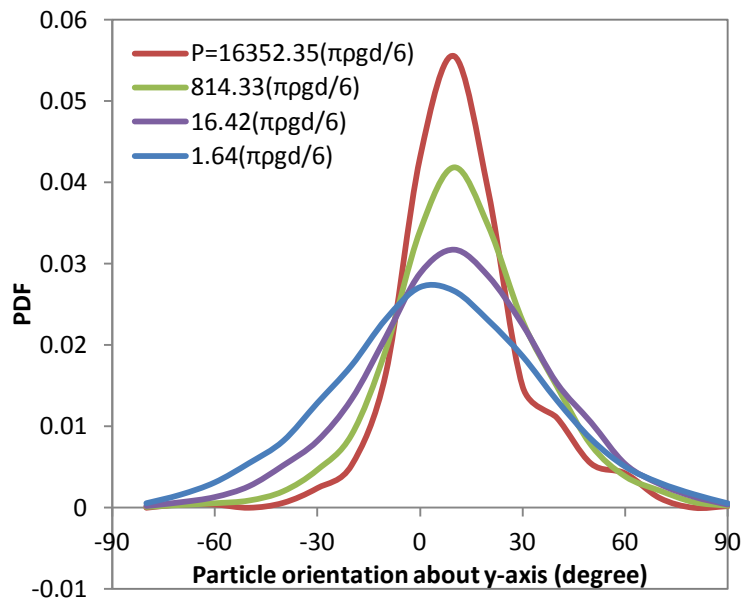
Fig. 5. 17: Overall fluctuation of energy within individual particles (standard deviation) for a) damping energy and b) slip energy (unit:  $\pi\rho d^4 g/6$ ).

As a result, force network is more varied due to varying particle interactions with less elongated particles. Consequently, energy fluctuation is higher. As the constituent particles become more elongated and the particle alignment becomes more uniform, the ability to squeeze in between gaps reduces and the particle interactions become streamlined. Hence, less fluctuation of energy is observed. However, there is a peak in energy fluctuation which is slightly higher than flow of spherical particles. Consistently, there is a dip in the porosity slightly above case of spherical particles. Perhaps it is related to the squeezing phenomenon explained earlier which causes the porosity to drop and energy fluctuation to increase due higher number of contact forces in multiple directions.

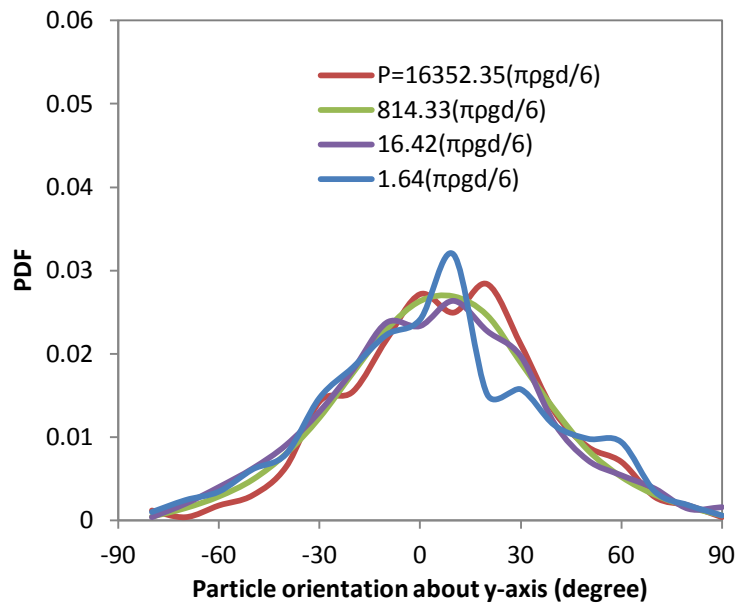
### **5.3.6. Role of particle alignment on volume fraction**

An additional study is undertaken to investigate the possible relationship between particle alignment and volume fraction for ellipsoidal particles.

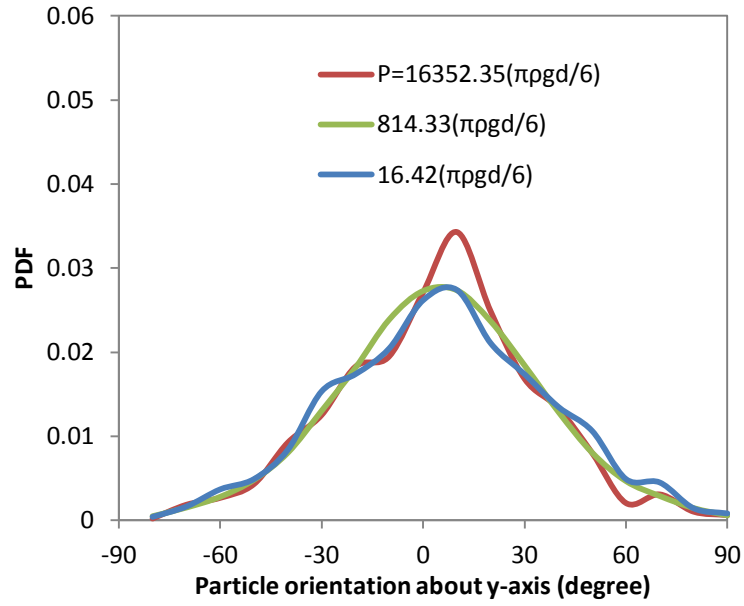
Fig. 5.18 shows the probability distribution of particle orientation angle (between -90 and 90 degree about y-axis) for different applied loads and different shear velocities. The distribution curves for different shear velocities are presented separately to avoid clutter. Regardless of load and shear combination, all curves are found to have a Gaussian nature with their peaks being slightly higher than zero degree angle. It physically means that more particles are aligned in the direction of flow which causes the rotation angle of the particles around y-axis to be almost zero. This finding agrees with results of the experiment mentioned earlier [162] as well as numerical analyses [66].



(a)



(b)



(c)

Fig. 5.18: Probability distribution of particle orientation angle about y-axis for particle assembly subjected to different loads at shear rates a)  $1.07\sqrt{gd}$ , b)  $4.02\sqrt{gd}$  and c)  $12.8\sqrt{gd}$ .

However, more interesting to note here is that at low shear velocity ( $1.07\sqrt{gd}$ ) as shown in Fig. 5.18a, applied load variation has a very clear effect on the particle alignment statistics. When particle assembly is subjected to high applied load, more particles are aligned towards the flow. However, as the applied load is reduced for the same shear velocity, the tendency of particles to undergo preferential alignment in the flow direction reduces. The reduction follows a systematic gradual trend.

On the other hand, variation of load on particle assembly subjected to higher shear has a less noticeable effect on particle preferential alignment. Firstly, the overall probability of particle preferential alignment reduces. Then the variation of load demonstrates an insignificant effect on the peak of the curves. Extensive observation of the intrinsic structure of particle assembly shows that a combination of applied load and induced shear yields a strong influence on the assembly's porosity. Porosity is greater for higher shear velocity as shear force contributes to the constant stress that the upper platen is required to maintain. Therefore, particles are more relaxed in order to obtain alignment away from parallel to flow



direction. In contrast to this, at low shear, porosity reduces when the applied load increases in a systematic manner. (A similar observation is found for spherical particles [13].) As a result, particles are less able to escape from the preferential alignment position during flow.

Since particle preferential alignment is such a significant phenomenon for non-spherical granular rheology, the relationship between particle alignment and porosity, which is another crucial parameter in granular rheology, requires a deeper consideration. Figure 5.19 shows the relationship between time-averaged particle orientation angle about the y-axis and time-averaged overall assembly volume fraction at different combinations of applied load and induced shearing velocity. We find there is a similarity between the relationship between kinetically scaled load (which is a function of shear rate) and volume fraction [8, 9]. Here the data collapse in the correlation curves below the assembly volume fraction, which is similar to the volume fraction at which granular rheology transits between the inertial and intermediate regimes. Thus any variation of shearing velocity does not affect the relationship between particle alignment and volume fraction. Despite this, above the key volume fraction the effect of shear velocity variation becomes apparent as the particle orientation angle drastically reduces at higher volume fraction in contrast to the orientation angle at higher shear velocity.

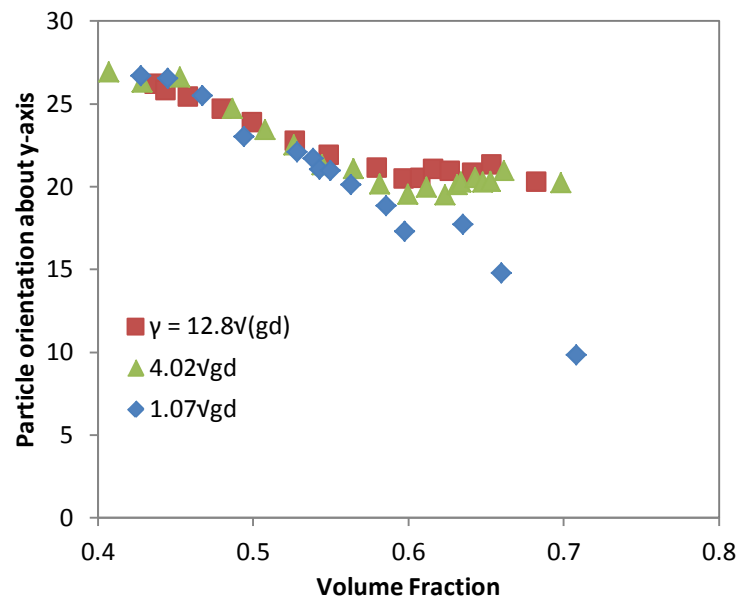


Fig. 5.19: Relationship between particle orientation angle and volume fraction for different combinations of externally applied load and induced shear velocity.

This is a remarkable and novel finding since we have identified the unreliability or usefulness of the coordination number and volume fraction relationship, in order to identify regime transition in a broader non-spherical context. It is in line with the observation of statistical distribution of orientation angle observed earlier, making it possible for the physical interpretation on porosity and particle alignment presented earlier to be further strengthened. This is a new approach in light of regime transition and motivates further research.

## 5.4. CONCLUSION

This chapter identified the effect of particle elongation on granular rheology by investigating flow in a shear cell. Microdynamic analysis of granular flow was conducted for spherical and elongated ellipsoidal particles.

- An examination of particle orientation reveals that the more elongated the particles, the more they tend to orient themselves towards the shear direction. This is a significant feature of non-spherical particles in that it dictates their flow behaviours which were observed in the investigation of some of the key variables. Furthermore, the distribution of particle alignment about Euler angles is relatively uniform and does not vary much with particle shape variation when the aspect ratio is small. However, at higher aspect ratios, the particle alignment distributes nearly symmetrically about a line slightly tilting to the radial line at  $0\circ$ . These findings are similar to those obtained in earlier research work on spherical particles and non-spherical particles of other shapes.
- In the study of velocity distribution, particle elongation does not significantly affect flow velocity gradient at the steady state condition. The probability distribution of particle velocity at the microdynamic level slightly varies with particle elongation, such that peak at the mean value increases as the aspect ratio of ellipsoidal particle increases. However, the fluctuation of linear velocity is strongly affected by particle elongation. It decreases when an increase in particle aspect ratio occurs. Another property affected by particle elongation is angular velocity. As the particle aspect ratio becomes higher, the rotations of particles are more restricted at the microdynamic level causing angular velocity to reduce. Therefore, similar to linear velocity fluctuation, angular velocity

also shows a clear negative relationship with aspect ratio. For the same reason, angular velocity dispersion in spherical assembly occurs at a much wider range compared to ellipsoidal particles.

- Analysis of spatial distribution of porosity shows that the signature gradient of porosity from the shear cell's central region towards the boundaries becomes less prominent as the particle elongation increases. This is further confirmed quantitatively, based on the observation of probability distribution where there is a gradually reducing peak as assembly constituents become elongated. This is because porosity becomes gradually spatially and uniformly distributed throughout the flow region. This characteristic evolves as porosity increases with particle elongation, which is due to increased contact surface area enhancing the dilatancy effect.
- Variation of angular velocity and fluctuation of linear velocity strongly link to the distribution of inter-particle forces. While restricted ellipsoidal particle rotation damps particle momentum, the spherical particle enjoys the freedom to attain higher granular temperature from unrestricted rotation resulting in higher particle momentum, and consequently, force. However, adjacent to the boundary, spherical particles are more likely to be locked in the roughness groove of the platen than ellipsoidal particles; this is manifested in the jag at the boundary found in the force profile. Overall total particle force falls sharply near the spherical side which gradually becomes nearly constant for more elongated particles' assemblies.
- When taking a microdynamic look at the flow, force chain network helps to explain the observations on the flow properties of spherical and ellipsoidal particles. For spherical particles there are relatively less uniformly distributed contact networks with large forces being sparsely spread out. As a result, the average contact force is high. On the other hand, in the context of the most elongated particles considered, the contact network is very dense, uniform and tightly knit with weak force chains. Hence, the average contact force is low. Nevertheless, the tightly knit network achieves its best uniform distribution beyond which even though contact number increases, the uniformity of force distribution does not change. As a result we find the much less impact of particle aspect ratio on flow properties such as velocity fluctuation and angular velocity. Particle velocity fluctuation and angular velocity only increases to a level before they stop varying with an increase of particle aspect ratio.

- From a general perspective both total normal and shear force indicate a steady rise while there is a reduction in both types of forces per contact with an increase of particle elongation. This becomes less effective of aspect ratio for more elongated particles. In the statistic study of normal and shear force, normal contact force does not show a clearly different probability distribution for non-spherical particles with different shapes, yet for shear force we find a distribution similar to particle force. The reduced influence of shear force for high aspect ratios is thus evident, suggesting that the influence of particle elongation is stronger on shear contact force than normal force.
- When three types of energies, i.e., strain, slip and damping energies, are observed at the macro scale, it is found in terms of magnitude that strain energy is the least affected, followed by damping energy and finally slip energy which is the most impacted. Probability distribution of damping and slip energies show a very clear effect of particle elongation similar to what was found for angular velocity, thus reflecting how the properties are connected to each other.
- Finally, a new preliminary approach is tested where a relationship between particle orientation angle and volume fraction is obtained for various sets of externally applied pressure and induced shear velocity. A novel finding achieved indicating a collapse of data for the correlation curves below a volume fraction is similar to that of regime transition to an inertial one. No effect of variation of shear rate on particle preferential alignment below this volume fraction is suggested here. A study of probability distribution shows there is a systematic graduation of an increase in the orientation angle's peak at a near zero degree value in polar direction, which is not so profound at higher shear velocity. A physical interpretation is drawn from understanding how porosity works: at a higher shear rate, the overall volume fraction is high even at higher load providing more room for constituent particles to be further away from preferential alignment position. Meanwhile at lower shear rate, the overall volume fraction systematically increases when pressure also rises as expected, reducing the particles' ability to not require preferred alignment. This new finding inspires research into regime transition for non-spherical particles using a whole new approach. It had not been considered earlier for spherical particles because of their isotropic shape. More work is proposed.

# **Chapter 6: Macrodynamic analysis of granular rheology for Ellipsoidal and Spherical Particle Assemblies in a Model Annular Shear Cell**

## **OVERVIEW**

A comparative investigation is performed from the macrodynamic perspective between granular rheology of spherical particle assembly and that of ellipsoidal particle assembly of 2.5:1 aspect ratio in a similar flow condition. Here, stress-controlled flow condition is applied using DEM on specimen particle assemblies flowing through double-shear annular shear cell to obtain data for the study of velocity, normal and shear forces, and stress tensors. Further, the effect of aspect ratio on these properties is observed using varying elongated ellipsoidal particles. Here we find velocity and stress tensors are uniform across the flow in y-direction (perpendicular to both the direction of applied load and shear) regardless of particle shape. A linear relationship between normal and shear stress exists for external loads as well as internal particulate forces. However, ellipsoidal particles indicate a higher slope than spherical ones, thus suggesting higher friction. Aspect ratio has a strong effect on macrodynamic values of shear stress tensor, shear-normal stress ratio, particle friction coefficient and inertia number. We found a similar positive relationship between inertia number and assembly friction coefficient for spherical particles but such an effect was not seen for ellipsoidal particles.

## 6.1. INTRODUCTION

Granular rheology is concerned with flow dynamics of particles that are neither small enough like molecules of water or gas, nor large enough to be considered as solid bodies. It is an essential field of study because it includes vast materials and phenomena both in natural events and industrial activities. Non-spherical particle assembly is important in granular rheology because of its relevance to practical applications. Yet it is a complex subject because of the infinite possibilities of the shape that any existing particles can have. Also with the shape, dynamics of particles changes which makes it very difficult to develop a general constitutive numerical model that can describe granular flow dynamics well.

Macrodynamic approach to study granular rheology involves study of dynamic properties like velocity, internal stress and external stress from walls. The importance of this study is that it allows to obtain data from experiment more easily than in case of microdynamic approach. Then numerical analysis using methods such as discrete element methods, one can obtain further internal macrodynamic properties of granular flow. This approach is utilized to develop constitutive relations using predicted velocity and stresses [27, 187] following kinetic theory. In this approach averaging method is applied to understand flow mechanism of granular particles. Extensive work is done on averaging method (eg. [24, 45]) to the benefit of applying it in macrodynamic studies of granular flow behavior. Macrodynamic investigation has been performed in multiple applications. Chou et. al. studied dynamic properties of granular particles in a rotating drum [188] where they showed effect of interstitial medium on spherical particles rotating at varying speed and how dynamic properties are affected by viscosity of interstitial medium. Zhu et. al. investigated dynamic flow behaviour of granular particles through hopper using macrodynamic approach [189] where they observed spherical particles in order obtain data for time-averaged spatial distribution of velocity, mass density and internal stresses. Wang et. al. observed flow properties through shear cell for macrodynamic properties like velocity and stress tensors [14] under varying external conditions for spherical particles. Similarly, many more work has been done from macrodynamic approach (eg.[190-192]). In all the cases it is noticeable, that all these works involve spherical particles only. Macrodynamic studies have not been found much for non-spherical particles which actually is more relevant to practical applications.

In our study, we use ellipsoidal particle assembly to do the macrodynamic analysis where we: firstly, compare the properties of spherical and ellipsoidal particles in granular flow; and secondly, show the effects of particle elongation on various variables. These include velocity, porosity, normal and shear stress, inertia number and particle friction coefficient. The reason why we choose this shape is that we find it closest to spherical particles, thus enlightening us on spherical to non-spherical particulate flow dynamics relatively easily. This will add value to developing a general constitutive model.

## **6.2. SIMULATION METHOD AND CONDITIONS**

We use the numerical model developed by Hertz-Mindlin and Deresiewicz to simulate granular flow through a rectangular segment of annular shear cell. We use the commercial software Particle Flow Code as a virtual platform for our numerical analysis. Details of the numerical method can be found in our earlier chapters 3, 4 and 5 and in [30]. At first we create a rectangular domain space with the dimensions  $12d \times 30d \times h$  where 'd' is the diameter of particles and place the lower platen above the bottom plane of the space. We place the upper platen at an arbitrary height initially. We make these platens using monodispersed spherical particles of 1d diameter. The constituent particles are glued together so that they form one rigid platen devoid of any dynamics. Then, 5000 specimen particles, whether spherical or ellipsoidal, are generated in the confined space between the upper and lower platens and the side walls in a highly dense and compressed state. The walls in the path of direction of flow which is parallel to the x-axis are kept periodic so that particles exiting from one wall will enter at the same position with the same force and velocity vectors from the other wall. Then the simulation is run with a very slow shear velocity in x-direction from the plates in opposite directions. After some time, based on the numerical model, the particles are rearranged and fill up the entire confined space. The slight shear from the platens helps the particles to evenly spread throughout the space. At this stage the model is ready for investigation (this setup is shown in Fig.5.1).

Then, gradually the two platens' shear velocity is increased to induce shear in the specimen particle assembly while the upper platen adjusts its height to put pressure on the specimen particle assembly. In this way, we obtain a stress controlled model through an analysis of annular shear cell. The necessary parametric values are given below for our numerical analysis. It should be noted that we used the intermediate regime of flow here.

Table 6.1: Parameters used in simulation

Property	Value	Unit
Friction coefficient, $\mu$ (particle-particle and particle-wall)	0.3	(-)
Critical damping ratio, D (normal and shear)	0.3	(-)
Young's modulus, $E_y$	$2.5 \times 10^6$	$\pi \rho d g / 6$
Poisson's ratio, $\vartheta$	0.3	(-)
Time-step	0.00001	$\sqrt{(d/g)}$
Normal pressure in (-)ve z direction	1434.75	$\pi \rho d g / 6$
Shear rate	6.5	$\sqrt{(gd)}$
Density (glass bead)	2450	$\text{Kg/m}^3$

In order to create ellipsoidal particles, bubble-pack algorithm is used as discussed in chapter 5.

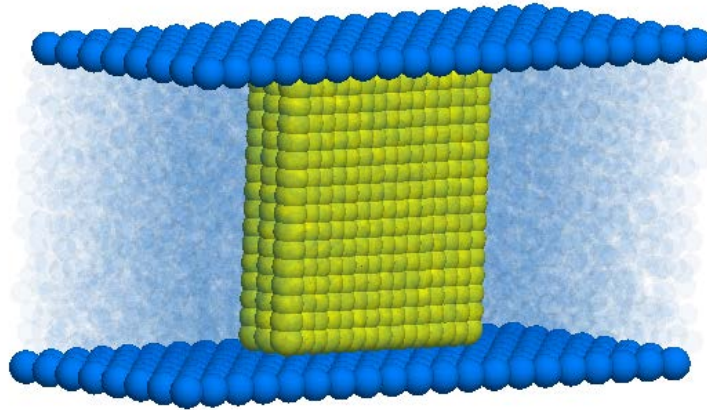


Fig. 6.1: Example of spherical regions to obtain data for stress, density and velocity.

In order to calculate macroscopic property for, say stress, using time-volume averaging method at any point (i,j) of the flow region we used the following formula given in [43]:

$$\mathbf{T}_{xx}(i, j) = -\frac{1}{V} \sum_t \sum_{N_c} \mathbf{F}_{xx} \times \mathbf{L}_{xx} \quad (6.1)$$



where,  $F_{xx}$  is the contact force vector,  $L_{xx}$  is the branch vector in in x direction,  $V$  is the volume of the point considered,  $t$  is the time length from which data collected and  $N_c$  is the number of contacts within the region. The same method is applied for  $T_{yy}$ ,  $T_{zz}$  and  $T_{xz}$ .

Investigation of inertia number is considered in this work. Inertia number is an important parameter to study dynamic effects in granular flow and it shows the relationship between particle inertia and externally applied force. It is given by:  $I = \frac{\dot{\gamma}d}{\sqrt{P/\rho}}$  where, where  $\dot{\gamma}$  is the shear rate,  $d$  the average particle diameter,  $P$  is the pressure and  $\rho$  is the density. Here, we observe inertia number from a local point of view. The following equation is used at any point  $(i,j)$ :

$$I_{(i,j)} = \frac{|\dot{\gamma}_{(i,j)}|d}{\sqrt{P_{(i,j)}/\rho_{p(i,j)}}} \quad (6.1)$$

$$\text{where } P_{(i,j)} = \frac{1}{2} \left| \overline{T_{zz(i,j)}} + \overline{T_{xx(i,j)}} \right| \quad (6.2)$$

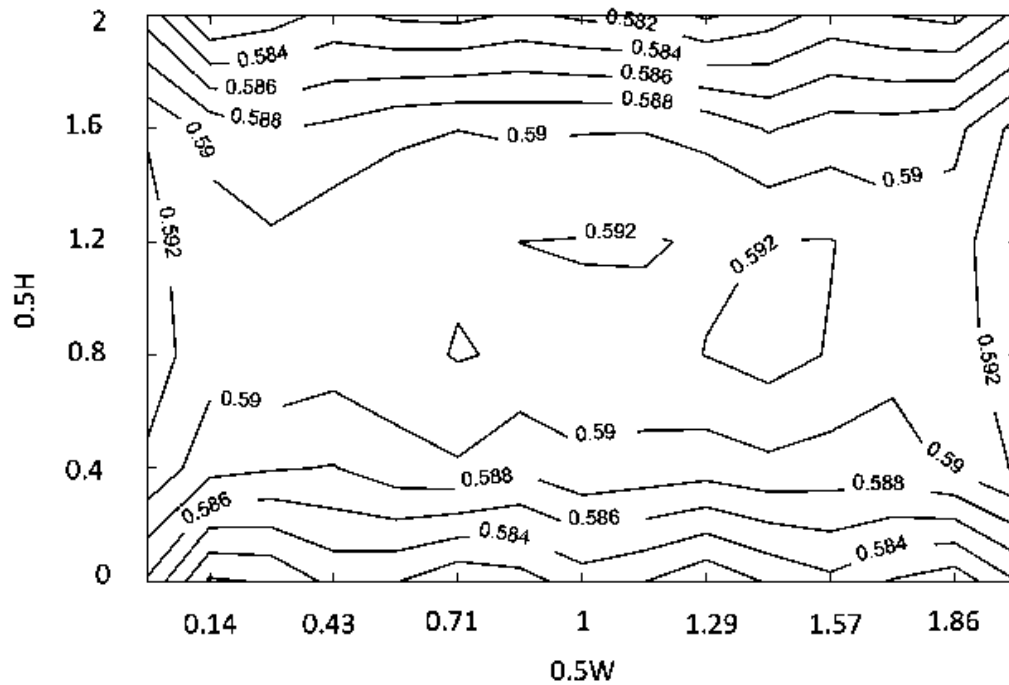
and,  $\dot{\gamma}_{(i,j)}$  is the shear rate at point  $(i,j)$ . We use series of spherical region organised to form a slice within shear cell segment to obtain data for stress, density and velocity as shown in Fig. 6.1.

## 6.3. RESULTS AND DISCUSSION

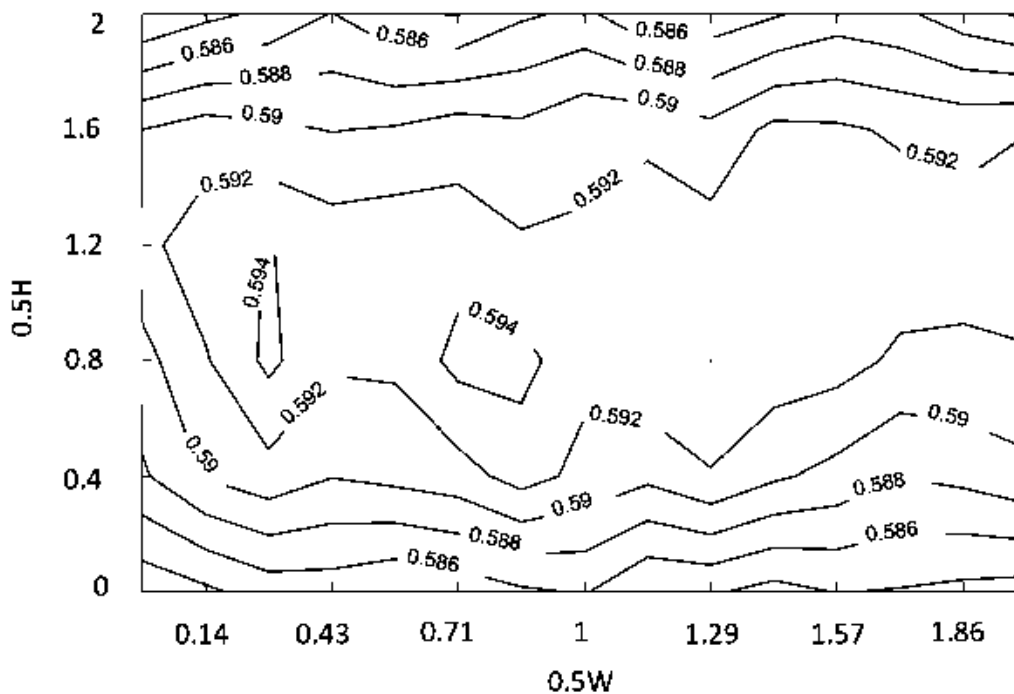
### 6.3.1. Density and Velocity

We start by comparing local density spatial distribution of spherical and ellipsoidal particle assemblies. Here, we use ellipsoidal particles with aspect ratio 2.5:1 as a standard for ellipsoidal particle assembly because of its median value among the range of elongated ellipsoidal particles considered in this work. Only one case of ellipsoidal particle aspect ratio is considered here to highlight the distinguishing comparison between spherical and elongated particles. The cases of different aspect ratios have also been considered and showed similar results. So, the results of these cases are not shown here for the brevity of this thesis Figs. 6.2a and b show the distribution of density across the flow. This figure is obtained by considering symmetrically spaced and equal sized regions to calculate particle density of the flow's particle assembly. We can see that the spatial distribution of flow

density is similar for ellipsoidal and spherical particles. Both show a similar trend: higher density at the central flow region which is the farthest away from the platens. The density of the particles decreases gradually towards the platens with the lowest density adjacent to them.



(a)

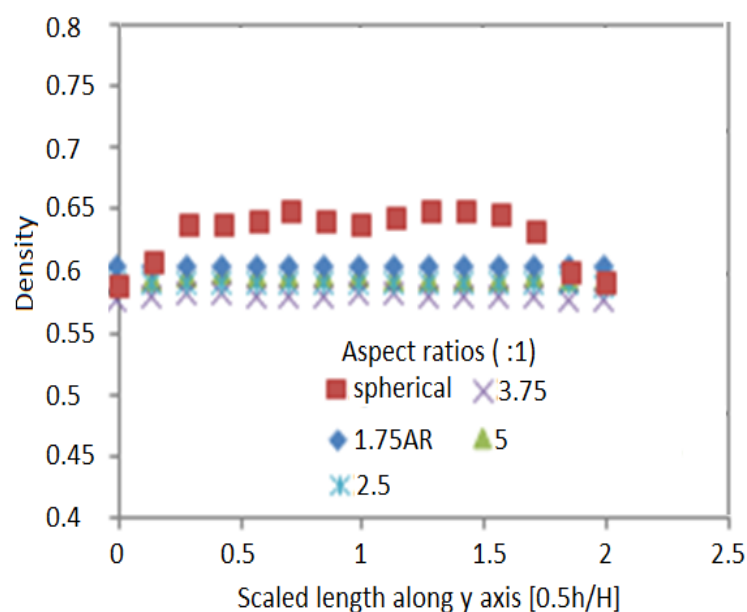


(b)

Fig. 6.2: Contour plot of particle density for a) spherical particle assembly, b) ellipsoidal particle assembly.

This agrees with what has been found for spherical particles in earlier studies [14] and here confirms that it also holds true for elongated ellipsoidal particles. Although the trend is similar, if we look more deeply, we find that the range of density variation is higher for spherical particles compared to that of ellipsoidal particles. In other words, ellipsoidal particles are more uniformly distributed in the confined space of flow relative to spherical particles.

Fig. 6.3a provides a profile of time-spaced averaged density distribution along the y-axis. The length along this axis is scaled as  $0.5W$  where  $W$  is the width of the shear cell segment. The finding here confirms that the uniform distribution of density holds true for ellipsoidal particles of any aspect ratios when compared with spherical particle assembly, revealing larger variation between density of the central region and region near the platens. Fig. 6.3b shows the relationship between time-averaged overall density of particle assembly and aspect ratio. Here, we find there is not much variation in magnitude of overall density as a whole except that density slightly reduces when particle shape changes from sphere to ellipsoid. This happens because particle alignment (discussed in more detail in Chapter 5) causes uniformity of density across the flow region, which also results in reduction of density due to increased friction between layers.



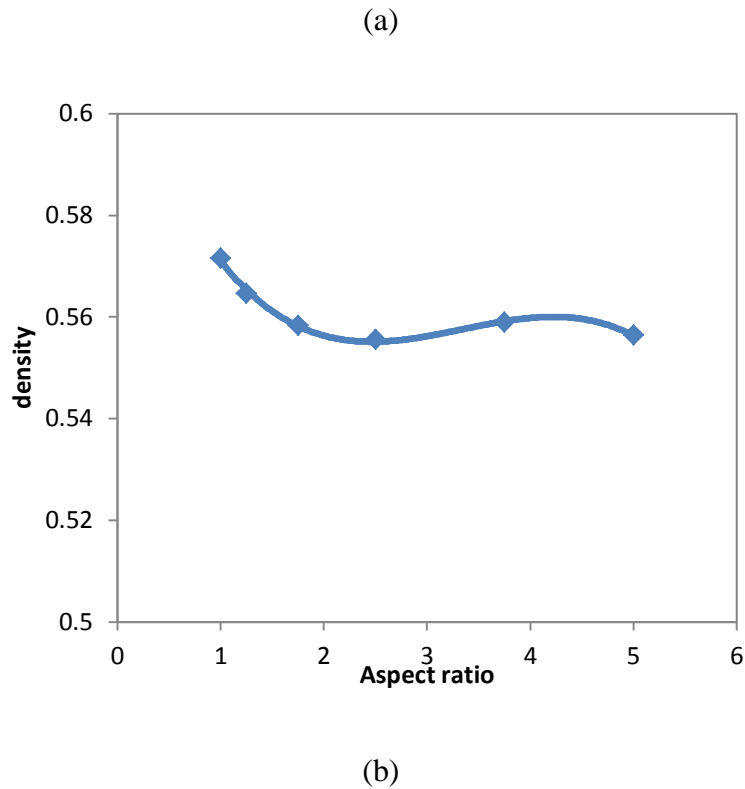
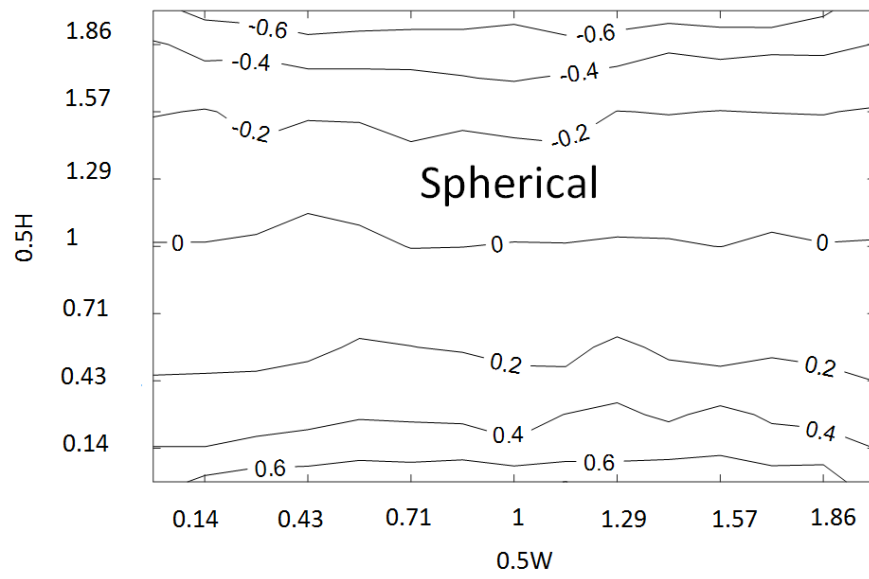
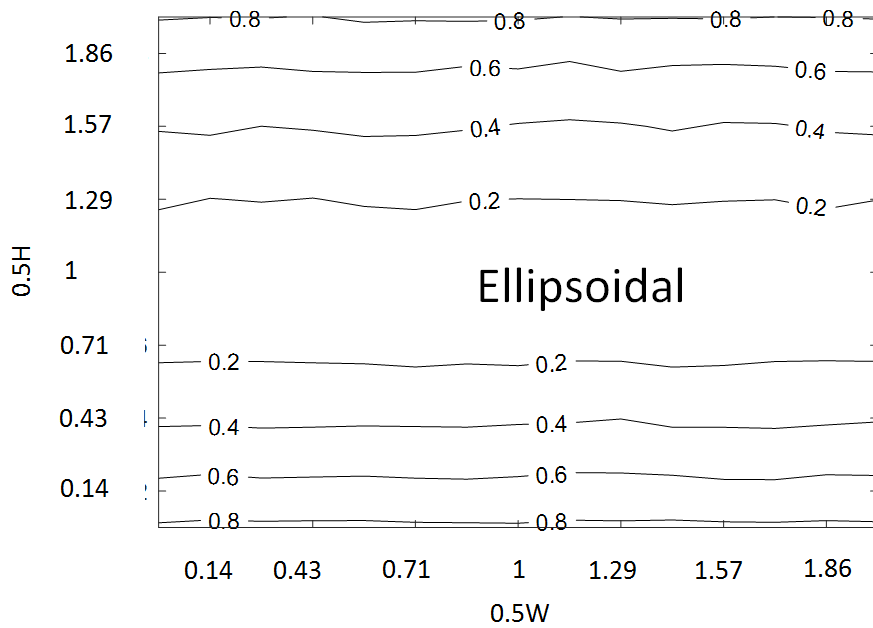


Fig. 6.3: a) variation of macrodynamic value of density across the flow in y axis; b) relationship with density of assembly and particle aspect ratio.

Velocity profiles obtained spherical and ellipsoidal particles are obtained parallel to the yz-plane in Fig. 6.4. Here, the velocity is time-averaged and scaled by the shearing velocity of the upper and lower platens that are moving in opposite directions. We find similarities in how velocity gradually changes across the region, and we also discover similarities in how they have near-zero magnitude at the central region which is furthest away from the shearing platens. The velocity gradually increases as the moving particles get nearer to the shearing platens until it is the highest in magnitude adjacent to the platens. This is quite reasonable because, shear force from the platens transmits velocity to the immediately next particles and those particles transmit it to the next. The friction dissipates the energy and consequently flow velocity reduces. At the center the least amount of force transmitted by the platens can be received by specimen particles. Moreover, these particles obtain near equal and opposite shear force from both platens which tend to neutralize each other. Hence, the particles appear to be stationary.



(a)



(b)

Fig. 6.4: Scaled velocity distribution of a) spherical particle assembly, b) ellipsoidal particle assembly.

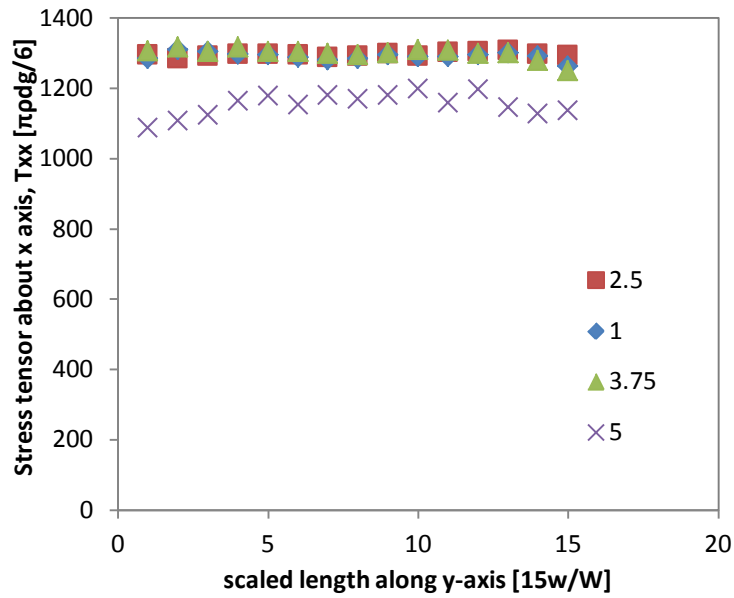
Not much variation is noted across the flow here in the y-direction. However, what is new and interesting to note is that the graduation of force variation in the z-direction for ellipsoidal particle assembly is much finer than that of spherical particles. Because of the particle preferential alignment for elongated particles in the ellipsoidal particle assembly, the transmission of the shear force is much smoother than that of spherical particles. This finding is further strengthened by the observation of macrodynamic observation of velocity fluctuation across the flow in Chapter 5. Here, we find that as the particle aspect ratio increases, the fluctuation of velocity, shown in terms of standard deviation, decreases drastically from spherical to ellipsoidal particle assembly at earlier stages and later becomes stable and constant.

It means that when particles are spherical and there is no possibility of preferential alignment, particles can rotate in any direction at any point of assembly and fluctuation is highest. As a result, the smooth distribution of velocity spatial distribution cannot be obtained. As the particles become elongated, the fluctuation quickly drops until it reaches a minimum fluctuation level, which obviously results in smooth graduation of velocity spatial distribution across the flow.

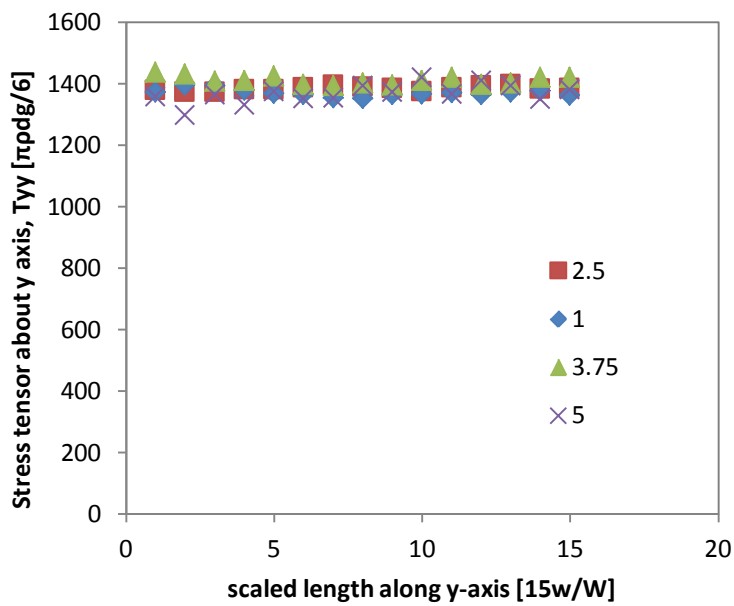
### **6.3.2. Stresses**

Next, we show the effect of particle aspect ratio on global contact stress  $T_{xx}$ ,  $T_{yy}$ ,  $T_{zz}$  and  $T_{xz}$ . Figure 6.5 shows the stress distribution along the y-axis of the flow region. From Fig. 6.6a-c we find that the principal components of stress have no noticeable effect along the y-axis except for the particles with the highest aspect ratio (5:1). There is a slight reduction in magnitude for stress in direction of flow  $T_{xx}$ . Other than that, the distribution is generally uniform and consistent with velocity distribution along the y-axis, where we showed earlier we find there is no noticeable variation of velocity in the y-direction. If we read it in conjunction with Fig. 6.3, we may say that the main impact of particle shape (here, elongation) occurs in the z-direction which is the direction of externally applied load, i.e. load applied by the upper platen. As for shear stress in Fig. 6.2b, we find there is a visible effect of variation of particle elongation, i.e. particle elongation causes shear stress to increase. It is logical because preferential alignment of elongated ellipsoidal particles causes the surface friction between layers to increase. More contacts are needed to be broken for the layers of particles to shear from adjacent ones to produce a particle flow. These are interesting

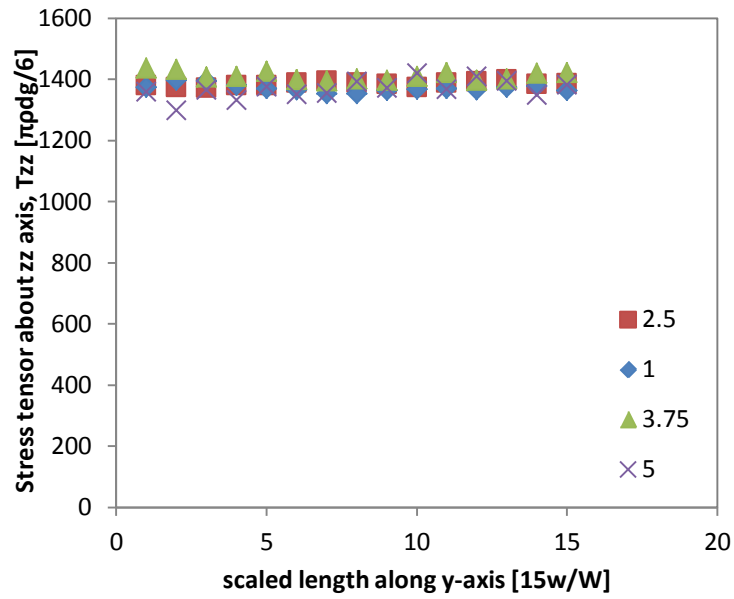
contrasts that need to be addressed for moving from what we know about spherical particle rheology to non-spherical particle rheology.



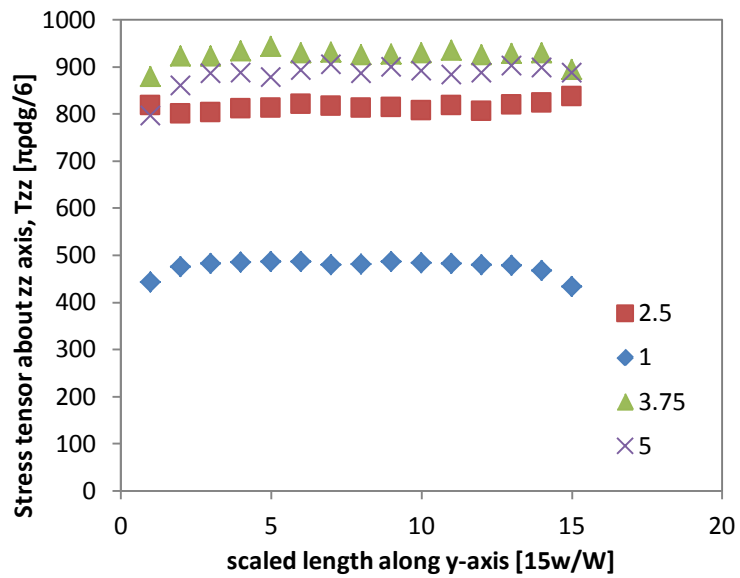
(a)



(b)



(c)



(d)

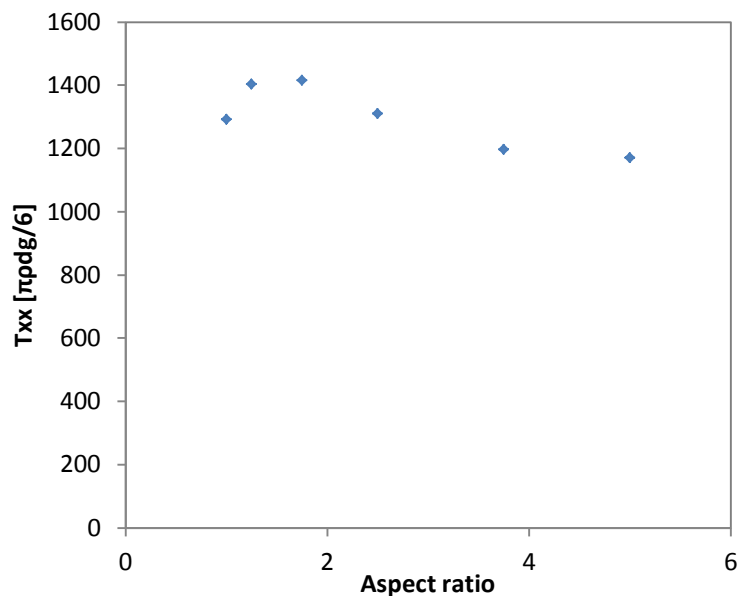
Fig. 6.5: Variation of the magnitude of stress tensor components along the y-axis: (a)  $T_{xx}$ , (b)  $T_{yy}$ , (c)  $T_{zz}$ , and (d)  $T_{xz}$  for particles of four different aspect ratios (spherical, 2.5:1, 3.75:1 and 5:1). Note that different scales are used for stress components.

Effect of particle aspect ratio on time-averaged macrodynamic (overall) magnitude of different global stresses is shown in Fig. 6.6. Here, we have added an additional data for

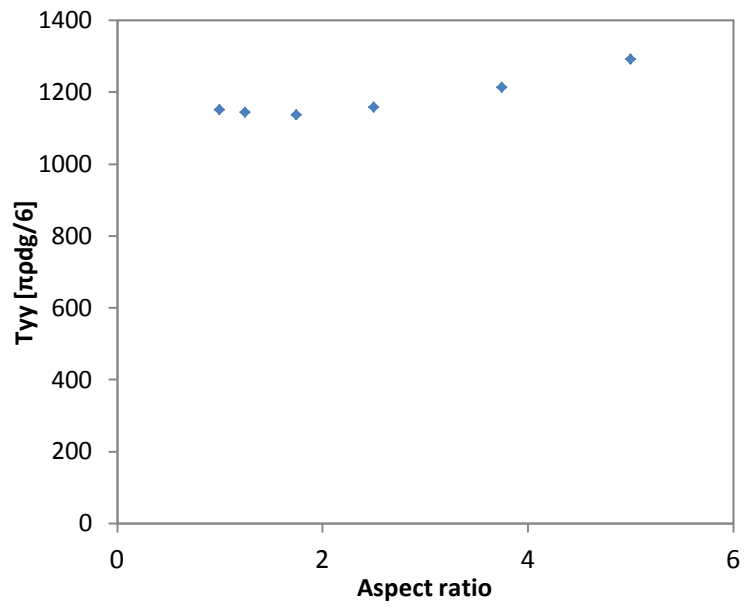


particle aspect ratio 1.25:1 to highlight the transitional effect where particle is elongated from spherical to ellipsoidal shape similar to what has been shown in Fig. 6.3. In Fig. 6.6a-c we find that there is no significant change in principal stresses  $T_{xx}$ ,  $T_{yy}$  and  $T_{zz}$ . There is a slight increase in  $T_{xx}$  in direction of flow at the early stage of increasing elongation which again decreases when particles are further elongated. This is a new finding and considered for further analysis. At this early stage of the investigation, it can be suggested that preferential alignment causes mild variation on how resultant forces are distributed into global component forces in direction of flow. Effect of aspect ratio is much milder in direction parallel to y-axis and z-axis.

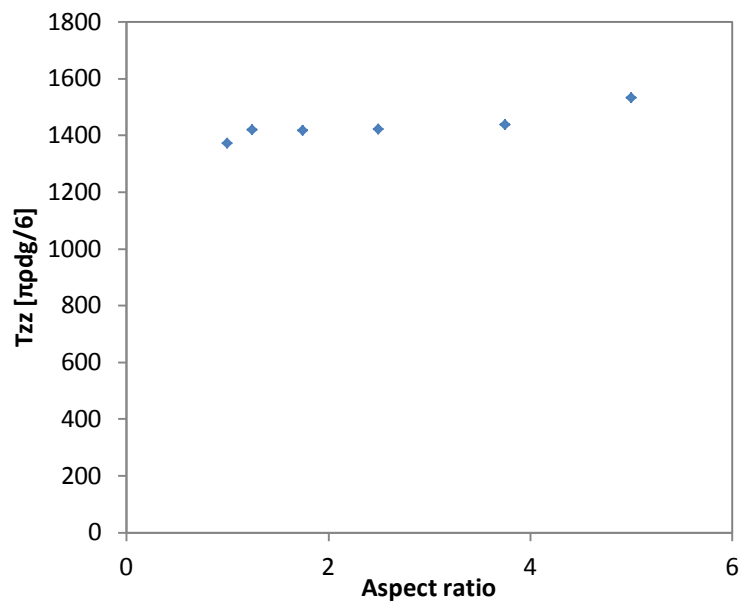
It is understandable because preferential alignment causes the stresses to be uniformly distributed along the length of the particles. So, while the spatial distribution we found earlier is much smoother in the case of ellipsoidal particles' internal stress structure, it does not impact much on the overall magnitude. The exception is a slight increase which is an indirect result of shear stress appearing. In Fig. 6.6d, we find particle elongation (aspect ratio) strongly influences shear stress  $T_{xz}$ . This is consistent with the earlier discussion on shear stress where particles need to overcome larger shear effect due to preferential alignment.



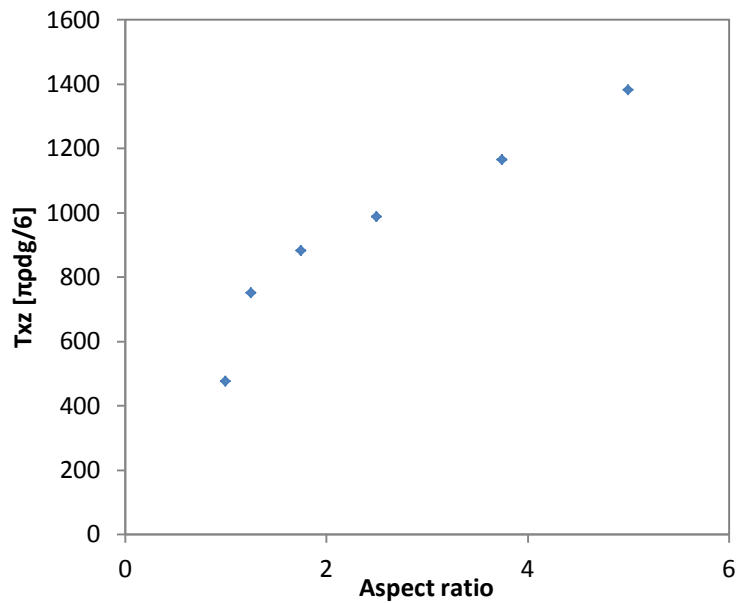
(a)



(b)



(c)



(d)

Fig. 6.6: Effect of particle aspect ratio on a)  $T_{xx}$ , b)  $T_{yy}$ , c)  $T_{zz}$  and  $T_{xz}$ .

Moreover, this figure suggests there is a consistent rise in this shear effect with the particle elongation. At the very early start of elongation there is a jump in shear stress between spherical and ellipsoidal particle of 1.25 aspect ratio because that is where the preferential alignment begins. After that, there is a systematic increase in magnitude of overall  $T_{xz}$  because the longer the particles are, the more contacts occur between layers of flow, consequently, greater force is required to break the force chains.

Next, we discover the ratio of global forces  $T_{xz}$  and  $T_{zz}$  does influence particle elongation on shear effect. Fig. 6.7 shows a linear and positive relationship with particle aspect ratio. Physically it means that the more elongated particles there are, then shear component  $T_{xz}$  will dominate normal component stress  $T_{zz}$  more. This finding is consistent with expectations because preferential alignment results in increased surface area for friction between particles. The particles in shear are somewhat parallel along their major axis and therefore are more likely to be in contact along their largest dimension.

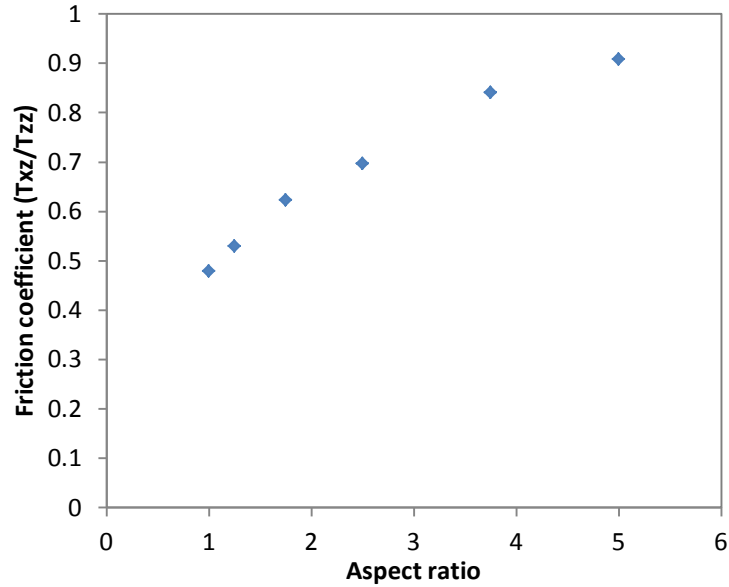
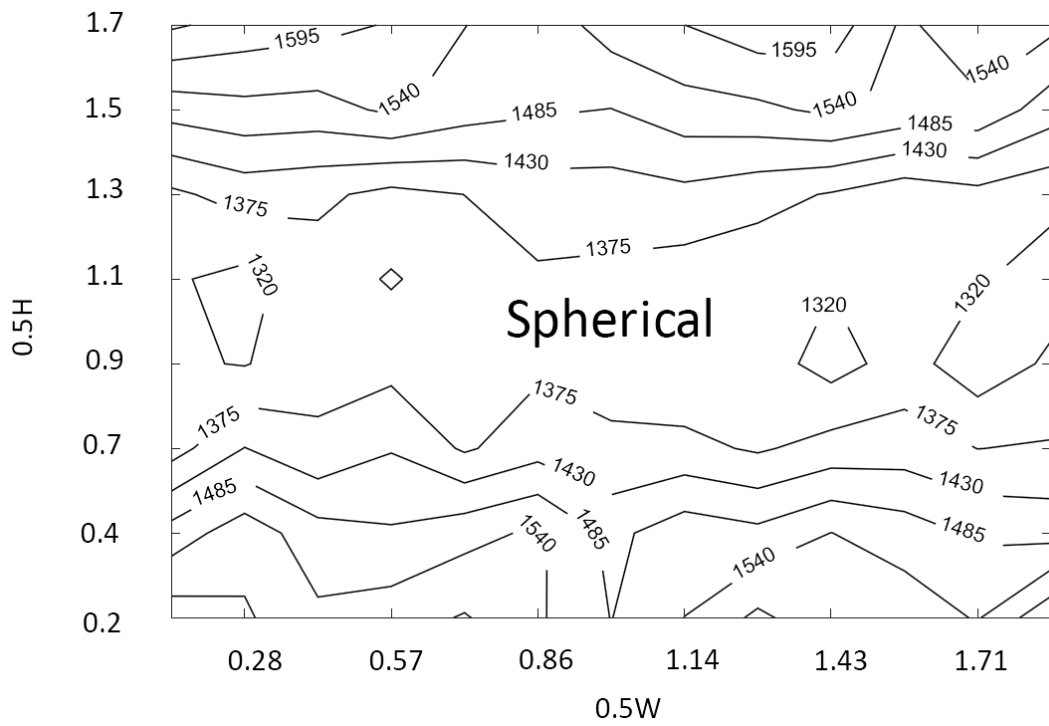


Fig. 6.7: Effect of particle aspect ratio on  $T_{xz}/T_{zz}$ .

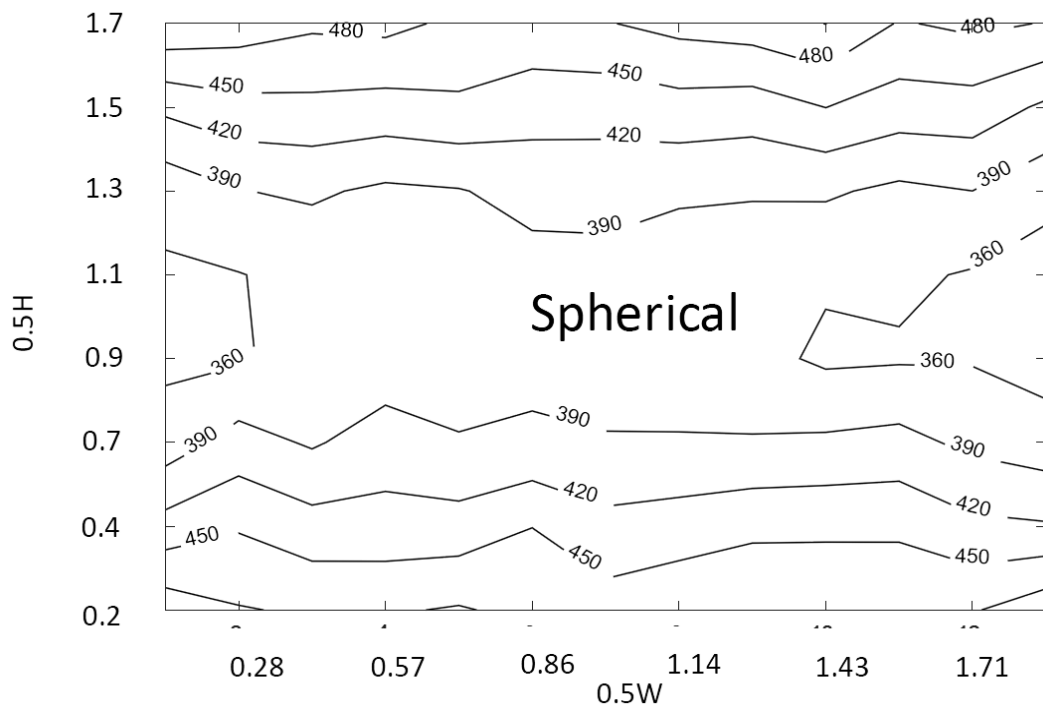
As a result, the longer the particles are the more surface area two adjacent particles are exposed to; consequently, the more likely shear stress will influence the friction coefficient of particle flow. In the next section, we will investigate the phenomenon of friction coefficient in more detail and from more perspectives.

### 6.3.3. Forces

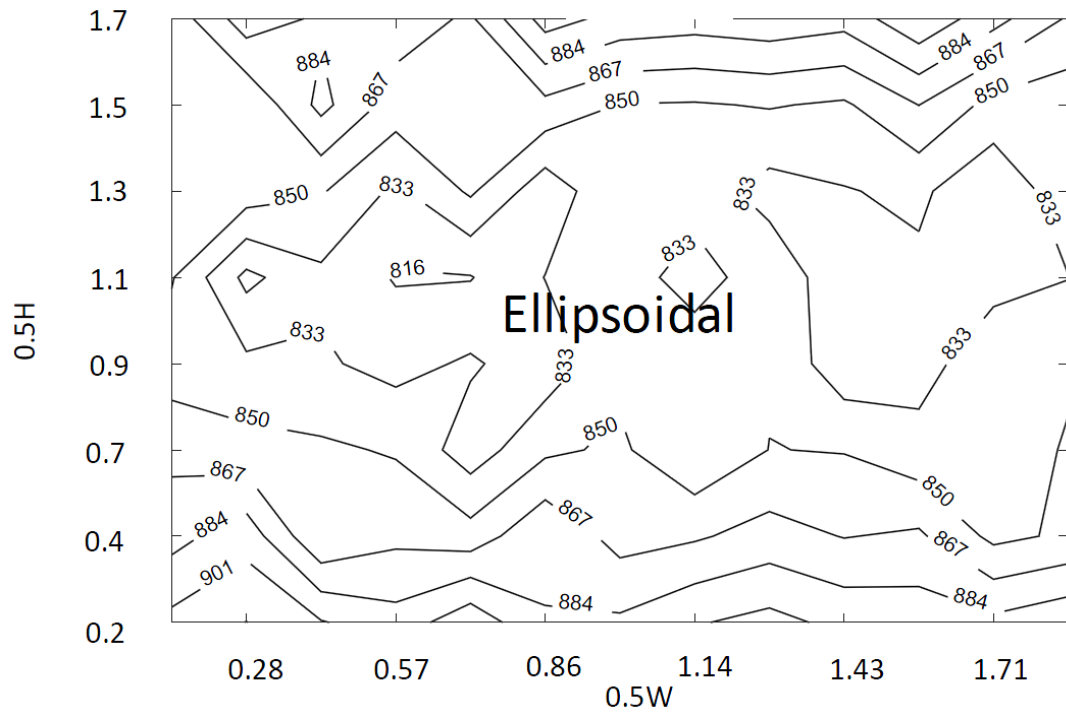
Next, normal and shear forces across the particle flow region are observed in Fig. 6.8. Similar to the earlier observation, here also time-space averaged value parallel to the  $yz$  plane is considered which is perpendicular to the flow. However, here we have considered one layer away from the walls to avoid anomalies that arise from trapped particles near the walls and platens. The first thing to notice is that there is a qualitatively similar pattern of how forces vary: force near the central region is less near the central region for both normal and shear components. Force gradually increases near the platens and the highest for the particles is nearest to the platens. A similar finding can be seen in [14]. We further notice similarities in the trend between spherical and ellipsoidal particle assembly flow region. The main difference, however, originates from magnitude. In case of spherical particles, magnitude of both the normal and shear force is higher compared to that of ellipsoidal particle assembly.



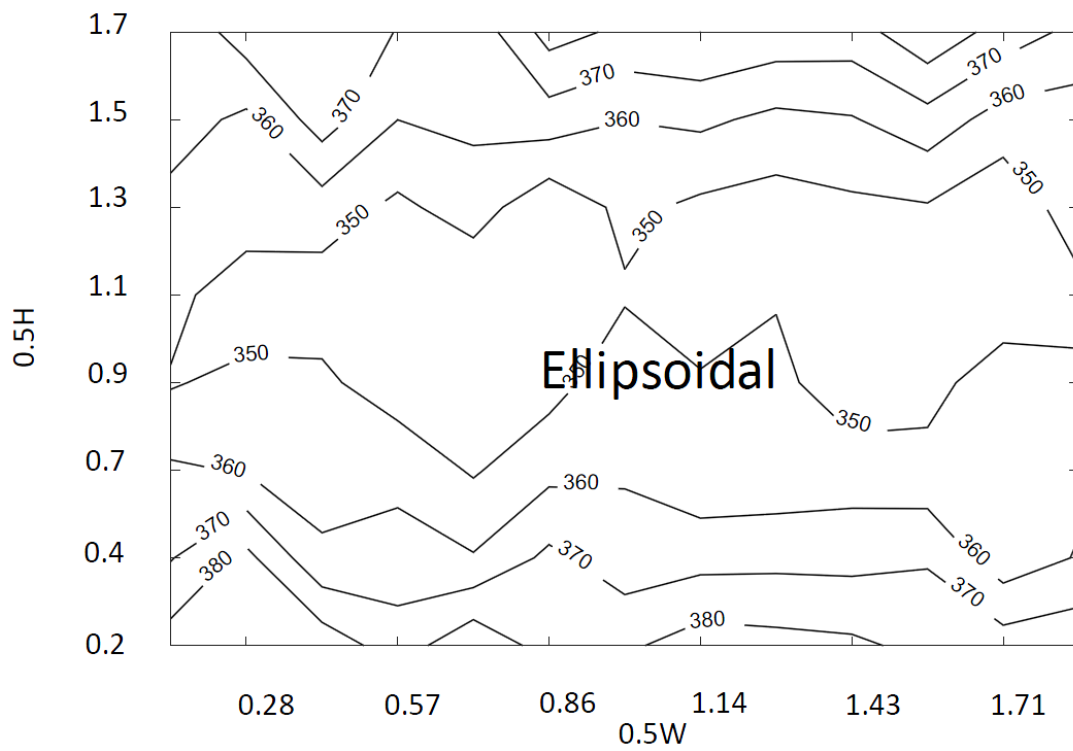
(a)



(b)



(c)



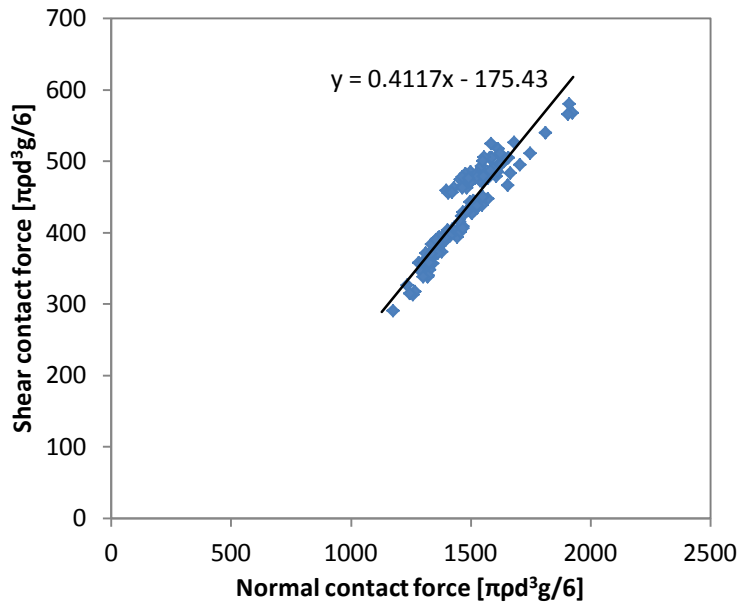
(d)

Figure 6.8: Spatial distribution of normal and shear forces for spherical particles in a) and b), respectively, and for ellipsoidal particles (2.5:1 aspect ratio) in c) and d), respectively.

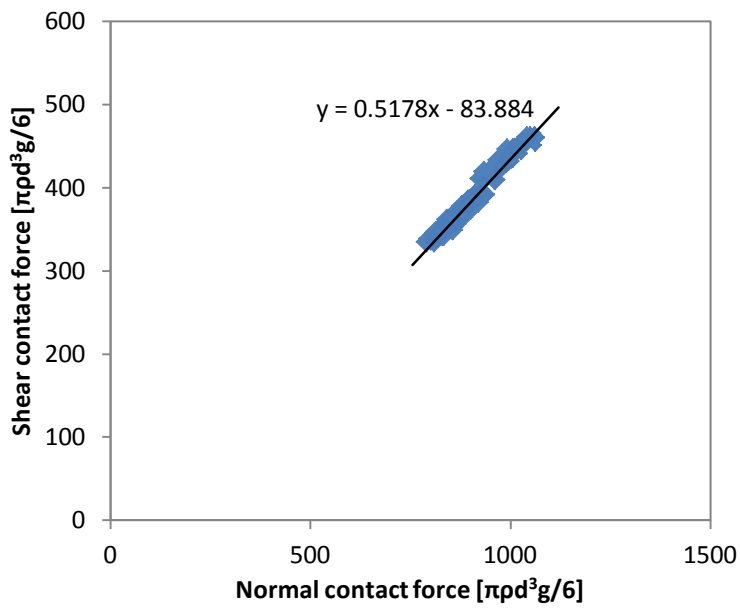
This happens because for ellipsoidal particles, the number of contacts increases drastically as we have seen in earlier chapters. This causes the contact forces, i.e. force chains to become weaker for ellipsoidal particles. As a result, the force arising from the forces becomes less as well. Another difference is the band of variation of force across the region. Band of variation for normal force in the case of spherical particle assembly is much higher than for ellipsoidal particle assembly. The same is found regarding shear force for spherical particle assembly with respect to that for ellipsoidal particle assembly. This observation further strengthens the suggestion made earlier that forces transmitted by loading and shearing platens are more uniformly distributed in the ellipsoidal particle assembly flow region compared to the spherical particle assembly flow region.

#### **6.3.4. Relationship between shear and normal forces and stresses**

Next, we compare the relationship between individual pairs of shear and normal forces for ellipsoidal and spherical particle assembly under similar a flow condition. Figure 6.9 shows the relationship between individual normal contact forces and their corresponding shear contact force for spherical and ellipsoidal particles. Apart from the difference in range of magnitude difference in magnitude of corresponding parameters, we find a linear positive relationship between shear and normal contact force for both cases. This observation is consistent with previous papers on spherical particles [14] and further shows that this holds true for ellipsoidal particles. Then the best fitting linear curve is generated to obtain the friction coefficient for each particle assembly.



(a)



(b)

Figure 6.9: Relationship between shear and normal contact force for a) spherical and b) ellipsoidal particles.

Here we find that friction coefficient is higher for ellipsoidal than spherical particle assembly. In other words, with increase of normal force, shear force increases at a higher



proportion since more of the normal force is converted to shear force due to increased frictional surface area between particles.

To view it from a more macrodynamic perspective, we investigate the externally applied normal and shear forces by the platens to obtain the relationship. In Fig. 6.10 we compare between spherical and ellipsoidal particle assembly and we find a similar pattern: a positive linear relationship between externally applied normal stress and induced shear stress for the platens. We choose only one shear rate ( $1.07\sqrt{(gd)}$ ) because it has already been shown in earlier studies [14] that shear rate variation does not affect this relationship. However, here we find again there is a difference between the slopes of the curves; slope of ellipsoidal curve is much higher than that of ellipsoidal particles. Again, it proves that friction coefficient of flow is significantly higher for elongated particles than what we can find for spherical particles.

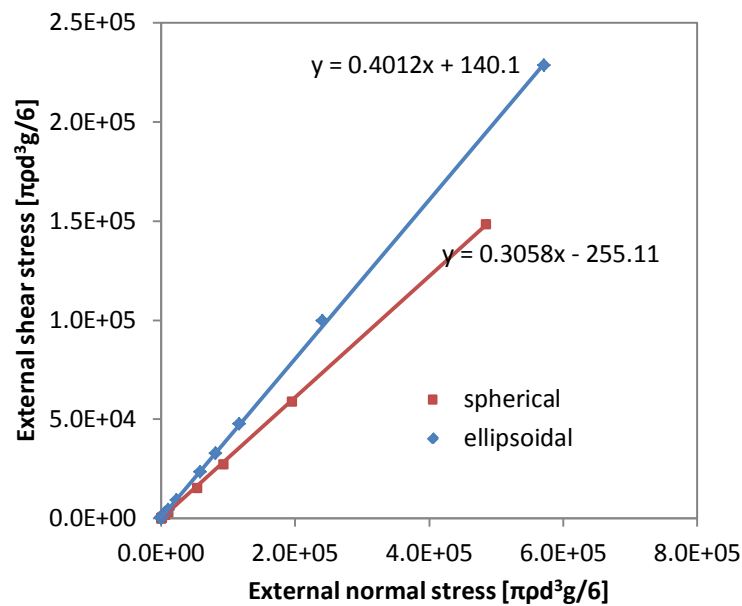


Figure 6.10: Relationship between externally shear and normal stress.

### 6.3.5. Inertial number

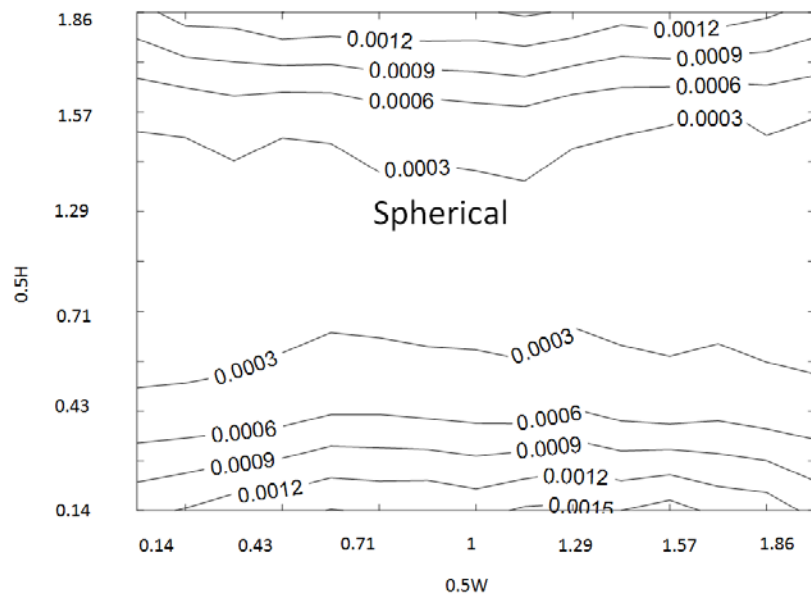
Next we investigate the effect of particle shape on inertia number. Spatial distribution of inertia number is perpendicular to flow parallel to the  $yz$  plane in Fig. 6.11. It shows

symmetric distribution for both spherical and ellipsoidal particle assembly. We find higher value near the platens which gradually diminishes as we near the central region of the shear cell segment. It means that externally applied force can produce a greater inertial effect near the platens than near the center.

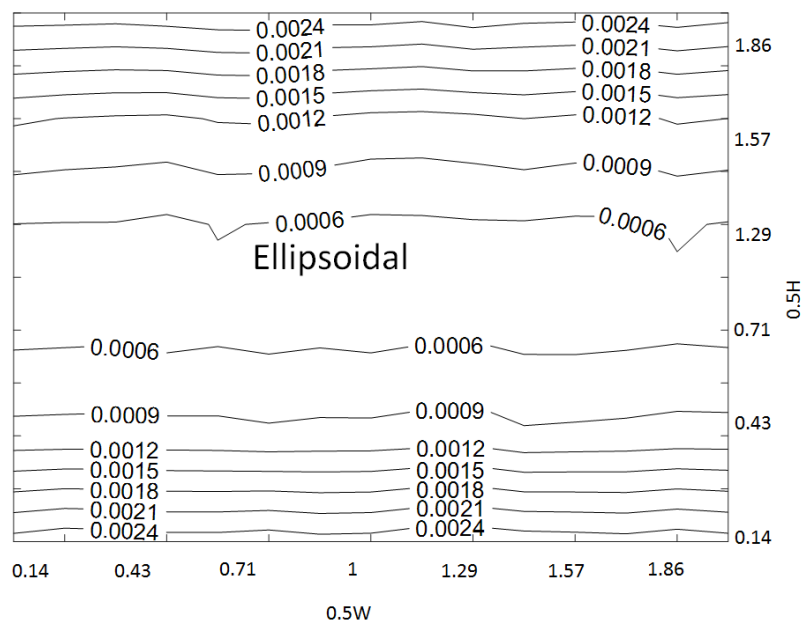
Then, we compare the relationship between inertia number and friction coefficient for spherical and ellipsoidal particles. Figure 6.12 depicts the relationship between friction coefficient and inertia number for various points of flow region in semi-log graph. This relationship is drawn by Pouliquen et al. for inclined planes in [193] and tested in annular shear cell in [14]. The friction for I-rheology was given by:

$$\mu(I) = \mu_s + \frac{\mu_2 - \mu_s}{\frac{I_0}{I} + 1} \quad (6.4)$$

where,  $I_0$  is the initial inertia number and  $\mu$  is a ratio of shear stress, normal pressure.



(a)



(b)

Figure 6.11: Spatial distribution of inertia number for left: spherical and right: ellipsoidal particles.

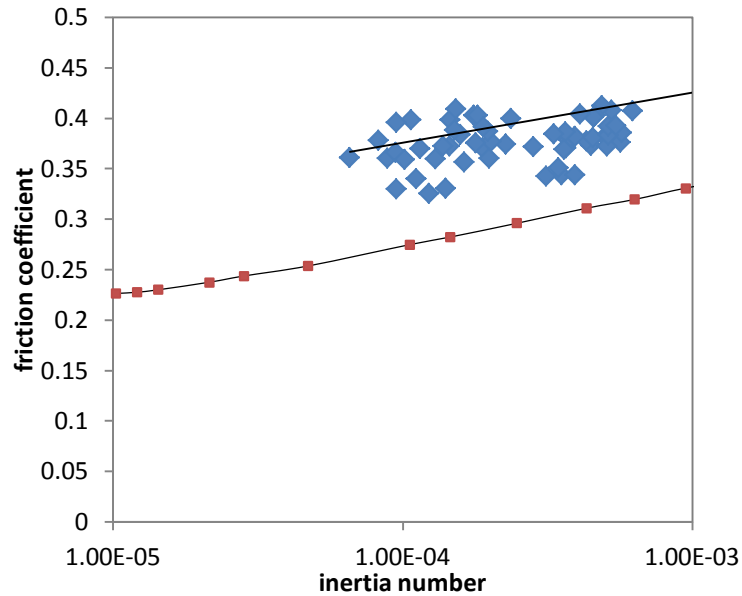
It was found that a positive relationship holds true when shear rate is sufficiently high. In our work, we apply this method for spherical and ellipsoidal particle flow at a moderately high shear rate. We found  $\mu=0.28$  for spherical particles and  $\mu=0.4$  for ellipsoidal particles at the platen for same load and shear rate ( $12.7\sqrt{gd}$ ). It indicates that friction is much higher for ellipsoidal particles. We use the following equation:

$$\mu_{(i,j)} = \frac{1}{2} \sqrt{\frac{[\mathbf{T}_{xx(i,j)} - \mathbf{T}_{zz(i,j)}]^2 + 4(\mathbf{T}_{xz(i,j)})^2}{\mathbf{T}_{xx(i,j)} \mathbf{T}_{zz(i,j)} - (\mathbf{T}_{xz(i,j)})^2}} \quad (6.5)$$

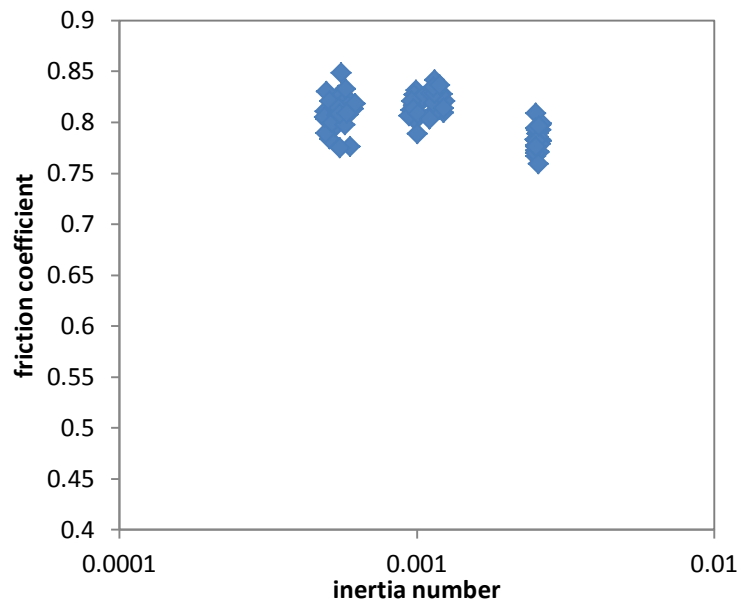
where, we used the method discussed earlier for  $T_{xx}$ ,  $T_{xz}$  and  $T_{zz}$ .

We find the relationship for spherical particles is similar to that of previous studies although magnitude is different. This may be due to different considerations of magnitude of variables such as applied load. However, the relationship for ellipsoidal particles is not so clear. From what we find here the friction coefficient is very high and is not affected by

inertia number for ellipsoidal particles. Please note that we have only showed the red dotted points from best fitted curve. If the figure in [14] is observed, the data points from which the best fitted curve is derived are scattered like the data obtained in our analysis.



(a)



(b)

Figure 6.12: relationship between friction coefficient and inertia number: (a) spherical, (b) ellipsoidal. The red dotted line refers to existing data from fitted curve in [14].

Finally, we examine the effect of particle aspect ratio on macrodynamic value of overall inertia number of particle flow in Fig. 6.13. Here, we find that inertia number increases as the increase in particle elongation with spherical particle assembly has the lowest value. The rising inertia number systematic implies that the inertia force from particle assembly resisting the externally applied force increases with particle elongation. We have seen earlier that an increase in particle elongation does not significantly affect the principal stresses, whereas an increase in particle aspect ratio strongly influences shear stress tensor. Therefore, we can say that shear effect is a major contributor to the increase in inertia force working against externally applied force. It is reasonable and consistent because with the particle elongation and preferential alignment, more contacts between layers of flowing particles build and hence more shear force is required to sever these contacts in order to obtain flow of particles.

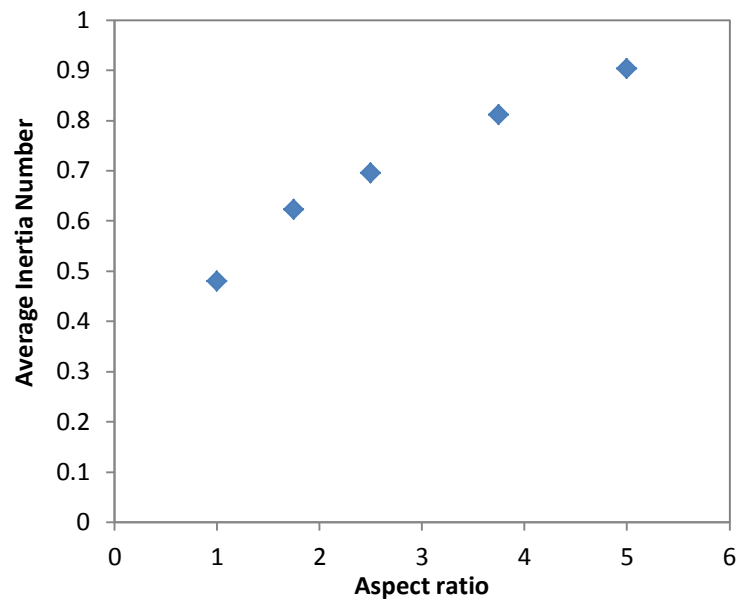


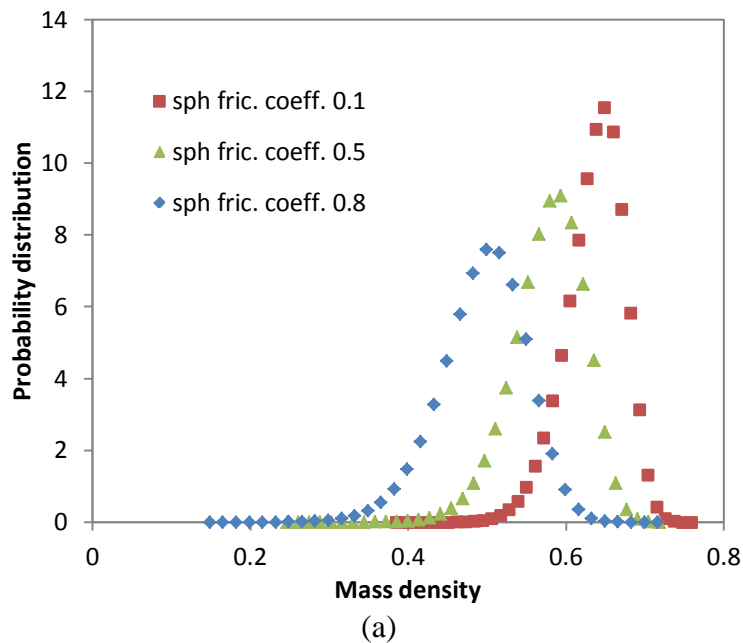
Figure 6.13: Effect of aspect ratio on overall inertia number.

### 6.3.6. Effect of particle friction coefficient

Since there is a big difference in the way spherical and elongated ellipsoidal particles interact, it is imperative that we assess the influence of a material property of particles: particle friction coefficient. In Fig. 6.14 we find the probability distributions of local volume

fraction (particle density in assembly) with different material friction coefficient particles. The impact of particle friction coefficient is significant as it shows a clear variation of probability distribution for both spherical and ellipsoidal particle assembly (aspect ratio 2.5:1). Here we find that, for both cases, as particle friction coefficient increases the bell curve shifts towards the left. Simultaneously, the peak of the curve reduces. It means that average volume fraction reduces with increase of particle friction coefficient while deviation from the mean value of volume fraction increases.

A similar finding was observed for spherical particle flow in [14]. However, for ellipsoidal particle assembly, we discover that the rise in peak is much higher for ellipsoidal particle assembly than that of spherical ones. The reason is that the particles are distributed in an orderly fashion as a result of preferential alignment. Furthermore because this reduces the dispersed state of particle assembly, the volume fraction is more uniform across the flow and hence the high peak at mean value of volume fraction. For ellipsoidal particles, because of the preferential alignment, the uniformity of flow structure is much higher with the increase of particle friction coefficient which results in non-linear rise of peak.



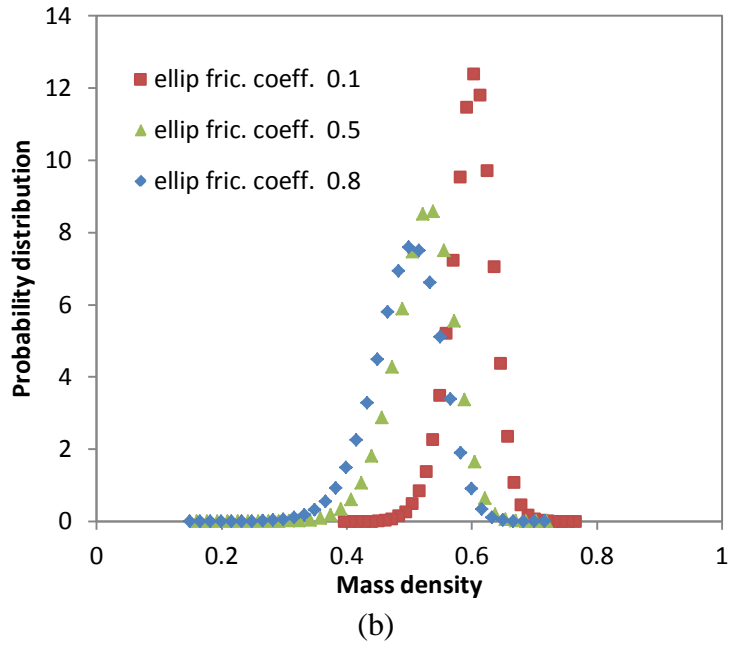
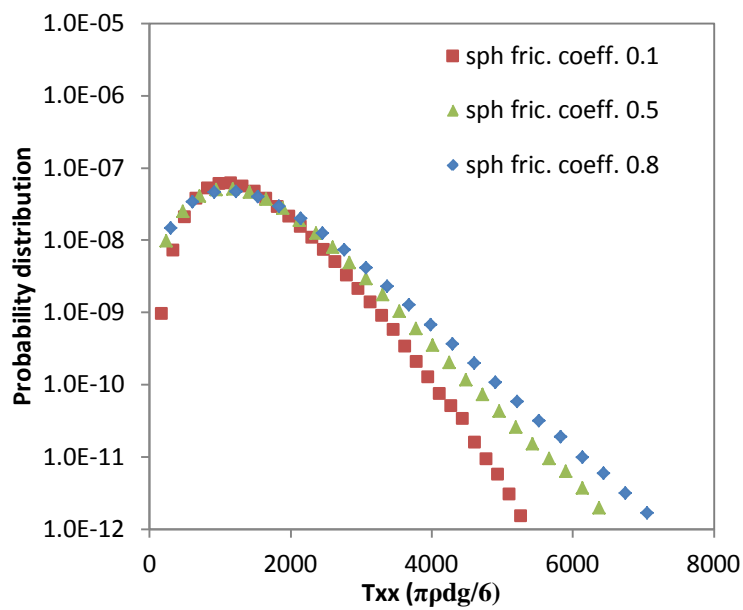


Fig. 6.14: Probability distribution of density of particle assembly (volume fraction) for different particle friction coefficients a) spherical, b) ellipsoidal.

Next we investigate the effect of particle friction coefficient on stress tensors on the global scale. Figure 6.15 shows probability distribution of key stress components  $T_{xx}$ ,  $T_{xz}$  and  $T_{zz}$  for both spherical particle assembly and ellipsoidal particle assembly in the base case. We did not scale the data with average value because all the cases are subject to identical flow condition including the same magnitude of externally applied load. Only the material property of particle friction coefficient is varied to highlight its effect on granular flow. We observe the distribution in semi-log plot as the stresses vary in wide range.

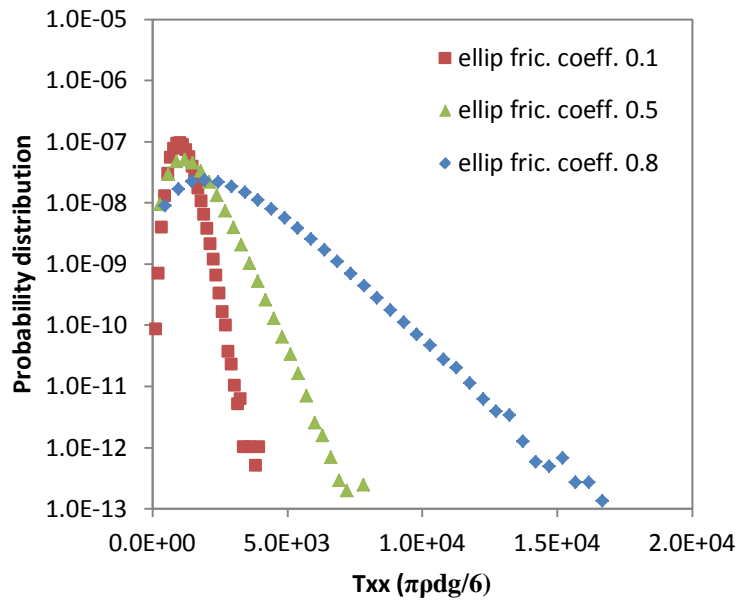
We find here that in all case studies for the considered stress tensors, they show variation at the tail of distribution representing the higher end of force range. Similar to the effect of friction coefficient on probability distribution of contact forces in [14], spherical particle assembly shows the effect whereby the increased friction coefficient increases deviation of forces at a higher range. This is shown by the raised tail of distribution and the finding is consistent with our observation of volume fraction probability distribution, where reduced peak meant an increase in deviation of local density from mean value of density of flow.

Further, when we compare data trends between spherical and ellipsoidal particle assemblies, we find that there is a significant difference in terms of magnitude where local stress tensors of ellipsoidal particle assemblies vary in much higher order of magnitude than that of spherical particles. This happens because, since ellipsoidal particles interact more strongly in layers, the frictional surface area is much higher. As a result, not only does it increase the need to overcome much a higher stress magnitude to produce a similar shear effect, also the friction coefficient has a significantly stronger effect. Even for the case of  $T_{zz}$  where we find minimal effect of friction coefficient for spherical particles in Fig. 6.14e similar to [14], effect on ellipsoidal particles is much stronger as shown in Fig. 6.14f.

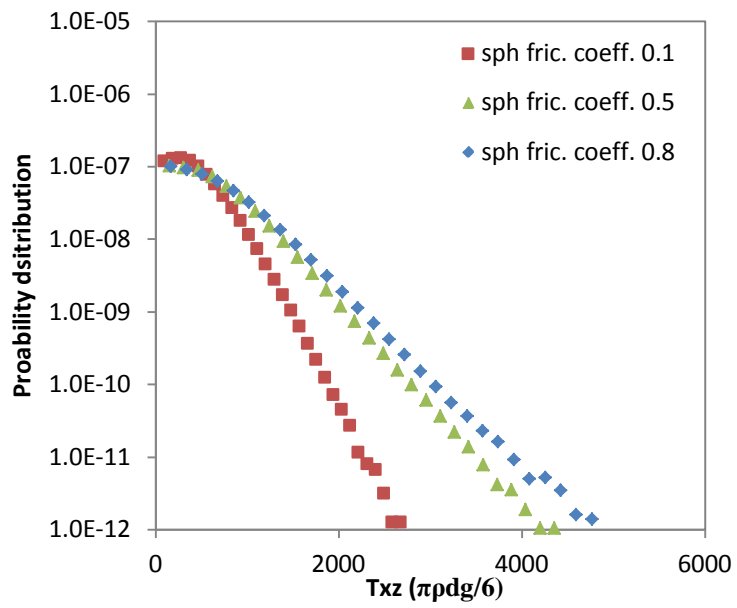


(a)

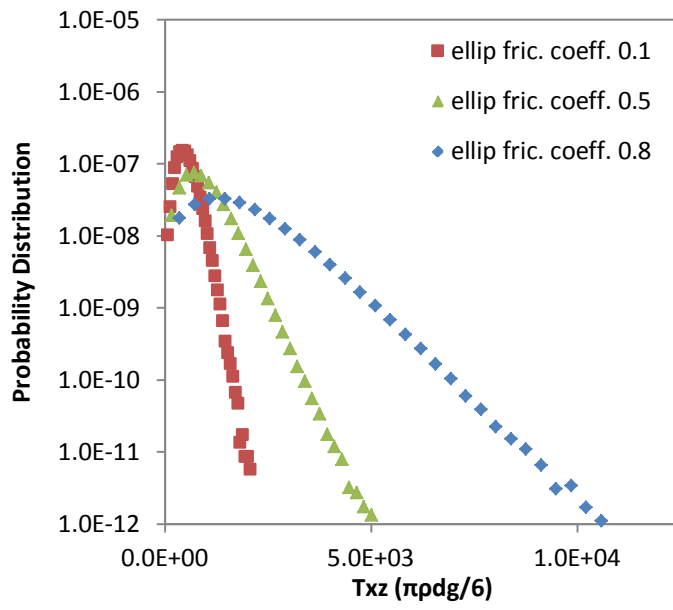




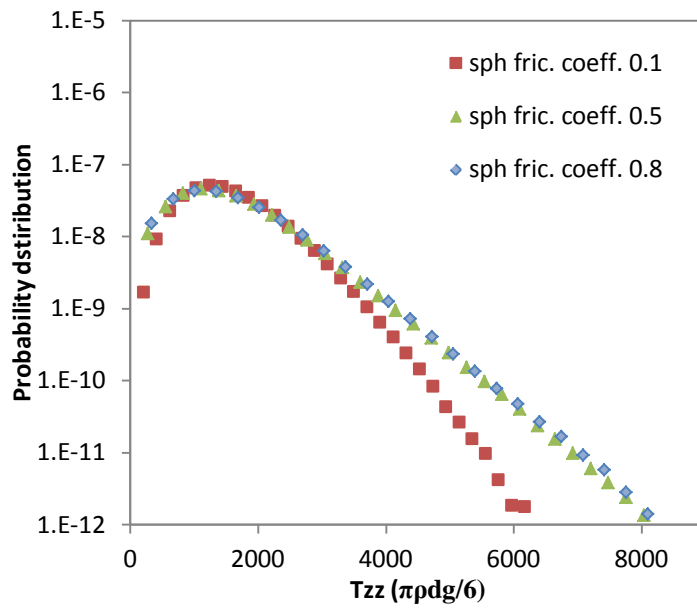
(b)



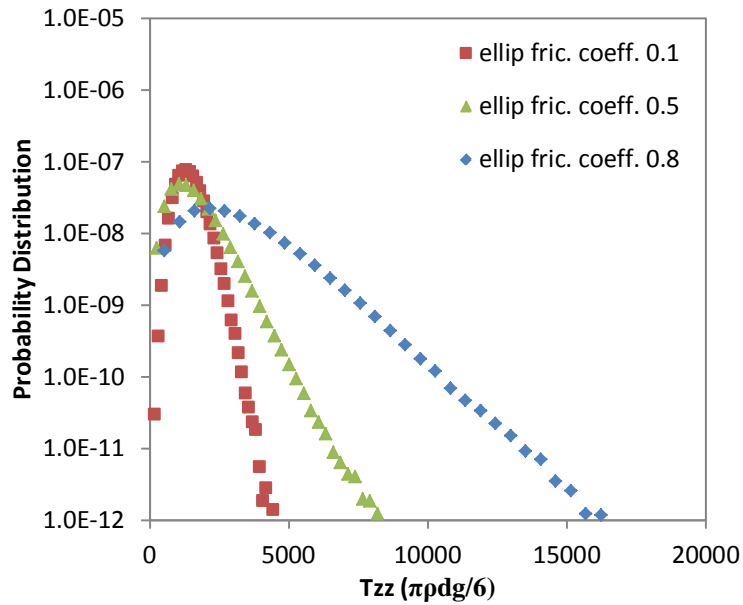
(c)



(d)



(e)



(f)

Fig. 6.15: Probability distribution of different stress components for spherical particles at (a)  $T_{xx}$ , (c)  $T_{xz}$  and (e)  $T_{zz}$ , and for ellipsoidal particles with aspect ratios of 2.5:1 in (b)  $T_{xx}$ , (d)  $T_{xz}$  and (e)  $T_{zz}$  (base case: friction coefficient 0.5).

## 6.4. CONCLUSIONS

Flow properties of spherical and ellipsoidal particles are observed in virtual platform under double-shear stress-controlled condition through a representative rectangular segment of shear cell. Intermediate regime was chosen to conduct the analysis. Under similar flow conditions the effect of particle shape is analysed macrodynamically.

- Investigation of velocity spatial distribution shows both spherical and ellipsoidal particle assembly reveal a similar distribution with higher velocity near the platens and near zero velocity at the central region. Meanwhile velocity across the flow parallel to platens is uniform at any given layer of particles. However, the variation of velocity in the vertical direction is much smoother. It is a response of particle preferential alignment where the particle shape affects the velocity fluctuation; the higher the

particle aspect ratio the lower the fluctuation with a sharp drop initially from spherical to ellipsoidal particles. Then the rate of reduction decreases until it becomes constant.

- In our observation of stress we find that the spatial distribution of stress has a gradient profile with highest stress occurring near the platens and lowest away from them. A similar pattern is found for both spherical and ellipsoidal particle assembly and the difference only occurred in terms of magnitude. This is understandable because regardless of particle shape, the main driver here are the platens applying load and shear externally having the maximum effect on the adjacent particles while particles at the central region are furthest from the platens. Next, we see how the stress is distributed in the y-direction which is perpendicular to both externally applied normal load and shear. Here, spherical and ellipsoidal particles of varying elongation are compared. The pattern shows that the distribution is uniform in the direction regardless of any elongation of particles. Moreover, for principal stresses  $T_{xx}$ ,  $T_{yy}$  and  $T_{zz}$  there is not much difference in magnitude either. However, a significant effect is seen for  $T_{xz}$  with particle elongation. It is logical because regardless of particle elongation, they are subjected to the same normal load. Therefore, variation may occur in terms of how much individual force chains carry the load, but overall stress at any point remains the same. On the other hand, any increase in force chains as discussed in Chapter 5 means more chains will be broken to obtain shear, hence  $T_{xz}$  is higher. This observation is further corroborated by the microdynamic analysis of effect of particle aspect ratio on stress tensors. For the same reason increased force chain causes an increase in shear to normal force ratio as well as externally applied load and shear ratio.
- In our study of inertia number we first looked at spatial distribution. We find that inertia number is highest near the platens and tapers off near the center. It is related to the platens' shear effect. The more particles mobilized then the more inertia force created relative to externally applied force. At the central region particles are not very mobile; hence the low inertia number. The trend is similar for both spherical and ellipsoidal particles. We further investigate the relationship between inertia number and friction coefficient particle assemblies. Here, we find a similar positive relationship for both spherical particles. However, for the ellipsoidal particles, friction coefficient seems to be constant with respect to inertia number.
- We find there is a relationship between particle aspect ratio and inertia number as such that the higher the particle aspect ratio is, the higher is the inertia number. It is

suggested this is directly related to increased contact number and consequently shear stress. The more elongated the particles are, more contacts develop between layers of flowing particles, more shear stress developed in creating flow, i.e. higher inertia force work against applied force resulting in higher inertia number. Finally we study the effect of particle friction coefficient in a comparative examination of spherical and ellipsoidal particulate rheology. It is demonstrated here that friction coefficient has a significantly stronger influence on granular flow in the case of elongated non-spherical particles.

# Chapter 7: Regime transition of non-spherical particle flow in shear cell

## OVERVIEW

The regime transition is investigated for granular flow of spherical and ellipsoidal particles regarding various aspect ratios under stress controlled double-shear flow condition. The correlation among elastically and kinetically scaled stress, kinetically scaled stiffness and volume fraction is analysed and a set of volume fractions is obtained for each specimen particle assembly that corresponds to quasistatic-intermediate and intermediate-inertial regime transitions. It is found that, results from ellipsoidal particle flow are similar to that of spherical particles. From these values, regime transition points are identified. Using these values, a regime map is obtained for all specimen particle assemblies. It is found that while, quasistatic-intermediate regime transition point remains similar; inertial-intermediate regime transition point has lower volume fraction than spherical particles which decreases with particle elongation. Then the internal structure of force network for base case ellipsoidal particle assembly is compared with earlier studies on spherical particle assembly; similarities are found. However, ellipsoidal particle assembly has tight-knit force network which makes it hard to distinguish between transition while the transition is much clearer in case of spherical particle analysis. Next, the novel approach of  $P(f) = \exp(-cf)^n$  for identifying quasistatic regime [9] is compared for ellipsoidal and spherical particle assembly. It is found that this method is not useful in ellipsoidal particle study as it is for spherical particle flow study. Then another method is applied to obtain inertial regime transition by investigating the relationship between shear-to-normal stress ratio and volume fraction. Similar results emerged for both spherical and ellipsoidal particle assembly.

## 7.1. INTRODUCTION

Regime transition is a crucial subject in granular rheology. It is the point of change in the condition where granular flow behavior transforms dramatically. It is an essential component for understanding the goal of attaining a general constitutive mathematical model that can describe flow behavior at all stages. For this reason, much work has been done on regime transition but it mostly related to spherical particles. Campbell analysed regime transition in volume controlled [48] and stress controlled [6] double-shear flow conditions through shear cell. His study was based on contact force only and non-contact forces were overlooked. He studied contact force chain network, and different combinations of correlations between volume fraction, scaled stress, scaled stiffness relationship, apparent coefficient of friction and contact time to obtain the regime map. This map shows how variation of applied pressure on shear rate by boundaries of annular shear cell on granular flow can transit flow from one regime to the next. Volume fraction is used to pinpoint the point of regime transition. Here, curve collapse in the correlation figure is utilized to find the transition point from quasistatic to inertial regime which is explained through force chain analysis. He suggested that a volume-controlled condition generates outcomes that differ from a stress-controlled condition. He suggested that, shear rate variation has opposite effect on direction of regime transition in case of volume- and stress-controlled flows.

Sundaresan et al. also studied regime transition of granular flow in volume controlled [7] and stress controlled [8] double-shear flow conditions. However, they took into account cohesive force. While like Campbell they examined similar correlations, they incorporated scaling method into the cohesive force. Also, they looked at the coordination number but concluded that volume controlled and stress controlled studies produce the same results. It should also be noted that gravity is ignored. Sundaresan et al. also made effort to obtain regime map in [194]. Yang et al. attempted to find the regime transition in a different setup, i.e. rotating drum [195]. Here, they investigated angle of repose, rotation speed, particle velocity, volume fraction, coordination number and collisional energy of particles. Here, however, probability distribution function has been extensively used alongside correlation graphs. Wang et al. studied regime transition of particle flow in stress controlled annular shear cell [9] where they used a scaling method similar to Campbell's. They considered gravity in the work although used it in scaling method. Their analysis consisted of a

collapsing correlation curve study, contact network distribution and probability distribution of similar variables as used by Campbell and Sundaresan et al. In addition, they found a probability exponential function which includes a power index that may serve as new flow regime indicator.

Boyer et al. experimentally [127] and Trulsson et al. [196] numerically did similar research on regime transition in a varying interstitial medium. They used single shear stress controlled granular flow through annular cell. Ji et al. [142] considered volume controlled granular flow condition in shear cell to obtain the regime map. Along with the regular observation applied by Campbell and Sundaresan et al. they introduced the concept of studying spatial distribution of coordination number and scaled stiffness relationship in identifying regime transition. However, these papers have not considered non-spherical particles. Campbell et al. [64] investigated ellipsoidal particle flow through shear cell in volume controlled condition but have not taken into account boundary conditions or regime transition. Our work leaps forward from spherical to non-spherical particle flow study in regime transition, going one step closer to practical application with focus on achieving a universal constitutive model of granular rheology.

In this chapter, regime transition of spherical and ellipsoidal particles of varying aspect ratios are compared to learn how this specific type of non-spherical particle is characteristically related to spherical particle assembly. Important variables - elastically scaled stress, kinetically scale stress, volume fraction, scaled stiffness, and particle contact force - are investigated with a specific focus on regime transition and effects of particle elongation. This study will help correlate the yet to be undertaken numerical study to the already obtained experimental results.

## **7.2. SIMULATION**

In this work, granular rheological analysis is performed numerically by means of the discrete element method (DEM) using spring dashpot model for soft particle simulation. This method applies Newton's law of motion to calculate forces and displacement related variables based on contact information such as contact pressure and deformation of individual particles for each time-steps which are then collectively considered to determine granular flow dynamics. The non-linear model based on Hertz-Mindlin and Deresiewicz model is used



to calculate the contact forces between particles. The details on the DEM has been discussed earlier in chapter 2 and 3.

In this work, PFC commercial software is used to develop a rectangular segment of annular shear cell which is small enough compared to the full sized annular shear cell where the radial curvature at the side walls is negligible. The dimension of the segment is assigned as  $12d \times 30d \times H$  where  $d$  is the average diameter of particles in the assembly and  $H$  is the height of the upper platen. The upper and lower platens are constructed with 360 spherical particles each of size ' $d$ ' so that they have sufficient roughness to induce shear on particle assembly. Side walls are kept smooth to minimize wall effect. The advantage of using ' $d$ ' as the scaling method is that it can be applied to particles of any size, ranging from rice grains to boulders. However, in this study large sized particles are considered to make the study simple in the sense that non-contact forces like electrostatic, van der Waals and capillary forces are negligible. 5000 slightly polydispersed ellipsoidal or spherical particles with an effective diameter ranging from  $0.9d$  to  $1.1d$  are randomly generated inside the shear cell segment at high concentration. Effective diameter means that elongated particles of different aspect ratios will have the same volume and mass of a spherical particle. After generation the particles are allowed to relax and fill the entire space between the walls and platens.

As the shear is planned to be in the  $x$ -direction, the side walls parallel to the  $yz$ -plane are made periodic so that a particle leaving one of the walls will enter the other at the same  $y$ - and  $z$ - coordinate, and with the same velocities and forces in terms of both magnitude and direction. It is as if the flow is in an infinite loop. The upper and lower platens are then given small velocity in opposite directions along the  $x$ -axis. This will rearrange the particles in the space so that they are evenly distributed inside the segment. The shear is gradually increased to the desired velocity while the upper platen is used to apply pressure on the particle assembly residing inside the cell. The pressure is calculated from the reactionary force from adjacent particles on the upper platen and accordingly the upper platen is slowly lowered at each time-step. When it reaches defined load this platen adjusts its height continuously to maintain constant pressure on the assembly. When the fluctuation of the height of the upper platen reaches a minimum level, it can be assumed that the granular flow has reached steady state condition. Then various data are extracted over a length of time to obtain time-averaged values. This method is applied for each combination of shear velocity and applied load.

## 7.3. RESULTS AND DISCUSSION

### 7.3.1. Determination of regime transitions

In Fig. 7.1a, c, e, g and i we find the correlation between elastically scaled applied stress  $\sigma^*$  by the upper platen, scaled stiffness  $k^*$  which is a function of shear rate by the upper and lower platens and volume fraction  $\nu$  of the assembly for particles with different aspect ratios. Here,

$$\sigma^* = \frac{\sigma d}{k} \quad (7.1)$$

where,  $\sigma$ ,  $d$  and  $k$  are applied stress by upper platen, effective particle diameter and particle stiffness.

$$k^* = \frac{\sigma^*}{\sigma'} \quad (7.2)$$

where, kinetically scaled stress is

$$\sigma' = \frac{\sigma}{\rho d^2 \dot{\gamma}^2} \quad (7.3)$$

Here,  $\dot{\gamma}$  is the induced shear rate produced by the upper and lower platens. For more information see the following references [6, 48].

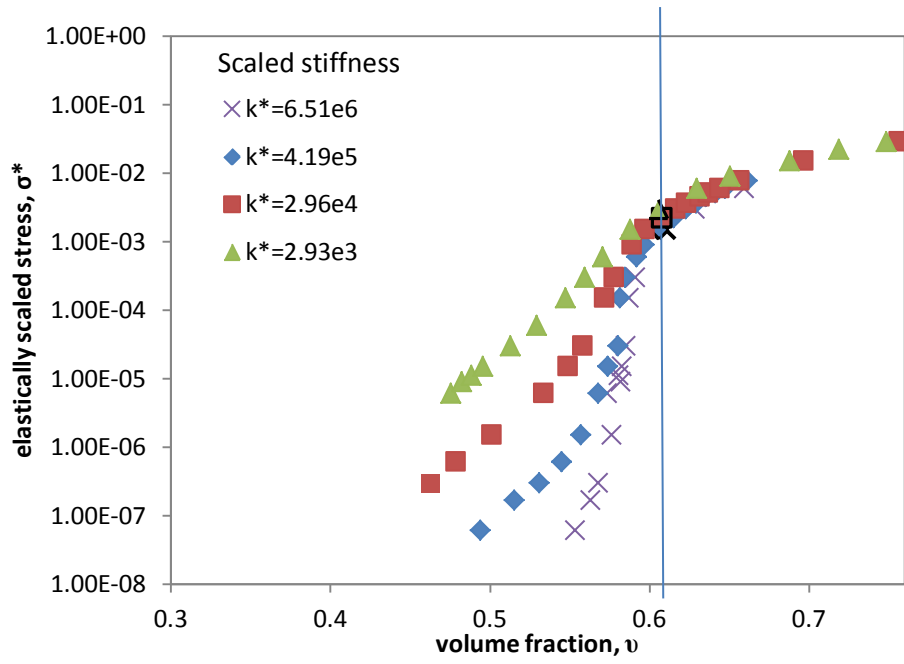
In this work, scaled stiffnesses  $k^*$  considered are:  $2.92 \times 10^3$ ,  $2.96 \times 10^4$ ,  $4.19 \times 10^5$  and  $6.51 \times 10^6$ . Similar considerations were done in [9]. In these figures we find as expected [6-9, 48] that when the applied pressure is high, particles are compacted indicated by high volume fraction. This stage is the quasistatic regime where induced shear rate is unable to influence through inertial effect and neighboring particles interact only elastically. It is evident by the collapse of the correlation curves for different  $k^*$  (i.e. shear rate). In this regime, only applied stress affects deformation of particle assembly.

As the applied load is reduced, the impact of shear rate increases and the volume fraction, i.e. density of particle assembly reduces. This is evident from the observation that the volume fraction of the particle assemblies is no longer the same for any given load. This is the intermediate regime because here the inertial effect noticeably affects the flow assembly. The

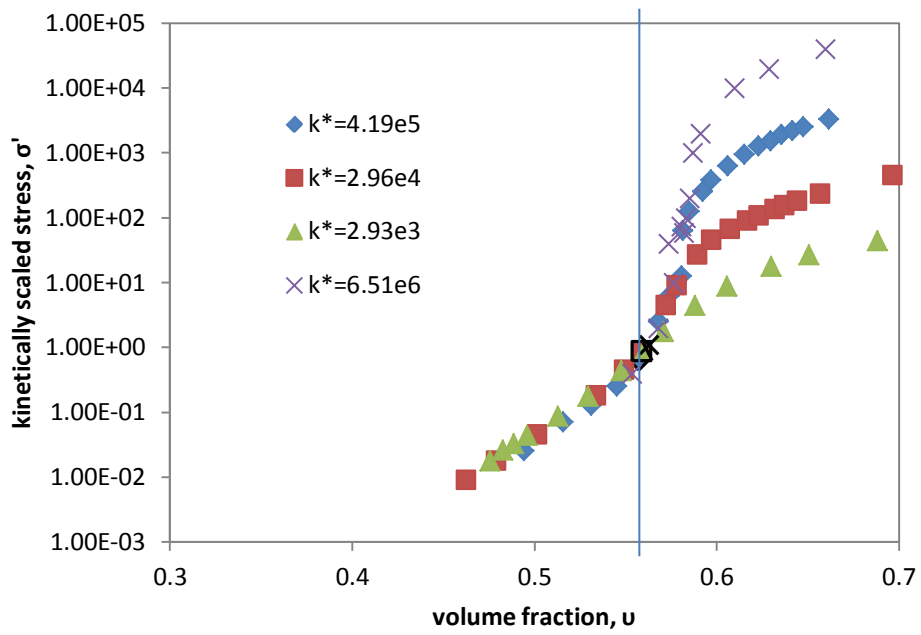
point at which correlation curves for different  $k^*$  collapse into a single one is the point of transition where particle assembly of flow enters (or exits) the quasistatic regime. The corresponding volume fraction for quasistatic regime transition are found to be  $\nu = 0.61, 0.64, 0.62, 0.66$  and  $0.62$  for spherical particle assembly, and ellipsoidal particle assemblies of aspect ratios  $1.75:1, 2.5:1, 3.75:1$  and  $5:1$ , respectively.

The inertial regime transition are shown in Figs. 7.1 b, d, f, h and j . These figures reveal the correlation between  $\sigma'$ ,  $k^*$  and  $\nu$ . A similar investigation was performed in [7, 9, 142]. We know from earlier propositions [48] that when particle assembly under flow is in inertial regime, applied stress has a quadratic relationship with shear rate. Observing this relationship,  $\sigma'$  is the indicator for inertial regime by definition of kinetically scaled shear rate. At lower volume fraction, when the externally applied load by platen is less the particles are very much relaxed, and particle assembly strictly follows the quadratic relationship mentioned above as indicated by the collapse of the  $\sigma'$ -  $\nu$  correlation curves for different  $k^*$  (i.e. shear rate). This means that the flow assembly is at inertial regime. When the load is increased and volume fraction consequently increases, the quadratic relationship between shear rate and kinetically scaled stress is no longer applicable.

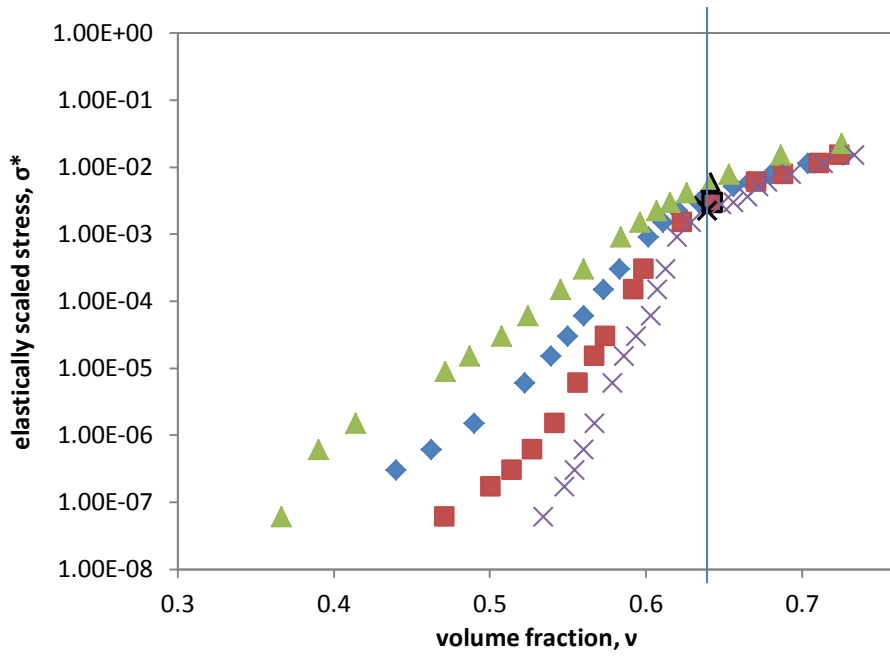
Consequently, the single curve disperses showing the shear rate has a varying effect. It indicates that the flow assembly has exited the inertial regime. The point at which the collapse occurs is the point of inertial regime transition to and from the intermediate regime, a find that agrees with previous studies (eg. [6,9]). A similar trend is observed for spherical as well as ellipsoidal particle assemblies of different aspect ratios. The volume fractions at which the inertial regime transition occurs are  $0.56, 0.54, 0.50, 0.46$  and  $0.42$ . However, it is interesting to note a distinguishing feature in that the intermediate regime between inertial regime transition point and quasistatic regime transition point is clear where large jump in  $\sigma^*$  (function of applied pressure) occurs with little to no change in volume fraction. This volume fraction is called critical volume fraction. This is not the case for ellipsoidal particle assemblies.



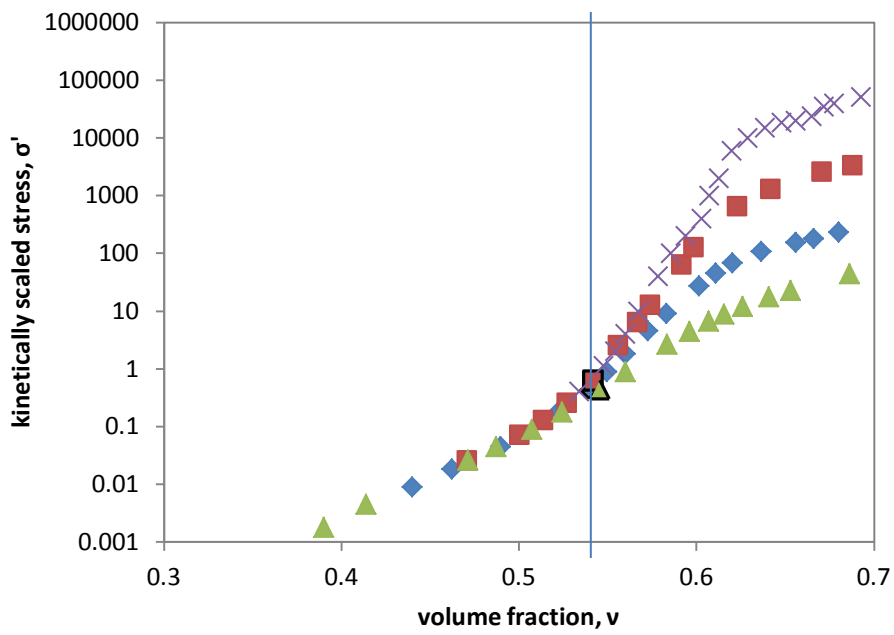
(a) Spherical



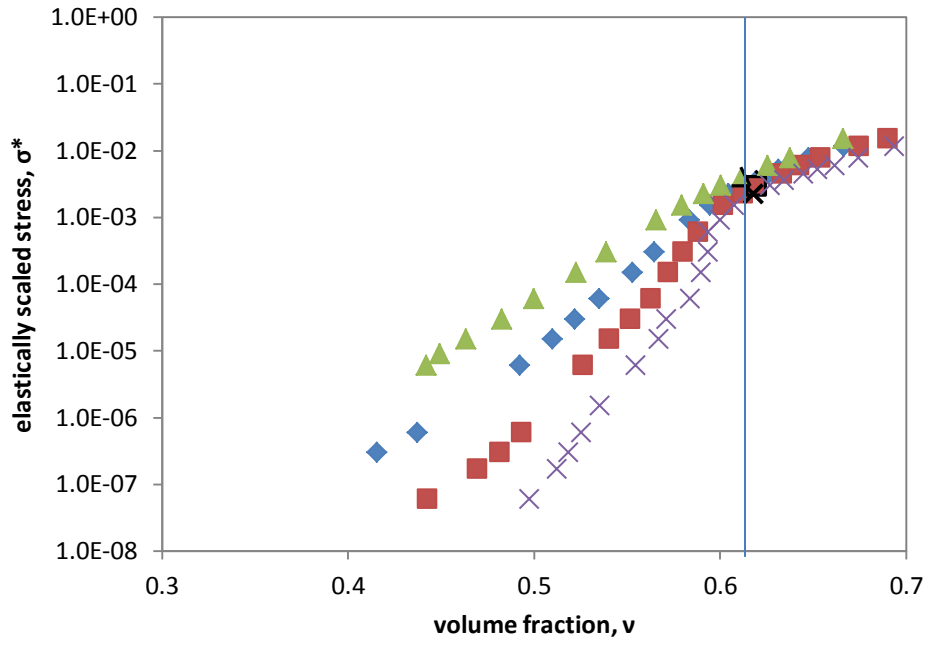
(b) spherical



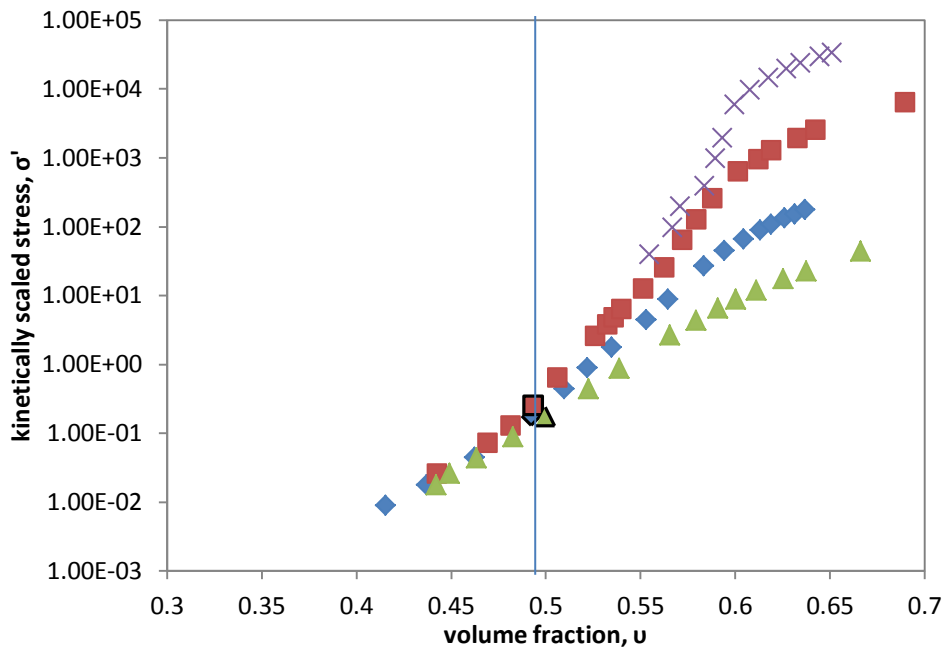
(c) 1.75AR



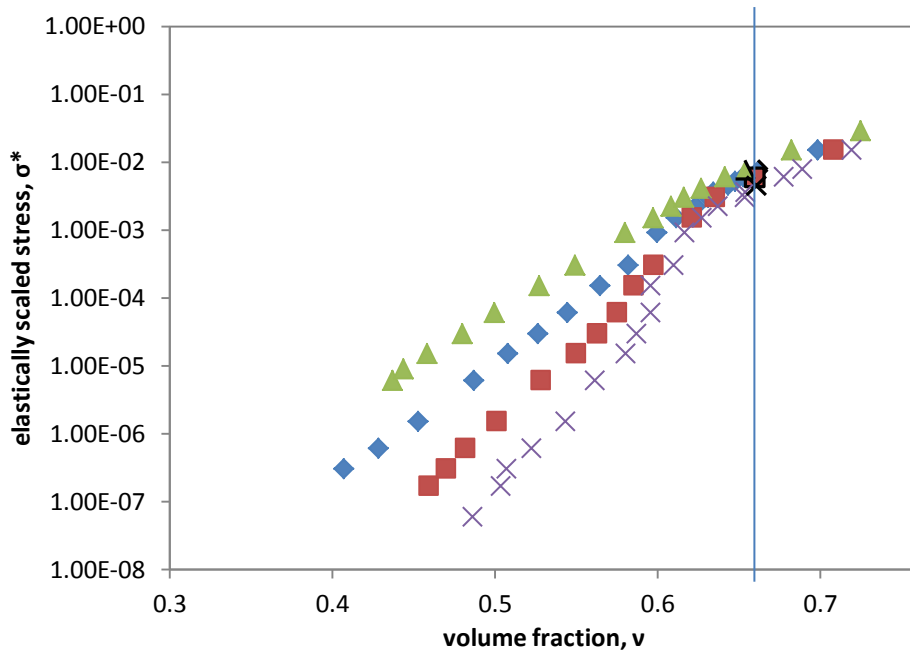
(d) 1.75AR



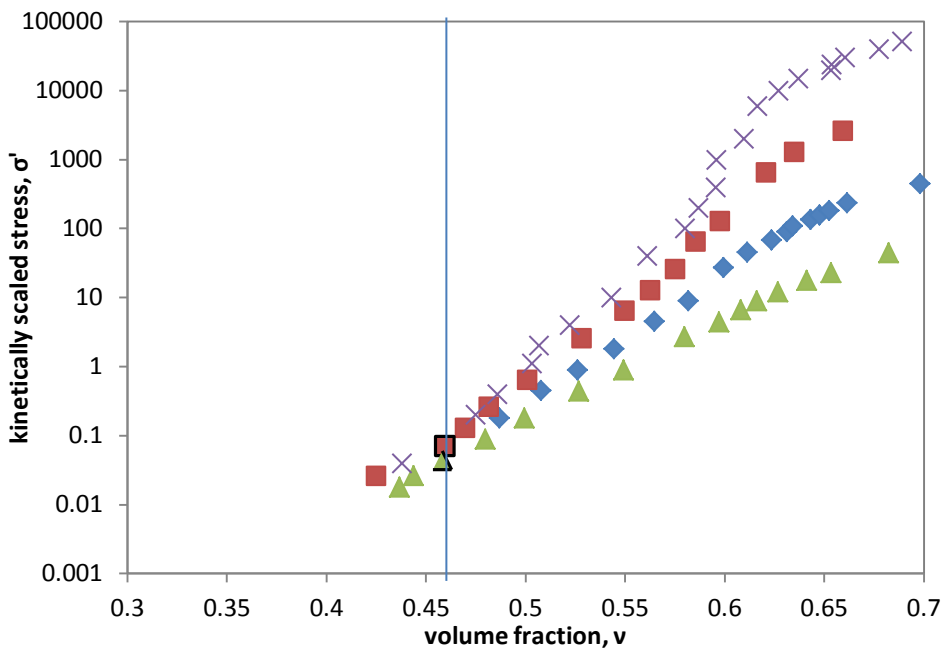
(e) 2.5AR



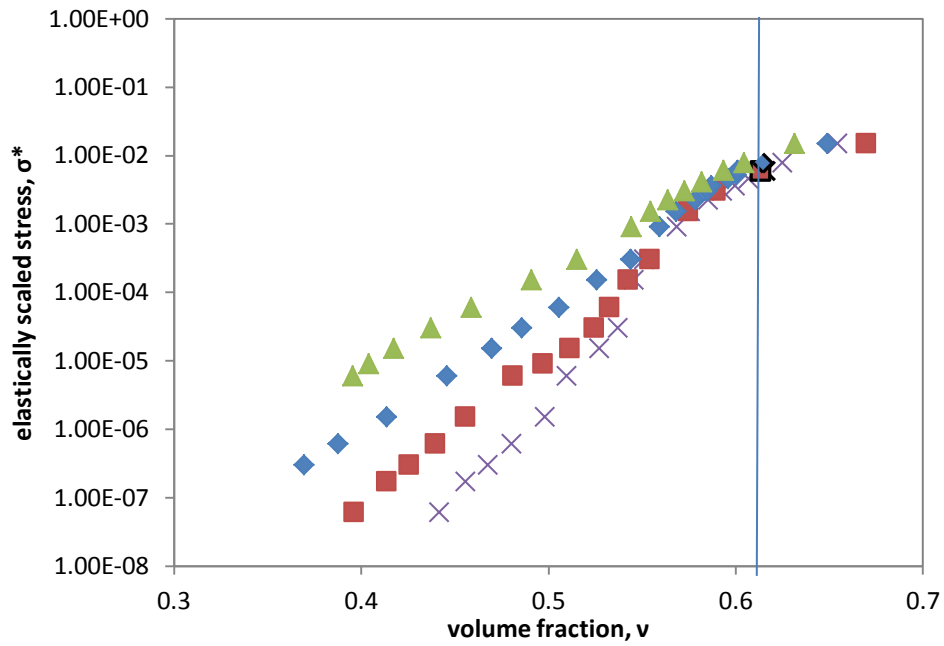
(f) 2.5AR



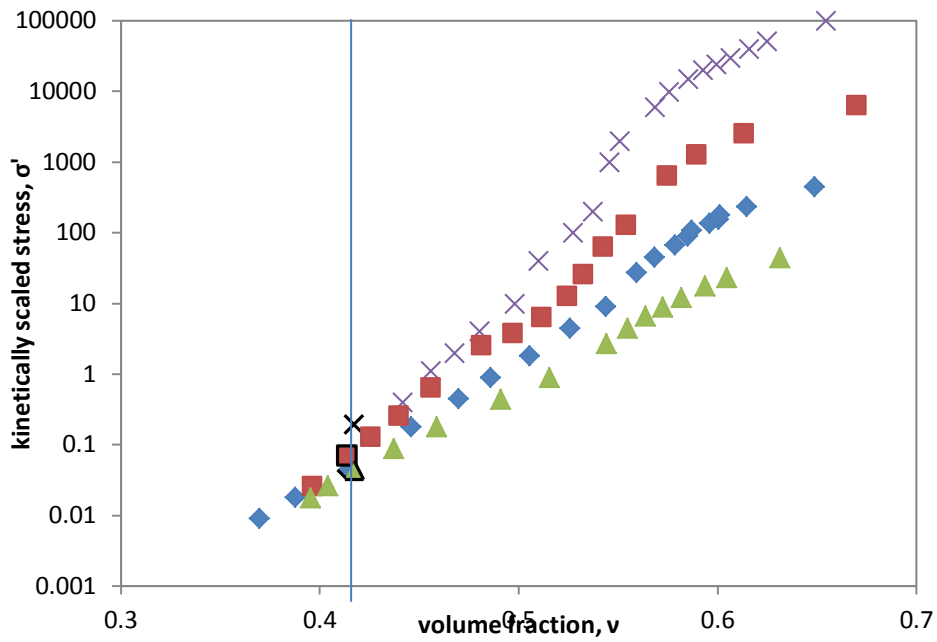
(g) 3.75AR



(h) 3.75AR



(i)\_5AR



(i) 5AR

Figure 7.1: Variation in elastically scaled applied stress ( $\sigma^*$ ) with packing fraction ( $\nu$ ) for different values of scaled stiffness in a), c), e), g) and i). Also, variation in kinetically scaled applied stress ( $\sigma'$ ) with packing fraction ( $\nu$ ) for different values of scaled stiffness in b), d), f), h) and j) for spherical particles, ellipsoidal particles of 1.75:1, 2.5:1, 375:1 and 5:1 aspect ratios, respectively (regime transition data points are marked with dark edges).



From the figures in 7.1, the following scaled stress and stiffness combinations are identified for quasistatic and inertial regime transitions for particles of varying shapes and elongations. Regarding the transitions between quasistatic and intermediate regime the values are summarised in table 7.1. For the transitions between inertial and intermediate regime the values are summarised in table 7.2. Applying the data from tables 7.1 and 7.2, we obtain a flow regime map for assemblies of spherical and ellipsoidal particles of different aspect ratios. One regime map consists of  $\sigma^*$  and  $k^*$  as shown in Fig. 7.2 a, c, e, g and i. From these maps, we find for constant shear rate, i.e.  $k^*$ , how the regime transition occurs from the quasistatic to intermediate and inertial regime step by step following the decrease of  $\sigma^*$  (which is a direct function of applied load by upper platen). A similar observation is found in [6, 9]. As discussed earlier, this is due to the decline in volume fraction with a decrease of applied load which allows particles free to be affected by inertial effect of shear velocity. At a given lower  $\sigma^*$ , assemblies can transit from the intermediate to inertial regime for a small increase of  $k^*$  (shear rate) whereas at very high  $\sigma^*$ , assembly is always in quasistatic regime regardless of  $k^*$  values.

Table 7.1. Data point between quasistatic and intermediate regime

Aspect ratio	$\sigma^*$	$\sigma'$	$k^*$	Aspect ratio	$\sigma^*$	$\sigma'$	$k^*$
1:1 (spherical)	0.0015	9.76E+03	6.51E+06	1.75:1	0.002248	1.46E+04	6.51E+06
	0.0015	6.28E+02	4.19E+05		0.002995	1.25E+03	4.18E+05
	0.00224	6.65E+01	2.96E+04		0.002778	8.21E+01	2.96E+04
	0.00299	8.74E+00	2.93E+03		0.006014	1.76E+01	2.92E+03
Aspect ratio	$\sigma^*$	$\sigma'$	$k^*$	Aspect ratio	$\sigma^*$	$\sigma'$	$k^*$
2.5:1	0.002249	1.46E+04	6.50E+06	3.75:1	0.004517	2.93E+04	6.51E+06
	0.002995	1.25E+03	4.18E+05		0.006014	2.52E+03	4.18E+05
	0.003623	1.07E+02	2.96E+04		0.007778	2.30E+02	2.96E+04
	0.004106	1.20E+01	2.92E+03		0.00939	2.74E+01	2.92E+03
Aspect ratio	$\sigma^*$	$\sigma'$	$k^*$				
5:1	0.006014	3.91E+04	6.51E+06				
	0.006014	2.52E+03	4.18E+05				
	0.007778	2.30E+02	2.96E+04				
	0.010621	3.10E+01	2.92E+03				

Table 7.2. Data point between inertial and intermediate regime

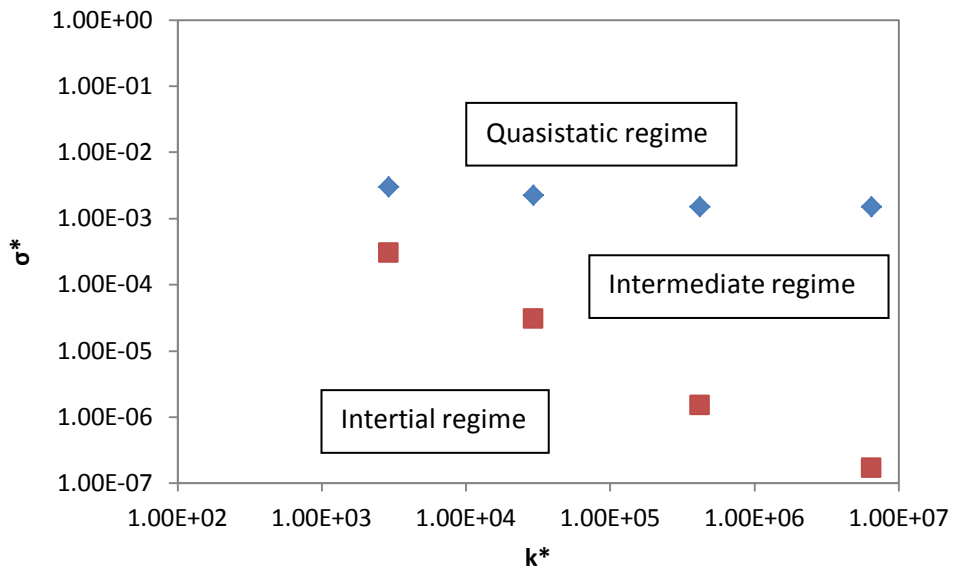
Aspect ratio	$\sigma^*$	$\sigma'$	$k^*$	Aspect ratio	$\sigma^*$	$\sigma'$	$k^*$
1:1 (sph)	1.50E-06	0.628	4.19E+05	1.75:1	1.15E-07 <sub>+</sub>	0.745396	6.51E+06
	2.99E-05	0.886	2.96E+04		1.5E-06	0.628394	4.18E+05
	2.99E-04	0.874	2.93E+03		1.5E-05	0.444202	2.96E+04
	1.69E-07	1.098	6.51E+06		0.00015	0.438564	2.92E+03
Aspect ratio	$\sigma^*$	$\sigma'$	$k^*$	Aspect ratio	$\sigma^*$	$\sigma'$	$k^*$
2.5:1	6.04E-06	0.178538	2.96E+04	3.75:1	1.94E-08 <sub>+</sub>	0.126057	6.51E+06
	6.04E-07	0.25257	4.18E+05		1.69E-07	0.07072	4.18E+05
	6.04E-08	0.392314	6.50E+06		6.08E-06 <sub>+</sub>	0.179634	2.96E+04
	6.01E-05	0.175567	2.92E+03		1.50E-05	0.043856	2.92E+03
Aspect ratio	$\sigma^*$	$\sigma'$	$k^*$				
5:1	3.02E-08	0.196157	6.51E+06				
	1.69E-07	0.07072	4.18E+05				
	1.5E-06	0.044202	2.96E+04				
	1.5E-05	0.043856	2.92E+03				

+ interpolated data points

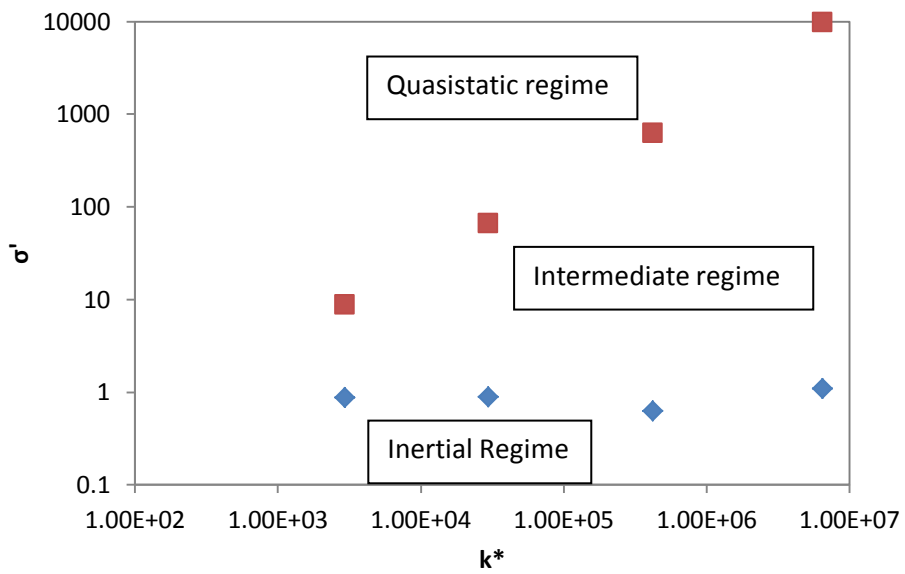
The second regime map consists of  $\sigma'$  and  $k^*$  as shown in Fig. 7.2 b, d, f, h and j. From these maps, we find, for constant  $k^*$ , how the regime transition occurs from quasistatic to intermediate to inertial regime as the  $\sigma'$  reduces. Here, for relatively high  $\sigma'$ , flow assembly transits from the quasistatic to intermediate regime with increase of  $k^*$ . However, below the threshold value of  $\sigma'$  (which happens because of very high shear rate as squared denominator), the flow assembly is constantly in inertial regime regardless of shear rate. However, it should be mentioned that it is applicable for high shear rates only because although theoretically it is possible to obtain such a  $\sigma'$ - $k^*$  combination for low load and low shear rates, particles are more likely to get settled due to gravitational effect. This constant state of inertial regime occurs because particles are very much agitated from high shear velocity while low applied loads are less able to overpower inertial effect from shearing.

Although the regime maps are found to show a consistent trend for ellipsoidal particles with a different elongation, there is one difference. The joining point of the threshold limit bars is very clear for spherical particles; this is not evident for ellipsoidal particles. Perhaps this is consistent with the observation made earlier that the intermediate regime for ellipsoidal

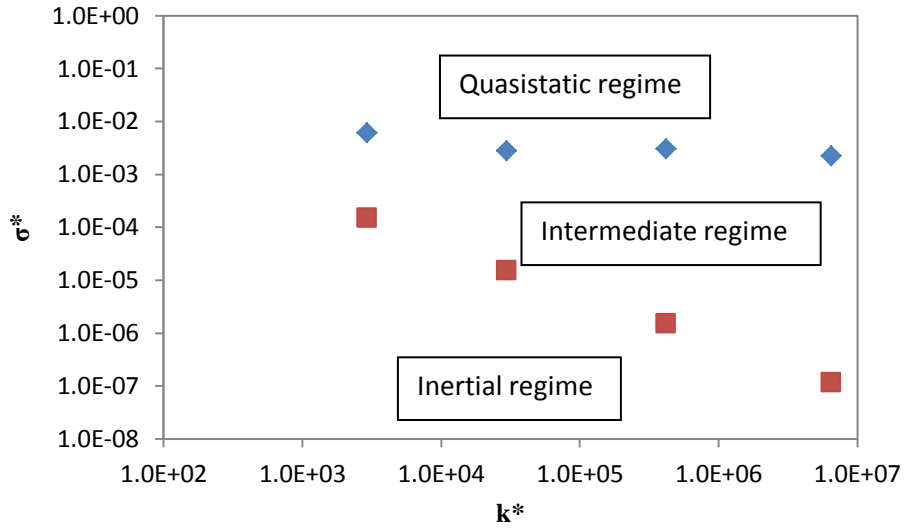
particle assemblies is not as sharp as it is for spherical particle flow.



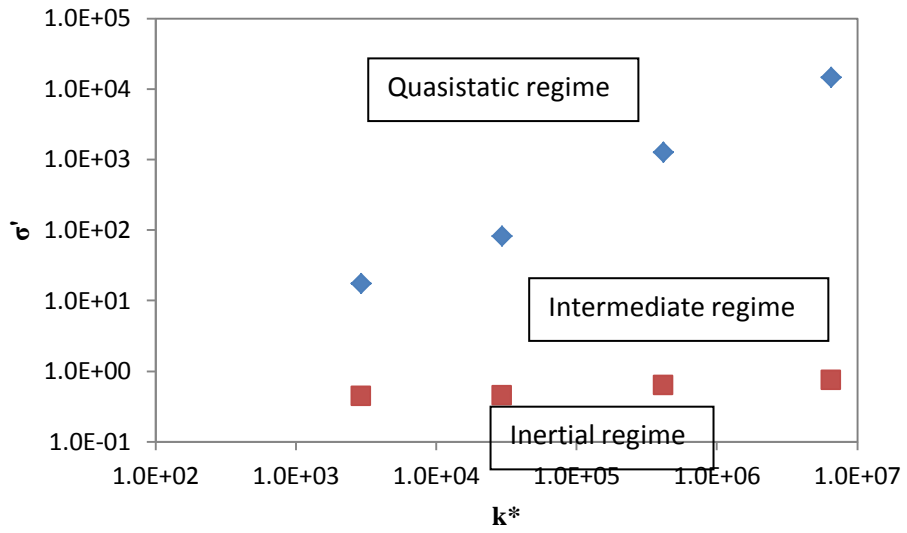
(a)



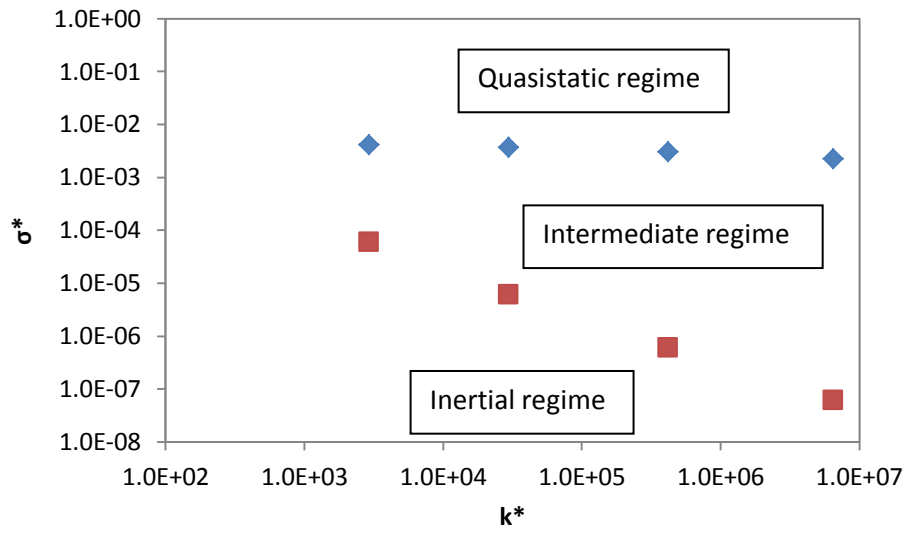
(b)



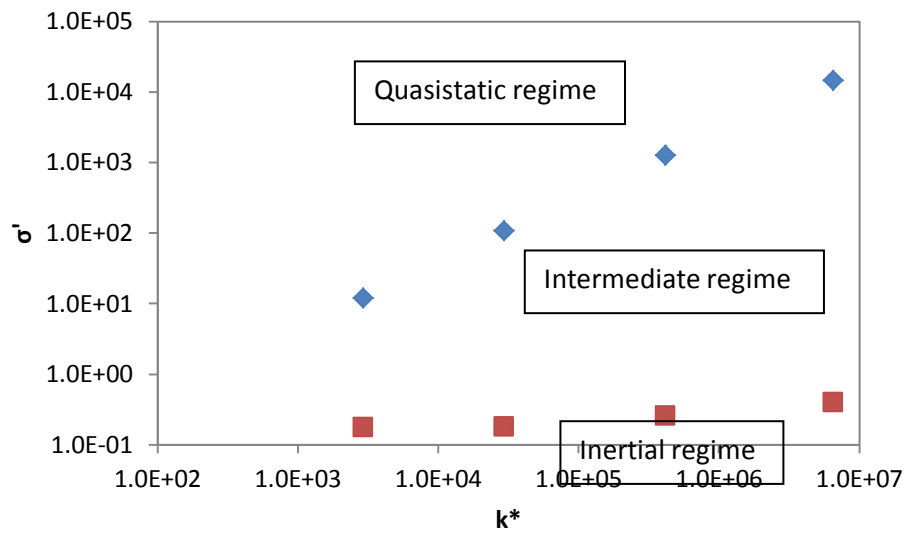
(c)



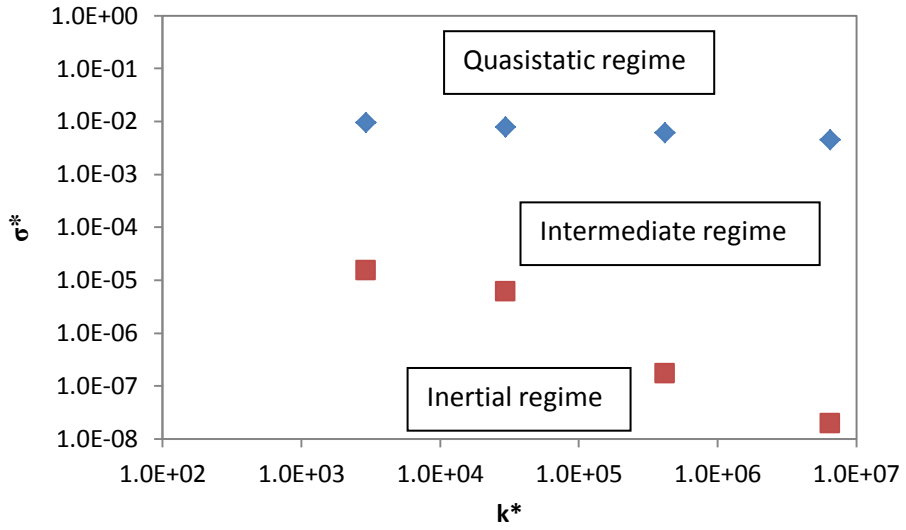
(d)



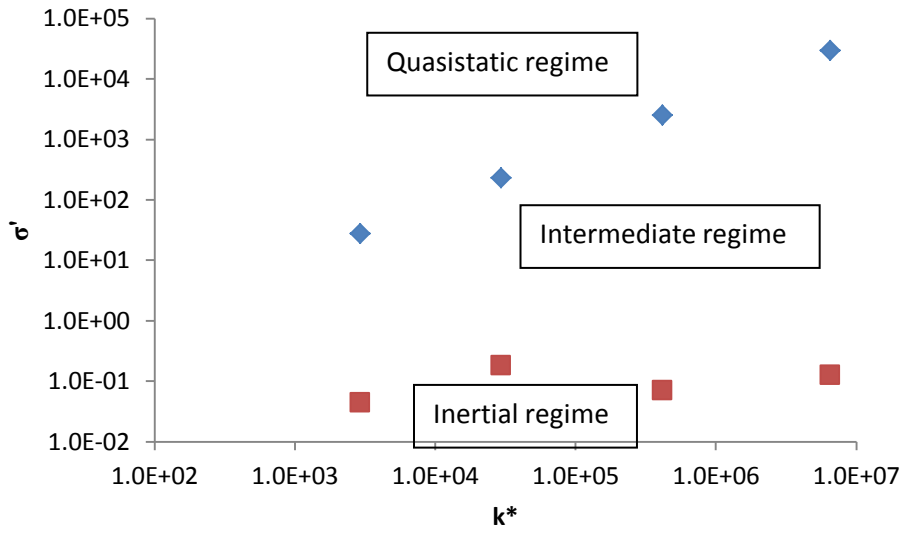
(e)



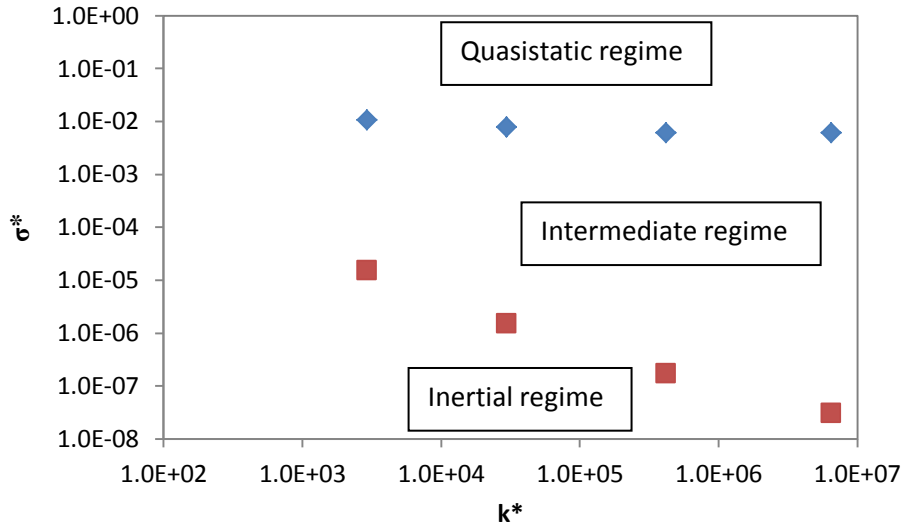
(f)



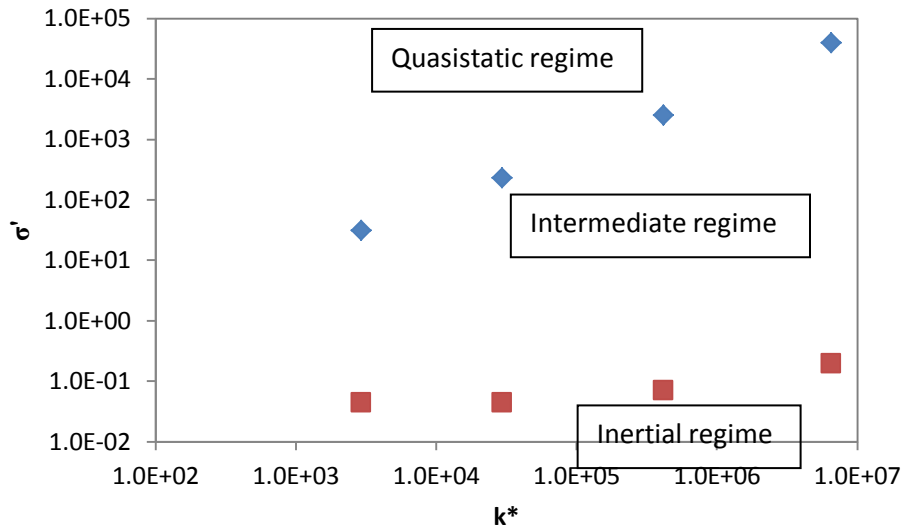
(g)



(h)



(i)



(j)

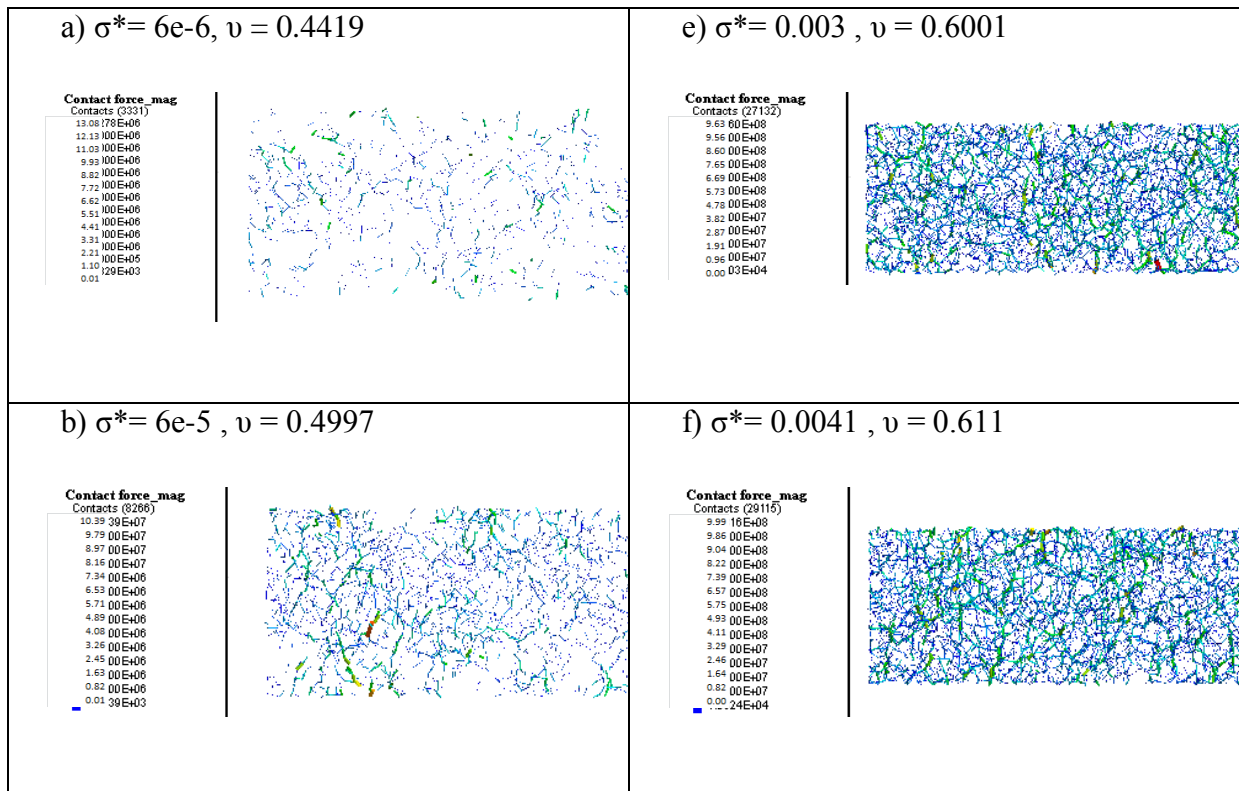
Figure 7.2: Regime map in the parametric space of:  $(\sigma^*, k^*)$  in a), c), e), g) and i) and  $(\sigma', k^*)$  in b), d), f), h) and j) for spherical particles, ellipsoidal particles of 1.75:1, 2.5:1, 375:1 and 5:1 aspect ratios, respectively.

### 7.3.2. Structural analysis

Next, structure of force network is analysed to investigate the phenomenon at

microdynamic level. In our previous study we observed similar results for spherical particles in [9] where a 2d thick slice was considered through a shear cell segment. Normal contact forces were scaled by macrodynamic mean value of normal contact force and the thickness as well as color gradient of the sticks representing force chains were proportional to scaled magnitude. In our study we use a similar method of observation for ellipsoidal particle assembly (2.5:1 aspect ratio). Again, similar to chapter 6, we choose this aspect ratio as it is in median position of the cases considered here to highlight the difference between ellipsoidal and spherical particle assembly.

In Fig. 7.3 we show the contact force chain network for eight different applied load conditions at the scaled stiffness 2920. The eight points are selected because they best represent regime transition. Similar to what we have seen for spherical particles in [9] the change in the force network structure is rather gradual: at lower load in Fig. 7.3a, the force network is very diluted and discontinuous. It means that particles are more disconnected and consequently free to produce varied dynamics.





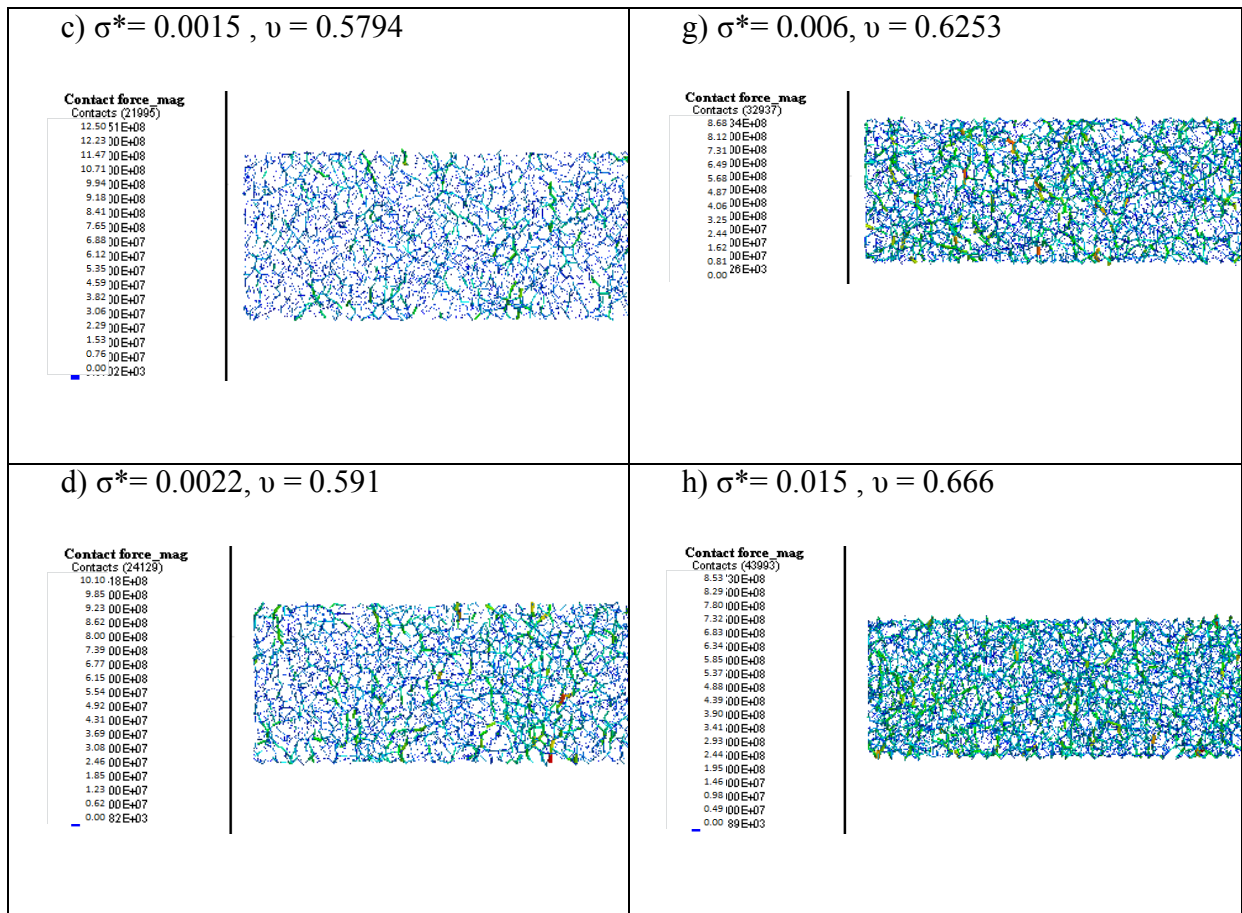


Figure 7.3: Networks of scaled forces ( $f = F_n / \langle F_n \rangle$ ),  $\sigma^*$  and  $\nu$  when  $k^* = 2920$  different loads for ellipsoidal particles of 2.5:1 aspect ratio.

It is also evident from the height of the upper layer of force chains that particle assembly has more space to move about. As load increases through Figs. 7.3b and c, the network gradually becomes denser and more continuous although scattered high load force chains can be seen. The externally applied load is still carried by some larger force chains but they are supported by surrounding weak force chains.

At the same time, the height of the upper platen is lower, and particle assembly is squeezed in. The particles' movement become more restricted and consequently inertial effect is systematically overpowered by the force chain network produced by upper platens. In Fig. 7.3d, the force chain network becomes fully continuous and tightly knit and the high load force chains have disappeared. In Fig. 7.3e, the assembly is further compressed and the

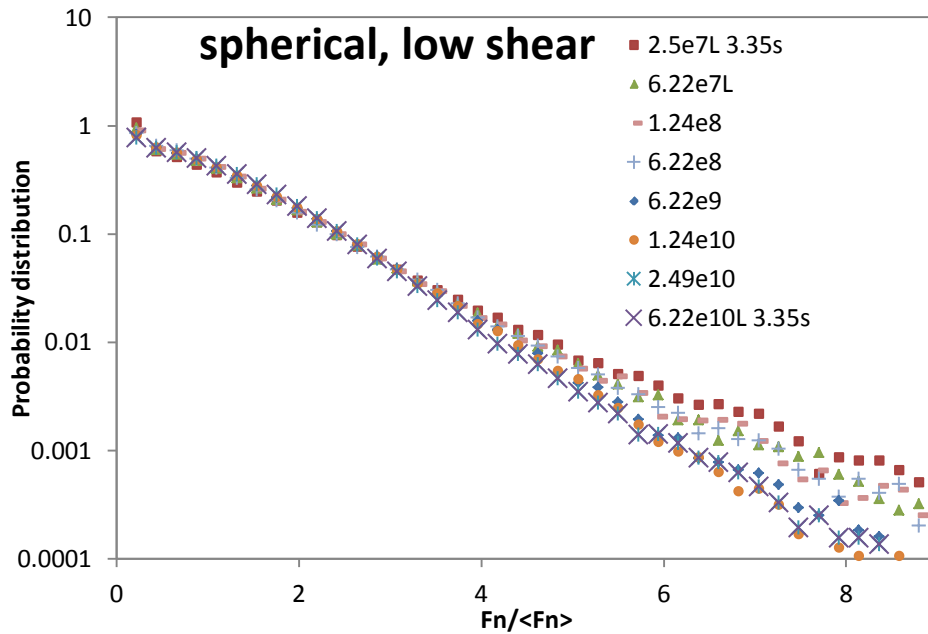
structure remains stable through 7.3e to h. During these conditions, the externally applied load by the upper platen is carried by a large number of weak force chains in a collective way. So the regime transition from intermediate to quasistatic regime occurs somewhere between Fig. 7.3d and e which is consistent with the point identified earlier.

### 7.3.3. Force statistics

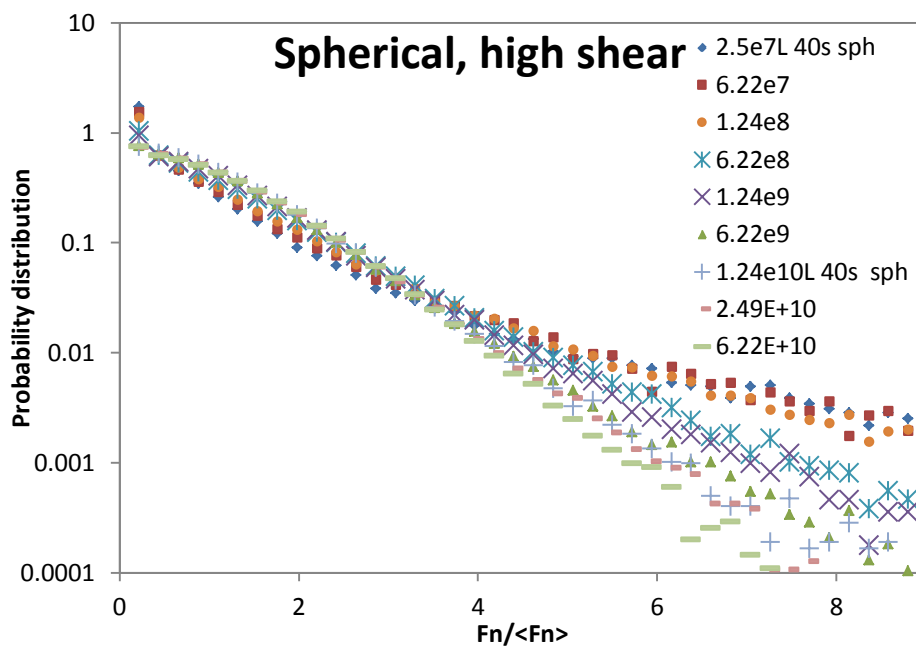
Probability distribution of contact forces is a popular indicator for the effect of various influencers of granular rheology (eg. [76, 197-199]). In our study of effect of platen roughness on granular flow, we found that as the platen roughness increases, force fluctuation declines at higher band of forces. In our study on the effect of particle elongation on granular flow, we found that as the particle elongation increases, probability distribution of force decreases at higher value forces. We use a similar method to investigate the effect of particle shape on force statistics with respect to regime transition. An earlier study by Wang et al. [9] developed a novel method to identify quasistatic regime transition point using probability distribution of scaled normal contact forces. In our study, we will verify that method and then apply it for ellipsoidal particle flow to observe its usability.

Figures 7.4 a-d shows probability distribution of scaled normal contact force  $F_n/\langle F_n \rangle$  during granular flow of ellipsoidal (aspect ratio 2.5:1) and spherical particles under low and high shear. At first, if we look at the trend for spherical particles we see in Fig. 7.4 a and b a similarity to what was observed by Wang et al. [9]: semi-log graph showing that probability trend collapses near the mean normal contact force while the tail of the distribution becomes higher at low applied load for both low and high shear. This finding is also in agreement with [13] which shows that increase in load lowers the tail of probability distribution where the band of very large forces exists. Physically it means that when applied pressure on particle under flow is less, probability of large contact forces in the chain network to exist is higher which is also evident from spherical force chain network shown in [9]. When, the applied pressure increases, the distribution of force chains becomes more uniform and random large force chains disappear, hence, there is less probability of high normal contact forces. If we compare Fig. 7.4 a with b, we find that the tail of probability distribution tends to be wider for high shear rate (low  $k^*$ ) compared to that of low shear rate (high  $k^*$ ). Next, following the method of Wang et al., we obtain the best fitting exponential curve for each distribution curve

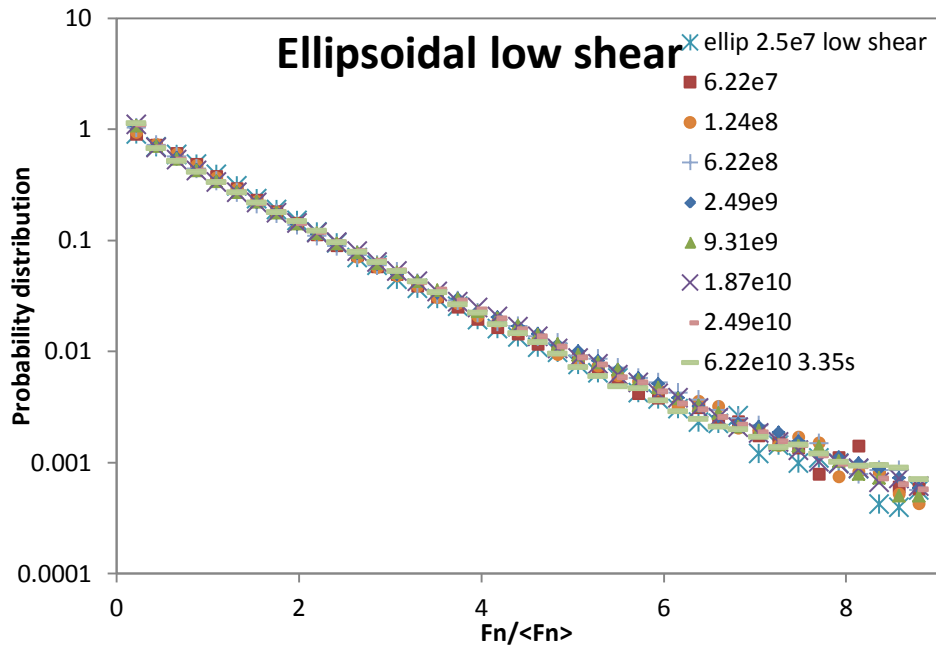
for low and high shear rate and different applied load combinations in the form of  $P(f) = \exp(-cf^n)$ . Figure 7.5a depicts the relationship between parameter ‘n’ and volume fraction, and produces a similar collapse near the quasistatic regime transition point with volume fraction of 0.58.



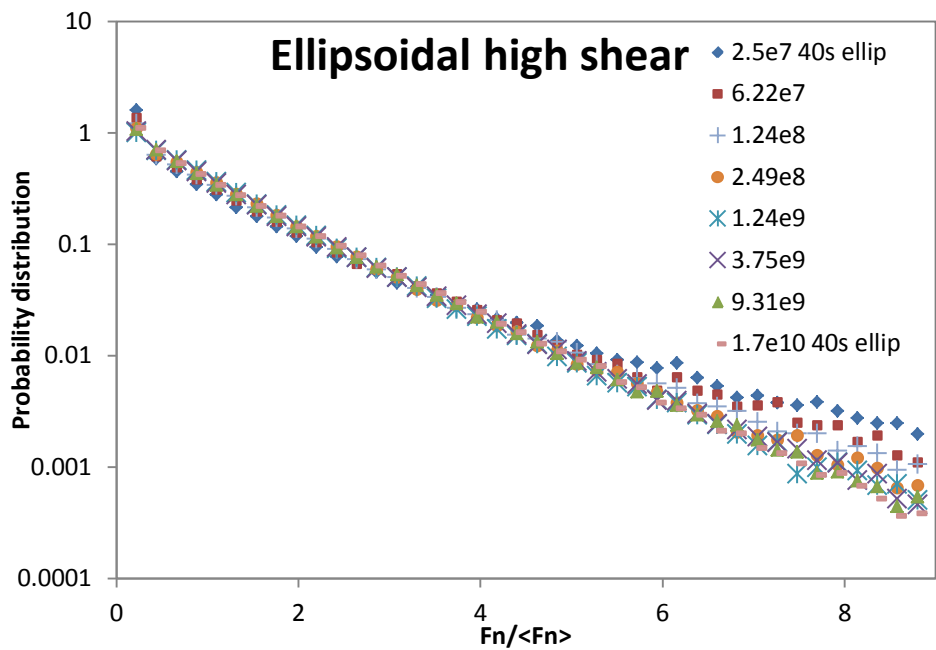
(a)



(b)



(c)

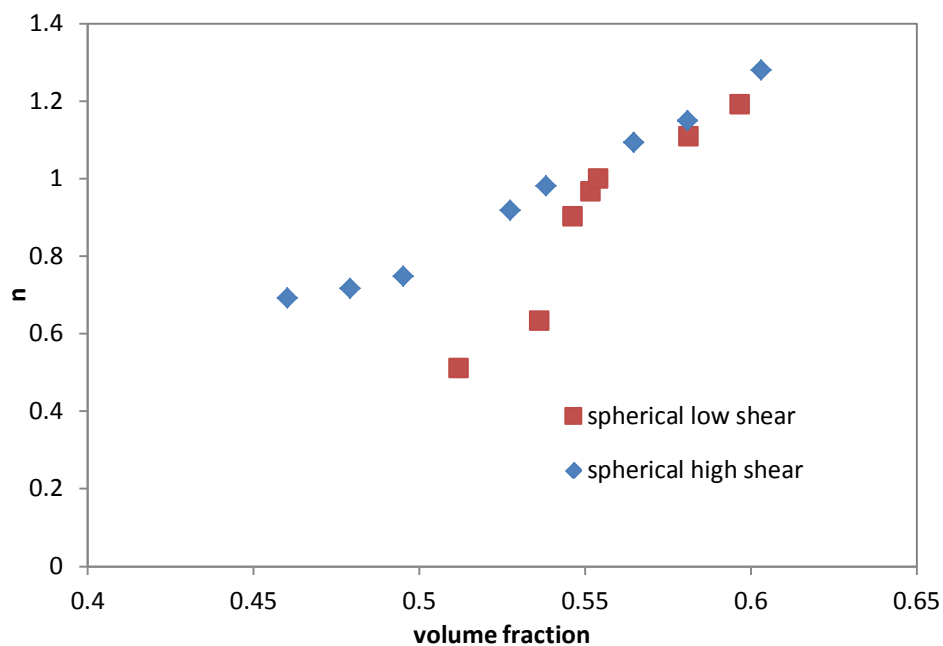


(d)

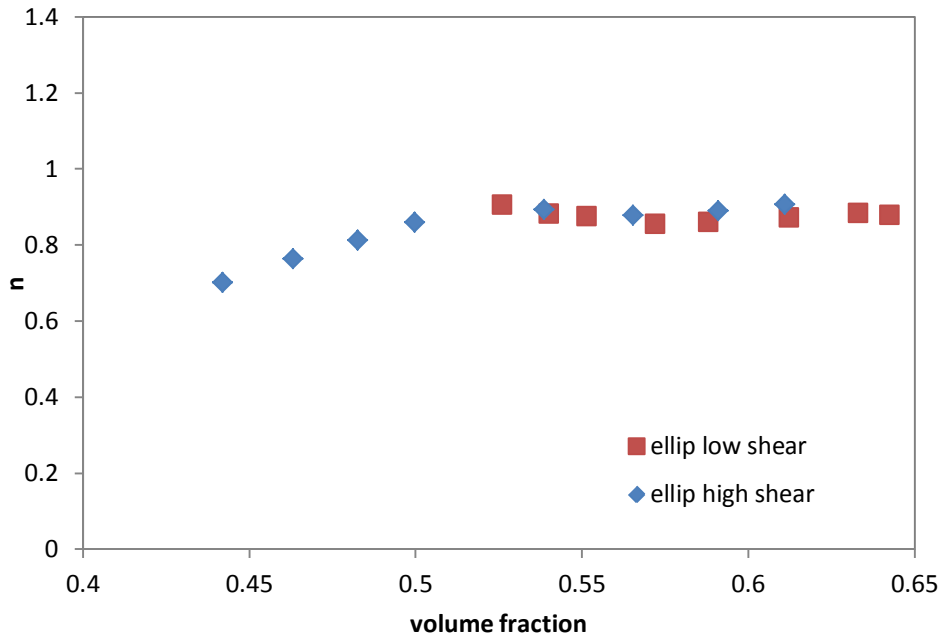
Figure 7.4: Probability density distributions of the scaled normal forces ( $f = F_n / \langle F_n \rangle$ ) for different  $\sigma^*$ 's for spherical particles (a) at low shear and (b) high shear rate and for ellipsoidal particles (2.5:1 aspect ratio) (c) at low shear and (d) high shear rate, respectively.

In contrast, Fig. 7.4c and d shows probability distribution of scaled normal contact forces of ellipsoidal particles under varying load conditions in low and high shear rate, respectively. In the case of low shear in Fig. 7.4c, we find that the widening of scaled normal forces at the tail of distributions is absent. Then, if we investigate high shear condition in Fig. 6d and find that although widening of tail end of distribution curves is indicated, it is not in the same noticeable order of magnitude as occurred with the spherical particles.

Further we plot the relationship between fitting parameter ‘n’ with volume fraction for ellipsoidal particle flow in Fig. 7.5b and as was done in Fig. 7.5a, we do not find varying load and shear condition having a noticeable impact on ‘n’. The reason may be that the uniform force chain network forms much more quickly for elongated ellipsoidal particles due to preferential alignment which is not the case for spherical particle flow. This consequently results in scattered large contact force chains disappearing from the granular flow region much earlier that what is found for spherical particle flow. While much of this has been discussed in earlier chapters, we can say for now that the ‘n’ and volume fraction relationship cannot be universally applicable for particles of any shape.



(a)



(b)

Figure 7.5: Variation in the power index  $n$  with volume fraction for high and low shear rate for a) spherical and b) ellipsoidal particles.

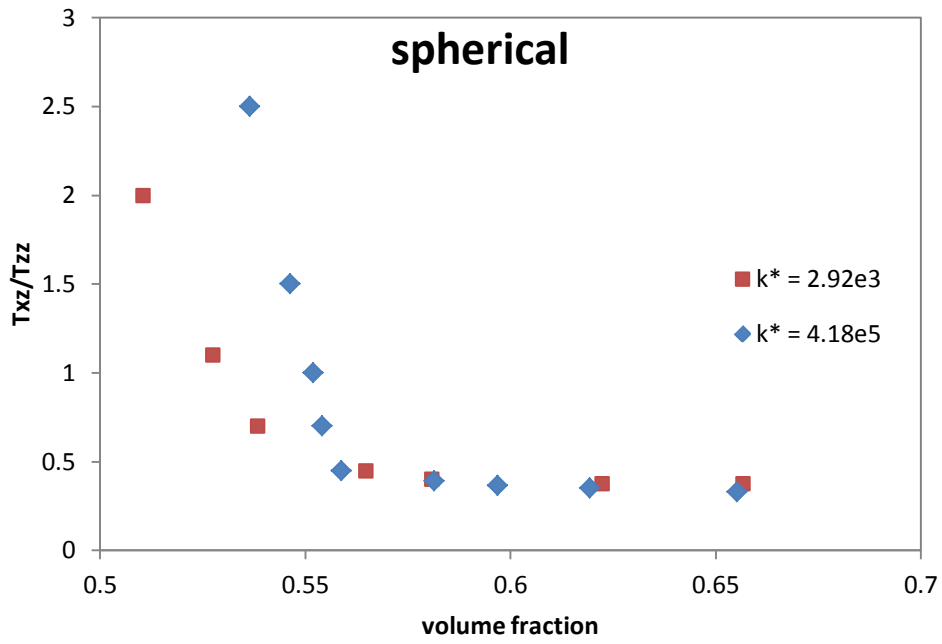
### 7.3.4. Shear to normal stress ratio

In order to identify the inertial regime, another method of observation is tried here. Figure 7.6 shows the relationship between shear to normal stress ratio and volume fraction for two different scaled stiffness in varying load condition for spherical and ellipsoidal (2.5:1 aspect ratio) particle assembly. Here we find for both cases, two correlation curves (each corresponds to one  $k^*$  value) are separated at lower volume fraction, i.e. lower applied load. As the externally applied load increases, the volume fraction granular assembly under shear increases too until it reaches volume fraction that is close to the point of intermediate to inertial regime transition identified earlier. Above this volume fraction, the two curves collapse into a single curve. Clearly, a transition has occurred at that point and we can relate this to inertial point of regime transition from our investigation earlier. Above this volume fraction point, the relationship between  $T_{zz}$  and  $T_{xz}$  becomes almost constant and

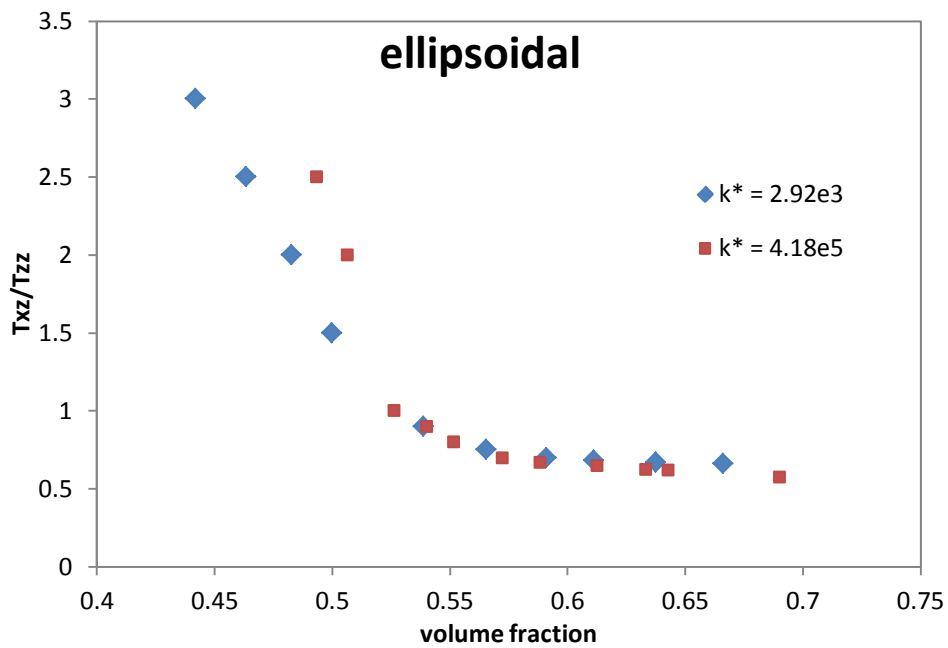
independent of volume fraction and hence applied pressure as well. Interestingly, if we look more closely into this value, it is near the value of particle friction coefficient of 0.5.

From a physical point of view, it means that while granular assembly is in inertial state of flow, its overall global shear stress can be much higher compared to overall global normal stress. In other words, the shear to normal stress ratio not only depends on the particle material property of friction coefficient but also inertial effect. In this circumstance, any magnitude of stress ratio can be obtained at a much lower volume fraction with higher shear rate compared to the volume fraction corresponding to lower shear rate. This is because of inertial effect resulting from increased shear. However, following the transition of granular flow out of inertial regime, it depends only on the friction coefficient. When we compare Fig. 7.6a and b, we find that the transition occurs rather sharply for spherical particles at low shear rate (high  $k^*$ ) while the transition is smooth and gradual for ellipsoidal particles. It is similar to our finding in the analysis of regime transition where intermediate regime for ellipsoidal particle assembly is not as contrast as it is for spherical particle assembly.

The relationship corresponding to shear to normal stress ratio has been examined earlier also [48] for spherical particle assembly. However, it was in volume controlled granular flow. In that study, the relationship between  $T_{xz}/T_{zz}$  with  $k^*$  was observed for various loads, shear rates and friction coefficients. Nevertheless, the relationship curve still indicated transition. Therefore in our study, we can show that it can also be used in stress-controlled granular flow and moreover it is applicable for both spherical and non-spherical (in our case ellipsoidal) particles.



(a)



(b)

Figure 7.6: Relationship between shear to normal stress ratio and volume fraction for high and low shear rate for a) spherical and b) ellipsoidal particles (2.5:1 aspect ratio)



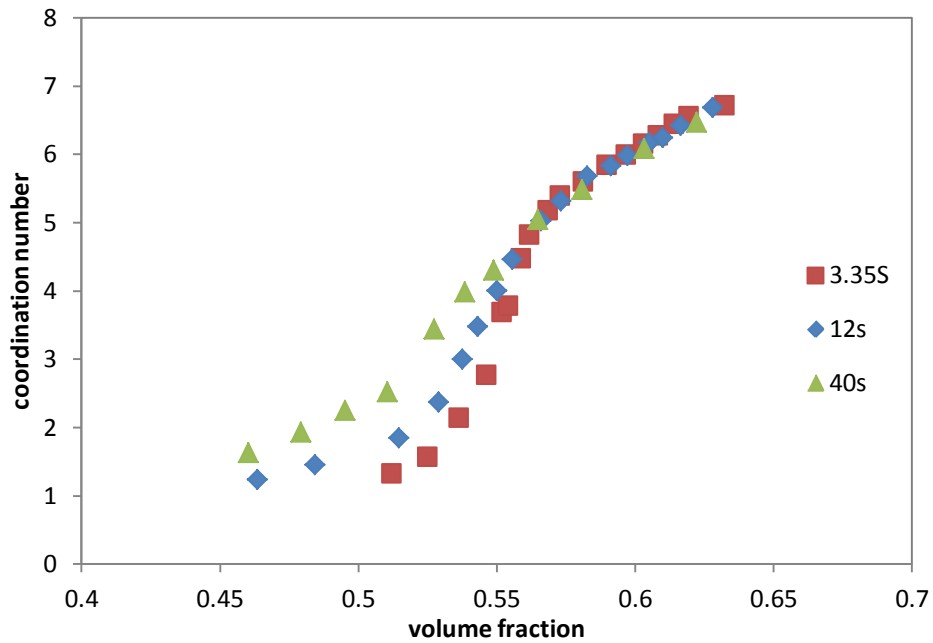
### 7.3.5. Coordination number

Fig. 7.7 displays the relationship between overall coordination number and volume fraction of the particle assemblies at different flow conditions in terms of  $\sigma^*$  and  $k^*$ . Coordination number is obtained by the equation:  $CN = 2 N_c/N$ , where  $N_c$  is the number of contacts and  $N$  is the number of particles. It has a clear differentiating element between the ellipsoidal and spherical particle assemblies. Fig. 7.7a illustrates a similar relationship to Fig. 7.2a, in that there exists a critical volume fraction for low shear rate (high  $k^*$ ) flow condition at which the coordination number changes rapidly with little change in volume fraction. Again, it disappears as the shear rate increases (or  $k^*$  decreases). A similar observation was found in [9]. Then, at higher volume fraction, the data collapse into a single curve. Coordination number for the ellipsoidal particle assembly is much higher than that of the spherical particle assembly. Similar observations were found in [66]. But a striking finding in Fig. 7.7b shows very little change in the coordination number volume fraction relationship in the flow of ellipsoidal particles. It is the explicit depiction of the organized structure of ellipsoidal particles in the steady-state condition.

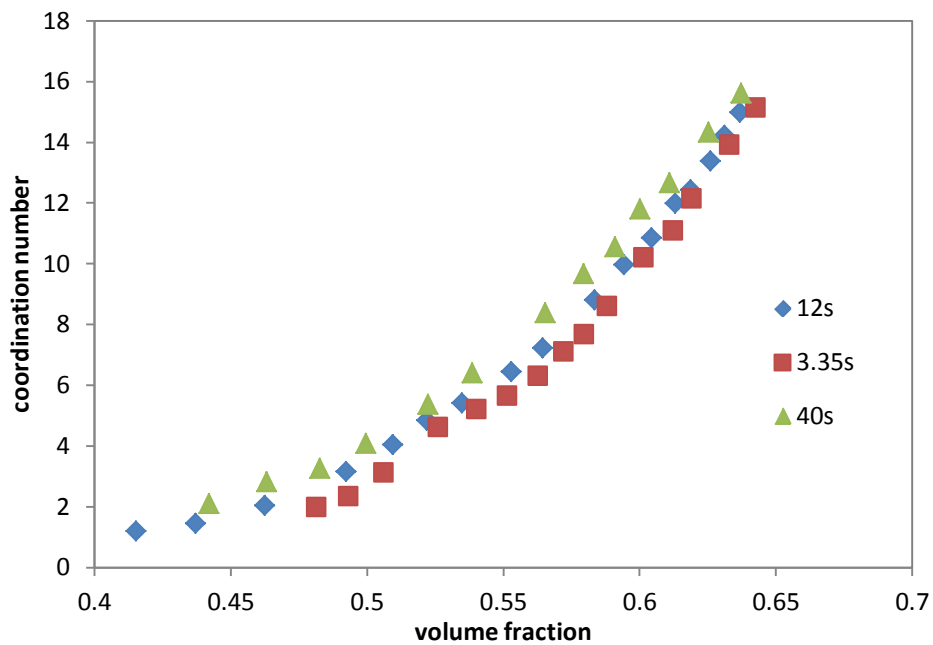
However, there still exists a minor effect of induced shear with increasing shear rate (or decreasing  $k^*$ ), which marginally increases the overall coordination number which simply can be due to faster movement causing more rapid interaction of particles. It is worth mentioning that in all cases, there exists a positive relationship between coordination number and volume fraction which concurs with [13]. It is an interesting finding suggesting that the relationship between coordination number and volume fraction may not be universally applicable. In an extension of the discussion in Section 7.3.1 in light of physical events, the stage regarding critical volume fraction region can be observed from Fig. 7.7a. At a diluted condition, the compressibility of spherical particle assembly is high due to the abundant free path for particles. Thus, the volume fraction reduces without having much impact on the inertial regime-like contact network [9].

Once the capacity compressing the assembly in its diluted state reaches its peak point, the process of continuously rearranging the structure cannot be maintained any further and load bearing contact network starts building up rapidly (as seen in Fig. 7.7a). On the other hand, for ellipsoidal particles, since the particle alignment causes the load to be propagated in layers, there is no distinguishing shift from random rearrangement of individual particles into

the restricted dense state. As a consequence, shear rate does not affect the steady build-up of a load bearing contact network with increase in applied pressure. This is shown by the insensitivity of shear rate on coordination number variation with respect to volume fraction, as found in Fig. 7.7b.



(a)



(b)

Figure 7.7: Correlation between coordination number and volume fraction at different scaled stiffness for a) spherical particles and b) ellipsoidal particles of 2.5:1 aspect ratio.

### 7.3.6. Effect of aspect ratio on regime transition

In final part of this investigation, we investigate particle elongation points of regime transition. Figure 7.8 shows volume fraction for the two regime transition points for each shape of particles: spherical and ellipsoidal particles of 1.75:1, 2.5:1, 3.75:1 and 5:1 aspect ratio. Here, we find that changes in particle shape in terms of elongation do not much affect the volume fraction corresponding to regime transition into and out of the quasistatic regime. This is regardless of the significant rise in number of contacts we found in earlier chapters with changes in particle elongation. In other words, when particles interact and transmit force elastically, it does not make much difference how elongated the particles are. On the other hand, if we observe volume fraction corresponding to inertial regime transition for different elongated particles, we find that the magnitude of volume fraction gradually lowers. It means that the granular assembly under shear exits the inertial regime at lower volume fraction as the externally applied load is being increased. Here, we can state that the number of contacts plays a significant role in dissipating the inertial effect. Also, the fact that particle preferential alignment in the direction flow causes the stress transmission across the flow in prominent layers plays a major part in subduing inertial effect.

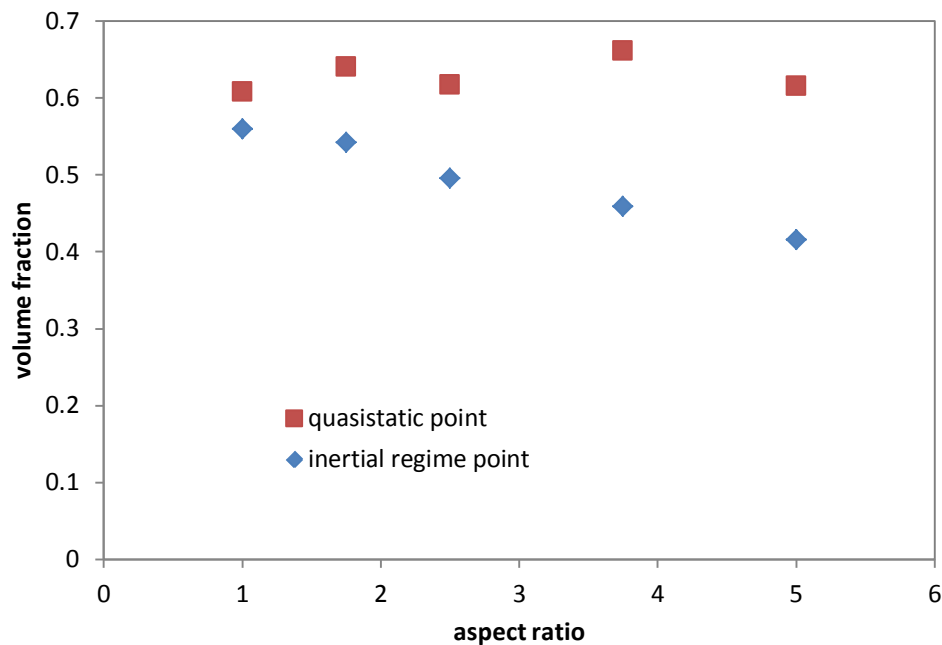


Figure 7.8: Effect of particle aspect ratio (elongation) on regime transition in terms of volume fraction.

This widening gap between transition points of the quasistatic and inertial regimes is another reason why the intermediate regime is not as sharp for ellipsoidal particles with higher elongation as it is for that of spherical particles.

## 7.4. CONCLUSION

Granular rheology of spherical and ellipsoidal particles of varying aspect ratios is studied through a segment of annular shear cell under stress-controlled condition for regime transition.

- Regime transition is observed from the correlation between volume fraction  $\nu$ , scaled stiffness  $k^*$  (function of shear rate), kinetically scaled stress  $\sigma'$  and elastically scaled stress  $\sigma^*$  for particles of different shapes. Particles of all shapes have produced a similar collapse of the  $\sigma^*$ - $k^*$ - $\nu$  relationship curves for quasistatic regime, depicting the independence of granular rheology from the effect of variation of shear rate.
- A similar observation regarding the collapse of  $\sigma'$ - $k^*$ - $\nu$  relationship curves highlights the inertial regime at the flow region where stress quadratically scales with shear rate. However, it can be seen that the regime is one where scaled stresses rapidly increase. There is little change in critical volume fraction particularly at lower scaled stiffness values in the case of spherical particles. Similar observation is not so sharp for the cases of ellipsoidal particles.
- Next we identify the regime transition points to obtain a map demarking regime transition for quasistatic and inertial regime. We find that a similar trend is followed by particles regardless of particle elongation or spherical shape. However, the point where the region-demarking shaded area meets is not so sharp for ellipsoidal particles as it is for spherical particles.
- A comparison of transition of internal force structure is presented between ellipsoidal particles and the study of spherical particles in [9]. The transition structure is similar in that force chains are scattered and sporadic at lower load which slowly builds up a tighter network as the pressure on particle assembly is increased. This is until the quasistatic regime transition point where the tight network of weak force chains are fully set up and remains stable regardless of increase in pressure. The only difference here is in the number of force chains which dramatically increase as particle elongation

also increases. As a result, the force per chain weakens too as they share more or less equally the externally applied load from the upper platen.

- We obtain scaled normal contact force data for a large period of time to observe change in probability distribution of force during regime transition for spherical particles and base case ellipsoidal particle of 2.5:1 aspect ratio. Here we find a notable difference between the results for spherical and ellipsoidal particles. The tail of the distribution in the curves lowers as the load is decreased as expected for spherical particles. No such effect, however, is evident for the ellipsoidal particles regardless of variation of scaled stiffness, i.e. shear rate. Further, we apply the force distribution best fitting exponential curve method used by Wang et al. in [9] and found that the correlation still holds true for spherical particles but is not applicable for ellipsoidal particles. So, this method's universal applicability to identify regime transition is questionable, especially when particle shape is taken into consideration.
- Next we try out a method of identifying regime transition from the relationship between  $T_{xz}/T_{zz}$  and volume fraction. A similar observation has been tried earlier in the case of volume-controlled rheological study in [48] between  $T_{xz}/T_{zz}$  and  $k^*$  to obtain the point of regime transition. Here we find similar results for ellipsoidal and spherical particle assembly, where the correlation curves collapse at the point of inertial regime transition. This suggests that the stress ratio is not affected by variation of shear rate. The physical interpretation is retained for further study.
- An important difference is that coordination number is negligibly affected by the change of flow condition for the ellipsoidal particle flow, unlike what has been found for the spherical particle flow resembling  $\sigma^*$ - $v$  curve study. The moderate regime transition for the ellipsoidal particle flow originates from the organized structure of these elongated particles through preferential orientation in the direction flow in steady state flow condition.
- Finally, we observe the effect of particle elongation on regime transition points in terms of volume fraction. Here we find that not much difference occurs for the quasistatic regime. However, for inertial regime transition the volume fraction systematically reduces along with elongation of ellipsoidal particles. This explains why critical volume fraction is not sharp for ellipsoidal particles. This also explains why the regime map does not have demarking regions meeting for ellipsoidal particles as it does for spherical particles.

# Chapter 8: Summary and Future Work

## 8.1. SUMMARY

The discrete element method is applied in this thesis to investigate granular rheology of spherical and ellipsoidal particle assembly flowing through shear cell. Key properties pertaining to granular shear flow are analysed using a virtual platform to compare between spherical and non-spherical particles:

1. Linear Velocity
2. Angular velocity
3. Particle orientation angle about y-axis (for elongated particles only)
4. Particle orientation angle about z-axis (for elongated particles only)
5. Contact normal force
6. Contact shear force
7. Total contact force
8. Slip contact energy
9. Contact force chain network
10. Coordination number
11. Volume fraction
12. Shear rate
13. Principal stress tensors (xx-, yy-, zz-)
14. Shear stress tensor (xz-)
15. Density
16. Gravitational force
17. Elastically scaled stress
18. Kinetically scaled stress

19. Scaled stiffness

20. Apparent friction coefficient (normal to shear stress ratio)

Further, the effect of shape is closely observed in an effort to derive relationships with important parameters. Finally, a novel method of identifying regime transition for non-spherical particles is introduced that could not have been possible for spherical particles. A summary of the conclusions in this thesis is presented below.

In Chapter 3, the study of linearity non-linearity of velocity profile, we find:

- as the platen particles increase in size, the velocity gradient profile becomes gradually linear. This transformation is more visible between 1.1d and 1.3d. Velocity slip is higher at the flow region near smoother platens. As a result, there is less transfer of shear effect which causes the core region to not be affected. When the platen particles are larger and the platen is rough, the flow distribution remains reasonably uniform across the cell. However, when the platens have less friction, there is non-linearity with higher variations near the platens.
- When platen particles are smaller causing the platens to be less frictional, angular velocity varies more strongly across the flow with the highest being near the platens and not so much at the core. As the platens become more frictional with larger particles, the angular velocity becomes converted to linear velocity increasingly and angular velocity is more uniformly distributed.
- When the platen particles are smaller, force profile is non-linear with the lowest values being at the core region. As the platen particles increase in size, the force is more uniformly distributed and the velocity profile becomes linear.
- Moment distribution shows similar a pattern to that of contact force. This variable, however, has another indicator near the driving boundaries, i.e. platens. Although this is a stress controlled model and contact force at the boundary adjacent region is constant, contact moment increases with size of platen particles, i.e. platen surface roughness. This phenomenon is considered to significantly contribute to angular velocity, granular temperature and velocity slip. Porosity is increasingly homogeneous across regions as the platens become more frictional.

In Chapter 4, the study of effect of gravity, we find:

- the pattern is asymmetric particularly at low load when gravity is having an effect and gradually becomes symmetric as the load is increased. When there is no gravitational effect, symmetric gradient profiles in all the cases are considered. When the applied load is the highest in magnitude, profiles with and without gravity become completely overlapped. This observation implies that the flow has become independent of gravity. At this point, applied load at the upper platen of the cell has the same influence on flow as that at the lower platen. When gravitational effect is active, particle velocity in the double-shear condition is unbalanced at low applied load. In this scenario, more particles tend to flow in the direction where the lower platen is moving to.
- Porosity and coordination number have distribution trends similar to what is found in the case of velocity. Their distributions are symmetric for all cases. An exception is observed for the cases with low load where the gravitational effect is in place. In this circumstance, porosity increases with the increase in height, while the coordination number decreases. Overall coordination number decreases with an increase in overall porosity. The relationship between the coordination number and porosity is independent of gravity for high load, but is influenced by the effect of gravity significantly for low load.
- Analysis of network distribution finds that the load becomes uniformly distributed due to the organized structure of particle assembly at the lower region. As a result, individual particles are required to carry a smaller load compared to the upper region of the cell. This is because in the upper region, fewer sparsely dispersed contact networks carry the applied load from the upper platen. Consequently, there is asymmetry in force distribution with lower average particle force near the lower platen. Accordingly, the particle contact force at the lower region is lower while the total contact force at this region is higher due to gravity. This also creates asymmetry in the distributions of particle velocity, coordination number and porosity at low load. When applied load is low in magnitude, normal stress distribution is found to vary in the presence and absence of gravitational force. When there is no gravity, normal stresses indicate a similar trend to that found in the case of high load except that they have less magnitude. On the other hand, there is a different trend when gravitational effect is active. Interestingly, the trend of



shear stress distribution is similar across the flow except that gravity causes shear stress to increase by magnitude.

In Chapter 5, the study of comparison between rheology of spherical and ellipsoidal particles, we find:

- the major axes of ellipsoidal particles are approximately aligned with the direction of shear velocity of the flow. Both spherical and ellipsoidal particles exhibit linear velocity distributions. There is no significant difference for the two kinds of particles in terms of the velocity profile. The main difference is seen in velocity fluctuation as preferential alignment damps down velocity fluctuation.
- Angular velocity is strongly affected by particle elongation due to increased restriction of the ability to rotate.
- Overall coordination number and volume fraction are found to be higher in of the rheology of ellipsoidal particles. Like the spherical particle assembly, there exists a linear relationship between volume fraction and coordination number for ellipsoidal particle flow.
- The shape of ellipsoidal particles also affects forces in that ellipsoidal particle assembly has a much higher shear force than spherical particles. Overall, there is less dispersion in the distributions of velocity and forces for ellipsoidal particle assembly compared to the spherical particles.
- Force chain network for ellipsoidal particles shows a denser and more uniform tight-knit structure than that of spherical particles. This is also linked to the increased number of contacts. As a result each force chain needs to carry less load in ellipsoidal particle flow.
- Observation of energy shows that slip energy experiences a major impact from particle elongation as the rubbing between particles increases between layers.
- A preliminary study of probability distribution of orientation angle of elongated particles shows the peak of distribution for orientation angle gradually increasing at near zero value in polar axis. Externally applied load increases at low shear flow condition. In contrast, this effect is not so clear at higher shear velocity.
- Correlation between particle orientation angle and volume fraction is investigated for different shear rates. An interesting new finding is obtained which presents data

collapse for the correlation curves below a volume fraction similar to that of regime transition for inertial regime. More work on it proposed.

In Chapter 6, the macrodynamic analysis of spherical and ellipsoidal particle flow, we find:

- the spatial distribution of ellipsoidal granular flow is more uniformly distributed than the spherical one.
- Preferential alignment causes gradation of velocity across the layers in vertical direction more distinct for ellipsoidal particles.
- Particle aspect ratio impacts fluctuation of velocity at the earlier stage of particle elongation (from spherical shape) and eases off at higher elongated shape.
- Observation of stress tensors showed that there is not much effect on principal stresses  $T_{xx}$ ,  $T_{yy}$  and  $T_{zz}$ . Significant effect from particle elongation takes place for shear stress  $T_{xz}$  because of increased surface friction between layers. Higher number of force chain network has an important role to play in this phenomenon.
- Inertia number shows a clear gradient across flow which is more uniformly distributed for ellipsoidal particles.
- The friction coefficient seems to be independent of the inertia number for ellipsoidal particles which is not the case for spherical particle flow.
- A positive relationship is evident between particle aspect ratio and overall inertia number, suggesting higher inertia force at work against applied force for more elongated particles. An analysis on the effect of particle friction coefficient shows that its influence is much greater on elongated non-spherical particles because of the way non-spherical particles are arranged in the flow region.

In Chapter 7 concerning the regime transition of rheology of spherical and ellipsoidal particles, we find:

- the ellipsoidal assembly shows data collapse in the study of  $\sigma^*-v$  and  $\sigma'-v$  correlation curves, which is similar to what has been found for spherical particles. The regime map is created for spherical and ellipsoidal particles with reference to four aspect ratios.

- The gap between two regime transition points obtained from the  $\sigma^*$ - $v$  and  $\sigma'$ - $v$  curves is observed to be higher for ellipsoidal particles which progressively increases with aspect ratio. This is also reflected in the inertial regime transition point.
- Critical state volume fraction (or concentration) exists for the spherical particles at lower shear rate, but is almost absent for the ellipsoidal particle flow when compared to the trend concerning spherical particles.
- An important distinguishing feature is that the coordination number is negligibly affected by the change in flow condition for the ellipsoidal particle flow, unlike what has been found for the spherical particle flow resembling  $\sigma^*$ - $v$  curve study.
- The new method of identifying regime transition tried in [9] is found to be applicable for spherical particle assembly but not ellipsoidal particle assembly.
- The moderate regime transition for the ellipsoidal particle flow and their striking difference in the coordination number's dependence on volume fraction derives from the organized structure of these elongated particles. Specifically, it is caused by preferential orientation in the direction flow in steady state flow condition.

## 8.2. FUTURE WORK

In this thesis, spherical particles were used to create only monotype ellipsoidal shaped non-spherical particles. In a practical scenario, different shaped particles can exist. Moreover, the same assembly is likely to contain particles of different shapes. Considering these factors some future investigations are proposed.

1. The scope of research has the potential to examine more interesting and complex shapes of granular rheology. Only ellipsoidal particles were considered here for examining the effect of particle shape on granular rheology. However, there are a number of ways particles can be shaped: cube, cylindrical, amorphous and so on. All these shapes provide opportunities for research of regime transition in the future to observe if shapes affect transitional properties or not.
2. This thesis considered only coarse particles in the investigation of regime transitions and regime charts of the shear flow in the cell. Therefore the cohesive forces such as the electrostatic force, Van der Waals force were neglected. In reality, most often there are fine particles which are commonly used in industry tend to retain such forces

among them. Although there are studies for spherical particles with such forces, these forces have not been tried extensively on non-spherical particles. It would be interesting to examine the influence of such non-contact forces on the regime transitions in the present cell.

3. Interstitial medium is another prospective element for research for non-spherical particles. Based on the observation of higher number of contacts and more tightly knit force chain network for non-spherical elongated particles, it can be expected that interstitial medium will have much stronger influence on elongated non-spherical particle assemblies than spherical ones. So, we plan for extending research of effect of interstitial medium on granular rheology of non-spherical particles.
4. As mentioned earlier, the same assembly may have particles of multiple shapes. So, it is important perform analysis on granular flow which constitutes particles of different shapes. Therefore we propose, extensive study of granular rheology which constitutes similar shape, say ellipsoidal, but different elongations in the same assembly. There onwards, we observe how different elongated particles are distributed, how force distribution is affected and how velocity is disseminated across flow region.

# References

1. Hertz, H., *Hertz Theory (Über die Berührung fester elastischer Körper)*. Journal für die reine und angewandte Mathematik, 1881(92): p. 156-171.
2. Cundall, P.A. and O.D. Strack, *A discrete numerical model for granular assemblies*. Geotechnique, 1979. **29**(1): p. 47-65.
3. Cundall, P., *Computer simulations of dense sphere assemblies*. Micromechanics of granular materials, 1988. **4**: p. 113-123.
4. Hart, R., P. Cundall, and J. Lemos. *Formulation of a three-dimensional distinct element model—Part II. Mechanical calculations for motion and interaction of a system composed of many polyhedral blocks*. in *International Journal of Rock Mechanics and Mining Sciences & Geomechanics Abstracts*. 1988. Elsevier.
5. Campbell, C.S., *Elastic granular flows*. International Journal of Chemical Reactor Engineering, 2004. **2**(2): p. 2.
6. Campbell, C.S., *Stress-controlled elastic granular shear flows*. Journal of Fluid Mechanics, 2005. **539**(-1): p. 273.
7. Aarons, L. and S. Sundaresan, *Shear flow of assemblies of cohesive and non-cohesive granular materials*. Powder Technology, 2006. **169**(1): p. 10-21.
8. Aarons, L. and S. Sundaresan, *Shear flow of assemblies of cohesive granular materials under constant applied normal stress*. Powder Technology, 2008. **183**(3): p. 340-355.
9. Wang, X., et al., *Regime transitions of granular flow in a shear cell: A micromechanical study*. Physical Review E, 2013. **88**(3): p. 032203.
10. Bell, N., Y. Yu, and P.J. Mucha. *Particle-based simulation of granular materials*. in *Proceedings of the 2005 ACM SIGGRAPH/Eurographics symposium on Computer animation*. 2005. ACM.
11. Zhu, H., et al., *Discrete particle simulation of particulate systems: theoretical developments*. Chemical Engineering Science, 2007. **62**(13): p. 3378-3396.
12. Zhu, H., et al., *Discrete particle simulation of particulate systems: a review of major applications and findings*. Chemical Engineering Science, 2008. **63**(23): p. 5728-5770.
13. Wang, X., H. Zhu, and A. Yu, *Microdynamic analysis of solid flow in a shear cell*. Granular Matter, 2012. **14**(3): p. 411-421.
14. Wang, X., H. Zhu, and A. Yu, *Flow properties of particles in a model annular shear cell*. Physics of Fluids (1994-present), 2012. **24**(5): p. 053301.
15. Jaeger, H.M. and S.R. Nagel, *Physics of the granular state*. Science, 1992. **255**(5051): p. 1523-1531.
16. Aranson, I.S. and L.S. Tsimring, *Continuum theory of partially fluidized granular flows*. Physical Review E, 2002. **65**(6): p. 061303.
17. Börzsönyi, T., et al., *Orientational order and alignment of elongated particles induced by shear*. Physical review letters, 2012. **108**(22): p. 228302.
18. Corwin, E.I., H.M. Jaeger, and S.R. Nagel, *Structural signature of jamming in granular media*. Nature, 2005. **435**(7045): p. 1075-8.
19. Edwards, S., *Equations of granular materials*. Physica A: Statistical Mechanics and its Applications, 1999. **274**(1): p. 310-319.
20. Savage, S.B., *The mechanics of rapid granular flows*. Advances in applied mechanics, 1984. **24**: p. 289-366.
21. Jop, P., Y. Forterre, and O. Pouliquen, *A constitutive law for dense granular flows*. Nature, 2006. **441**(7094): p. 727-730.
22. Potyondy, D., *PFC3D flat joint contact model version 1*. Itasca Consulting Group, Minneapolis, Technical Memorandum ICG7234-L, 2013.

23. Potyondy, D. and P. Cundall, *A bonded-particle model for rock*. International journal of rock mechanics and mining sciences, 2004. **41**(8): p. 1329-1364.
24. Zhu, H. and A. Yu, *Averaging method of granular materials*. Physical Review E, 2002. **66**(2): p. 021302.
25. Shadloo, M., G. Oger, and D. Le Touzé, *Smoothed particle hydrodynamics method for fluid flows, towards industrial applications: Motivations, current state, and challenges*. Computers & Fluids, 2016. **136**: p. 11-34.
26. Subramaniam, S., *Lagrangian–Eulerian methods for multiphase flows*. Progress in Energy and Combustion Science, 2013. **39**(2-3): p. 215-245.
27. Lun, C. and S. Savage, *A simple kinetic theory for granular flow of rough, inelastic, spherical particles*. J. Appl. Mech, 1987. **54**(1): p. 47-53.
28. Bercovier, M. and M. Engelman, *A finite-element method for incompressible non-Newtonian flows*. Journal of Computational Physics, 1980. **36**(3): p. 313-326.
29. Bharadwaj, R., et al. *A comparison of discrete element modeling, finite element analysis, and physical experiment of granular material systems in a direct shear cell*. in *Space Technology and Applications International Forum-STAIF 2008: 12th Conference on Thermophysics Applications in Microgravity; 1st Symposium on Space Resource Utilization; 25th Symposium on Space Nuclear Power and Propulsion; 6th Conference on Human/Robotic Technology and the Vision for Space Exploration; 6th Symposium on Space Colonization; 5th Symposium on New Frontiers and Future Concept*. 2008. AIP Publishing.
30. *PFC Help File*.
31. Mindlin, R., *Force at a point in the interior of a semi-infinite solid*. 1953, DTIC Document.
32. Mindlin, R.D. and H. Deresiewica, *Elastic spheres in contact under varying oblique forces*. Journal of applied mechanics, 2013. **20**.
33. Walton, O.R. and R.L. Braun, *Viscosity, granular-temperature, and stress calculations for shearing assemblies of inelastic, frictional disks*. Journal of Rheology (1978-present), 1986. **30**(5): p. 949-980.
34. Walton, O.R., *Numerical simulation of inclined chute flows of monodisperse, inelastic, frictional spheres*. Mechanics of materials, 1993. **16**(1-2): p. 239-247.
35. Langston, P., U. Tüzün, and D. Heyes, *Continuous potential discrete particle simulations of stress and velocity fields in hoppers: transition from fluid to granular flow*. Chemical Engineering Science, 1994. **49**(8): p. 1259-1275.
36. Langston, P., U. Tüzün, and D. Heyes, *Discrete element simulation of granular flow in 2D and 3D hoppers: dependence of discharge rate and wall stress on particle interactions*. Chemical Engineering Science, 1995. **50**(6): p. 967-987.
37. Lu, L.-S. and S.-S. Hsiau, *Mixing in vibrated granular beds with the effect of electrostatic force*. Powder technology, 2005. **160**(3): p. 170-179.
38. Yoshino, H., T. Nogawa, and B. Kim, *Vortex jamming in superconductors and granular rheology*. New Journal of Physics, 2009. **11**(1): p. 013010.
39. Zhu, H.P., et al., *Discrete particle simulation of particulate systems: Theoretical developments*. Chemical Engineering Science, 2007. **62**(13): p. 3378-3396.
40. Vun, S., J. Naser, and P. Witt, *Extension of the kinetic theory of granular flow to include dense quasi-static stresses*. Powder Technology, 2010. **204**(1): p. 11-20.
41. Drescher, A., *A. Drescher and G. de Josselin de Jong, J. Mech. Phys. Solids 20, 337 (1972)*. J. Mech. Phys. Solids, 1972. **20**: p. 337.
42. Rothenburg, L. and A. Selvadurai, *A micromechanical definition of the Cauchy stress tensor for particulate media*. Mechanics of structured media, 1981: p. 469-486.
43. Christoffersen, J., M. Mehrabadi, and S. Nemat-Nasser, *A micromechanical description of granular material behavior*. Journal of applied mechanics, 1981. **48**(2): p. 339-344.
44. Kanatani, K.-i., *A theory of contact force distribution in granular materials*. Powder Technology, 1981. **28**(2): p. 167-172.

45. Babić, M., *Average balance equations for granular materials*. International journal of engineering science, 1997. **35**(5): p. 523-548.
46. Baran, O. and L. Kondić, *On velocity profiles and stresses in sheared and vibrated granular systems under variable gravity*. Physics of Fluids (1994-present), 2006. **18**(12): p. 121509.
47. Babić, M., H.H. Shen, and H.T. Shen, *The stress tensor in granular shear flows of uniform, deformable disks at high solids concentrations*. Journal of Fluid Mechanics, 1990. **219**: p. 81-118.
48. Campbell, C.S., *Granular shear flows at the elastic limit*. Journal of Fluid Mechanics, 2002. **465**.
49. Campbell, C.S., *Granular material flows—an overview*. Powder Technology, 2006. **162**(3): p. 208-229.
50. Labuz, J.F. and A. Zang, *Mohr–Coulomb failure criterion*, in *The ISRM Suggested Methods for Rock Characterization, Testing and Monitoring: 2007-2014*. 2012, Springer. p. 227-231.
51. Mohr, O., *Welche Umstände bedingen die Elastizitätsgrenze und den Bruch eines Materials*. Zeitschrift des Vereins Deutscher Ingenieure, 1900. **46**(1524-1530): p. 1572-1577.
52. Aharonov, E. and D. Sparks, *Rigidity phase transition in granular packings*. Physical Review E, 1999. **60**(6): p. 6890.
53. O’Hern, C.S., et al., *Jamming at zero temperature and zero applied stress: The epitome of disorder*. Physical Review E, 2003. **68**(1): p. 011306.
54. Ciamarra, M.P. and A. Coniglio, *Jamming at zero temperature, zero friction, and finite applied shear stress*. Physical review letters, 2009. **103**(23): p. 235701.
55. Jackson, R., *Some mathematical and physical aspects of continuum models for the motion of the granular materials*. 1983.
56. Lechenault, F., et al., *Critical scaling and heterogeneous superdiffusion across the jamming/rigidity transition of a granular glass*. EPL (Europhysics Letters), 2008. **83**(4): p. 46003.
57. Majmudar, T., et al., *Jamming transition in granular systems*. Physical review letters, 2007. **98**(5): p. 058001.
58. Fiocco, D., G. Foffi, and S. Sastry, *Oscillatory athermal quasistatic deformation of a model glass*. Physical Review E, 2013. **88**(2): p. 020301.
59. Babić, M., H.H. Shen, and H.T. Shen, *The stress tensor in granular shear flows of uniform, deformable disks at high solids concentrations*. Journal of Fluid Mechanics, 1990. **219**: p. 81-118.
60. Gu, Y., A. Ozel, and S. Sundaresan, *Rheology of granular materials with size distributions across dense-flow regimes*. Powder Technology, 2016. **295**: p. 322-329.
61. Buchholtz, V., T. Pöschel, and H.-J. Tillemans, *Simulation of rotating drum experiments using non-circular particles*. Physica A: Statistical Mechanics and its Applications, 1995. **216**(3): p. 199-212.
62. Džiugys, A. and B. Peters, *An approach to simulate the motion of spherical and non-spherical fuel particles in combustion chambers*. Granular matter, 2001. **3**(4): p. 231-266.
63. Langston, P.A., et al., *Distinct element modelling of non-spherical frictionless particle flow*. Chemical Engineering Science, 2004. **59**(2): p. 425-435.
64. Campbell, C.S., *Elastic granular flows of ellipsoidal particles*. Physics of Fluids (1994-present), 2011. **23**(1): p. 013306.
65. Wouterse, A., S.R. Williams, and A.P. Philipse, *Effect of particle shape on the density and microstructure of random packings*. Journal of Physics: Condensed Matter, 2007. **19**(40): p. 406215.
66. Guo, Y., et al., *Granular shear flows of flat disks and elongated rods without and with friction*. Physics of Fluids (1994-present), 2013. **25**(6): p. 063304.

67. Matuttis, H., S. Luding, and H. Herrmann, *Discrete element simulations of dense packings and heaps made of spherical and non-spherical particles*. Powder technology, 2000. **109**(1): p. 278-292.
68. Peña, A.A., et al., *Avalanches in anisotropic sheared granular media*. Granular Matter, 2009. **11**(4): p. 243-252.
69. Seyedi Hosseininia, S.E., *Stress–force–fabric relationship for planar granular materials*. Geotechnique, 2013. **63**.
70. Vu-Quoc, L., X. Zhang, and O. Walton, *A 3-D discrete-element method for dry granular flows of ellipsoidal particles*. Computer methods in applied mechanics and engineering, 2000. **187**(3): p. 483-528.
71. Guises, R., et al., *Granular packing: numerical simulation and the characterisation of the effect of particle shape*. Granular Matter, 2009. **11**(5): p. 281-292.
72. Zhao, D., et al., *Three-dimensional discrete element simulation for granular materials*. Engineering Computations, 2006. **23**(7): p. 749-770.
73. Jia, X., et al., *Validation of a digital packing algorithm in predicting powder packing densities*. Powder Technology, 2007. **174**(1): p. 10-13.
74. Wang, G. and X. Pu, *A Numerical Study on Fracture-Plugging Behaviour of Granular Lost Circulation Materials*. Sains Malaysiana, 2014. **43**(5): p. 807-812.
75. Mollanouri Shamsi, M. and A. Mirghasemi, *Numerical simulation of 3D semi-real-shaped granular particle assembly*. Powder Technology, 2012. **221**: p. 431-446.
76. Azéma, E. and F. Radjaï, *Force chains and contact network topology in sheared packings of elongated particles*. Physical Review E, 2012. **85**(3): p. 031303.
77. Tao, H., et al., *Discrete element method modeling of non-spherical granular flow in rectangular hopper*. Chemical Engineering and Processing: Process Intensification, 2010. **49**(2): p. 151-158.
78. Grof, Z., M. Kohout, and F. Štěpánek, *Multi-scale simulation of needle-shaped particle breakage under uniaxial compaction*. Chemical engineering science, 2007. **62**(5): p. 1418-1429.
79. Taghavi, R. *Automatic clump generation based on mid-surface*. in *Proceedings, 2nd International FLAC/DEM Symposium, Melbourne*. 2011.
80. Azéma, E. and F. Radjaï, *Stress-strain behavior and geometrical properties of packings of elongated particles*. Physical Review E, 2010. **81**(5): p. 051304.
81. Guo, Y., et al., *Computational study of granular shear flows of dry flexible fibres using the discrete element method*. Journal of Fluid Mechanics, 2015. **775**: p. 24-52.
82. Cleary, P.W. and M.L. Sawley, *DEM modelling of industrial granular flows: 3D case studies and the effect of particle shape on hopper discharge*. Applied Mathematical Modelling, 2002. **26**(2): p. 89-111.
83. Abou-Chakra, H., J. Baxter, and U. Tüzün, *Three-dimensional particle shape descriptors for computer simulation of non-spherical particulate assemblies*. Advanced Powder Technology, 2004. **15**(1): p. 63-77.
84. Dong, K., C. Wang, and A. Yu, *A novel method based on orientation discretization for discrete element modelling of non-spherical particles*. Chemical Engineering Science, 2015.
85. Lu, G., J. Third, and C. Müller, *Discrete element models for non-spherical particle systems: From theoretical developments to applications*. Chemical Engineering Science, 2014.
86. Lin, X. and T.-T. Ng, *A three-dimensional discrete element model using arrays of ellipsoids*. Geotechnique, 1997. **47**(2): p. 319-329.
87. Torquato, S. and Y. Jiao, *Dense packings of the Platonic and Archimedean solids*. Nature, 2009. **460**(7257): p. 876-879.
88. S.H.L. Kriebitzsch, M.A.v.d.H.a.J.A.M.K., *Fully resolved simulation of flows with non-spherical particles using an immersed boundary method*. Ninth 1International Conference on CFD in Minerals and Process Industries, 2012.



89. Li, L. and R. Holt, *Approaching real grain shape in the simulation of sandstone using DEM*. P&G05, 2005. **2**: p. 1368-1373.
90. Mortensen, P., et al., *Dynamics of prolate ellipsoidal particles in a turbulent channel flow*. Physics of Fluids (1994-present), 2008. **20**(9): p. 093302.
91. Zhou, Z., et al., *Discrete particle simulation of gas fluidization of ellipsoidal particles*. Chemical Engineering Science, 2011. **66**(23): p. 6128-6145.
92. Donev, A., et al., *Underconstrained jammed packings of nonspherical hard particles: Ellipses and ellipsoids*. Physical Review E, 2007. **75**(5): p. 051304.
93. Fraige, F.Y., P.A. Langston, and G.Z. Chen, *Distinct element modelling of cubic particle packing and flow*. Powder Technology, 2008. **186**(3): p. 224-240.
94. Nougier-Lehon, C., *Effect of the grain elongation on the behaviour of granular materials in biaxial compression*. Comptes Rendus Mécanique, 2010. **338**(10): p. 587-595.
95. Stroeven, P. and H. He. *Packing of non-spherical aggregate particles by DEM*. in *ACCTA 2013: International Conference on Advances in Cement and Concrete Technology in Africa, Johannesburg, South Africa, 28-30 January 2013*. 2013.
96. *The Evolution Powder Tester compared to Shear Testers*. (Evolution Application Bulletin 2, Mercury Scientific Inc., [www.mercuryscientific.com](http://www.mercuryscientific.com)).
97. Jenike, A.W., *Gravity flow of bulk solids*. Bulletin No. 108, Utah State University, 1961.
98. Sun, C.C., *Setting the bar for powder flow properties in successful high speed tableting*. Powder technology, 2010. **201**(1): p. 106-108.
99. Opaliński, I., M. Chutkowski, and M. Stasiak, *Characterizing moist food-powder flowability using a Jenike shear-tester*. Journal of Food Engineering, 2012. **108**(1): p. 51-58.
100. Chen, P., et al., *Flow properties of three fuel powders*. Particuology, 2012. **10**(4): p. 438-443.
101. Chatteraj, S., L. Shi, and C.C. Sun, *Profoundly improving flow properties of a cohesive cellulose powder by surface coating with nano-silica through comilling*. Journal of pharmaceutical sciences, 2011. **100**(11): p. 4943-4952.
102. Härtl, J. and J.Y. Ooi, *Numerical investigation of particle shape and particle friction on limiting bulk friction in direct shear tests and comparison with experiments*. Powder Technology, 2011. **212**(1): p. 231-239.
103. Aigner, A., et al. *Determining the coefficient of friction by shear tester simulation*. in *3rd International Conference on Particle-Based Methods*. 2013.
104. Bilgili, E., et al., *Stress inhomogeneity in powder specimens tested in the Jenike shear cell: myth or fact?* Particle & Particle Systems Characterization, 2004. **21**(4): p. 293-302.
105. *Configuration of triaxial cell.*; Available from: [https://www.hydro.geo.tum.de/fileadmin/\\_processed\\_/csm\\_Triax\\_2406\\_8392d20b86.png](https://www.hydro.geo.tum.de/fileadmin/_processed_/csm_Triax_2406_8392d20b86.png).
106. Von Karman, T., *Festigkeitsprobleme im maschinenbau*. 1910: publisher not identified.
107. Lade, P.V. and J.M. Duncan, *Cubical triaxial tests on cohesionless soil*. Journal of geotechnical and geoenvironmental engineering, 1975. **101**(ASCE# 11269 Proceeding).
108. Cerni, G., et al., *Resilient behaviour of unbound granular materials through repeated load triaxial test: influence of the conditioning stress*. Road Materials and Pavement Design, 2015. **16**(1): p. 70-88.
109. Wu, K., et al., *Experimental and numerical study of cylindrical triaxial test on mono-sized glass beads under quasi-static loading condition*. Advanced Powder Technology, 2016.
110. Chen, J.-Y. and Y. Hai, *Mechanics properties of sand under triaxial test simulated by particle flow code*, in *Mechanics and Architectural Design*. 2016, WORLD SCIENTIFIC. p. 205-210.
111. Zhou, W., et al., *Macro-micro responses of crushable granular materials in simulated true triaxial tests*. Granular Matter, 2015. **17**(4): p. 497-509.
112. Saada, A. and F. Townsend, *State of the art: laboratory strength testing of soils*, in *Laboratory shear strength of soil*. 1981, ASTM International.
113. Schwedes, J., *Review on testers for measuring flow properties of bulk solids*. Granular matter, 2003. **5**(1): p. 1-43.

114. *Configuration of biaxial test*. Available from: <http://www.biomechanicalenvironments.com/engineering-physics-lab/tissue-mechanics-2/biaxial-mechanical-testing/>.
115. Le Bouil, A., et al., *A biaxial apparatus for the study of heterogeneous and intermittent strains in granular materials*. *Granular Matter*, 2014. **16**(1): p. 1-8.
116. Bi, Z.W., W.F. Huang, and G.X. Xiao, *Simulation of the Mechanical Characteristics of a Granular Matter Tested Under Biaxial Loading*. *Strength of Materials*, 2015. **47**(1): p. 192-197.
117. Jiang, M., et al., *An investigation on loose cemented granular materials via DEM analyses*. *Granular Matter*, 2013. **15**(1): p. 65-84.
118. Zhu, H., F. Nicot, and F. Darve, *Meso-structure evolution in a 2D granular material during biaxial loading*. *Granular Matter*, 2016. **18**(1): p. 3.
119. Freeman, T., *An introduction to uniaxial shear testing*.
120. *Uniaxial test step by step*. Available from: [http://www.azom.com/images/Article/Images/ImageForArticle\\_5668\(1\).jpg](http://www.azom.com/images/Article/Images/ImageForArticle_5668(1).jpg).
121. Ma, Q.-W., et al., *Characterization of Elastic Modulus of Granular Materials in a New Designed Uniaxial Oedometric System Supported by the National Natural Science Foundation of China under Grant Nos 11372038 and 11402023*. *Chinese Physics Letters*, 2016. **33**(3): p. 038101.
122. Neugebauer, A., et al., *Thermal conductivity and characterization of compacted, granular silica aerogel*. *Energy and Buildings*, 2014. **79**: p. 47-57.
123. Imole, O.I., et al., *Micro-macro correlations and anisotropy in granular assemblies under uniaxial loading and unloading*. *Physical Review E*, 2014. **89**(4): p. 042210.
124. Thakur, S.C., et al., *Micromechanical analysis of cohesive granular materials using the discrete element method with an adhesive elasto-plastic contact model*. *Granular Matter*, 2014. **16**(3): p. 383-400.
125. Hvorslev, M.J. *A ring shearing apparatus for the determination of the shearing resistance and plastic flow of soil*. in *Proceedings of the 1st International Conference on Soil Mechanics and Foundation Engineering*. 1936.
126. Carr, J. and D. Walker, *An annular shear cell for granular materials*. *Powder Technology*, 1968. **1**(6): p. 369-373.
127. Boyer, F., É. Guazzelli, and O. Pouliquen, *Unifying suspension and granular rheology*. *Physical review letters*, 2011. **107**(18): p. 188301.
128. Gaume, J., G. Chambon, and M. Naaim, *Quasistatic to inertial transition in granular materials and the role of fluctuations*. *Physical Review E*, 2011. **84**(5): p. 051304.
129. Henann, D.L. and K. Kamrin, *A predictive, size-dependent continuum model for dense granular flows*. *Proceedings of the National Academy of Sciences*, 2013. **110**(17): p. 6730-6735.
130. Osano, S., *Direct shear box and ring shear test comparison: why does internal angle of friction vary*. *ICASTOR Journal of Engineering*, 2009. **5**(2): p. 77-93.
131. Campbell, C.S. and C.E. Brennen, *Computer simulation of granular shear flows*. *Journal of Fluid Mechanics*, 1985. **151**: p. 167-188.
132. Campbell, C.S. and A. Gong, *The stress tensor in a two-dimensional granular shear flow*. *Journal of Fluid Mechanics*, 1986. **164**: p. 107-125.
133. Campbell, C.S., *Boundary interactions for two-dimensional granular flows. Part 1. Flat boundaries, asymmetric stresses and couple stresses*. *Journal of Fluid Mechanics*, 1993. **247**: p. 111-136.
134. Campbell, C.S., *Boundary interactions for two-dimensional granular flows. Part 2. Roughened boundaries*. *Journal of Fluid Mechanics*, 1993. **247**: p. 137-156.
135. Campbell, C.S., *The stress tensor for simple shear flows of a granular material*. *Journal of Fluid Mechanics*, 1989. **203**: p. 449-473.

136. Savage, S. and R. Dai, *Studies of granular shear flows Wall slip velocities, 'layering' and self-diffusion*. Mechanics of Materials, 1993. **16**(1): p. 225-238.
137. Da Cruz, F., et al., *Macroscopic friction of dry granular materials*. Tribology series, 2003. **43**: p. 53-61.
138. Ning, Z. and M. Ghadiri, *Distinct element analysis of attrition of granular solids under shear deformation*. Chemical engineering science, 2006. **61**(18): p. 5991-6001.
139. Shojaee, Z., et al., *Shear flow of dense granular materials near smooth walls. II. Block formation and suppression of slip by rolling friction*. Physical Review E, 2012. **86**(1): p. 011302.
140. Baran, O. and L. Kondic, *Velocity profiles, stresses, and Bagnold scaling of sheared granular system in zero gravity*. Physics of Fluids (1994-present), 2005. **17**(7): p. 073304.
141. da Cruz, F., et al., *Rheophysics of dense granular materials: Discrete simulation of plane shear flows*. Physical Review E, 2005. **72**(2): p. 021309.
142. Ji, S. and H.H. Shen, *Internal parameters and regime map for soft polydispersed granular materials*. Journal of Rheology (1978-present), 2008. **52**(1): p. 87-103.
143. Pena, A., R. Garcia-Rojo, and H. Herrmann, *Influence of particle shape on sheared dense granular media*. Granular Matter, 2007. **9**(3-4): p. 279-291.
144. Guo, Y., et al., *Some computational considerations associated with discrete element modeling of cylindrical particles*. Powder technology, 2012. **228**: p. 193-198.
145. Tong, Z., et al., *Discrete element method analysis of non-coaxial flow under rotational shear*. International Journal for Numerical and Analytical Methods in Geomechanics, 2014.
146. Howell, D., R. Behringer, and C. Veje, *Stress fluctuations in a 2D granular Couette experiment: a continuous transition*. Physical Review Letters, 1999. **82**(26): p. 5241.
147. Hsiao, S.-S. and W.-L. Yang, *Stresses and transport phenomena in sheared granular flows with different wall conditions*. Physics of Fluids (1994-present), 2002. **14**(2): p. 612-621.
148. Hsiao, S.-S. and W.-L. Yang, *Transport property measurements in sheared granular flows*. Chemical engineering science, 2005. **60**(1): p. 187-199.
149. Chambon, G., et al., *Shear with comminution of a granular material: Microscopic deformations outside the shear band*. Physical Review E, 2003. **68**(1): p. 011304.
150. Cheng, X., et al., *Three-dimensional shear in granular flow*. Physical review letters, 2006. **96**(3): p. 038001.
151. Lätzel, M., et al., *Comparing simulation and experiment of a 2D granular Couette shear device*. The European Physical Journal E, 2003. **11**(4): p. 325-333.
152. Jasti, V. and C.F. Higgs III, *Experimental study of granular flows in a rough annular shear cell*. Physical Review E, 2008. **78**(4): p. 041306.
153. Jenkins, J. and M. Richman, *Boundary conditions for plane flows of smooth, nearly elastic, circular disks*. Journal of Fluid Mechanics, 1986. **171**: p. 53-69.
154. Wildman, R., et al., *Experimental investigation and kinetic-theory-based model of a rapid granular shear flow*. Journal of Fluid Mechanics, 2008. **602**: p. 63-79.
155. Orlando, A.D. and H.H. Shen, *Effect of particle size and boundary conditions on the shear stress in an annular shear cell*. Granular Matter, 2012. **14**(3): p. 423-431.
156. Orlando, A.D. and H.H. Shen, *Using the annular shear cell as a rheometer for rapidly sheared granular materials: a DEM study*. Granular Matter, 2013. **15**(2): p. 183-194.
157. Orlando, A.D. and H.H. Shen, *Particle size and boundary geometry effects on the bulk friction coefficient of sheared granular materials in the inertial regime*. Comptes Rendus Mécanique, 2014. **342**(3): p. 151-155.
158. Murdoch, N., et al., *Granular shear flow in varying gravitational environments*. Granular Matter, 2013. **15**(2): p. 129-137.
159. Lu, K., E. Brodsky, and H. Kavehpour, *Shear-weakening of the transitional regime for granular flow*. Journal of Fluid Mechanics, 2007. **587**: p. 347-372.

160. Koval, G., et al., *Annular shear of cohesionless granular materials: from the inertial to quasistatic regime*. Physical Review E, 2009. **79**(2): p. 021306.
161. Salmon, J.-B., et al., *Velocity profiles in shear-banding wormlike micelles*. Physical review letters, 2003. **90**(22): p. 228303.
162. Börzsönyi, T., et al., *Shear-induced alignment and dynamics of elongated granular particles*. Physical Review E, 2012. **86**(5): p. 051304.
163. Ghadiri, M., et al., *Attrition of granular solids in a shear cell*. Chemical Engineering Science, 2000. **55**(22): p. 5445-5456.
164. Zhu, H.P. and A.B. Yu, *Steady-state granular flow in a 3D cylindrical hopper with flat bottom: macroscopic analysis*. Granular Matter, 2005. **7**(2): p. 97-107.
165. Staron, L., P.-Y. Lagrée, and S. Popinet, *The granular silo as a continuum plastic flow: The hour-glass vs the clepsydra*. Physics of Fluids (1994-present), 2012. **24**(10): p. 103301.
166. Yang, R., R. Zou, and A. Yu, *Microdynamic analysis of particle flow in a horizontal rotating drum*. Powder Technology, 2003. **130**(1): p. 138-146.
167. Hsiau, S.-S. and S.-C. Yang, *Numerical simulation of self-diffusion and mixing in a vibrated granular bed with the cohesive effect of liquid bridges*. Chemical Engineering Science, 2003. **58**(2): p. 339-351.
168. Silbert, L.E., et al., *Granular flow down an inclined plane: Bagnold scaling and rheology*. Physical Review E, 2001. **64**(5): p. 051302.
169. Lätzel, M., S. Luding, and H.J. Herrmann, *Macroscopic material properties from quasi-static, microscopic simulations of a two-dimensional shear-cell*. Granular Matter, 2000. **2**(3): p. 123-135.
170. Vescovi, D., C. Prisco, and D. Berzi, *From solid to granular gases: the steady state for granular materials*. International Journal for Numerical and Analytical Methods in Geomechanics, 2013. **37**(17): p. 2937-2951.
171. Jop, P., *Hydrodynamic modeling of granular flows in a modified Couette cell*. Physical Review E, 2008. **77**(3): p. 032301.
172. Luding, S. and F. Alonso-Marroquín, *The critical-state yield stress (termination locus) of adhesive powders from a single numerical experiment*. Granular Matter, 2011. **13**(2): p. 109-119.
173. Hsiau, S.-S. and Y.-M. Shieh, *Fluctuations and self-diffusion of sheared granular material flows*. Journal of Rheology (1978-present), 1999. **43**(5): p. 1049-1066.
174. *Simulation of blender*. Available from: <http://www.youtube.com/watch?v=Wjsx7U7yJME>.
175. *Simulation of conveyor and mixer*. Available from: <http://www.youtube.com/watch?v=mzY1MSQKsXU>.
176. Crossley, F., *Coefficient of restitution interpreted as damping in vibroimpact*. Journal of Applied Mechanics, Transactions ASME, 1975. **42**.
177. Zhou, Y., et al., *Microdynamic analysis of the particle flow in a cylindrical bladed mixer*. Chemical engineering science, 2004. **59**(6): p. 1343-1364.
178. Guerin, E., et al., *Rheological characterization of pharmaceutical powders using tap testing, shear cell and mercury porosimeter*. International journal of pharmaceutics, 1999. **189**(1): p. 91-103.
179. Sun, Q. and G. Wang, *Mechanics of granular matter*. 2013: WIT Press.
180. Vescovi, D., et al., *Plane shear flows of frictionless spheres: Kinetic theory and 3D soft-sphere discrete element method simulations*. Physics of Fluids (1994-present), 2014. **26**(5): p. 053305.
181. Losert, W., et al., *Particle dynamics in sheared granular matter*. Physical review letters, 2000. **85**(7): p. 1428.
182. Hassanpour, A., Y. Ding, and M. Ghadiri, *Shear deformation of binary mixtures of dry particulate solids*. Advanced Powder Technology, 2004. **15**(6): p. 687-697.

183. Wegner, S., et al., *Alignment and dynamics of elongated cylinders under shear*. *Soft Matter*, 2012. **8**(42): p. 10950-10958.
184. Reddy, K.A., V. Kumaran, and J. Talbot, *Orientational ordering in sheared inelastic dumbbells*. *Physical Review E*, 2009. **80**(3): p. 031304.
185. Mueth, D.M., H.M. Jaeger, and S.R. Nagel, *Force distribution in a granular medium*. *Physical Review E*, 1998. **57**(3): p. 3164.
186. Müller, M.-K., S. Luding, and T. Pöschel, *Force statistics and correlations in dense granular packings*. *Chemical Physics*, 2010. **375**(2): p. 600-605.
187. Campbell, C.S., *Rapid granular flows*. *Annual Review of Fluid Mechanics*, 1990. **22**(1): p. 57-90.
188. Chou, S. and S. Hsiau, *Dynamic properties of immersed granular matter in different flow regimes in a rotating drum*. *Powder technology*, 2012. **226**: p. 99-106.
189. Zhu, H. and A. Yu, *Micromechanic modeling and analysis of unsteady-state granular flow in a cylindrical hopper*, in *Mathematics and Mechanics of Granular Materials*. 2005, Springer. p. 307-320.
190. Zhao, H. and L. Ge, *Investigation on the shear moduli and damping ratios of silica gel*. *Granular Matter*, 2014. **16**(4): p. 449-456.
191. Zhou, Y.C., A.B. Yu, and J. Bridgwater, *Segregation of binary mixture of particles in a bladed mixer*. *Journal of Chemical Technology and Biotechnology*, 2003. **78**(2-3): p. 187-193.
192. Liu, W., G. Tomlinson, and J. Rongong, *The dynamic characterisation of disk geometry particle dampers*. *Journal of Sound and Vibration*, 2005. **280**(3-5): p. 849-861.
193. Pouliquen, O. and F. Chevoir, *Dense flows of dry granular material*. *Comptes Rendus Physique*, 2002. **3**(2): p. 163-175.
194. Chialvo, S., J. Sun, and S. Sundaresan, *Bridging the rheology of granular flows in three regimes*. *Physical Review E*, 2012. **85**(2): p. 021305.
195. Yang, R., et al., *Numerical simulation of particle dynamics in different flow regimes in a rotating drum*. *Powder Technology*, 2008. **188**(2): p. 170-177.
196. Trulsson, M., B. Andreotti, and P. Claudin, *Transition from the viscous to inertial regime in dense suspensions*. *Physical review letters*, 2012. **109**(11): p. 118305.
197. Majmudar, T.S. and R.P. Behringer, *Contact force measurements and stress-induced anisotropy in granular materials*. *Nature*, 2005. **435**(7045): p. 1079-1082.
198. O'Hern, C.S., et al., *Force distributions near jamming and glass transitions*. *Physical Review Letters*, 2001. **86**(1): p. 111.
199. van Eerd, A.R., et al., *Tail of the contact force distribution in static granular materials*. *Physical Review E*, 2007. **75**(6): p. 060302.